Design and Evaluation of New Waveforms for High Mobility Communications

Tomás Domínguez Bolaño

Doctoral Thesis UDC / 2018

Advisors: Luis Castedo Ribas
José Antonio García Naya

PhD Program in Information Technology and Mobile Network Communication

Deseño e Avaliación de Novas Formas de Onda para Comunicacións de Alta Mobilidade

Tomás Domínguez Bolaño

Tese de Doutoramento UDC / 2018

Directores: Luis Castedo Ribas
José Antonio García Naya

Programa de Doutoramento en Tecnoloxías da Información e das Comunicacións en Redes Móbiles

Diseño y Evaluación de Nuevas Formas de Onda para Comunicaciones de Alta Movilidad

Tomás Domínguez Bolaño

Tesis Doctoral UDC / 2018

Directores: Luis Castedo Ribas
José Antonio García Naya

Programa de Doctorado en Tecnologías de la Información y de las Comunicaciones en Redes Móviles

Tomás Domínguez Bolaño

CERTIFICA / *CERTIFICA* / *CERTIFIES*

Que a presente memoria é o resultado do meu propio traballo de investigación e que o traballo doutros autores está citado axeitadamente.

Que la presente memoria es el resultado de mi propio trabajo de investigación y que el trabajo de otros autores está citado apropiadamente.

That the present report is the result of my own research work and that the work done by other authors is appropriately cited.

A Coruña, *setembro de 2018* / *septiembre de 2018* / *September 2018*

Tomás Domínguez Bolaño

Luis Castedo Ribas
José Antonio García Naya

CERTIFICAN / *CERTIFICAN* / *CERTIFY*

Que a presente tese titulada "Deseño e avaliación de novas formas de onda para comunicacións de alta mobilidade" foi realizada por Tomás Domínguez Bolaño baixo a nosa dirección no Departamento de Enxeñaría de Computadores da Universidade da Coruña e preséntase para obter o grao de Doutor.

Que la presente tesis titulada "Diseño y evaluación de nuevas formas de onda para comunicaciones de alta movilidad" fue realizada por Tomás Domínguez Bolaño bajo nuestra dirección en el Departamento de Ingeniería de Computadores de la Universidade da Coruña y se presenta para obtener el grado de Doctor.

That the present thesis titled "Design and evaluation of new waveforms for high mobility communications" was done by Tomás Domínguez Bolaño under our supervision in the Department of Computer Engineering at the University of A Coruña and it is submitted to obtain the Ph.D. degree.

Os directores da tese / *Los directores de la tesis* / *The Ph.D. supervisors*.
A Coruña, setembro de 2018 / *septiembre de 2018* / *September 2018*.

Dr. Luis Castedo Ribas
Catedrático de Universidade
Dpto. de Enxeñaría de Computadores
Universidade da Coruña

Full Professor
Dept. of Computer Engineering
University of A Coruña

Dr. José Antonio García Naya
Prof. Contratado Doutor
Dpto. de Enxeñaría de Computadores
Universidade da Coruña

Ph.D. Associate Professor
Dept. of Computer Engineering
University of A Coruña

Tese de Doutoramento / *Tesis Doctoral* / *Doctoral Thesis*

Título:	Deseño e avaliación de novas formas de onda para comunicacións de alta mobilidade
***Título*:**	*Diseño y evaluación de nuevas formas de onda para comunicaciones de alta movilidad*
***Title*:**	*Design and evaluation of new waveforms for high mobility communications*
Autor / *Autor* / *Author*:	Tomás Domínguez Bolaño
Directores / *Directores* / *Supervisors*:	Luis Castedo Ribas José Antonio García Naya
Data / *Fecha* / *Date*:	setembro de 2018 / *septiembre de 2018* / *September 2018*

Tribunal / *Tribunal* / *Evaluation Committee*

Presidente / *Presidente* / *President*:	Markus Rupp
Vogal / *Vocal* / *Member*:	Xuefeng Yin
Secretaria / *Secretaria* / *Secretary*:	Paula M. Castro Castro

To my family

Acknowledgements

I want to express my gratitude to my PhD advisors, Luis Castedo and José Antonio. Luis Castedo was also the advisor of my bachelor's thesis, and once finished, he gave me the opportunity to work at the GTEC these last 4 years. I thank José Antonio for all his invaluable support and effort during all these years, without which this thesis could not have been finished.

In the last four years I was fortunate to be able to work with Xose, I have to thank him also for all the support and help during these years. It is also thanks to him that this thesis has come to fruition. The last year, Xose decided to leave for a postdoc position at Tongji University (China, Shanghai). Thanks to that I was able to carry out a 4-month research stay there. Xosé's support was essential during the stay, not only for research purposes, but also for logistics. I also want to thank Yin Xuefeng, my supervisor at Tongji university. I also thank the students with whom I worked in China for all the good times that we had: Xuesong, Xiaokang, Liuyuan, Jingxiang, Sibo, Zeyu, Yejian, Kai, Hui, Chao and Le. I will always remember the measurement campaigns with the drone, in which we worked very hard.

I also thank my colleagues of the GTEC Lab, for all the help and good times during the last years: Pedro, Óscar, Ángel, Valentín, Manuel, Paula, José Francisco and José Pablo.

Finally, I thank my mother for all her support.

Resumo

Os servizos multimedia e de datos experimentaron un crecemento continuo nos últimos anos e espérase que crezan aínda máis nos anos seguintes. A xente está a usar cada vez máis os seus dispositivos móbiles para acceder a servizos baseados en datos para fins relacionados co traballo, entretemento ou socialización en liña. Ademais, as comunicacións masivas de tipo máquina tamén están en ascenso (por exemplo, as comunicacións en transporte e loxística, sensores, Internet das cousas, etc.), e serán moi importantes para a nova xeración de sistemas de comunicacións sen fíos. Para afrontar o aumento esperado no uso de servizos multimedia e baseado en datos, así como para soportar novos casos de uso que hoxe non son posibles, unha nova xeración de redes sen fíos é necesaria. Para iso, espérase que os sistemas de comunicación sen fíos 5G traian as melloras necesarias: maiores taxas de datos, baixas latencias, mellor eficiencia enerxética, alta fiabilidade, etc.

O coñecemento das características da canle sen fíos é fundamental para a planificación das redes de comunicación sen fíos e o deseño de transceptores. Como primeiro paso, centramos este traballo na caracterización completa da canle para diferentes escenarios, como son os trens de alta velocidade, metro e comunicacións vehículo a infraestrutura en estradas. A canle caracterizouse mediante a avaliación da relación sinal a ruído, a perda de traxecto (path loss) e os chamados parámetros condensados da canle (por exemplo, o factor K, o perfil potencia-retardo (power delay profile) e a densidade espectral de potencia Doppler.

Ademais, para a nova interface aérea das redes 5G, unha das principais cuestións foi a forma de onda a usar. Finalmente, o 3rd Generation Partnership Project (3GPP) decidiu usar a tecnoloxía de multiplexación por división de frecuencias ortogonais (OFDM polas súas siglas en inglés). Isto semella unha elección natural debido ás moitas vantaxes de OFDM e que tamén é a técnica de modulación empregada nas redes 4G. Con todo, nos últimos anos, esquemas multiportadora baseados en bancos de filtros (FBMC polas súas siglas en inglés) recibiron unha grande atención como alternativa a OFDM debido ás súas vantaxes: non utilizan un prefixo cíclico (proporcionan unha maior eficiencia espectral), os usuarios non precisan ser sincronizados no enlace ascendente, e un mellor rendemento teórico en contornas de alta velocidade debido a unha menor interferencia entre portadoras. Neste traballo comparamos experimentalmente o rendemento de FBMC e OFDM en contornas de alta velocidade. Tamén analizamos o rendemento de FBMC e OFDM no caso de uso práctico dun vehículo aéreo lixeiro pilotado remotamente. A maior parte do traballo realizado nesta tese requiriu o deseño e desenvolvemento do chamado GTEC 5G Simulator, que foi usado en conxunto co GTEC Testbed para realizar a maior parte das campañas de medicións e avaliacións de rendemento mediante transmisións polo aire.

Resumen

Los servicios multimedia y basados en datos experimentaron un crecimiento sin interrupciones en los últimos años, y se espera que crezcan aún más en los años siguientes. Las personas utilizan cada vez más sus dispositivos móviles para acceder a los servicios basados en datos con fines relacionados con el trabajo, el entretenimiento o la socialización en línea. Además, las comunicaciones masivas de tipo máquina también están en aumento (por ejemplo, comunicaciones en transporte y logística, sensores, Internet de las cosas, etc.) y serán muy importantes para la nueva generación de sistemas de comunicaciones inalámbricos. Para hacer frente al aumento esperado en el uso de servicios multimedia y basados en datos, así como para soportar nuevos casos de uso que no son posibles hoy en día, se requiere una nueva generación de sistemas inalámbricos. Para esto, se espera que los sistemas de comunicación inalámbrica 5G aporten las mejoras necesarias: mayores tasas de datos, menores latencias, mejor eficiencia energética, alta fiabilidad, etc.

El conocimiento de las características del canal inalámbrico es fundamental para la planificación de redes de comunicación inalámbricas y el diseño de transceptores. Como primer paso, centramos este trabajo en la caracterización completa del canal para diferentes escenarios, tales como trenes de alta velocidad, metro y comunicaciones vehículo a infraestructura en carreteras. El canal se caracterizó por medio de la evaluación de la relación señal a ruido, la pérdida de trayecto (path loss) y los llamados parámetros condensados de canal (por ejemplo, el factor K, el perfil potencia-retardo (power delay profile) y la densidad espectral de potencia Doppler).

Además, para la nueva interfaz aérea de las redes 5G, una de las preguntas principales ha sido la forma de onda a usar. Finalmente, el 3rd Generation Partnership Project (3GPP) decidió usar la tecnología de multiplexación por división de frecuencias ortogonales (OFDM por sus siglas en inglés). Esta es una elección lógica, debido a las muchas ventajas exhibidas por OFDM y dado que también es la técnica de modulación empleada en las redes 4G. Sin embargo, en los últimos años, los esquemas multiportadora basados en bancos de filtros (FBMC por sus siglas en inglés) han recibido una gran atención como una alternativa a OFDM debido a sus ventajas: no usan un prefijo cíclico (lo que proporciona una mayor eficiencia espectral), los usuarios no necesitan sincronizarse en el enlace ascendente, y un mejor rendimiento teórico en escenarios de alta velocidad debido a una menor interferencia entre subportadoras. En este trabajo comparamos experimentalmente el rendimiento de FBMC y OFDM en entornos de alta velocidad. También analizamos el rendimiento de FBMC y OFDM en el caso de uso práctico de un vehículo aéreo ligero tripulado remotamente. La mayor parte del trabajo llevado a cabo en esta tesis requirió el diseño y desarrollo del denominado GTEC 5G Simulator, que se utilizó junto con el GTEC Testbed para realizar la mayoría de las campañas de medidas y evaluaciones de rendimiento por medio de transmisiones por aire.

Abstract

Multimedia and data-based services experienced a non-stopping growth over the last few years and are expected to grow even more in the following years. People are using more and more their mobile devices to access data-based services for work-related purposes, entertainment or online socialization. Moreover, massive machine-type communications are also on the rise (e.g., transport and logistics communications, sensors, Internet of Things, etc.), and will be very important for the new generation of wireless communication systems. To cope with the expected increase in the usage of multimedia and data-based services, as well as to support new use cases which are not possible today, a new generation of wireless systems is required. For this, 5G wireless communication systems are expected to bring the necessary improvements: higher data rates, lower latencies, better energy efficiency, high reliability, etc.

Knowledge of the wireless channel characteristics is fundamental for the planning of wireless communication networks and transceivers design. As a first step, this work centered in the channel characterization for different scenarios such as high-speed trains, subways, and vehicle-to-infrastructure in roads. The channel was characterized by means of assessing the signal-to-noise ratio, the path loss, and the so-called channel condensed parameters (e.g., the K-factor, the power delay profile, and the Doppler power spectral density).

Moreover, for the new air interface of 5G networks, one of the main questions was the waveform to be used. Finally, the 3rd Generation Partnership Project (3GPP) decided to use orthogonal frequency-division multiplexing (OFDM). This seems a natural choice due to the many advantages exhibited by OFDM and it is also the modulation technique employed by 4G networks. However, over the last few years, schemes based on filter bank multicarrier (FBMC) using quadrature amplitude modulation have received a great attention as an alternative to OFDM due to their advantages: they do not use a cyclic prefix (thus providing a higher bandwidth efficiency), users do not need to be synchronized in the uplink, and they achieve a theoretical better performance in high-speed scenarios due to a lower inter-carrier interference. In this work, we have experimentally compared the performance of FBMC versus OFDM in high-speed scenarios. We have also analyzed the performance of FBMC versus OFDM in the practical use case of a lightweight remotely piloted aircraft. The majority of the work carried out in this thesis required the design and development of the so-called GTEC 5G Simulator, which was used in conjunction with the GTEC Testbed to perform most of the measurement campaigns and performance evaluations by means of over-the-air transmissions.

Table of Contents

List of Figures

List of Tables

Chapter I

Introduction

Multimedia and data-based services experienced a non-stopping growth over the last few years and are expected to grow even more in the following. People are using more and more their mobile devices to access data-based services for work-related purposes, entertainment or online socialization [SR16]. Moreover, massive machine-type communications (mMTC) are also on the rise (e.g., transport and logistics communications, sensors, Internet of things (IoT), etc.) and will be very important for the new generation of wireless systems. The fourth generation (4G) of wireless communications systems, using the Long Term Evolution (LTE) standards, have been commercially deployed since 2009. 4G systems following the international mobile telecommunications advanced (IMT-Advanced) requirements, as defined by ITU Radiocommunication Sector (ITU-R), provided a very large improvement over the previous third generation (3G). Some of the improvements included the increase of the peak data rate (for both low and high mobility situations), the ability to dynamically share and use the network resources, the usage of scalable channel bandwidths, and the increase of the spectral efficiency. However, in order to cope with the expected increase in the usage of multimedia and data-based services, as well as to support new use cases not possible today, a new generation of wireless systems is required. For this, the fifth generation (5G) wireless communication systems are expected to bring the necessary improvements, including higher data rates, lower latencies, a better energy efficiency, high reliability for communications, etc. 5G wireless systems will support three generic services [POP+18]:

- enhanced mobile broadband (eMBB): This service will be an evolution of the services already provided by 4G, providing stable connections with high peak data rates, low latencies, and moderate rates for users on the cell edges. In this service, different mobility classes are considered, ranging from stationary to high-speed mobility up to 500 km/h [ITU17].
- mMTC: this service is intended for sensors or IoT-like devices. It will support a high number of devices that can be active sporadically and send small data payloads.
- ultra-reliable and low-latency communications (URLLC): this service is intended for low-latency transmissions of small payloads with very high reliability.

To make all these improvements possible, 5G will use a new physical layer interface defined by the 3rd Generation Partnership Project (3GPP) and known as new radio (NR), as well as a new core network architecture.

One of the main effects impacting on wireless communications is the multipath propagation. In wireless communications, the signals reach the receiver from the transmitter following different paths. Usually, a direct line-of-sight (LoS) path exists, but also the signal will be reflected and diffracted by different objects in the environment. Different delayed multipath components are added up at the receiver, hence creating frequency-selective channels. One of the main tasks of a wireless receiver is to equalize the channel, i.e., undoing the effect of the channel on the signal. In this regard, multicarrier modulation techniques allow for solving this problem in a computationally effective way by dividing the channel frequency response into narrower sub-channels in which the frequency selectivity can be considered flat. More specifically, orthogonal frequency-division multiplexing (OFDM) is one of the most used multicarrier modulations today.

Another important effect impacting on wireless communications is the Doppler effect, named after the Austrian physicist Christian Doppler, who postulated the effect in 1842. The movement of a receiver relative to the transmitter leads to a frequency shift of the received signal, which is called a Doppler shift. More specifically, each of the multipath components of the signal arriving at the receiver will experience a different Doppler shift depending on the relative angle of arrival with respect to the receiver. Also, as this effect depends on the speed, the magnitude of the frequency shift will be proportional to the relative velocity between the transmitter and the receiver, i.e., higher speeds lead to greater frequency shifts. These shifts on the received paths can create notorious inter-carrier interferences on the received signals when moving at high speeds, for example in the case of high-speed trains (HSTs).

For the new air interface of the 5G networks, one of the main questions was the technology to be used. Finally, the 3rd Generation Partnership Project (3GPP) decided that OFDM was adopted for the new 5G networks [TECa]. This seems a natural choice due to the many advantages provided by OFDM and because OFDM is also the modulation technique used in the 4G LTE standard. Some of the most remarkable features of OFDM are its robustness against multipath (frequency-selective channels), and that it can be implemented very efficiently by using an inverse fast Fourier transform (IFFT) at the transmitter and a fast Fourier transform (FFT) at the receiver. However, the robustness against multi-path channels is achieved by inserting a cyclic prefix (CP) into each OFDM symbol, which reduces the spectral efficiency, whereas the time-domain rectangular-shape of the symbols leads to a large out-of-band power radiation observed in the signal frequency spectrum. Moreover, for high-speed conditions, the large out-of-band power radiation of the sub-carriers will lead to a large inter-carrier interference level.

Over the last few years, schemes based on filter bank multicarrier (FBMC) using offset quadrature amplitude modulation (OQAM) have received some attention as a promising

alternative to OFDM [FAR11]. These schemes offer some advantages with respect to OFDM. For example, they do not use a CP, hence providing a higher bandwidth efficiency with respect to OFDM; the different users in the uplink do not need to be synchronized, and can yield a better performance in high-speed channels due to a lower inter-carrier interference level.

1.1 Thesis Overview

Two different parts can be distinguished in this thesis. First, a complete channel characterization is carried out for different scenarios such as HSTs, subways, and vehicle-to-infrastructure (V2I) in roads. Next, the performance of FBMC vs OFDM is experimentally compared in high-speed environments. We have also analyzed the performance of FBMC vs OFDM in the practical use case of a remotely piloted aircraft (RPA). The majority of the work carried out in this thesis has required the design and development of the so-called GTEC 5G simulator, which has been used in conjunction with the GTEC Testbed to perform most of the measurement campaigns and performance evaluations by means of over-the-air transmissions.

The present thesis is structured in eight chapters, including this one. A brief summary of each chapter is presented below.

Chapter 2 presents in detail a testbed and a modular link-level simulator developed by the GTEC group at the University of A Coruña, known as the GTEC Testbed and GTEC 5G simulator, respectively. This testbed and simulator were developed in order to evaluate the current 4G and future 5G communication techniques, and were used to obtain many of the results presented in the successive chapters.

Chapter 3 accounts for the detailed characterization of the downlink between an LTE Evolved Node B (eNodeB) and a HST based on measurements carried out in a commercial HST line. Two links are considered: the one between the eNodeB and the antennas placed outdoors on the train roof, and the direct link between the eNodeB and a receiver inside the train. Such a characterization consists in assessing the path loss, the signal-to-noise ratio (SNR), the K-factor, the power delay profile (PDP), the delay spread, and the Doppler power spectral density (PSD) for different train speeds.

Chapter 4 accounts for the characterization of the wireless channel in a modern subway station and its corresponding entrance tunnel, a topic greatly overlooked in the literature. We setup an LTE eNodeB transmitter in the middle of the platform of a modern station in the Madrid Metro, Spain, to cyclically transmit frequency-division duplex (FDD) LTE signals at a carrier frequency of 2.6 GHz with a bandwidth of 10 MHz. Two receivers were used to investigate both the eNodeB-train and the eNodeB-mobile links. The train was moving at a constant speed of 18 km/h from the entrance tunnel until it is completely stopped at the end of the station. Using the multipath components extracted with the space-alternating generalized expectation-maximization (SAGE) algorithm we characterized the wireless channel response for both links based on the following parameters: power delay profile, root mean square delay spread, Doppler

power spectral density, small-scale fading distribution, and K-factor.

Chapter 5 presents the characterization of the wireless channel using LTE signals (employing a time-division duplex mode) in an urban scenario at the University of A Coruña, considering a V2I setup with a car equipped with four receive antennas. We study typical channel parameters such as SNR, PDP, Doppler PSD, and root mean square (RMS) delay profile, together with a diversity gain assessment by means of typical antenna combining methods, namely selection combining (SC), equal gain combining (EGC), and maximum ratio combining (MRC). We show that, in this case, although EGC and MRC offer the best theoretical performance at the expense of a higher complexity, the presence of LoS conditions and a strong SNR difference between the receive antennas yield favorable conditions for simple schemes such as SC.

Chapter 6 considers the performance analysis of FBMC. Firstly, the performance of two common prototype filters for FBMC is studied analytically and by means of computer simulations considering standardized channel models for static scenarios. The results are also compared to OFDM. FBMC is next experimentally evaluated through over-the-air transmissions in different environments using the GTEC Testbed, devoting special attention to the performance of FBMC in high-speed scenarios. We also include the results obtained for OFDM signals for comparison purposes. To carry out this analysis, we considered a technique to induce effects caused by highly-time varying channels on multicarrier signals while conducting measurements at low speeds. This technique has been proved to be accurate for the cases of Worldwide Interoperability for Microwave Access (WiMAX) and LTE signals, as well as the waveforms proposed for 5G systems, such as FBMC.

Chapter 7 investigates experimentally the feasibility of serving aerial vehicles using LTE network deployments with eNodeB antennas targeting terrestrial coverage. The performed measurement campaign comprised a wide set of results. On the one hand, horizontal flights at eight different height values, ranging from $15\,\mathrm{m}$ to $105\,\mathrm{m}$, were performed for two different suburban scenarios with varying obstacle density. On the other hand, vertical flights, from $20\,\mathrm{m}$ to $100\,\mathrm{m}$, were also considered for different horizontal distances to the transmitter. In order to study the effect of the transmit antenna radiation pattern, two configurations were considered, one corresponding to an omnidirectional antenna, and the other corresponding to a typical base station antenna. Finally, five different carrier frequency values were considered, from $850\,\mathrm{MHz}$ to $3.5\,\mathrm{GHz}$. We transmitted commercial signals (we considered both LTE signals ($10\,\mathrm{MHz}$ profile) as well as a FBMC-based signals with similar characteristics and bandwidth) and evaluate high-level figures of merit such as (coded and uncoded) bit error rate (BER), error vector magnitude (EVM) and throughput.

Finally, Chapter 8 end the thesis by presenting the main conclusions derived from this work and the proposed future work.

1.2 Thesis Methodology and Resources

In this thesis, two different parts can be distinguished. First, we characterized the wireless communication channel for several environments: HSTs, subways, and V2I in roads. Second, the performance of FBMC vs OFDM was experimentally assessed in high-speed environments and in a practical use case of an RPA.

For the first part the methodology was the following:

- Study the available literature to learn how the wireless communications channels can be analyzed and described based on several parameters. Among others, one of the topics studied was the usage of high resolution parameter estimation (HRPE) algorithms to characterize the channel response.
- Perform a characterization of the channel in novel scenarios or with novel characteristics. This characterization was performed using already available measurements, that were carried out in the past in our research group.

For the second part where we performed an assessment of the performance of FBMC, the methodology was the following:

- Study the available literature to learn the details of FBMC.
- Implement a software to evaluate the performance of FBMC and OFDM. This software is the so-called GTEC 5G Simulator which is detailed in Chapter 2.
- Perform several measurement campaigns in order to evaluate FBMC and OFDM. First, two measurement campaigns were performed at the University of A Coruña to evaluate the performance of FBMC in high-speed environments. For this, a technique to emulate the effects of high-speed while conducting measurements at low speed was used. Later, a measurement campaign considering an RPA was conducted at the Tonji University, Shanghai.
- The performance of FBMC and OFDM was evaluated using the GTEC 5G Simulator.

The following resources were employed

- Bibliographic resources: scientific publications, information on the web, etc.
- The necessary hardware resources for performing the measurements. The specific hardware used for the measurements is explained in the respective chapters of the thesis.
- The necessary software for numerical simulation (i.e. MATLAB™), as well as for document edition (LaTeX).

1.3 Co-authored Publications

The work presented in this thesis led to the following co-authored publications included in the list below.

Journal Papers

1. Tomás Domínguez-Bolaño, José Rodríguez-Piñeiro, José Antonio García-Naya, Xuefeng Yin, and Luis Castedo. "**Measurement-based characterization of train-to-infrastructure 2.6 GHz propagation channel in a modern subway station**". Accepted in *IEEE Access*, 2018
2. Tomás Domínguez-Bolaño, José Rodríguez-Piñeiro, José Antonio García-Naya, and Luis Castedo. "**Experimental characterization and modeling of LTE wireless links in high-speed trains**". *Wireless Communications and Mobile Computing*, vol. 2017, no. 5079130, 2017, pp. 1–20.
   DOI: 10.1155/2017/5079130

Conference Papers

1. Tomás Domínguez-Bolaño, José Rodríguez-Piñeiro, José Antonio García-Naya, Xuefeng Yin, and Luis Castedo. "**Vehicle-to-infrastructure channel characterization based on LTE measurements**". *Proc. of 19th IEEE International Workshop on Signal Processing Advances in Wireless Communications (SPAWC 2018).* Kalamata, Greece, 2018
2. Tomás Domínguez-Bolaño, José Rodríguez-Piñeiro, José Antonio García-Naya, and Luis Castedo. "**Throughput-based performance evaluation of 5G-candidate waveforms in high speed scenarios**". *Proc. of 25th European Signal Processing Conference (EUSIPCO 2017).* Kos, Greece, 2017
3. José Rodríguez-Piñeiro, Tomás Domínguez-Bolaño, José Antonio García-Naya, and Luis Castedo Ribas. "**Performance assessment of 5G-candidate waveforms in high speed scenarios**". *Proc. of 27th IEEE International Symposium on Personal, Indoor and Mobile Radio Communications (PIMRC'16).* Valencia, Spain, 2016
4. Tomás Domínguez-Bolaño, José Rodríguez-Piñeiro, José A. García-Naya, and Luis Castedo. "**The GTEC 5G link-level simulator**". *Proc. of International Workshop on Link- and System-Level Simulations (IWSLS2 2016).* Vienna, Austria, 2016, pp. 64–69
5. José Rodríguez-Piñeiro, Martin Lerch, Tomás Domínguez-Bolaño, José Antonio García-Naya, Sebastian Caban, and Luis Castedo. "**Experimental assessment of 5G-candidate modulation schemes at extreme speeds**". *Proc. of Ninth IEEE Sensor Array and Multichannel Signal Processing Workshop (SAM 2016).* Río de Janeiro, Brazil, 2016
6. Tomás Domínguez-Bolaño, José Rodríguez-Piñeiro, José A. García-Naya, and Luis Castedo. "**Experimental evaluation of 5G modulation schemes in quasi-static scenarios**". *Proc. of 20th International ITG Workshop on Smart Antennas (WSA 2016).* Munich, Germany, 2016
7. José Rodríguez-Piñeiro, Tomás Domínguez-Bolaño, Pedro Suárez-Casal, José Antonio García-Naya, and Luis Castedo Ribas. "**Affordable evaluation of 5G modulation schemes in high speed train scenarios**". *Proc. of ITG Workshop on Smart Antennas*

(WSA 2016). Online access: https://www.vde-verlag.de/proceedings-en/454177072.html. Munich, Germany, 2016

Chapter II

The GTEC Testbed and the GTEC 5G Simulator

The recent rapid evolution of wireless communications constitutes a challenge for their versatile and flexible evaluation by means of over-the-air transmissions in different scenarios. In order to evaluate the current fourth generation (4G) and future fifth generation (5G) communication techniques, a testbed and a modular link-level simulator were developed at the GTEC group of the University of A Coruña. The testbed and the simulator were used to obtain the results that will be presented in the successive chapters. In this chapter, the testbed and the simulator are presented in detail.

This chapter is mainly based on the following co-authored publication:

- Tomás Domínguez-Bolaño, José Rodríguez-Piñeiro, José A. García-Naya, and Luis Castedo. "**The GTEC 5G link-level simulator**". *Proc. of International Workshop on Link- and System-Level Simulations (IWSLS2 2016)*. Vienna, Austria, 2016, pp. 64–69

This chapter is structured as follows. Section 2.1 introduces the chapter. Section 2.2 provides an overall description of the GTEC Testbed, including both the hardware and the software elements. We also explain how the GTEC 5G Simulator is integrated into the testbed structure. Section 2.3 describes the simulator architecture in detail, whereas Section 2.4 shows the way to perform simulations, including some exemplary results. Finally, Section 2.5 introduces the typical measurement methodology that we follow to perform evaluations using real world measurements. Section 2.6 concludes the chapter.

2.1 Introduction

The development of a versatile way of evaluating the performance of a new generations of wireless communications systems by means of over-the-air transmissions under different scenarios is a fundamental issue. In order to allow for the evaluation of the current fourth generation (4G) communication techniques, as well as the new fifth generation (5G) proposals,

a versatile and flexible testbed and simulator were developed by the GTEC group at the University of A Coruña. The testbed and the simulator are named GTEC Testbed and GTEC 5G Simulator, respectively. The related software and documentation were made publicly available [TEA] under the GPLv3 license [FRE]. The GTEC Testbed allows for performing experimental evaluations, by transmitting signals over the air, as well as receiving the signals for further processing. The GTEC 5G Simulator allows for performing link layer simulations both for orthogonal frequency-division multiplexing (OFDM) and filter bank multicarrier (FBMC) signals (see Chapter 6 for more details on FBMC). It includes fully-functional transmitter and receiver implementations, as well as different channel models and functions for processing the obtained results. Its modular implementation enables us to easily modify or add functionalities by changing or implementing new modules, respectively. Several data structures are defined for parameters and constants, providing a standardized way to configure any module of the simulator. Moreover, the GTEC 5G simulator is fully integrated with the GTEC Testbed, enabling not only to perform simulation-based evaluations, but also to carry out over-the-air measurements in different environments. Hence, the GTEC Testbed and the GTEC 5G Simulator are very valuable tools for evaluating wireless communication systems in a versatile and flexible way.

2.2 The GTEC Testbed

In this section we briefly describe the testbed developed in our research group (GTEC), which was extensively used for experimental evaluations of Worldwide Interoperability for Microwave Access (WiMAX) signals in high speed environments (see [SUÁ+14b; ROD+14; SUÁ+14a]), Long Term Evolution (LTE) signals in subways, railway scenarios and high-speed environments (see Chapters 3 and 4, [ROD+16c; ZHA+16b; FEI+16]). Finally, it has been used also for experimental evaluations of the new waveform proposals for 5G systems (see Chapter 6). The GTEC Testbed allows us to convert previously generated data into electromagnetic waveforms that are transmitted over-the-air, as well as to receive and store the acquired samples for further processing. The testbed consists of several nodes which are evolved versions of the ones described in [ROD+13]. Both the hardware and the software parts of the nodes are described below. Figure 2.1 shows a typical configuration of the testbed, in which one of the nodes is used in transmit-only mode while the other is set up in receive-only mode.

2.2.1 Hardware

The heart of each node of the GTEC Testbed is an Universal Software Radio Peripheral (USRP™)[1] B210 board [RESa] built from the AD9361 chip [ANA] by Analog Devices, which

[1] USRP™ is a registered trademark of National Instruments Corp.

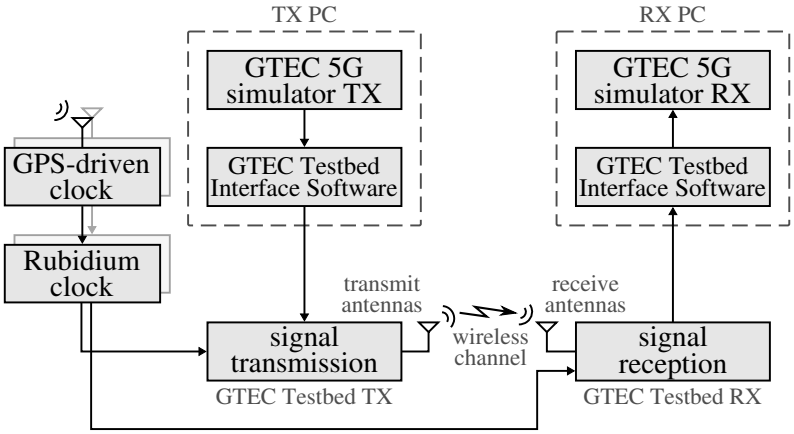

Figure 2.1: GTEC Testbed structure. Exemplary configuration with one transmitter node and one receiver node.

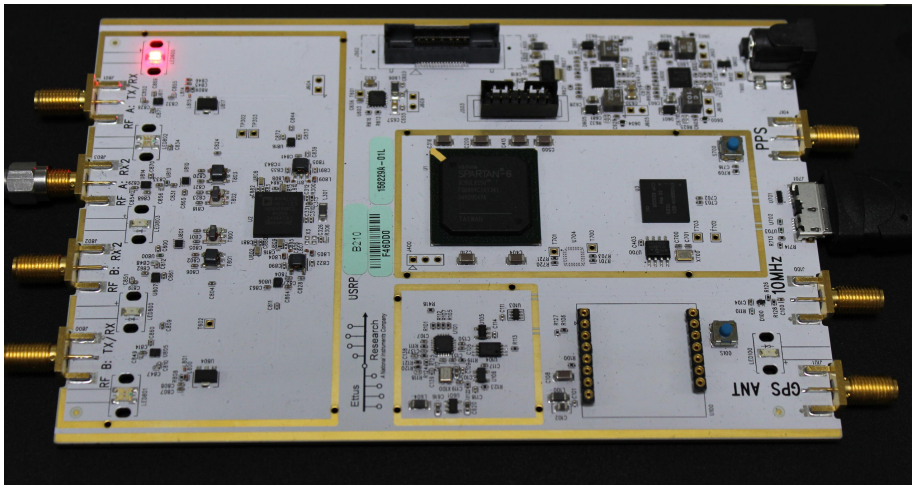

Figure 2.2: Picture of the USRP™ B210 board.

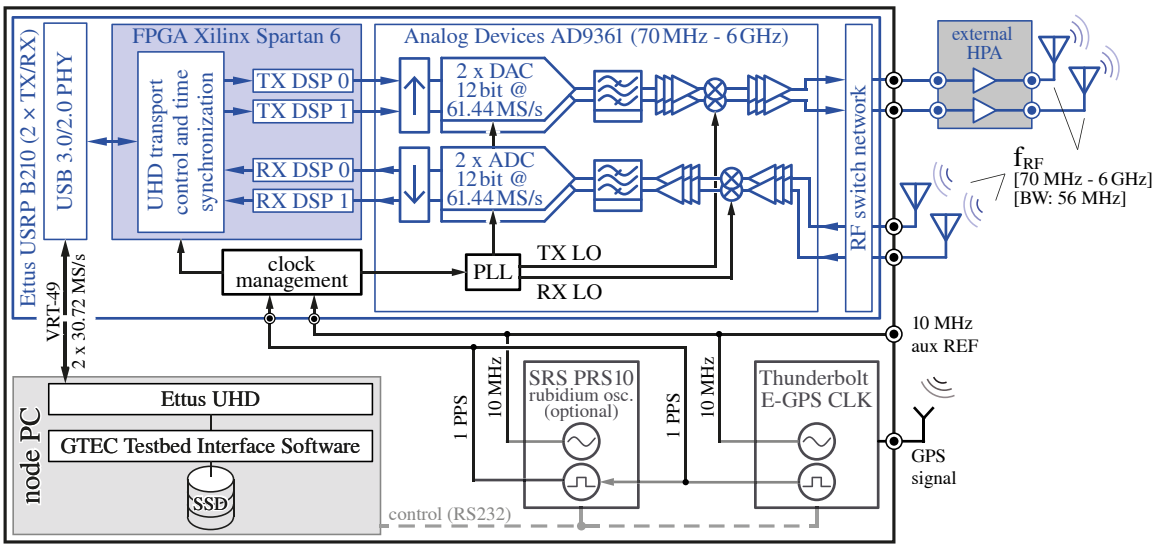

Figure 2.3: Block diagram of a node of the GTEC Testbed.

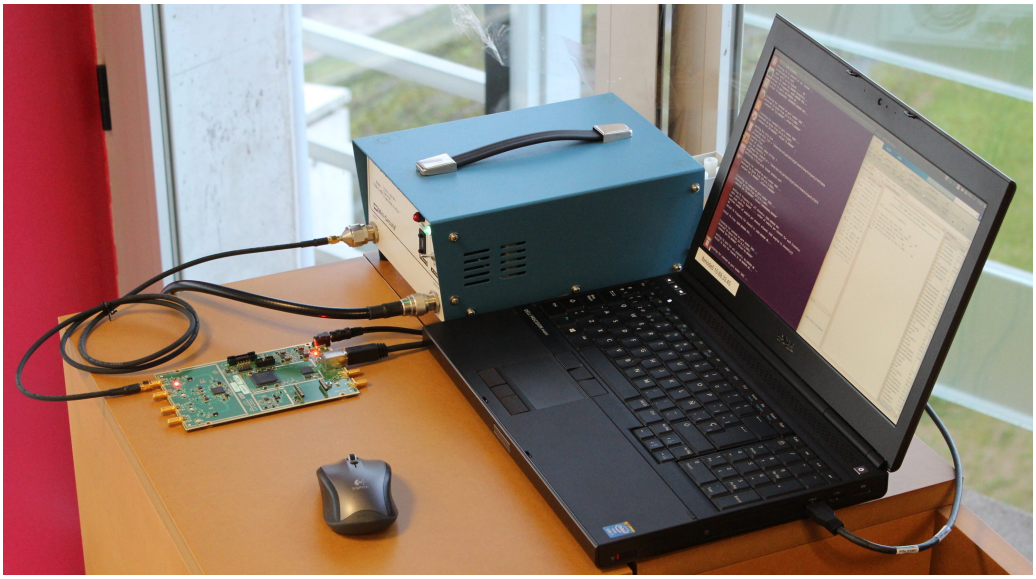

Figure 2.4: GTEC Testbed node acting as a transmitter. The USRP is connected through its USB 3.0 port to a laptop running a GNU/Linux operating system. On the other side, one of the RF outputs of the USRP is connected to the input port of a high power amplifier.

supports a continuous frequency coverage from 70 MHz to 6 GHz; full-duplex multiple-input-multiple-output (MIMO) operation with up to two antennas, and a maximum bandwidth of 56 MHz; USB 3.0 connectivity; on-chip 12 bit analog to digital converters (ADCs) and digital to analog converters (DACs) up to 61.44 Msample/s; and configurable transmit and receive gain values. A Rubidium oscillator, optionally driven by a Global Positioning System (GPS)-disciplined clock, may also be used at each node to provide very accurate time and frequency synchronization. A picture of the USRP™ B210 board is shown in Fig. 2.2. A block diagram of a node of the GTEC Testbed is shown in Fig. 2.3. In the diagram, the Stanford Research Systems PRS10 (SRS PRS10) and Trimble Thunderbolt E-GPS modules provide the rubidium oscillator and the GPS-disciplined clock, respectively. Both of them are optional. A GPS-disciplined clock available from Ettus can be also used. The advantage of the latter is that it allows for capturing National Marine Electronics Association (NMEA) records to get the position and velocity (among other parameters) of the node.

2.2.2 Software

USRP™ boards at each node are connected to a laptop equipped with two solid-state drives: one containing a GNU/Linux operating system and the custom-developed measurement software, whereas the other is dedicated to store the transmitted/acquired signals. The laptops are labeled in Fig. 2.1 as “TX PC” (transmitter) and “RX PC” (receiver). There are two main software components used in both nodes, as shown in Fig. 2.1: the GTEC Testbed interface software (GTIS) and the “GTEC 5G Simulator TX/RX”. We show in Fig. 2.4 a picture of a GTEC Testbed node acting as a transmitter, where the USRP™ is connected through its USB

port to a computer and through one of its radio frequency (RF) output ports to the input port of a high power amplifier.

2.2.2.1 GTEC Testbed Interface Software (GTIS)

This software component communicates directly with the USRP™ and is used to set up or change the node configuration, read the signals to be transmitted from disk, and store the acquired samples. We use a custom-developed multi-threaded software implemented in C++ with Boost [DA+] and based on the Ettus USRP™ hardware driver (UHD) [RESb]. At the receiver, the main thread of the GTIS software pre-processes the samples coming from the USRP™ through the USB 3.0 bus and stores them into a set of circular buffers in the main memory of the host laptop. A secondary thread reads the samples from the buffers and saves them into a dedicated solid-state drive. There is an additional low-priority thread that is responsible for logging important information of the measurements such as the GPS data [ROD16]. At the transmitter, a single thread is responsible for transmitting the signal samples cyclically. Several wrapper calls were also developed in MATLAB™ to allow for controlling the testbed directly from MATLAB™.

2.2.2.2 GTEC 5G Simulator

This software component is used to generate and process the signals of interest and it is fully integrated with the GTIS part. It could be easily replaced by other software implementations of any desired communication system that meets the constraints of the testbed. For example, the Vienna LTE Simulator [RST16] was integrated with the GTEC Testbed. The GTEC 5G Simulator is described in detail in the following section.

2.3 The GTEC 5G Simulator

The GTEC 5G Simulator can be used jointly with the GTEC Testbed to perform measurements or in a standalone fashion to perform simulations. In this section we describe its usage in a standalone way.

2.3.1 Overall Description of the Simulator

The GTEC 5G Simulator was built as a versatile tool to allow us to perform link-level simulations of different kinds of multicarrier modulated signals. Currently, OFDM and FBMC signals are supported. At the transmitter side, signals are generated using a custom-developed signal generator. For the case of FBMC, two different prototype filters were implemented, namely the one defined by the PHYDYAS project [BEL+10] and the so-called Hermite pulse [HB97]. The latter one is specially suited for transmissions over doubly

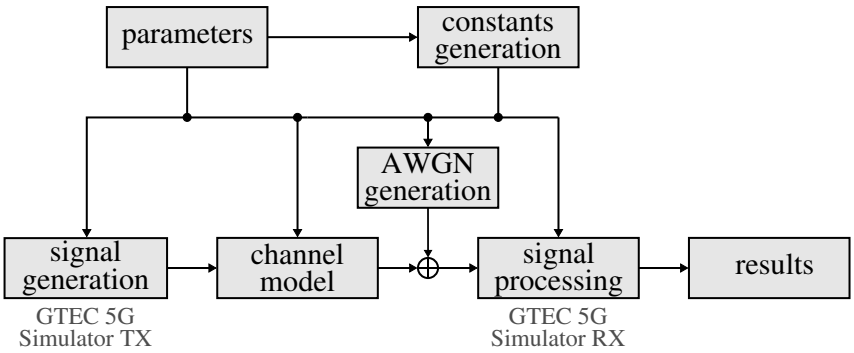

Figure 2.5: GTEC 5G Simulator structure for performing simulations.

dispersive channels [HB97]. At the receiver side, a custom-developed receiver is used, which includes algorithms for channel estimation and equalization, as well as time and frequency synchronization. For the case of FBMC signals, channel estimation is not as straightforward as in OFDM, since the lack of orthogonality of FBMC pulses causes interference in the imaginary part of the adjacent symbols. Therefore, channel estimation for FBMC requires using specific algorithms, being the most popular ones those based on the so-called auxiliary pilots. Several auxiliary pilot schemes were implemented on the simulator [JLR03; STI+10; CUI+15].

The simulator is implemented in a modular way, which enables us to easily modify or add functionalities by changing or implementing new modules, respectively. Several data structures are defined for parameters and constants, providing a standardized way to configure any simulator module.

2.3.2 Structure of the Simulator

The overall structure of the GTEC 5G Simulator is shown in Fig. 2.5. The GTEC 5G link level simulator can be divided into five basic blocks, namely, “parameters”, “constants generation”, “signal generation”, “channel model,” and “signal processing”. These blocks are described in the following subsections.

2.3.3 Configuration of Parameters and Constants

To configure the different blocks of our simulator we use a parameters file which is represented in Fig. 2.5 by the “parameters” block. From this file, a MATLAB variable of struct type containing the value of each parameter is generated. This is the first step in setting up the configuration of the different blocks of the system. Among others, the following parameters can be configured:

- **Number of subcarriers:** total number of subcarriers to be considered for the generated signal, including the guard subcarriers.
- **Number of time symbols:** number of symbols, in the time domain, of the generated signal.

- **Subcarriers conforming guard bands:** specified as a vector with two elements, indicates the number of guard subcarriers at both sides of the spectrum.
- **Modulation and demodulation technique to use:** OFDM or FBMC.
- **Modulation dependent setup:** specific parameters for the different modulation techniques. For OFDM, the CP length must be specified, whereas for FBMC, the prototype filter to be used must be specified.
- **Payload setup:** different parameters such as the type and modulation order used for the symbols can be configured. Moreover, we can transmit in a single frame several "streams" of data and each one can be configured independently. In the simulator we refer to each stream as a "data block". For each data block to be inserted in the signal, the following parameters can be configured:
  - **modulation of the symbols:** i.e., QAM or PAM.
  - **modulation order of the symbols.**
  - **mean power of the symbols:** by default, it is 1, but can be changed.
  - **resource elements**[2] **assignment:** several resource elements are assigned to the given data block. The modulation, modulation order, and number of resource elements assigned, will determine the maximum number of bits that the data block can carry.
  - **forward error correction (FEC) code:** A convolutional code was implemented in the simulator and can be used to correct the transmission errors. Moreover, if the MATLAB LTE toolbox is installed, the LTE turbo code can also be used. The usage of a FEC code can be disabled, which is useful if, for example, we are only interested in results for uncoded bit error rate (BER).
  - **number of uncoded bits in the data block:** when a FEC is used, the code rate, or equivalently the number of uncoded bits, must be specified.
- **Pilot setup:** the pilot pattern to be used as well as the modulation and modulation order of the pilot symbols is configured in this point. For the case of FBMC, the usage of auxiliary pilots must be also configured. Currently, the single auxiliary pilot scheme [JLR03; STI+10], and the so-called coded auxiliary pilot (CAP) scheme [CUI+15] are implemented.
- **Channel model and noise related parameters:** for performing simulations, the channel model to be used and the noise power are configured.
- **Channel estimation:** the channel response is estimated by means of the grid of pilots as configured in the "Pilots setup" point. Zero-forcing (ZF) and minimum mean square error (MMSE) channel estimation algorithms are implemented.
- **Channel equalization:** the received symbols are equalized with the estimated channel response. ZF and MMSE channel equalization algorithms are implemented.

[2]The term "resource element" is used here with the same meaning as in the LTE specification, i.e., one symbol in one subcarrier.

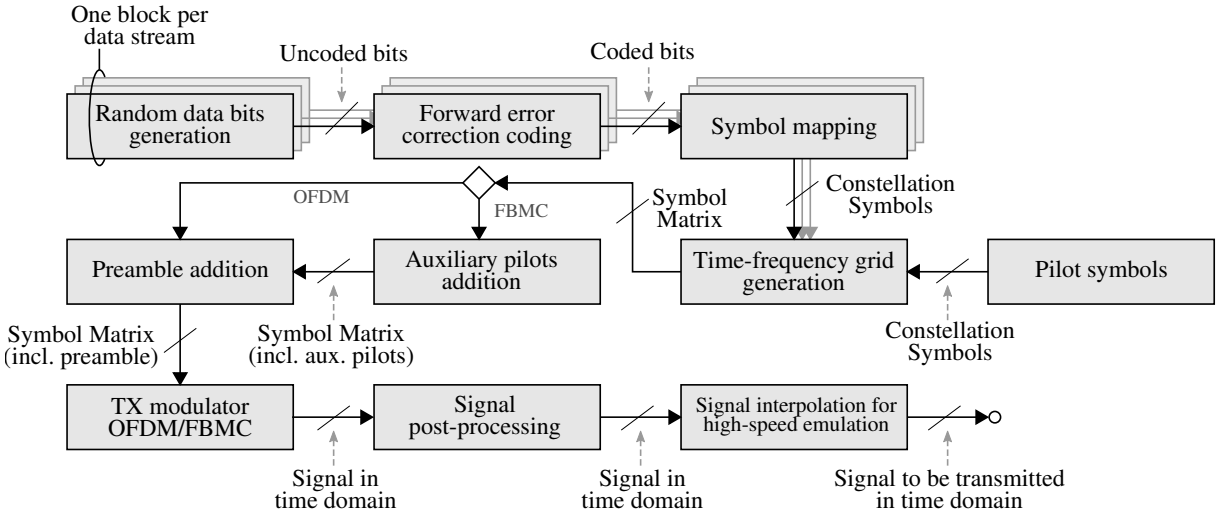

Figure 2.6: GTEC 5G Simulator transmitter structure.

- **Synchronization:** time and frequency synchronization algorithms were also implemented. For the OFDM case, two synchronization algorithms were implemented, one based on the Schmidl & Cox method [SC97], as well as one custom-made method based on the cyclic prefix (CP). For FBMC, a method based on the one defined in [ZC14] was considered.
- **High-speed emulation:** we implemented in our simulator a method for emulating high-speed receiver velocities designed by our research group and extensively used in previous works (see [ROD+14; ROD+15a; SUÁ+14b; SUÁ+14a; ZHA+16b; ROD+15b; ROD+16b; FEI+16; ROD+16d]). We can configure the high-speed simulation in this point.

Another basic block of the system is the "constants generation" block. From the previously established parameters, several constants required by the rest of the blocks are defined. These data include, among others, the following:

- Samples of the prototype filter (for the FBMC case).
- Channel model related data.
- Transmitted pilot symbols.
- Different Boolean matrices to access the distinct elements of the time-frequency grids, such as the pilots, the auxiliary pilots (for the FBMC case), or the individual data blocks.
- Samples of the preamble used for time and frequency synchronization.

2.3.4 Transmitter

The transmitter structure is shown in Fig. 2.6. There is no strong dependency between blocks and the configuration of each of them is established by means of the parameters file. This enables for easily modifying or replacing the implementation associated to each block.

The first step is to generate the data bits to be transmitted. As stated in Section 2.3.3, our

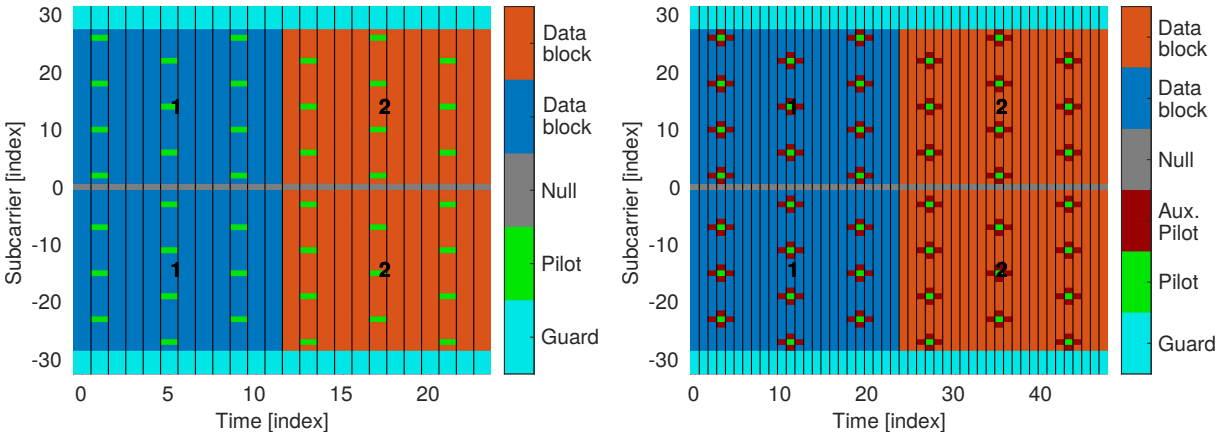

(a) OFDM.

(b) FBMC.

Figure 2.7: Examples of frame structures for OFDM and FBMC.

simulator allows for the transmission of several data streams in a frame. Therefore, N streams (being N the number of streams previously configured in the simulator parameters) of data bits are generated in the "Random data bits generation" blocks. The data bits generated are then coded by the "Forward error correction coding" blocks. Each data stream can be coded with a different coding or coding rate. Once the bits are coded, they are mapped to the corresponding constellation symbols, which is done by the "Symbol mapping" blocks. Each data stream can be mapped to a different constellation. Together with the symbol mapping, the symbol pilots to be inserted in the frame are also generated. Next, both data and pilot symbols are used by the "Time-frequency grid generation" block to assemble a matrix of data symbols that will be used to generate the transmit signal.

Insertion of the so-called auxiliary pilots [JLR03; STI+10; CUI+15] is performed by the block labeled "Auxiliary pilots addition", which is only required in FBMC in order to minimize the interference caused by the lack of the orthogonality between the received symbols. The block "Preamble addition" allows for extending the time-frequency grid by inserting a preamble for synchronization purposes at the receiver. The block "TX modulator" obtains the time-domain samples from the time-frequency grid. As stated before, the simulator currently supports OFDM and FBMC modulations. The block "Signal post-processing" allows us to perform different operations over the time-domain modulated signal such as normalization, clipping, filtering, etc. The specific post-processing functions considered, the order in which they are performed, and their parameters (if required) are set in the parameters file. Finally, the signal to be transmitted is the output of the block labeled "Signal interpolation for high-speed emulation", which implements a method for emulating high-speed receiver velocities designed at our research group. This block time-interpolates the signal by a factor I for emulating a receiver velocity I times higher, which is specially useful for assessing high-speed scenarios by measuring at low speeds with the GTEC Testbed.

Fig. 2.7 shows the time-frequency grid for two exemplary signals, an OFDM signal and

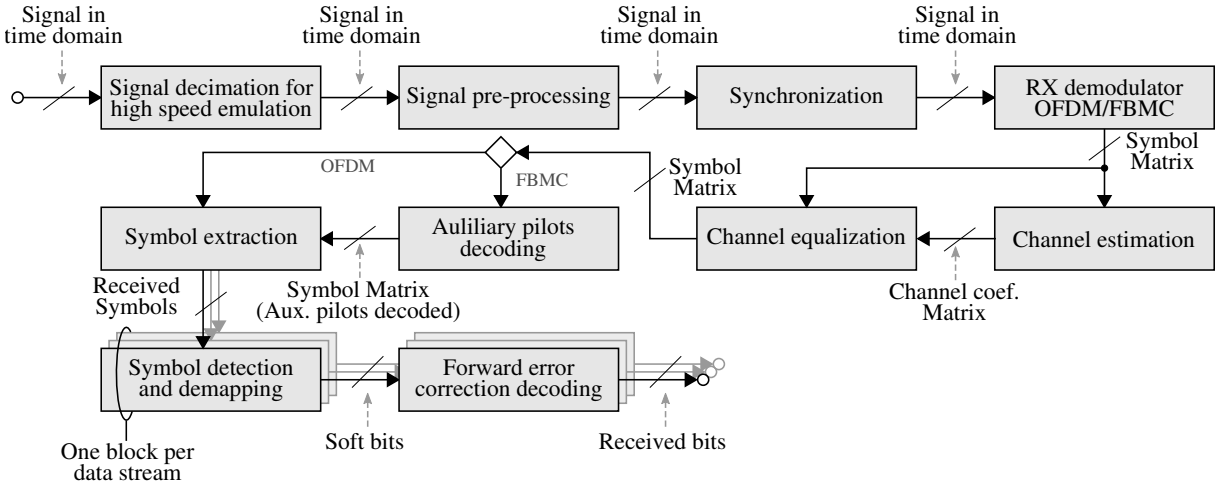

Figure 2.8: GTEC 5G Simulator receiver structure.

the equivalent FBMC signal. Note that the FBMC frame has twice the number of symbols in the time domain since PAM symbols are used for FBMC signals. These exemplary signals are generated with 64 subcarriers (being 8 of them guards and therefore not used), i.e., 24 time symbols for OFDM (48 time symbols for FBMC). The pilot grid is generated with a spacing of 8 symbols in frequency domain, 4 symbols in time domain for OFDM and 8 symbols in time domain for FBMC. For FBMC, the CAP method is used considering 4 auxiliary pilots. Two data blocks are considered for each signal, labeled in the figure by "1" and "2". Also, as shown in Fig. 2.7, the direct current (DC) subcarrier is not used.

2.3.5 Channel Model

The GTEC 5G Simulator supports several channel models. However, new channel models can be added easily. Currently, the following ones are supported:

- Additive White Gaussian Noise (AWGN).
- Flat Rayleigh fading.
- Standardized channel models, such as ITU-R outdoor-to-indoor and pedestrian A (ITU-R M.1225 (1997-2)), 3GPP typical urban channel model (3GPP TR 25.943 V6.0.0 (2004-12)), etc.

2.3.6 Receiver

The receiver structure is shown in Fig. 2.8. As in the transmitter case, there is no strong dependency between blocks and the configuration of each one is established by means of the parameters file, enabling for easily modifying or replacing the implementation associated to each block. The first step performed by the receiver is to decimate the signal at the block labeled "Signal decimation for high speed emulation" by the same factor I used to interpolate the signal at the transmitter. The "Signal pre-processing" block allows for performing different

operations in the time-domain over the received signal. As in the transmitter case, the specific operations performed, the order in which they are executed and their parameters (if required) can be configured in the parameters file. Next, the signal is synchronized in the "Synchronization" block, which estimates and corrects the time and frequency offsets of the received signal (depending on the synchronization algorithm, the preamble inserted by the "Preamble addition" block of the transmitter will be used here to perform the synchronization) . The synchronization can be omitted if we consider perfect synchronization between transmitter and receiver. The following block, "RX modulator", converts the time-domain samples of the signal into a time-frequency grid of symbols. Once the symbols are obtained, the channel response is estimated and the symbols are equalized by the blocks "Channel estimation" and "Channel equalization", respectively. Simple MMSE and ZF strategies are considered. For the case of FBMC, with the aid of the CAP technique, we can encode some user data as auxiliary pilots (see [CUI+15]). In this case, the data is decoded by the "Auxiliary pilot decoding" block. The next step is to extract (separate) the data symbols corresponding to the different transmitted data streams, this is done in the "Symbol extraction" block. Next, the detection and demapping procedure of the symbols is done for each of the streams by the "Symbol detection and demapping" blocks, which perform a soft symbol detection and return a stream of soft bits. Finally, the soft bits are passed to the blocks "Forward error correction decoding", which decode the message to obtain the originally transmitted bit if no errors occurred.

2.4 Executing Simulations

In this section we show the basic structure of the code required to perform simulations, as well as some exemplary results. The name of all the functions that we implemented start with "`FBMC_`". We explain two simple MATLAB functions that we have developed. First, we show the function `FBMC_systemSimulationByNoise`, which performs link layer simulations iterating through several noise variance values. Next, we present the sample MATLAB function `FBMC_systemSimulationBySpeed`, which performs link layer simulations iterating through several receiver speed values, while keeping the noise level fixed.

2.4.1 Simulations Iterating over Several Noise Values

The high-level function `FBMC_systemSimulationByNoise` allows for performing simulations iterating over different noise values, expressed in terms of signal-to-noise ratio (SNR) or E_b/N_0. Listing 2.1 shows an example of the aforementioned function, while Listing 2.2 details the code of such a function. Figure 2.9 shows sample results that were obtained using this function. The figure shows the BER versus E_b/N_0 for static conditions (speed of 0 km/h) for OFDM and FBMC (Hermite pulse) when using 4-QAM and 2-PAM constellations, respectively, and the 3GPP typical urban channel model (TUx) (see Section 6.3.4 for more details). Analytic curves

```
% Set configuration for the simulation
noisevec = 0:2.5:40; % Eb/No or SNR in dB
noisetype = 'EbNo'; % 'EbNo' or 'SNR'
niter = 1000;      % maximum number of iterations per value of EbNo or SNR

% Execute simulation
results = FBMC_systemSimulationByNoise(FBMC_parameters, noisevec, noisetype, niter);

% Save results to file
save('myresults', 'results');
```

Listing 2.1: Sample MATLAB code for performing simulations for several noise values.

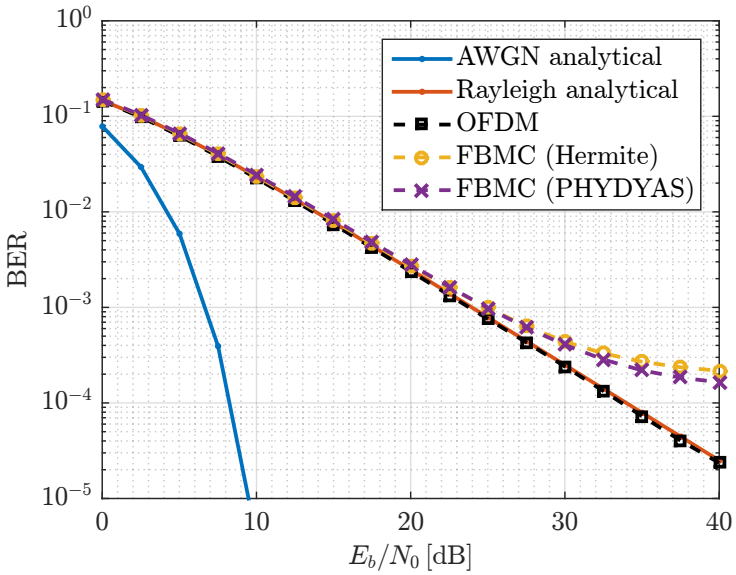

Figure 2.9: Uncoded BER versus E_b/N_0 for the TUx channel model and different modulation schemes.

for both AWGN and Rayleigh channels are also included.

2.4.2 Simulations Iterating over Several Speed Values

The high-level function `FBMC_systemSimulationBySpeed` allows for performing simulations iterating over several receiver speed values. Listing 2.3 shows a use case for the aforementioned function, whose associated code is not reproduced here for the sake of conciseness. Figure 2.10 shows exemplary results using such a function. The figure shows the BER versus emulated speed considering OFDM and FBMC with Hermite prototype filter, using 4-QAM and 2-PAM constellations, respectively, TUx channel model and $E_b/N_0 = 30\,\text{dB}$. It can be seen that for lower speeds values OFDM performs a little better, but for larger speed values FBMC performs better (see Chapter 6 for more details).

```
function simulationResults = FBMC_systemSimulationByNoise(...
FBMC_parameters, noisevec, noisetype, niter)

% precalculate the neccesary constants
constants = FBMC_pregenerateConstants(FBMC_parameters);

% Set up in the parameters 'SNR' or 'EbNo' for adding noise
FBMC_parameters = FBMC_setNoiseCalculationType(FBMC_parameters, noisetype);

% Execute the transmitter to obtain the signal to transmit
FBMC_txData = FBMC_transmitter(FBMC_parameters, constants);

% Initializate several matrices
detectvec = zeros(1, length(noisevec));
errorBitsMat = zeros(niter, length(noisevec));
EVMdBMat = zeros(niter, length(noisevec));

channelData = [];  %  always empty at the moment

% iterate through the different noise levels
for noiseind = 1:length(noiseVec)
    % set the current noise level in the parameters
    FBMC_parameters = FBMC_setNoiseValue(FBMC_parameters, noisevec(noiseind));

    for i = 1:niter
        % Pass signal through channel and add noise
        [channelOut, channelData] = FBMC_channelAndNoise(FBMC_parameters, constants, txData, channelData);

        % Execute receiver
        rxData = FBMC_receiver(FBMC_parameters, constants, channelOut.signal);

        if ~rxData.detected
            continue; % if signal not detected try again
        else
            detectvec(noiseind) = 1 + detectvec(noiseind);
        end

        % Calculate results (EVM, error bits, etc)
        results = FBMC_systemIterationResults(FBMC_parameters, constants, txData, rxData);

        % Save this iteration results
        errorBitsMat(i,noiseind) = results.errorBits;
        EVMdBMat(i,noiseind) = results.EVMdB;
    end
end
% Assign output values to simulationResults struct
% ...
end
```

Listing 2.2: FBMC_systemSimulationByNoise MATLAB code.

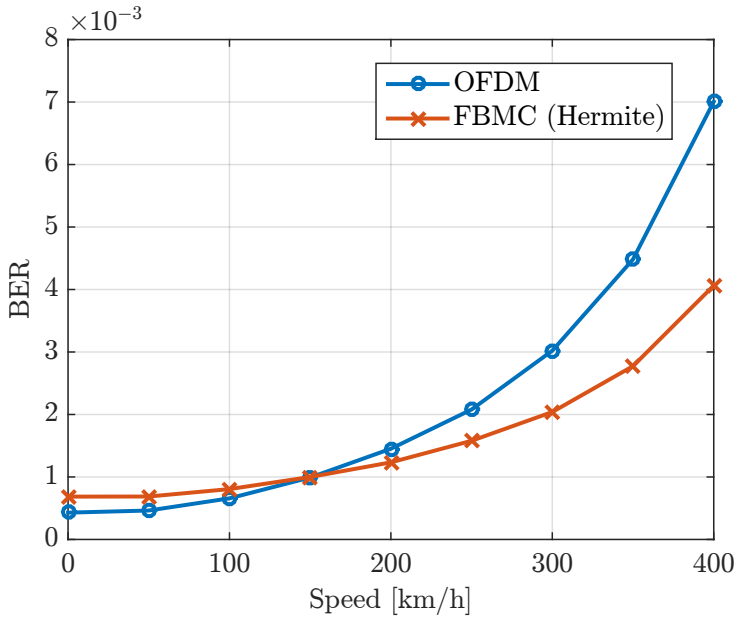

Figure 2.10: BER versus emulated speed for OFDM and FBMC with Hermite prototype filter, TUx channel model and $E_b/N_0 = 30\,\text{dB}$.

```
% Set random number generator seed
rng(12321)

% Set configuration for the simulation
speedVec = 0:50:400/3.6;  % speed(m/s)
niter = 200;  % maximum number of iterations per speed value

% Execute simulation
results = FBMC_systemSimulationBySpeed(FBMC_parameters, speedvec, niter);

% Save results to file
save('myresults', 'results');
```

Listing 2.3: Sample MATLAB code for performing simulations for several speed values.

2.5 Measurements Methodology

As mentioned before (see Section 2.2), our simulator can be used jointly with the GTEC Testbed in order to perform evaluations by means of over-the-air transmissions. In this section we briefly explain the measurement methodology followed in our experiments.

Figure 2.11 represents the typical workflow of a measurement campaign with our testbed and simulator. Firstly, we generate the signals to be transmitted and we perform several measurements by transmitting the generated signals using our testbed. Finally, the received samples are processed using the receiver of our simulator. Signal generation and processing operations are performed in an "offline" fashion, i.e., not in real time, while the signal transmission and acquisition are of course performed in real time.

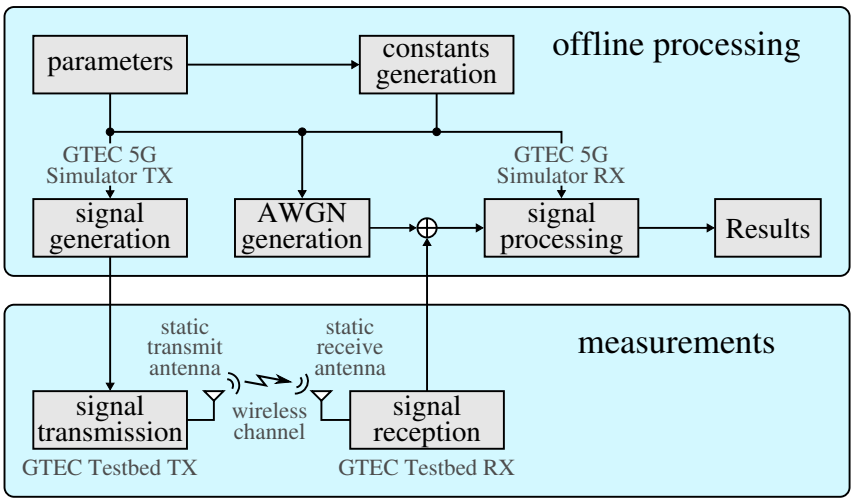

Figure 2.11: Measurement process using the GTEC 5G Simulator.

2.5.1 Offline Processing

The signal generation and signal processing steps are performed offline. Before the transmission, the desired signals must be generated using the desired parameters. After the measurements, we have to process the samples acquired by the receiver. Usually, we transmit the signals using the highest available power to maximize the SNR at the receiver. Then, in the processing step, we add artificially the necessary noise to adjust the SNR. This approach is simpler and less-time consuming (for the case of testing several SNR values) than changing the transmit power during the measurements. The acquired samples, after the noise addition, are processed by the "signal processing" block and the desired results are obtained.

2.5.2 Measurements

After the offline signal generation, the samples are saved into a dedicated solid-state drive. Next, such samples are transmitted over-the-air in a cyclic manner using one or two antennas at a time. Note that, even in single-input-single-output (SISO) measurements, switching the transmit antenna allows for obtaining different channel realizations from distinct spatial positions and polarizations. At the receiver, the samples received through one or two antennas from the set of four available are acquired and stored first in memory, and eventually recorded in a solid-state drive. Other important logging information is also stored, such as GPS timing and positioning information, which enables us to georeference the acquired samples. Results obtained by using this methodology are shown in Chapter 6.

2.6 Conclusions

The GTEC Testbed and GTEC 5G Simulator were introduced in this chapter. We presented the overall structure of the link-level simulator as well as the details of its main blocks, showing that its modularity enables for its extension. The link-level simulator is hence a very valuable tool for evaluating new communication systems in a versatile way. Moreover, we show that the simulator is fully integrated with the GTEC Testbed, enabling us to perform evaluations both by means of simulations or by means of over-the-air measurements. Finally, we described how to use the simulator as well as the typical workflow followed during a measurement campaign.

Chapter III

Experimental Characterization of 2.6 GHz LTE Wireless Links in High-Speed Trains

Multimedia and data-based services are experiencing a non-stopping growth. People are continuously on the move using devices to access multimedia contents or other data-based services. Due to this, railway companies are showing a great interest in deploying broadband mobile wireless networks in trains with the aim of supporting both passenger services provisioning as well as automatic train control and signaling. Nowadays, the most widely used technology for communications between trains and the railway infrastructure is GSM for Railways (GSM-R), which has limited capabilities to support such advanced services. Due to its success in the mass market, it seems reasonable to consider Long Term Evolution (LTE) as the best candidate to substitute GSM-R. In this chapter we account for the detailed characterization of the downlink between an LTE Evolved Node B (eNodeB) and a high-speed train (HST) based on measurements carried out in a commercial HST line. We consider two links: the one between the eNodeB and the antennas placed outdoors on the train roof, and the direct link between the eNodeB and a receiver inside the train. Such a characterization consists in assessing the path loss, the signal-to-noise ratio (SNR), the K-factor, the power delay profile (PDP), the delay spread, and the Doppler power spectral density (PSD) for different train speeds.

This chapter is mainly based on the following co-authored publication:

- Tomás Domínguez-Bolaño, José Rodríguez-Piñeiro, José Antonio García-Naya, and Luis Castedo. "**Experimental characterization and modeling of LTE wireless links in high-speed trains**". *Wireless Communications and Mobile Computing*, vol. 2017, no. 5079130, 2017, pp. 1–20.
  DOI: 10.1155/2017/5079130

The structure of the chapter is as follows. Section 3.1 introduces the chapter. Section 3.2 describes in detail the HST scenario as well as the experimental setup and procedure considered for the evaluations. Section 3.3 explains the basic aspects of the signal processing performed at the receiver, including the signal synchronization, channel impulse response estimation and SNR estimation. Section 3.4 characterizes the path loss for both the eNodeB-train and

direct eNodeB-passenger links, while Section 3.5 studies the eNodeB-train channel condensed parameters, such as the K-factor, the PDP, the delay spread and the Doppler PSD. In Section 3.6 we study significant regions of the train path in detail, showing how train infrastructure elements impact on the wireless link. Finally, Section 3.7 concludes the chapter.

3.1 Introduction

Railway wireless communications can be divided into two groups: *(a)* train control signaling and safety-related communications; and *(b)* non-critical communications, both for train staff and passengers. While the first kind of communications usually does not require high data rates, it in turn imposes stringent constraints to the quality of service (QoS) [ROD16; LAM+12; FRA+15; ROD+12; EUR10]. Operational and functional requirements for the railway environment require in fact reduced delays or call setup times, as well as very reduced service interruptions. The second type of railway communications demands higher throughputs (e.g., access to multimedia services), but they do not impose so strict requirements in terms of reliability.

Nowadays, the most widely used technology for train control signaling and safety-related communications between trains is based on GSM for Railways (GSM-R) and requires a specific network deployment with base stations located along the track. The GSM-R, which is based in the mature Global System for Mobile Communications (GSM) technology, provides a continuous communication channel between the train driver and the ground controllers, being well suited to perform emergency calls, selective phone calls or small data transmissions. However, GSM-R has reduced capabilities to support more advanced services, such as automatic pilot or provisioning broadband communications to train staff.

Besides that, multimedia and data-based services experienced a non-stopping growth over the last few years [ROD16]. Whereas sometimes the transmission of a few data bits is enough, continuous streaming of multimedia data is required in other situations. In most cases, users are connected to general-purpose mobile networks. However, railway companies are aware of the market opportunity and aim to provide passengers with multimedia services and/or broadband Internet access on-board. The mobile-relay technique has been proposed in [NET12] as a way to provide coverage to passengers based on a relaying scheme (a link from the cellular base station to an external antenna installed on the train, which is relayed to a local base station inside the train carriage).

Taking into account the big success of Long Term Evolution (LTE) in the evolution of mobile networks, it seems reasonable to consider LTE as the best candidate to substitute GSM-R as the fundamental technology for railway communications, as well as for provisioning services to passengers. While in previous publications we studied the suitability of LTE to fulfill the operational and functional requirements for the railway environment (e.g., see [ROD16; LAM+12; FRA+15; ROD+12]), in this chapter we account for the detailed characterization of

the wireless link based on LTE measurements in a high-speed train (HST) line in Spain. We consider both the channel between an Evolved Node B (eNodeB) and a passenger inside a HST, as well as the direct channel between the eNodeB and the outdoor antennas installed on the train carriage.

The first step for migrating GSM-R into LTE is to assess the performance of such a communications system for the railway environment. Knowledge of the wireless channel characteristics is the fundamental basis for planning wireless communication networks and designing transceivers [AI+14; ROD16]. However, HST communications demand for the evaluation of specific scenarios which are typical in most railway lines, such as rural macro cell, hilly terrain, viaducts, cuttings or tunnels, among others [ROD16]. Hence, in recent years, a lot of attention has been put on measurement-based analysis to characterize the different types of high-speed railway scenarios. In [HE+13c; HE+11a; HE+11b; HE+13d] several channel parameters were analyzed and modeled for a viaduct scenario based on measurements carried out using GSM-R base stations (BSs) at 930 MHz. In [HE+13a] the channel is characterized and modeled for a cutting scenario based on measurements carried out using GSM-R BSs at 930 MHz. [LIU+12; WEI+11; ZHO+14] analyze the channel for a viaduct scenario considering a carrier frequency of 2.35 GHz. In [ZHA+14] a hilly terrain scenario is considered, and the delay and Doppler spread is characterized for a carrier frequency of 2.4 GHz. In [YIN+15] the authors use the commercially deployed LTE base stations along the HST railway between Beijing and Shanghai (with a total distance of 1318 km) to characterize statistically the parameters of the observed channels.

In our case we did not perform the measurements by employing a general-purpose mobile network deployment during the train operation. Different from other works, we installed an eNodeB taking advantage of the available infrastructure for GSM-R in the HST line. We considered a carrier frequency of 2.6 GHz and the 10 MHz profile of LTE. Furthermore, we deployed two sectors, and the corresponding eNodeB antenna panels were placed in the same tower where the GSM-R antennas are installed. Since we measured LTE standard-compliant signals, tasks like time and frequency synchronization or channel estimation were performed considering exclusively the same information that a commercial receiver would use (i.e., synchronization signals, pilots...). We could also perform different train passes along a segment of about 7 km long centered at the eNodeB site with distinct train speeds and varying the data traffic. At the receiver (train) side we could access to the external antennas of the train, being able to evaluate the eNodeB-train wireless link in a realistic way. We also considered antennas installed indoors to model the direct eNodeB-passenger link. Furthermore, high-resolution results are obtained from our measurements (which are freely available for other research groups), since we continuously capture the signal at the receiver during the whole measurement campaigns.

In this chapter we present the complete and detailed characterization of the downlink between a commercial LTE eNodeB and a train moving at high velocities along a track in

commercial operation in a rural area in Spain. We consider two links: the one between the eNodeB and the antennas placed outdoors on the train roof, and the direct link between the eNodeB and a receiver inside the train. Such a characterization consists in assessing the path loss, the signal-to-noise ratio (SNR), the K-factor, the power delay profile (PDP), the delay spread, and the Doppler power spectral density (PSD) for different train speeds. Finally, we show the specific characteristics of the railway channel and the impact of the train speed on them. Besides that, the mathematical description of all the procedures followed to obtain the results is detailed. In particular, mathematical descriptions in both discrete time and frequency are provided for all the estimated parameters: channel response, synchronization, SNR, path loss, K-factor, PDP, delay spread and Doppler PSD. Additionally, guidelines about the drawbacks and pitfalls to be considered for the different analysis methods are provided.

3.2 Experimental Setup

We evaluated experimentally the links between an eNodeB and two receive antennas placed on the roof of a train carriage, as well as two antennas of a mobile receiver inside the train. By first evaluating the path loss, we motivate the need of a relay architecture to distribute the signal inside the train through repeaters or access points (APs), whereas employing external (train-mounted) antennas for the link between the train and the eNodeB. Then, the effects of the high speed on the latter link are studied in detail by means of parameters such as the K-Factor, the PDP or the Doppler PSD, taking into account the effects at high speeds.

A measurement campaign was conducted in a HST line in commercial operation. Different from other works, we could access to the railway environment and equipment, which enabled us to perform different experiments during maintenance periods (mainly overnight) by freely controlling the train movement as well as the transmitted signals. Even more, one of the most important features of our experiments is that instead of using eNodeBs deployed for general purpose mobile cellular communications, we installed an eNodeB in one of the GSM-R sites specifically devoted for railway communications. Furthermore, we obtained the permission to employ the $2.6\,$GHz carrier frequency, which is commercially used in such an area. Measurements were carried out along a track segment of approximately $7\,$km long centered at the GSM-R site in a rural area. The considered train was specifically designed to test all the systems each time a new line is opened, hence the access to some resources such as the external antennas installed on its roof was granted. This allowed us to analyze the use of LTE for HST applications at the actual environment and employing the specific infrastructure of the railway operator. It is also worth noting that the transmit power was high enough so that the SNR level exceeds $20\,$dB (when using antennas placed outdoors). This allows for correctly synchronizing most of the LTE frames without errors, hence enabling us to analyze the signal along the whole train path, i.e., instead of only sampling the acquired signal during short time intervals while the train moves along the track, our equipment acquires the transmitted

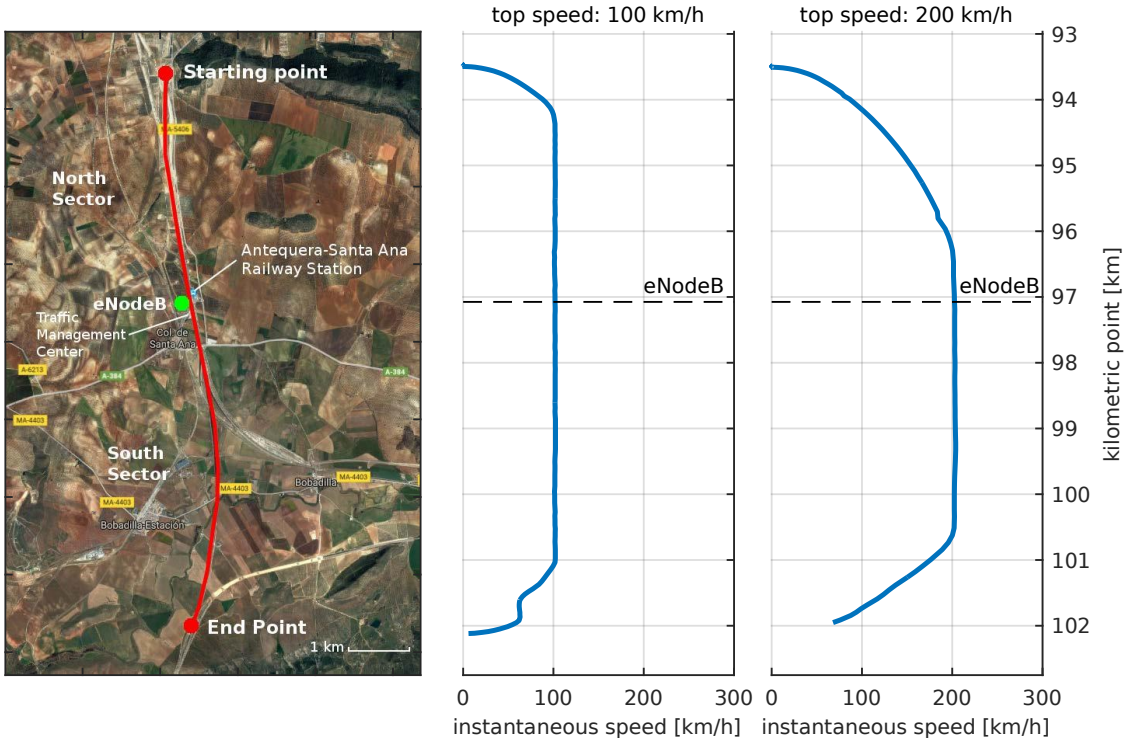

Figure 3.1: Map of the scenario considered for the measurements. The instantaneous train speed is shown for each point of the trajectory, both for the cases considering a maximum speed of 100 km/h and 200 km/h. The position of the eNodeB is also specified. *Map Image by ©2017 DigitalGlobe, Cartography Institute of Andalucía, Map Data by ©2017 Google, National Geographic Institute of Spain.*

LTE frames in a continuous fashion. The following subsections describe the details of the measurement environment, the equipment used and the methodology followed to perform the measurements.

3.2.1 Measurement Environment

3.2.1.1 Test Track

The considered HST line connects Córdoba and Málaga (Spain) and is designed to cope with speeds up to 330 km/h. The measured segment is located between the kilometric points (KPs)[1] 93.0 and 102.0, whereas the GSM-R site is located at KP 97.075[2], as imaged in Fig. 3.1. The Antequera-Santa Ana Railway Station (KP 96.800) as well as a Traffic Management Center are also located in the vicinity of the GSM-R site.

[1] A kilometric point (KP) is a term used in metricated areas, especially in France and Spain, to provide reference points alongside a transport route such as a road, a railway line or a canal [WIK].

[2] The exact Global Positioning System (GPS) coordinates of the site are 37° 4′ 3.14″ N, 4° 43′ 12.52″ W.

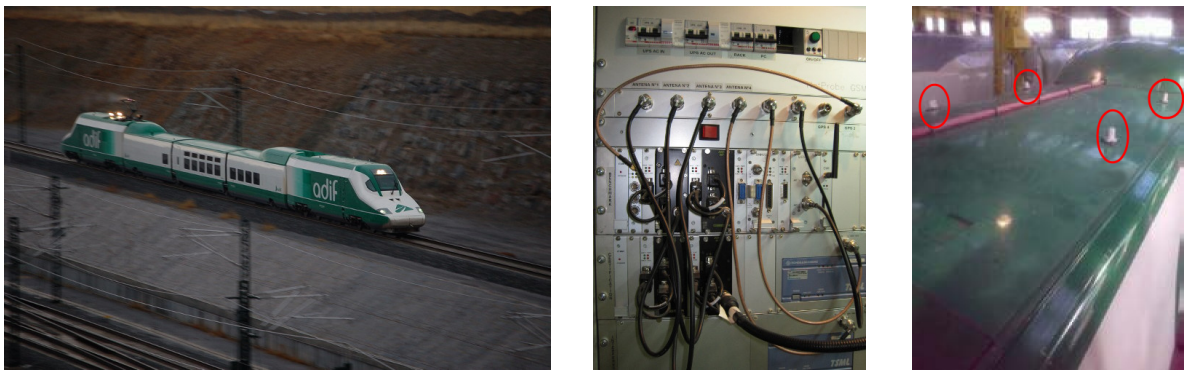

(a) (b) (c)

Figure 3.2: *Séneca* laboratory train (Talgo A-330). (a) Photography of the whole train. (b) Inner panel for connection to the outdoor antennas. (c) Outdoor antennas on the roof of the train carriage (Kathrein 870 10003 and 870 10007), the four antennas are marked with red ellipses.

3.2.1.2 Test Train

The considered test train was the so-called *Séneca* laboratory train (Talgo A-330), provided by the Spanish Railway Infrastructure Administrator (ADIF), imaged in Fig. 3.2a. The train was intended for infrastructure inspections and it was extensively used in testing activities for the deployment of the European rail traffic management system/European train control system (ERTMS/ETCS) standard in Spanish high-speed lines. Electrically-powered, the train can reach a maximum speed of 363 km/h, although the maximum considered speed for our measurements was limited to 200 km/h because the time (and also the distance) required to reach a higher speed is extremely large, thus limiting the number of trials to be performed in a typical measurement session during the night. The train is 80.92 m long and includes an inner panel (see Fig. 3.2b) which allows for the connection to the external antennas on its roof (see Fig. 3.2c): Two of them are multi-band antennas (800, 900, 1800, 1900, UMTS, UMTSII, W-LAN and GPS) Kathrein 870 10003, whereas the other two are Kathrein 870 10007 (without GPS), both featuring a 0 dB gain and a voltage standing wave ratio (VSWR) smaller than $2.0:1$ at the considered carrier frequency of 2.6 GHz. During the measurements we used two external antennas, one of each type. The GPS connection is used by the GPS-disciplined oscillators included in the measurement equipment and to match the acquired samples with the estimated position and velocity of the train.

3.2.2 Measurement Equipment

3.2.2.1 Ground Equipment

The GSM-R site, imaged in Fig. 3.3a, includes a 40 m height tower with antennas for different wireless technologies and two cabins where the communications equipment is installed. A commercial LTE eNodeB was set up inside one of the available cabins and two remote radio

(a) Image of the tower and the two cabins for telecommunications equipment.

(b) Antenna installed at the tower (for south sector).

Figure 3.3: Pictures of the GSM-R site.

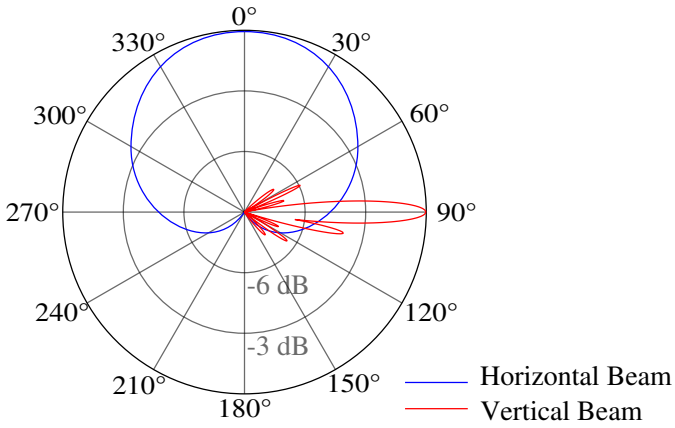

Figure 3.4: Radiation pattern for the transmit antennas (Moyano MY-DTBSBS17276518). Both the vertical and horizontal radiation patterns are shown.

heads were mounted at the tower structure, each one connected to two antenna elements of a different antenna panel (see Fig. 3.3b). Such antenna panels (Moyano MY-DTBSBS17276518) were placed at a height of 20 m and orientated as the available GSM-R antennas. At the considered carrier frequency (2.6 GHz), these cross-polarized antennas feature a gain of 18 dBi and a half-power beam width of 62° (horizontal) and 5° (vertical), as imaged in the radiation pattern shown in Fig. 3.4. Each antenna panel is used to deploy a sector, hence two sectors are used, named as "north sector" and "south sector", respectively (see Fig. 3.1). Table 3.1 shows the orientation of the ground antennas.

The eNodeB was configured to transmit an LTE signal with the profile of 10 MHz

Table 3.1: Ground antennas orientation, both in vertical (with respect to the horizontal plane) and horizontal (with respect to the north direction) dimensions.

	antenna orientation [°]	
Sector	azimuth	elevation
north	355	0
south	175	−1.4

bandwidth, transmit diversity[3] and normal cyclic prefix (CP) length[4]. More details regarding the transmit signal configuration are specified in Table 3.2. Note that two configurations for data traffic transmission were considered[5]:

- **Maximum Throughput**: All the resource blocks of the LTE signal are filled in with data. Hence, the maximum payload of LTE is used for the configuration parameters specified in Table 3.2.
- **ETCS+VoIP**: A stream of European Train Control System (ETCS) data traffic is transmitted simultaneously with a voice over Internet Protocol (VoIP) call.

In both cases, the receiver used in the measurements has no *a priori* knowledge about the transmitted data.

Table 3.2: LTE testbed configuration parameters.

Parameter	Value
Sampling frequency, f_s	15.36 MHz
Transmit power	46 dBm
Maximum antenna gain	18 dBi (TX), 0 dBi (RX)
Carrier frequency	2.6 GHz
Bandwidth	10 MHz (9 MHz occupied)
Transmission scheme	Transmission mode 2 (Transmit diversity) [3GPc]
Cyclic prefix length	Normal

[3] A single transmit block is encoded and transmitted through two different antennas. Precoding is performed in order to separate the two different antennas.

[4] The first orthogonal frequency-division multiplexing (OFDM) symbol of an LTE slot (a slot occupies half a subframe) has a cyclic prefix length of $N^{\text{CP}}_{\text{long}} = 80$ samples (5.2083 microseconds), whereas for the remaining six OFDM symbols the cyclic prefix is reduced to $N^{\text{CP}}_{\text{short}} = 72$ samples (4.6875 microseconds).

[5] A commercial LTE receiver (different than those employed to produce the results shown in the chapter) is connected as the only user to the eNodeB, this way we can capture the signals between the eNodeB and the commercial receiver to be used for our evaluations.

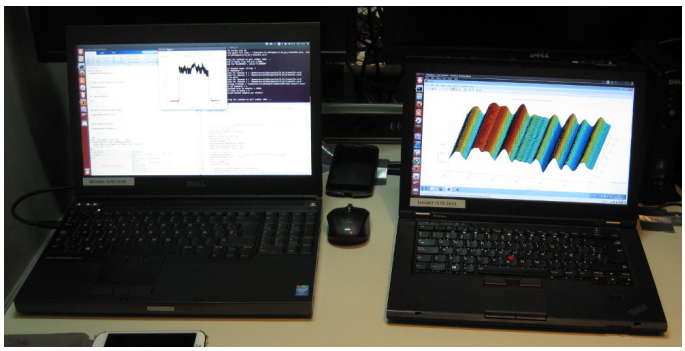

(a) Two laptops mounted onboard running the GTEC 5G Simulator as part of two GTEC Testbed nodes.

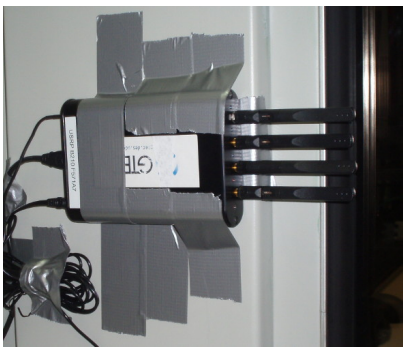

(b) USRP employed as part of a GTEC Testbed node, equipped with the indoor antennas. Only the two antennas in the middle out of the four antennas are used.

Figure 3.5: Onboard measurement equipment.

3.2.2.2 On-board Equipment

The on-board equipment consists of two GTEC Testbed nodes (see Chapter 2) operating in receive-only mode. Each of them includes an Ettus/National Instruments Universal Software Radio Peripheral (USRP™) B210 (see Fig. 3.5b) board connected to a laptop running a GNU/Linux operating system (see Fig. 3.5a) and the Mathworks LTE Toolbox. Whereas one of the nodes was connected to two external antennas available on the carriage roof, the other was connected to two omni-directional antennas (MobileMark PSKN3-24/55S) directly attached to the USRP™ installed inside the carriage. The outdoor antennas allow us to evaluate the link between the eNodeB and the train, while the indoor ones are used to investigate the direct connection between the mobile receiver of a passenger (or staff) and the eNodeB. Additionally, each node was provided with a GPS-disciplined temperature-controlled oscillator (Ettus/National Instruments GPSDO 783454-01) that is also used for geo-referencing (time and position) the measurements. Given that the eNodeB also employs a GPS-disciplined oscillator, the frequency offset between the eNodeB and the GTEC Testbed nodes is minimized. Notice that whereas the USRP connected to the external antennas uses the Kathrein 870 10003 GPS antenna, the USRP connected to the indoor antennas uses a separate Trimble 66800-40 GPS antenna which is also placed indoors.

3.2.3 Measurement Procedure

Different train passes were performed at different speeds, in both north and south directions, considering different transmitter configurations and different data traffic types. GPS-based geolocation of the measurements allowed us to accurately combine the results obtained from different train passes. It is worth noting that the obtained results exhibit a very high repeatability level for different train passes with identical configuration parameters. This enables us to

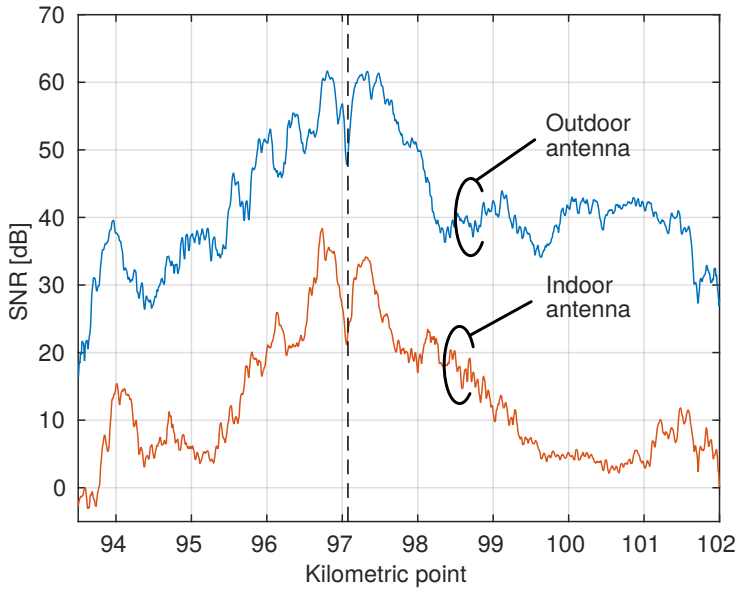

Figure 3.6: Estimated SNR versus KP for one of the indoor and one of the outdoor antennas.

compare consistently the results at different speeds. It is also interesting to mention that we capture the data continuously at the receiver during the whole measurements session. This not only requires a huge amount of available storage (approximately 4 TB of raw data for two measurement sessions of about 3 hours each), but also challenges the measurement equipment in terms of acquisition speed and stability, demanding extremely powerful hardware to process all the data. In this sense, also the software developed has to be prepared to cope with such a huge amount of data.

The main advantage of our approach is that we can obtain high-resolution results.

3.2.3.1 Low Speed Measurements

Train passes at 50 km/h were performed to characterize the propagation environment in terms of large-scale parameters. Hence, the SNR and path-loss for the antennas placed indoors and outdoors was evaluated. For these measurements, we independently switched on and off the two deployed sectors. This enabled us to measure not only the desired received power in a sector (e.g., received power when the train is in the north sector and only the north sector is active), but also the interference caused to the adjacent sector (e.g., received power when the train is in the north sector and only the south sector is active).

Fig. 3.6 shows the average SNR per data subcarrier versus the KP. In order to maximize the number of occupied subcarriers devoted to the SNR estimation, the so-called "Maximum Throughput" is considered. The SNR was evaluated as described in Section 3.3.3 for one antenna placed indoors and another one placed outdoors. Obviously, the highest SNR values are obtained in the vicinity of the eNodeB. When the train passes in front of the eNodeB, the handover between the two sectors occurs. However, the SNR is higher than 20 dB for all the

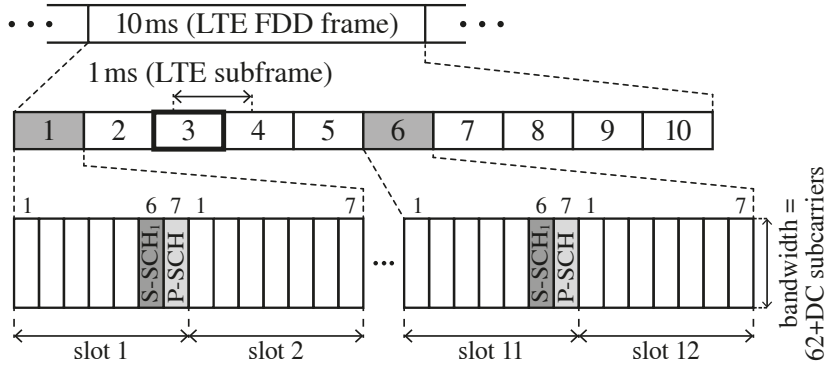

Figure 3.7: Synchronization signals for frequency-division duplex (FDD) LTE.

points of the train trajectory when the outdoor antennas are used, being the maximum value about 60 dB. The shape of the SNR curves for the antennas placed indoors is similar, although the received power decreases dramatically due to the penetration losses. On average, a loss of about 26 dB is measured.

3.2.3.2 High-Speed Measurements

Once the large-scale parameters were characterized by means of low-speed measurements, measurements at higher velocities, such as 100 km/h and 200 km/h, were performed. This way we evaluated the effect of the speed in parameters such as the K-Factor, the PDP and the Doppler PSD. In this case, the considered model for the data traffic is the one labeled as "ETCS+VoIP" in Section 3.2.2.1. However, this does not impact on the results since only the pilots are used to perform the evaluations. Due to the time required to accelerate and decelerate the train, it was not possible to measure at high speeds during the whole train path. Fig. 3.1 shows the instantaneous speed of the train versus the KP for both measurement cases: 100 km/h and 200 km/h. As shown in Fig. 3.1, the speed is maximum along the central part of the trajectory. In the result graphs shown along this chapter for the case of 200 km/h, we over-impose a pattern of gray diagonal lines to emphasize the KPs where the train was accelerating or decelerating (see Fig. 3.11b as an example).

3.3 Signal Processing at the Receiver

Several relevant parameters are estimated directly from the LTE-compliant acquired signal, such as path loss, PDP, delay spread, and Doppler PSD. Most of the estimates depend on the wireless channel response estimation, which is done by means of the pilot symbols included in the LTE transmit signal. In the following subsections we detail all the steps followed to process the acquired signals in order to obtain the aforementioned estimates.

3.3.1 Synchronization in LTE

Before proceeding with the channel response estimation, the first step consists in detecting and synchronizing the LTE signal. LTE provides two synchronization signals, namely the Primary Synchronization Signal (P-SCH) and the Secondary Synchronization Signal (S-SCH), to enable time and frequency synchronization as well as to detect the physical cell ID which defines the pilot sequence, as described in [3GPb, Section 6.11]. For FDD LTE signals –the ones considered in our experiments– the P-SCH is transmitted occupying the 62 central subcarriers of the last OFDM symbol contained in the first and the eleventh slots of each LTE frame, as shown in Fig. 3.7. This enables the receiver to detect the P-SCH regardless of the configuration of the CP length. Once the P-SCH has been detected, the signal is time-synchronized at slot level. While the P-SCH is repeated twice per LTE frame, the S-SCH comprises two different signal sequences per each LTE frame, being the first one transmitted in the 62 central subcarriers of the OFDM symbol previous to the one used to transmit the first copy of the P-SCH, whereas the second one is located at the OFDM symbol preceding the one used to transmit the second copy of the P-SCH (see Fig. 3.7). Once the S-SCH has been detected, the signal is time-synchronized at LTE-frame level. Given that only the central 62 subcarriers are employed for synchronization, the receiver can synchronize without prior knowledge about the total signal bandwidth.

The P-SCH is constructed from a frequency-domain Zadoff-Chu sequence of length 63 [STB11]. Among its properties, the ability to detect it even with a frequency offset up to ± 7.5 kHz is highlighted. Hence, the time offset can be estimated initially without performing a frequency synchronization[6]. On the other hand, the S-SCH sequence is based on maximum length sequences, known as M-sequences [STB11]. Since the S-SCH is detected after the P-SCH, the P-SCH itself can be used to perform a rough channel response estimation to aid in the detection of the S-SCH [STB11].

Since our environment comprises two different sectors, each of them having a different physical cell ID, we can easily determine both the P-SCH and the S-SCH sequences per sector. Hence, both of them can be found by using a simple correlation, thus acquiring the symbol and LTE frame timing.

3.3.2 Channel Response Estimation

The wireless channel response between the eNodeB and the receiver is estimated by taking advantage of the pilot structure defined by LTE. Firstly, an estimate of the discrete-time frequency-domain channel response $\tilde{H}^l[n, \lambda]$ is obtained for each LTE frame $l \geq 0$, where $n = 0, \ldots, s_{\mathrm{F}} - 1$ denotes the OFDM symbol index, being s_{F} the number of OFDM symbols per LTE frame, and $\lambda = -N/2, \ldots, N/2 - 1$ the subcarrier index, with N the fast Fourier

[6]Notice also that both the eNodeB and the GTEC Testbed nodes use GPS-disciplined oscillators, thus the frequency offset between them is very small.

Table 3.3: LTE signal configuration parameters.

Parameter	Notation	Value
OFDM symbols per frame	s_F	140
Samples per frame	s_F^S	153600
Samples per slot	s_{slot}^S	7680
FFT size	N	1024 points
Number of used subcarriers	N_u	600
OFDM symbols per LTE slot	N_{slot}	7
Long CP length	$N_{\text{long}}^{\text{CP}}$	80 samples
Short CP length	$N_{\text{short}}^{\text{CP}}$	72 samples
Mean CP length	$\overline{N^{\text{CP}}}$	≈ 73.14 samples

transform (FFT) size of the OFDM modulator. We used a minimum mean square error (MMSE) channel estimator. Refer to Table 3.3 for the definition of the constants employed in this section.

Notice that frequency synchronization is skipped since one of the parameters that we are estimating is the Doppler PSD, and this process will be altered due to the corrections introduced by the frequency synchronization algorithms. The estimated channel response in the discrete-time domain for the l-th frame, namely $\tilde{h}^l[n,\kappa]$, is obtained by applying the inverse fast Fourier transform (IFFT) operation to the corresponding discrete-time frequency domain channel response as

$$\tilde{h}^l[n,\kappa] = \text{IFFT}_\lambda\left(\tilde{H}^l[n,\lambda]\right), \tag{3.1}$$

where $\text{IFFT}_\lambda(\cdot)$ denotes the IFFT operation over λ, and $\kappa = -N/2,\ldots,N/2-1$ is the discretized delay index. Note that the channel seen by the signal comprises subcarriers with indices $\lambda = -N_u,\ldots,N_u$. However, the MMSE channel estimator provides an estimation of the channel response for the N subcarriers considered (i.e., it also includes the guard subcarriers). This enables us to avoid the spreading effect that would appear if guard subcarriers are set to zero due to the properties of the IFFT.

Since the LTE frames are transmitted in a continuous fashion (i.e., there are no gaps or silent periods between consecutive LTE frames), we can obtain an estimation of the wireless channel response along the train path, namely $\hat{h}[n,\kappa]$, by concatenating the estimates of successive LTE frames. However, for doing so, the propagation delay, and thus the synchronization points[7], must be taken into account.

The synchronization point for the l-th LTE frame (see Section 3.3.1 for more details about the synchronization procedure), namely p^l, can be expressed as a function of the frame index l

[7] A synchronization point is defined as the index of the first sample of the acquired signal corresponding to a valid LTE frame.

as

$$p^l = n_i + l \cdot s_F^S + \gamma^l, \tag{3.2}$$

being

$$\gamma^l = \left\lfloor \tau^l \cdot f_s \right\rceil + e^l, \tag{3.3}$$

where n_i is the index of the initial sample for the first transmitted LTE frame, s_F^S is the number of samples per LTE frame, τ^l is the propagation delay for the l-th frame, which depends on the distance between the receive antenna mounted on the train and the transmit antenna at the eNodeB, $\lfloor \cdot \rceil$ denotes the round operation, f_s is the sampling frequency, and e^l is an integer error term which depends on the actual channel and the noise.

The detected synchronization point, p^l, allows us to compensate for the propagation delay in the estimated channel responses, hence centering the most powerful tap around $\kappa = 0$. For the case of two consecutive frames l and $l+1$ being synchronized, if $\Delta\gamma^l \triangleq \gamma^{(l+1)} - \gamma^l \neq 0$, there will be a discontinuity in the estimated channel responses between the two frames (note that $\Delta\gamma^l = p^{(l+1)} - p^l - s_F^S$). The continuity can be preserved by accounting for the propagation delay of the received frames. This can be done since the IFFT size in Eq. (3.1) equals the number of subcarriers, thus the sampling time of the signal and the estimated channel delays match. To preserve the continuity we can follow different strategies:

A. Synchronize only the first frame

We can take advantage of the OFDM cyclic prefix (CP) and synchronize only the first frame. Then, instead of synchronizing each successive LTE frame (hence obtaining the synchronization points defined in Eq. (3.2)), the synchronization point for the l-th frame is obtained as $p_l = n_i + l \cdot s_F^S$, without accounting for the propagation delay. This way the overall channel response (i.e., the concatenation of the channel responses for the subframes along the whole path) is defined as

$$\tilde{h}[n, \kappa] = \tilde{h}^l[n - s_{\mathrm{F}} \cdot l, \kappa - \kappa^0], \quad l = \left\lfloor \frac{n}{s_{\mathrm{F}}} \right\rfloor, \tag{3.4}$$

where $\lfloor \cdot \rfloor$ is the floor operator and κ^0 is the delay of the first synchronized frame.

This method is only valid when the propagation delay is relatively small compared to the CP length, otherwise inter-symbol interference (ISI) will arise in the signal.

B. Synchronize each frame and find relative delays

When synchronizing all the frames, we obtain the synchronization points defined in Eq. (3.2). The corresponding delay, expressed as the number of samples for the l-th frame, namely κ^l, is

$$\kappa^l = \kappa^0 + \sum_{m=0}^{l-1} \Delta\gamma^l,$$

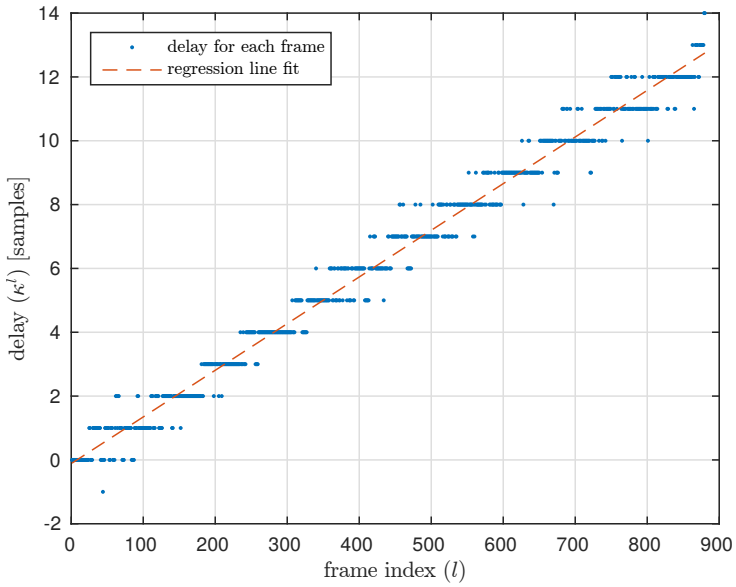

Figure 3.8: Exemplary results of delays (κ^l) for a portion of the captured frames.

where κ^0 is the delay (expressed in number of samples) for the first synchronized frame. Therefore, the overall channel response is

$$\tilde{h}[n,\kappa] = \tilde{h}^l[n - s_{\mathrm{F}} \cdot l, \kappa - \kappa^l], \quad l = \left\lfloor \frac{n}{s_{\mathrm{F}}} \right\rfloor . \tag{3.5}$$

Fig. 3.8 shows some exemplary results for the obtained delay samples, κ^l, versus the frame number l, considering $\kappa^0 = 0$. These results correspond to a portion of the captured frames for the case of the train moving away from the eNodeB at a speed of 100 km/h. We also show the fitting of the data obtained by a robust linear regression [HUB81]. The slope of the curve shows how the propagation delay increases as the frames are received while the train moves away from the eNodeB, thus increasing the distance between transmit and receive antennas.

C. Hybrid approach

We can use a hybrid approach from the two above-mentioned methods. Firstly, the acquired signals are grouped in sets of consecutive frames. Secondly, the channel response is estimated for each set as explained in Item A. Then, the propagation delays are estimated for each set following a procedure similar to the one in Item B.

The initial time (in seconds) corresponding to the estimated channel response $\tilde{h}[n,\kappa]$ for each value of n, namely t_n, can be approximated as

$$t_n \simeq n\frac{1}{f_s}\left(N + \overline{N^{\mathrm{CP}}}\right) + \hat{t}_0, \tag{3.6}$$

where $\hat{t}_0$ is the initial time of the estimated channel response for the symbol with $n = 0$, and

$$\overline{N^{\text{CP}}} = \frac{(N_{\text{slot}} - 1)\, N_{\text{short}}^{\text{CP}} + N_{\text{long}}^{\text{CP}}}{N_{\text{slot}}} \tag{3.7}$$

is the mean number of samples of the CP within the LTE frame, where $N_{\text{long}}^{\text{CP}}$ and $N_{\text{short}}^{\text{CP}}$ are the lengths of the long and short LTE CPs, and N_{slot} is the number of OFDM symbols per slot. Notice that the equality in Eq. (3.6) holds if $n \bmod N_{\text{slot}} = 0$.

The delay (in seconds) corresponding to the estimated channel response $\tilde{h}[n, \kappa]$ for each value of κ, namely τ_κ, is obtained as

$$\tau_\kappa = \frac{\kappa}{f_s}. \tag{3.8}$$

Note that it is possible to obtain an exact expression for t_n as

$$t_n = \frac{1}{f_s}\left(\left\lfloor \frac{n}{N_{\text{slot}}} \right\rfloor s_{\text{slot}} + u_{\text{slot}}\left(n \bmod N_{\text{slot}}\right)\right) + \hat{t}_0, \tag{3.9}$$

where

$$u_{\text{slot}}(m) = \left[N_{\text{long}}^{\text{CP}} + N + \left(N_{\text{short}}^{\text{CP}} + N\right)(m-1)\right](1 - \delta_{m,0}) \tag{3.10}$$

is the index of the starting sample of the m-th OFDM symbol within an LTE slot, s_{slot}^S is the number of time-samples per LTE slot, and $\delta_{p,q}$ is the Kronecker delta function defined as

$$\delta_{i,j} = \begin{cases} 1 & \text{if } i = j \\ 0 & \text{if } i \neq j. \end{cases} \tag{3.11}$$

For many of the estimations performed in the following sections (see, e.g., Section 3.5), it is more convenient to consider a channel with an impulse response starting at delay zero for all n, namely $\hat{h}[n, \kappa]$. This allows us to consider the same subset of delays[8] along the whole path for estimating each desired parameter. Therefore, we estimate the propagation delay for each frame l as the number of samples including a fractional part, namely $\hat{\kappa}^l = \kappa_i^l + \kappa_f^l$, where κ_i^l is the integer part and κ_f^l is the fractional one. Then, we can estimate the channel response for the l-th frame correcting the fractional part as

$$\hat{h}^l[n, \kappa] = \text{IFFT}_\lambda^N\left(\tilde{H}^l[n, \lambda] \cdot e^{-j2\pi \frac{\lambda}{N} \kappa_f^l}\right). \tag{3.12}$$

The integer part is compensated by applying an offset to the delay when obtaining the complete channel response, i.e.,

$$\hat{h}[n, \kappa] = \hat{h}^l[n - s_{\text{F}} \cdot l, \kappa - \kappa_i^l], \quad l = \left\lfloor \frac{n}{s_{\text{F}}} \right\rfloor. \tag{3.13}$$

[8] When estimating parameters from the channel (see Section 3.5), we use a finite number of delays less than $N_{\text{short}}^{\text{CP}}$.

3.3.3 SNR Estimation

The SNR is estimated considering exclusively the data subcarriers by means of the method described in [ROD16, Section 4.5.2]. Guard subcarriers, direct current (DC) subcarrier as well as pilot subcarriers are discarded *a priori*. Hence, the average SNR per data subcarrier is obtained. The SNR estimation is performed by considering the following steps:

1. Noise samples in the time domain are captured with the transmitter switched off (hence not transmitting any signal).
2. The captured noise samples in the time domain are then processed as if they were actual data samples, i.e., the cyclic prefix is removed, a FFT is performed and both guard and DC subcarriers are removed.
3. As a result, $w^{(n,\lambda)}$ noise samples are obtained in the frequency domain, each one corresponding to the λ-th subcarrier of the n-th OFDM symbol, where $\lambda \in \mathcal{D}^{(n)}$, being $\mathcal{D}^{(n)}$ the set of indexes of the data subcarriers for the n-th OFDM symbol.
4. All previous steps are repeated when the transmitter is switched on, so $r^{(n,\lambda)}$ data samples (of course affected by noise) are obtained in the frequency domain.
5. The average SNR for each OFDM symbol is then estimated by averaging out the instantaneous SNR values for the different data subcarriers. Defining

$$\bar{r}^{(n)} = \frac{1}{\left|\mathcal{D}^{(n)}\right|} \sum_{\lambda \in \mathcal{D}^{(n)}} \left|r^{(n,\lambda)}\right|^2 \tag{3.14}$$

and

$$\bar{w}^{(n)} = \frac{1}{\left|\mathcal{D}^{(n)}\right|} \sum_{\lambda \in \mathcal{D}^{(n)}} \left|w^{(n,\lambda)}\right|^2, \tag{3.15}$$

where $\left|\mathcal{D}^{(n)}\right|$ is the cardinality of $\mathcal{D}^{(n)}$, i.e., the number of data subcarriers for the n-th symbol. Then, the SNR for each OFDM symbol is calculated as

$$\text{SNR}^{(n)} = \frac{\bar{r}^{(n)} - \bar{w}^{(n)}}{\bar{w}^{(n)}}. \tag{3.16}$$

3.4 Path Loss Estimation

The path loss is defined as the ratio between the transmitted and the received power, and it is expressed in decibels as a function of the distance as [RAP+96]

$$\text{PL}(d) = 10 \log_{10} \frac{P_t}{P_r(d)}, \tag{3.17}$$

where $\text{PL}(d)$ is the path loss (in dB) for a distance d, P_t is the transmit power and $P_r(d)$ is the receive power at a distance d. In this work we adopt a simplified log-distance path loss model which allows us to characterize the large-scale path-loss as well as the shadow fading variations

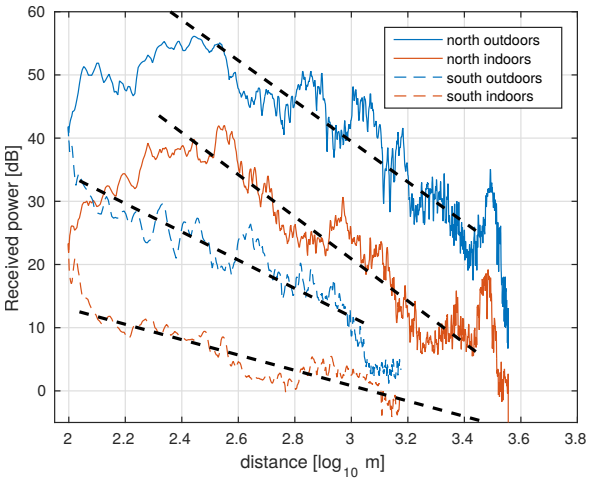

(a) Transmitting only with the antennas serving the north sector.

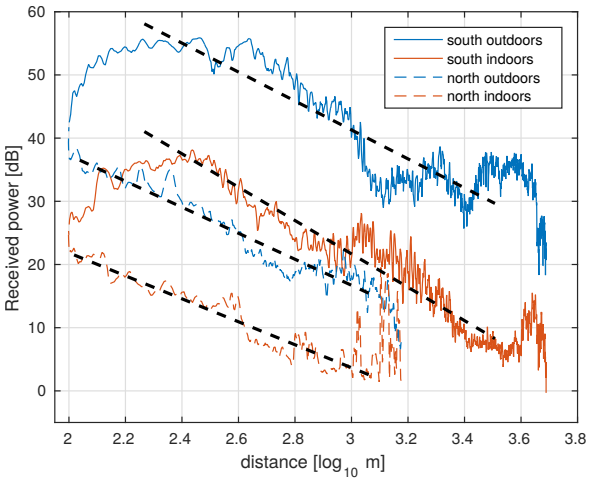

(b) Transmitting only with the antennas serving the south sector.

Figure 3.9: Received energy and least-squares fitting along both north and south sectors for the receive outdoor antenna 1 and the receive indoor antenna 1.

of the channel response. This model is expressed in decibels as in [RAP+96]

$$\mathrm{PL}(d) = \overline{\mathrm{PL}}(d_0) + 10\gamma \log_{10} \frac{d}{d_0} + X_\sigma = b + 10\gamma \log_{10} d + X_\sigma, \tag{3.18}$$

where γ is the so-called path loss exponent, d_0 is a distance relatively close to the transmitter known as "break distance" or "breakpoint", X_σ is a zero-mean Gaussian random variable with a standard deviation σ representing the variations due to the medium and small-scale fading, and $\overline{\mathrm{PL}}(d_0)$ corresponds to the mean path loss at the break distance. The terms depending on d_0 are reorganized to obtain the last expression in Eq. (3.18).

Using Eq. (3.18) (neglecting X_σ) we estimate b and γ for each combination of active sector, receive antenna and measured sector by using least squares fitting over the energy of the receive signal[9]. This way we obtain the large-scale fading curves for each scenario. Fig. 3.9 shows the received energy for both sectors when only a single sector was active. Note that only the results for outdoor antenna 1 and indoor antenna 1 are shown in all the plots; the results for the other antennas are similar. For each energy curve, the corresponding fitting is provided. As shown in Fig. 3.9, for the highest and the lowest considered distance values, the model does not fit well the data due to the high directivity of the transmit antennas. This is because the omnidirectional model assumed for the transmit antennas does not hold in this case. Fig. 3.9 also shows that the antennas serving the north sector cause an interference into the south sector and vice versa. This is due to the configuration of the eNodeB antennas.

Given that X_σ is modeled as a zero-mean Gaussian random variable with standard deviation σ, we subtract the obtained fittings from the received energies to estimate such a standard deviation σ. Fig. 3.10 show the estimated cumulative probabilities of X_σ when only a single

[9]Note that the low speed measurements, as explained in Section 3.2.3, are used here.

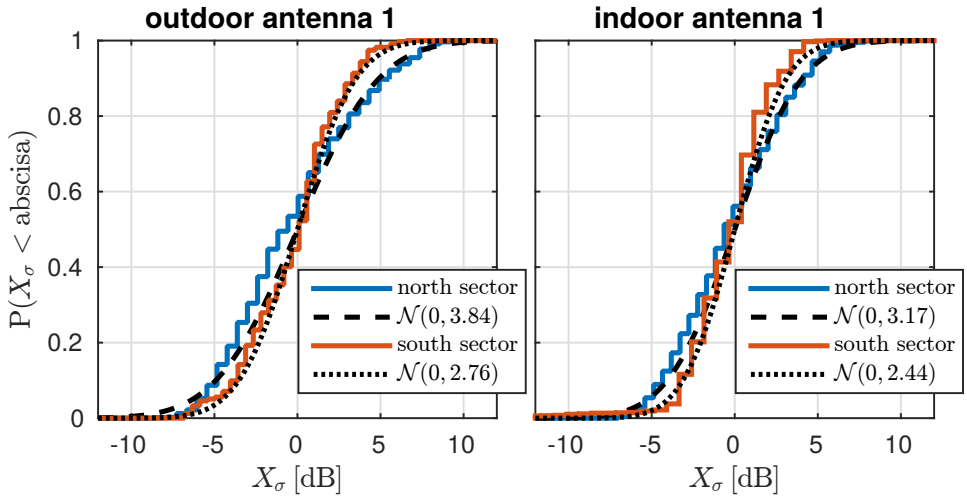

(a) Transmitting only with the antennas serving the north sector.

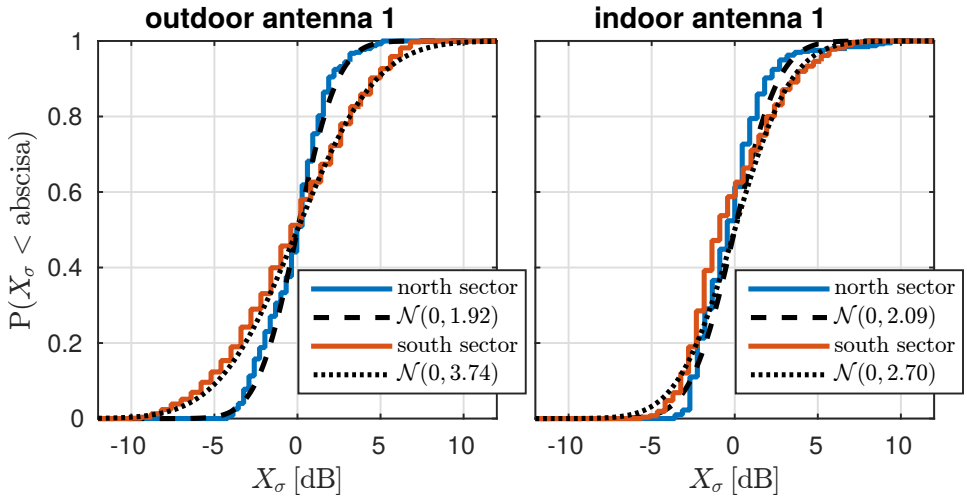

(b) Transmitting only with the antennas serving the south sector.

Figure 3.10: Cumulative probabilities of X_σ for receive outdoor antenna 1 and indoor antenna 1 along both north and south sectors.

sector (north or south) is active. We also plot the theoretical cumulative probabilities of zero-mean Gaussian distributions with the standard deviation σ estimated for each case. We can see that the fitting between the estimated and theoretical curves is very good. Finally, Table 3.4 shows the corresponding path loss parameters (γ, b and σ) estimated from the measurement data. As seen in Table 3.4, the path loss exponent is very similar for all cases (both sectors as well as indoor and outdoor receive antennas). However, a large penetration loss is observed for the indoor receiver. This justifies the utilization of a relay scheme for provisioning services to the users in a practical deployment. Hence, for the rest of the analysis, we consider exclusively the external link (eNodeB to outdoor antennas).

Table 3.4: Path loss parameters (γ, b and σ) estimated for both north (N) and south (S) sectors and for each of the four receive antennas. The column TX specifies the active sector, whereas the column RX denotes the sector along which the measurements are performed

		outdoor ant. 1			**outdoor ant. 2**			**indoor ant. 1**			**indoor ant. 2**		
TX	**RX**	γ	b	σ	γ	b	σ	γ	b	σ	γ	b	σ
N	N	3.20	-135.61	3.84	2.53	-113.34	4.08	3.33	-120.88	3.18	3.17	-115.93	2.85
	S	2.23	-78.63	2.76	1.80	-64.94	1.83	1.20	-36.94	4.38	0.74	-26.75	1.06
S	N	2.06	-78.44	1.91	2.23	-78.70	1.78	1.82	-58.16	2.09	1.89	-60.96	1.56
	S	2.29	-110.00	3.74	2.32	-103.36	1.68	2.64	-100.89	2.70	2.58	-98.91	2.39

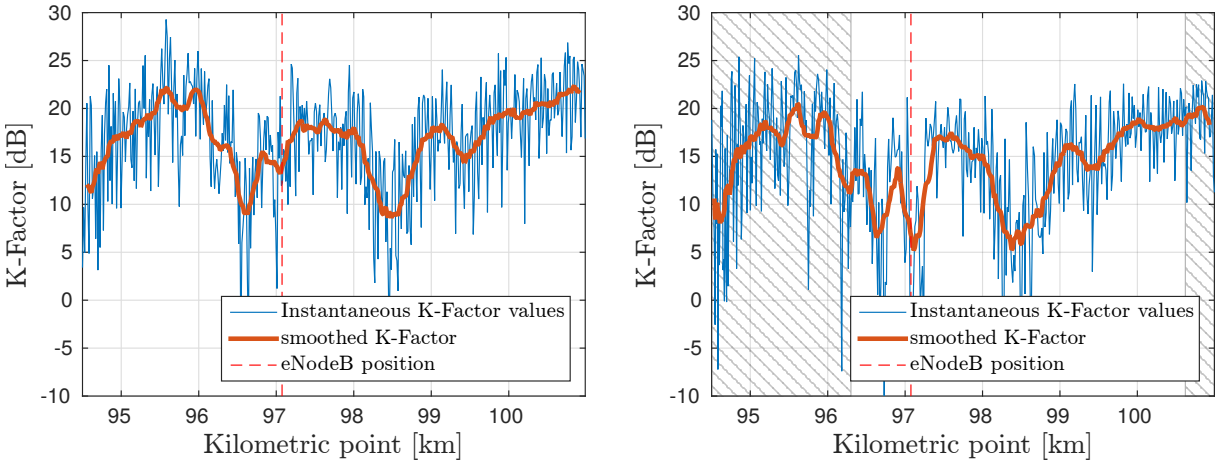

(a) Train moving at 100 km/h.

(b) Train moving at 200 km/h.

Figure 3.11: Estimated K-factor for outdoor antenna 1. The result of averaging out the instantaneous values by means of a sliding window are also shown. The over-imposed pattern of gray diagonal lines denotes the areas where the train speed was not constant

3.5 Estimation of Channel Condensed Parameters

The so-called condensed parameters allow us to characterize other effects of the channel different than the path loss. In this section we consider condensed parameters like K-factor, PDP, delay spread, and Doppler PSD. Note that the high-speed measurements, as explained in Section 3.2.3, are used here. In all the cases the train was moving from the north sector to the south one and both sectors were active.

3.5.1 K-factor

The evaluated scenario can be classified as rural area and exhibits a strong line-of-sight (LoS) component during most of the train trajectory. Thus, one of the channel paths presents a predominant power with respect to the others. Due to this, the fluctuations of the path gain

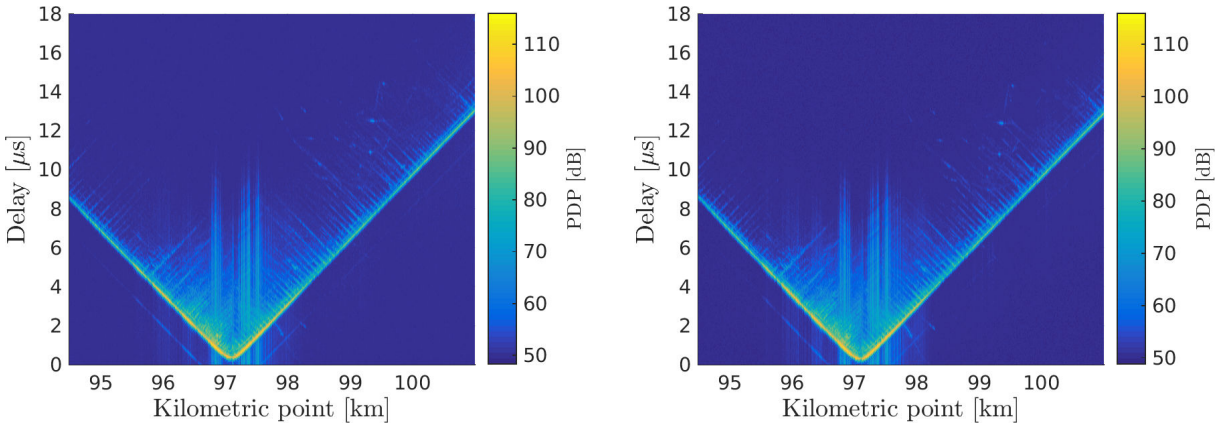

(a) Train moving at 100 km/h.

(b) Train moving at 200 km/h.

Figure 3.12: Estimated PDP for outdoor antenna 1.

follow a Rice distribution. The Rice distribution is parametrized by the power ratio of the fixed and fluctuating components of the path loss, namely the K-Factor.

The instantaneous values of the K-Factor are calculated according to the method proposed by Greenstein *et al.* in [GME99]. More specifically, the equation in [GME99, Eq. (9)] was evaluated for the experimental data, taking into account the tap corresponding to the LoS component.

Fig. 3.11 shows the instantaneous values of the K-Factor expressed in decibels versus the KP for the train speeds of 100 km/h and 200 km/h. Smoothed values of the K-Factor by using a sliding window are also plotted in such figures. The obtained results show that the K-Factor is noticeably higher than zero, which is coherent with the hypothesis of the existence of a strong LoS component. Only at certain positions along the train trajectory the K-Factor exhibits deep local minimum values (e.g., at KPs 96.6 km and 98.4 km), which are caused by reflecting obstacles along the train path (see Section 3.6 for more details). It can be also seen that the trend of the K-Factor does not change significantly with the train speed.

3.5.2 Power Delay Profile

A parameter typically used to analyze how much energy arrives at the receiver with a certain delay is the PDP. The PDP around the n-th OFDM symbol can be obtained from a complex-valued channel time response estimate as in [MOL12]

$$P[n,\kappa] = \frac{1}{2\alpha+1} \sum_{m=n-\alpha}^{n+\alpha} \left| \tilde{h}[m,\kappa] \right|^2, \tag{3.19}$$

where α adjusts the length of the considered segment of the time response[10].

Fig. 3.12 shows the estimated PDP for the train moving at 100 km/h and 200 km/h. The presented results are obtained by evaluating Eq. (3.19) for equally-spaced OFDM symbols.

[10]The considered segment includes the time responses for the OFDM symbols with indexes $n-\alpha, \ldots, n+\alpha$.

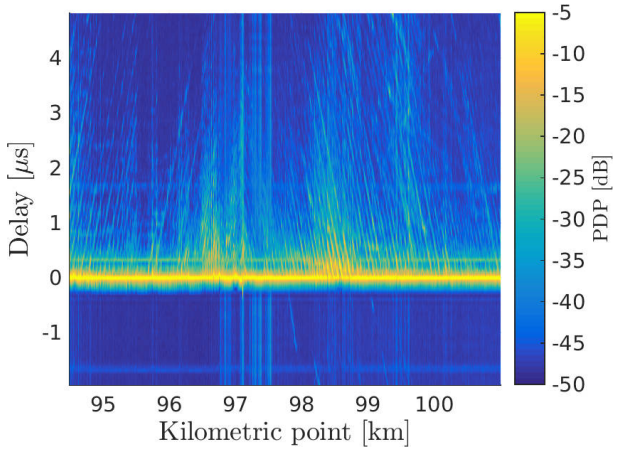

Figure 3.13: Normalized PDP for outdoor antenna 1 for the train moving at 100 km/h, not taking into account the propagation delay.

Note that the shape of the PDP curves accounts for the propagation delay, being the values with the lowest delay the ones corresponding to the KPs closer to the transmit antenna. Note also that the magnitude of the PDP decreases with the distance to the eNodeB antennas.

By comparing Figs. 3.12a and 3.12b, we can conclude that the PDP is independent from the train speed. It is important to note that the longer PDP responses around the eNodeB are caused by the energy spreading effect of the IFFT. This effect is not so noticeable for other KPs since their power is much lower.

Results corresponding to the train moving at 100 km/h are shown in Fig. 3.13 when the propagation delay is subtracted, i.e., we evaluate Eq. (3.19) by using $\hat{h}[n,\kappa]$ (instead of $\tilde{h}[n,\kappa]$) for equally-spaced OFDM symbols. Furthermore, the values obtained per frame were normalized; hence, the magnitude obtained does not depend on the distance to the transmit antenna. This way we can perform a fair comparison between the PDP results for different KPs, not taking into account the energy spreading effect of the IFFT. It can be seen that PDP responses are noticeable longer for some areas (e.g., at KPs 96.6 km and 98.4 km), which is caused by reflecting obstacles along the train path (see Section 3.6 for more details).

It has been shown that under some specific circumstances the error probability due to delay dispersion is proportional to the normalized second-order central moment of the PDP, namely the RMS delay spread [MOL12]. RMS delay spread can be calculated as

$$\sigma_\kappa[n] = \sqrt{\overline{\tau_\kappa^2}[n] - \left(\overline{\tau_\kappa}[n]\right)^2}, \tag{3.20}$$

where the second moment of τ_κ is given by

$$\overline{\tau_\kappa^2}[n] = \frac{\sum\limits_{\kappa} P[n,\kappa]\,\tau_\kappa^2}{\sum\limits_{\kappa} P[n,\kappa]} \tag{3.21}$$

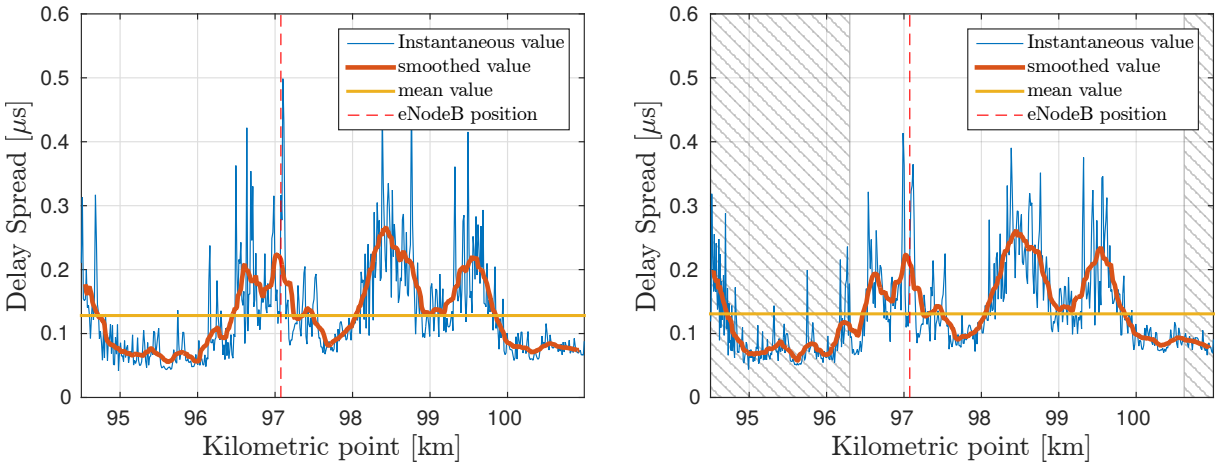

(a) Train moving at 100 km/h.

(b) Train moving at 200 km/h.

Figure 3.14: Estimated root mean square (RMS) Delay Spread. The over-imposed pattern of gray diagonal lines denotes the areas where the train speed was not constant. Smoothed instantaneous values by means of a sliding window are also shown, as well as the mean Delay Spread for the whole path.

and the first one is obtained as

$$\overline{\tau_\kappa}[n] = \frac{\sum_\kappa P\left[n,\kappa\right]\tau_\kappa}{\sum_\kappa P\left[n,\kappa\right]}. \tag{3.22}$$

Fig. 3.14 shows the RMS delay spread for the train moving at 100 km/h and 200 km/h. The plots also include the results of smoothing out the instantaneous RMS delay spread values by means of a sliding window, as well as the mean delay spread for the whole path followed by the train. In Fig. 3.14 we can see that the delay spread results are coherent regardless of the considered speed. Results shown in Fig. 3.14 are congruent with those in Fig. 3.13, showing a larger delay spread for the areas with more reflections.

3.5.3 Doppler Power Spectral Density

The Doppler power spectral density is related to the angle of arrivals (AoAs) of the multipath components and the direction of movement of the receiver. Doppler PSD around the n-th OFDM symbol for the delay index κ, namely $S\left[n,\kappa,\theta\right]$, can be obtained as the FFT of the autocorrelation of a certain segment of the time response of the channel centered at time index n. Considering the estimated channel response $\hat{h}\left[n,\kappa\right]$, the autocorrelation values are obtained as

$$R_{\hat{h}}[n,\kappa,\lambda] = \begin{cases} \sum_{m=n}^{n+2\alpha-\lambda} \hat{h}\left[m+\lambda,\kappa\right]\hat{h}^*\left[m,\kappa\right], & \lambda \geq 0 \\ \sum_{m=n}^{n+2\alpha+\lambda} \hat{h}\left[m,\kappa\right]\hat{h}^*\left[m+\lambda,\kappa\right], & \lambda < 0 \end{cases}, \tag{3.23}$$

where $\lambda = -2\alpha,\ldots,2\alpha$ is the lag of the autocorrelation and α adjusts the length of the considered segment of the channel time response. Then, the Doppler scattering function

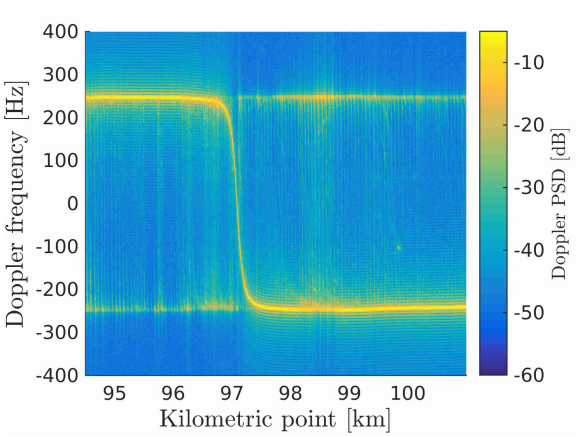

(a) Train moving at 100 km/h.

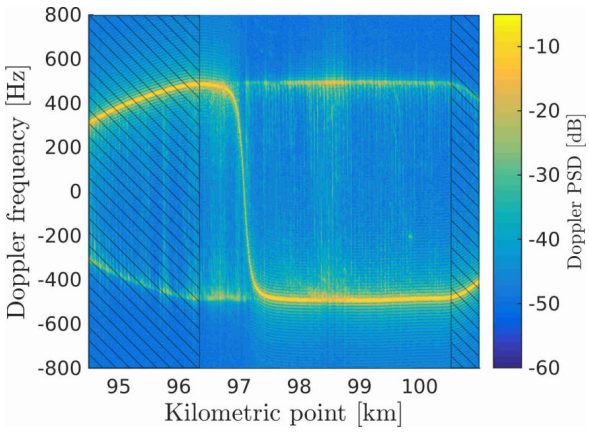

(b) Train moving at 200 km/h.

Figure 3.15: Doppler Spectrum for outdoor antenna 1. The over-imposed pattern of gray diagonal lines denotes the areas where the train speed was not constant.

[MOL12] can be written as

$$S\left[n,\kappa,\theta\right] = \text{FFT}_{\lambda}\left\{R_{\hat{h}}[n,\kappa,\lambda]\right\}, \tag{3.24}$$

where $\text{FFT}_{\lambda}\left\{\cdot\right\}$ denotes the FFT of the argument with respect to the autocorrelation lag λ, and θ is the discretized Doppler frequency index, being the corresponding Doppler frequency

$$\nu_{\theta} = \theta \frac{f_s}{N + \overline{N^{\text{CP}}}} \frac{N_{\text{corr}}}{N_{\text{D}}}, \tag{3.25}$$

where $N_{\text{corr}} = 4\alpha + 1$ is the number of samples of the autocorrelation, N_{D} the size of the FFT and $\theta = -\frac{N_{\text{D}}}{2}, \ldots, \frac{N_{\text{D}}}{2} - 1$. Note that $(N + \overline{N^{\text{CP}}})/f_s$ is the mean duration of an OFDM symbol. The Doppler PSD $\overline{S}$ is obtained after averaging out the Doppler scattering function S over the κ values as

$$\overline{S}\left[n,\theta\right] = \frac{1}{|\mathcal{K}|} \sum_{\kappa \in \mathcal{K}} S\left[n,\kappa,\theta\right], \tag{3.26}$$

where $\mathcal{K}$ denotes the set of considered values for κ.

Fig. 3.15 shows the normalized Doppler PSD for equally-spaced OFDM symbols when the train moves at 100 km/h and 200 km/h, obtained as indicated in Eq. (3.26). As expected, the module of the maximum Doppler value is related with the train speed as

$$|f_{\max}| \approx \frac{|v|\, f_c}{c_0}, \tag{3.27}$$

where $f_{\max}$ denotes the maximum Doppler frequency, v the velocity of the train, and $f_c = 2.6$ GHz the carrier frequency. This brings us to maximum Doppler PSD values of approximately 240.7 Hz and 480.5 Hz for train speeds of 100 km/h and 200 km/h, respectively. The sign of the instantaneous Doppler PSD values depends on the direction of the velocity vector of the train with respect to the transmitter. This causes the effect shown in Figs. 3.15a

and 3.15b, where the Doppler PSD values concentrate around $\pm|f_{\max}|$ and change abruptly when the train passes by in front of the eNodeB antennas.

When the train is in the north sector (i.e., it approaches the eNodeB) the Doppler PSD is maximum in $+|f_{\max}|$. Conversely, when the train is in the south sector (i.e., moving away from eNodeB), the Doppler PSD reaches its maximum at $-|f_{\max}|$. This is coherent with the measurement environment, which features a strong LoS component. However, significant reflections in $-|f_{\max}|$ for the north sector (conversely, values in $+|f_{\max}|$ for the south sector) can be seen, which are caused by obstacles along the train path (see Section 3.6 for more details).

3.6 Particularities of the Measured Train Scenario

In the previous section we showed different condensed parameters along the whole train trajectory. However, since the total distance shown is relatively large, small details cannot be appreciated. In this section we show and discuss the PDP and the Doppler PSD for three specific segments of the train trajectory, each of them being 250 m long, which are:

- **Segment (a)**: KPs between 98.375 and 98.625. There are strong reflections in this area, as shown by the Doppler results in Fig. 3.15. The K-factor also achieves the lowest values and the delay spread the highest ones in this area (see Fig. 3.11 for the K-factor and Fig. 3.14 for the delay spread). This supports the hypothesis of a weaker LoS condition.
- **Segment (b)**: KPs between 98.875 and 99.125. In this area, the K-factor and the delay spread take values close to the mean ones shown in Fig. 3.11, and in Fig. 3.14, respectively.
- **Segment (c)**: KPs between 100.25 and 100.5. In this area the K-factor achieves the highest values and the delay spread the lowest ones (see Fig. 3.11 for the K-factor and Fig. 3.14 for the delay spread).

Fig. 3.16 shows the Doppler Spectrum for the three aforementioned segments when the train moves at 100 km/h. For all the segments shown, the train moves away from the eNodeB within the south sector, hence the LoS Doppler component is located approximately at $-|f_{\max}| = -240.7$ Hz (see Section 3.5.3). Furthermore, a noticeable reflection component can be seen in the opposite frequency, $+|f_{\max}| = 240.7$ Hz. In addition, abrupt transitions in the Doppler from $-|f_{\max}|$ to $+|f_{\max}|$ occur periodically. These transitions in the Doppler are similar to the ones occurring when the train passes by in front of the eNodeB antennas (see Figs. 3.15a and 3.15b). In fact, these abrupt changes in the Doppler are due to the nearby objects reflecting the signal. More specifically, the masts supporting the overhead line (see Fig. 3.17b) are the origin of the stronger reflections. It can be seen that the distance between consecutive masts (see Fig. 3.17a) is coherent with the separation between consecutive Doppler transitions shown in Fig. 3.16. Finally, it is worth noting that the magnitude of the reflected components with respect to the LoS component depends on the position of the train along the path. This is related both with the distance and the angle with respect to the transmit antenna.

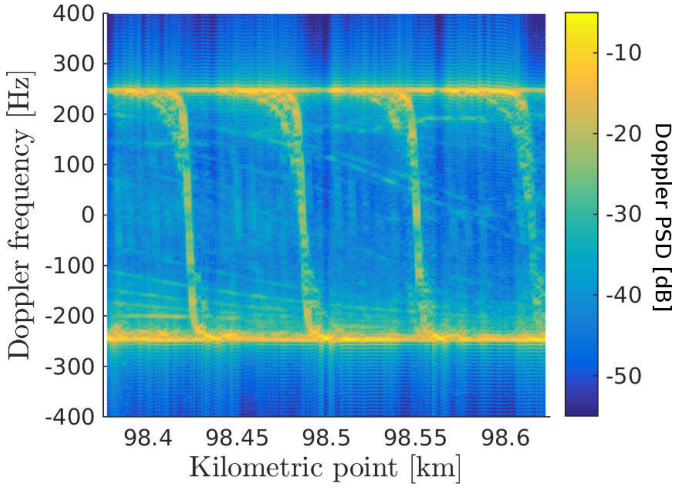

(a) Doppler Spectrum for the train moving at 100 km/h along segment (a).

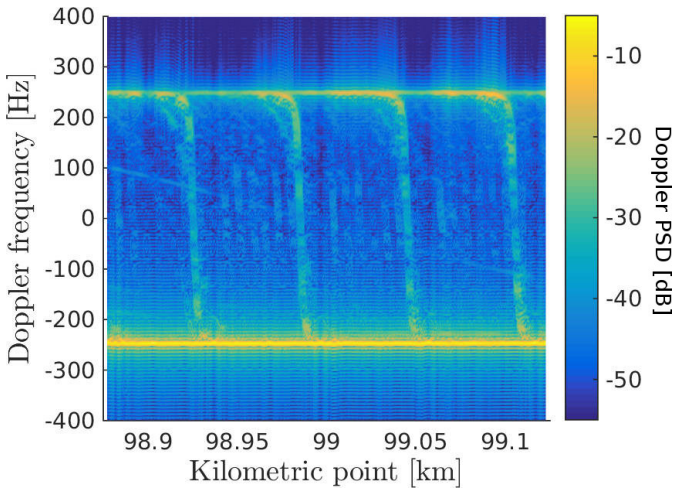

(b) Doppler Spectrum for the train moving at 100 km/h along segment (b).

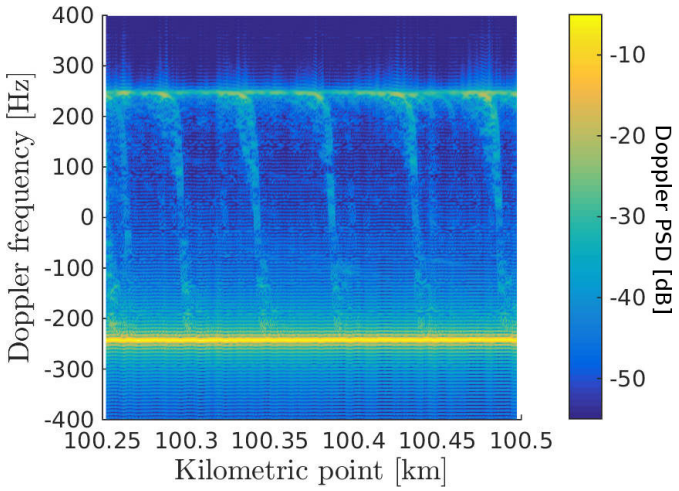

(c) Doppler Spectrum for the train moving at 100 km/h along segment (c).

Figure 3.16: Doppler Spectrum for outdoor antenna 1 for the train moving at 100 km/h along segments (a), (b) and (c).

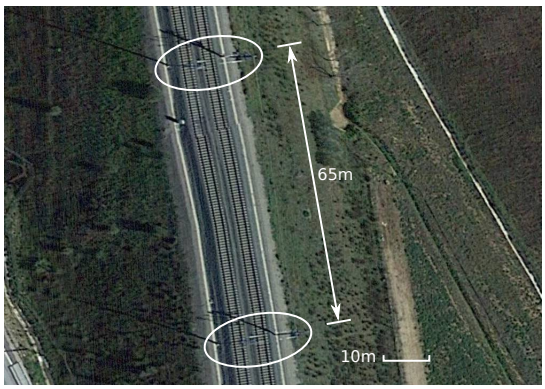

(a) Top view of a small section of the track. The masts supporting the overhead lines are shown enclosed in ellipses. The distance between masts is also shown. Map Image by ©2017 DigitalGlobe, Cartography Institute of Andalucía, Map Data by ©2017 Google, National Geographic Institute of Spain.

(b) Image of a train on the Córdoba - Málaga line. Some of the masts supporting the overhead line can be seen at both sides of the track. Image obtained from http://www.ferropedia.es licensed under CC BY-SA 3.0.

Figure 3.17: Detailed view of the train infrastructure elements that cause signal reflections to the receiver.

Fig. 3.18 shows the normalized PDP for the three segments, verifying the existence of reflection components coherent with those shown in Fig. 3.16. The PDP figures clearly show that the reflected component associated to each mast decreases its delay with respect to the LoS component (and increases its power) when the train moves towards the mast. The magnitude of the reflected components with respect to the LoS one is coherent with the relationship between the reflected component and the LoS one shown in Fig. 3.16. For example, the largest reflections in the PDP are obtained for segment (a). Coherently, the magnitude of the reflections with respect to the LoS component in Fig. 3.16 is also maximum for segment (a).

Fig. 3.19 shows the estimated Doppler PSD for the three considered segments. Note that the regular oscillations in these results are a manifestation of the Gibbs phenomenon, after evaluating Eq. (3.24), due to the use of time-limited signals to calculate Eq. (3.23). In agreement with Fig. 3.16, the maximum of the Doppler PSD is located at $-|f_{\max}|$ (due to the contribution of the main path). For the segments with stronger reflected components, a relevant peak is also appreciated at $+|f_{\max}|$. The magnitude of the peak with respect to the main component is reduced for the cases with lower reflections. For other frequencies, the Doppler values are distributed approximately according to a "U" shape. This suggests that, although there is a strong LoS in the railway environment, reflections caused by railway infrastructure elements may lead to a Doppler PSD with noticeable components in other frequencies, similar to the Jakes spectrum [WC 74]. It is worth noting that the condensed parameters are affected by the reflections, as they significantly change their respective trends in the areas where the reflections are stronger (e.g., segment (a)). Due to this, we can expect a severe effective link SNR degradation for such areas.

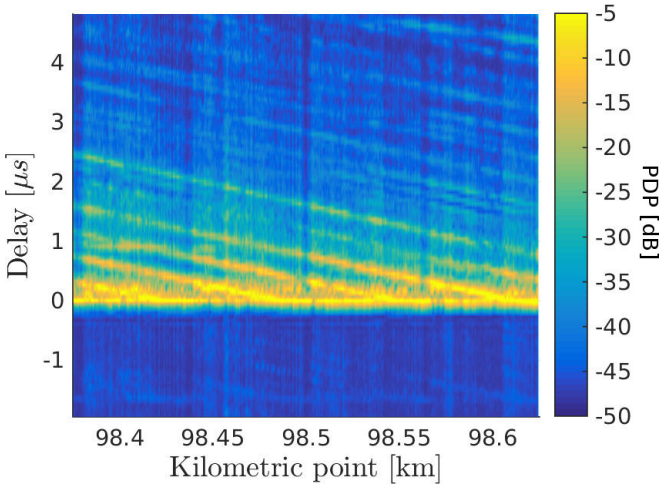

(a) Normalized PDP for the train moving at 100 km/h along segment (a).

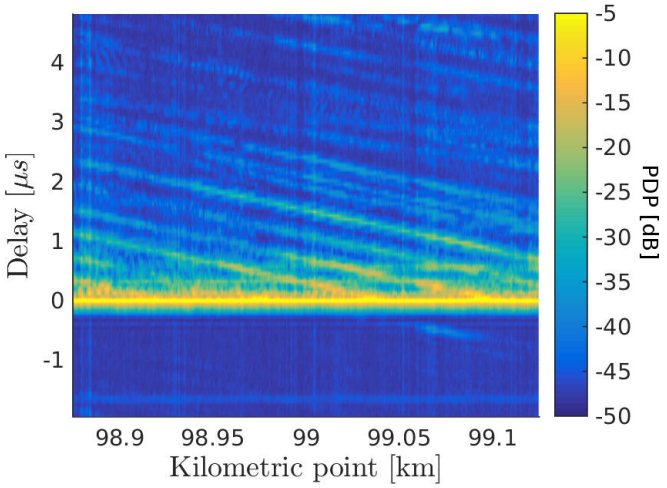

(b) Normalized PDP for the train moving at 100 km/h along segment (b).

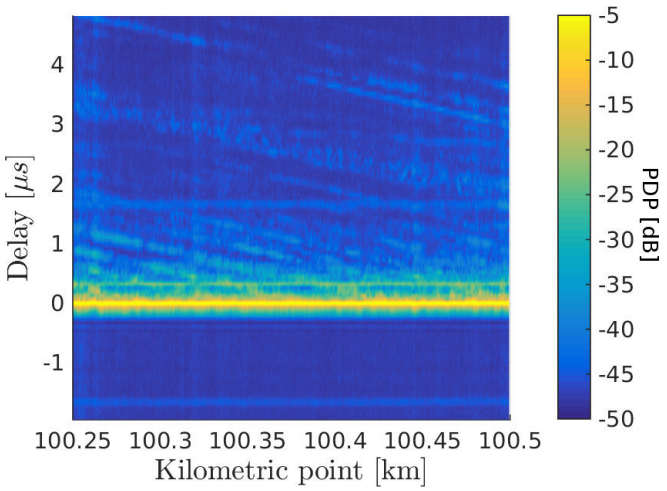

(c) Normalized PDP for the train moving at 100 km/h along segment (c).

Figure 3.18: Normalized PDP for outdoor antenna 1 for the train moving at 100 km/h along segments (a), (b) and (c). The propagation delay is not taken into account.

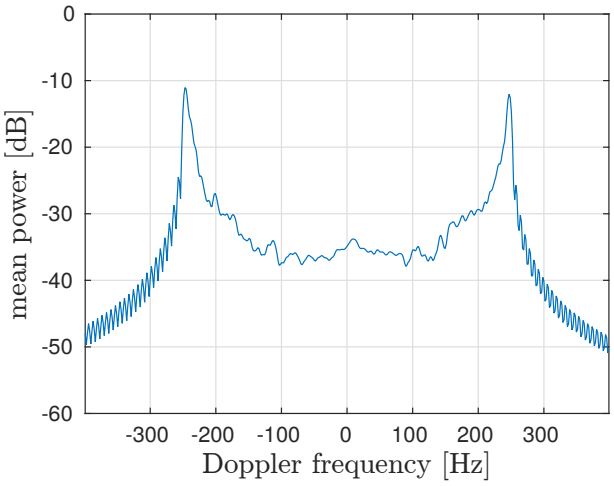

(a) Estimated Doppler PSD for the train moving at 100 km/h along segment (a).

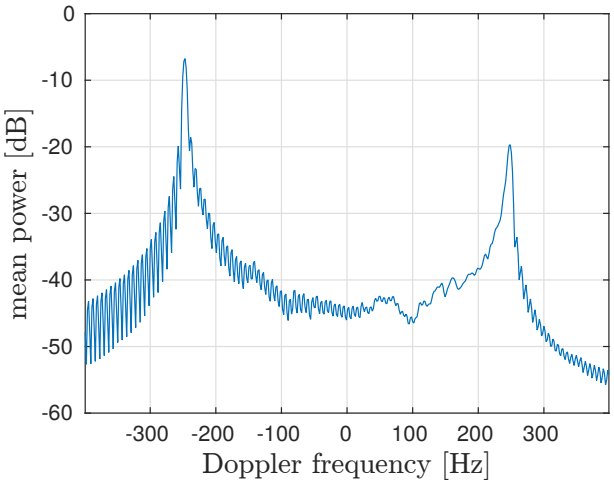

(b) Estimated Doppler PSD for the train moving at 100 km/h along segment (b).

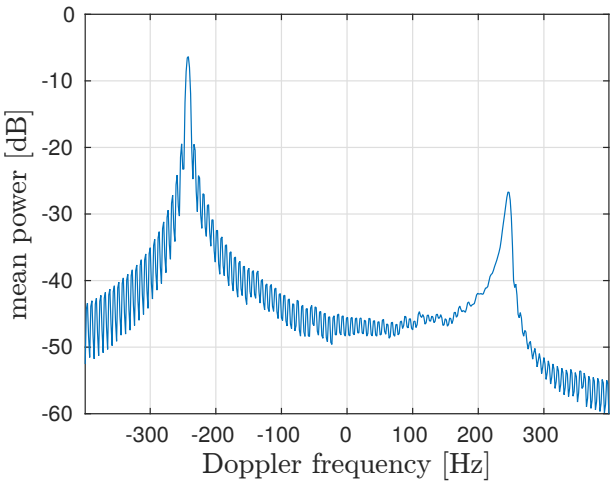

(c) Estimated Doppler PSD for the train moving at 100 km/h along segment (c).

Figure 3.19: Estimated Doppler PSD for outdoor antenna 1 for the train moving at 100 km/h along segments (a), (b) and (c).

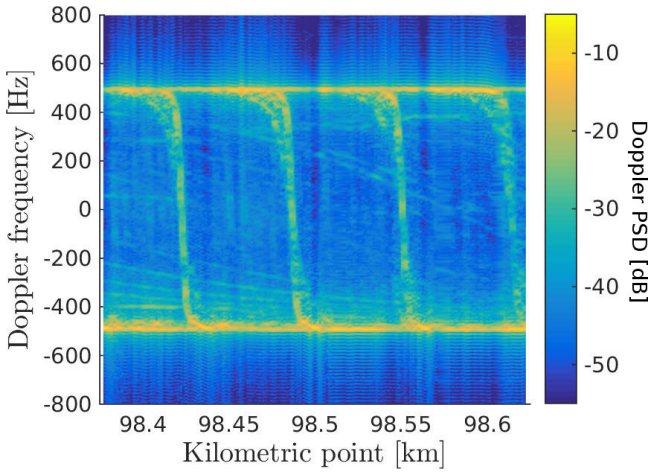

(a) Doppler Spectrum for the train moving at 200 km/h along segment (a).

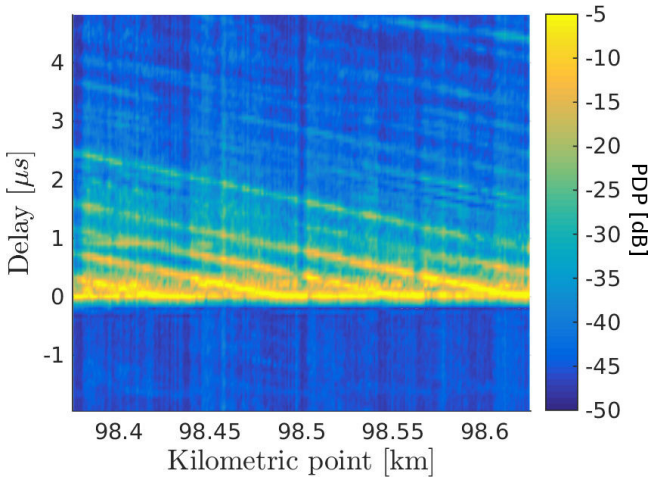

(b) Normalized PDP for the train moving at 200 km/h along segment (a). The propagation delay is not taken into account.

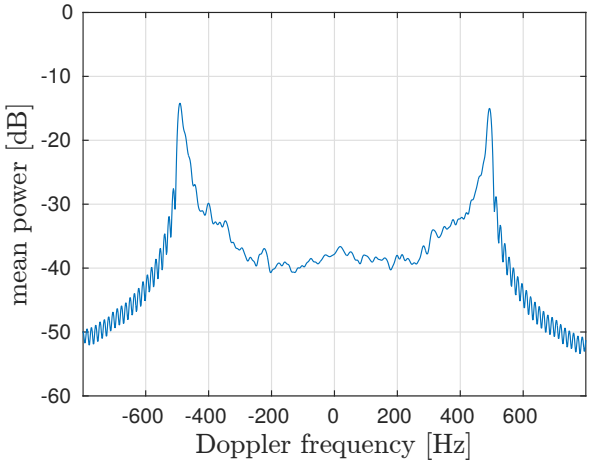

(c) Estimated Doppler PSD for the train moving at 200 km/h along segment (a).

Figure 3.20: Condensed parameters for outdoor antenna 1 and the train moving at 200 km/h along segment (a).

Finally, it is important to notice that the described effects are independent from the train speed. Figs. 3.20a to 3.20c, respectively, show the Doppler spectrum, the normalized PDP and the estimated Doppler PSD for segment (a) when the train moves at 200 km/h. The obtained results are coherent with those corresponding to a moving speed of 100 km/h.

3.7 Conclusions

In this chapter we provided a complete and detailed characterization of the downlink (FDD LTE for the 10 MHz bandwidth profile) between a commercial LTE eNodeB and a train moving at high velocities along a track in commercial operation in a rural area in Spain, considering a carrier frequency of 2.6 GHz. Instead of using an available eNodeB from a general-purpose mobile network, we installed an eNodeB for our measurements at the same location where a GSM-R base station is deployed, thus being able to control all the parameters of the eNodeB. The eNodeB served two sectors using two antennas per sector from different antenna panels installed in the same tower as the GSM-R antennas. We also considered two links: the one between the eNodeB and the antennas placed outdoors on the train roof, and the direct link between the eNodeB and a receiver inside the train. With respect to our hardware, the GTEC Testbed nodes were employed as receivers to acquire the transmitted data and were equipped with GPS modules with a twofold purpose: geo-referencing the acquired data and minimizing the frequency offset between the eNodeB and the receivers. Regarding the measurement procedure, different train speeds were considered, also with one or both sectors active. A high repeatability level was observed for different train passes with identical configuration parameters, thus enabling us to compare the results at different speeds consistently. Furthermore, high-resolution results were obtained from our measurements, since we continuously captured the signal at the receiver during the whole measurement campaign.

The aforementioned downlink characterization consisted in assessing the path loss, the SNR, the K-factor, the PDP, the delay spread, and the Doppler PSD for different train speeds. Furthermore, the estimation procedure for each aforementioned parameter was fully described mathematically, highlighting the drawbacks and pitfalls to be considered for the different analysis methods. In particular, the path loss was estimated from the received energy. Assuming a simplified log-distance model, we estimated the path loss exponent and variance of the medium- and small-scale fading. Although the path loss exponent was very similar in all cases (both sectors as well as indoor and outdoor receive antennas), a large penetration loss was observed for the indoor receiver. This would justify the utilization of a relay scheme for provisioning services to the users in a practical deployment. Therefore, we limited the rest of the analysis to the external link (eNodeB to outdoor antennas).

The results corresponding to the K-factor show that a dominant LoS component was present along the track and that its trend does not depend on the train speed. The same conclusions are obtained from the PDP results, which are also congruent with those obtained for the RMS delay

spread. With respect to the Doppler PSD, the largest magnitudes correspond approximately to the frequencies ± 240.7 Hz and ± 480.5 Hz for train speeds of 100 and 200 km/h, respectively, which is consistent with the presence of a strong LoS component. The sign of the Doppler PSD changes abruptly when the train passes by in front of the transmit antennas.

The obtained results exhibit a good level of agreement with the expected ones according to the assumed theoretical models. However, the utmost importance of carrying out measurements from actual LTE-compliant transmit signals is reflected in the so-called particularities found in the considered train scenario. In this chapter we devoted an entire section to study such particularities. More specifically, we observed periodic abrupt transitions in the Doppler PSD along the whole measured path. Such transitions –similar to the ones occurring when the train passes by in front of the eNodeB antennas– are mainly caused by the masts supporting the overhead line. Those effects, which are invariant with the train speed, are also observed in the PDP results. It is worth noting that the Doppler PSD results are distributed approximately according to a "U" shape with an additional peak caused by the LoS component. This shows that, although there is a strong LoS for the considered environment, reflections caused by the railway infrastructure elements may lead to noticeable Doppler components in other frequencies, similar to the Jakes spectrum. Overall, all the condensed parameters are affected by the reflections, as their respective trends change significantly in the areas where the reflections are stronger. Due to this, we can expect a severe effective link SNR degradation in such areas.

Chapter IV

Experimental Characterization of 2.6 GHz LTE Wireless Links in a Modern Subway Station

In this chapter we consider the wireless channel characterization in a modern subway station and its corresponding entrance tunnel. We setup a Long Term Evolution (LTE) Evolved Node B (eNodeB) transmitter in the middle of the platform of a modern station in the Madrid Metro, Spain, to cyclically transmit frequency-division duplex (FDD) LTE signals at a carrier frequency of 2.6 GHz and with a bandwidth of 10 MHz. Two receivers were used to study both the eNodeB-train and the eNodeB-mobile links. The train was moving at a constant speed of 18 km/h from the entrance tunnel until it is completely stopped at the end of the station. Using the multipath components extracted with the space-alternating generalized expectation-maximization (SAGE) algorithm, we characterized the wireless channel response for both links based on the following parameters: power delay profile, root mean square delay spread, Doppler power spectral density, small-scale fading distribution, and K-factor.

This chapter is mainly based on the following co-authored publication:

- Tomás Domínguez-Bolaño, José Rodríguez-Piñeiro, José Antonio García-Naya, Xuefeng Yin, and Luis Castedo. "**Measurement-based characterization of train-to-infrastructure 2.6 GHz propagation channel in a modern subway station**". Accepted in *IEEE Access*, 2018

The structure of the chapter is as follows. Section 4.1 introduces the chapter. Section 4.2 describes the experimental setup. Section 4.3 explains the signals used for transmission and the signal processing at the receiver based on the SAGE algorithm. Section 4.4 presents and discusses the wireless channel characterization based on the power delay profile (PDP), the root mean square (RMS) delay spread, the Doppler power spectral density (PSD), the small-scale fading distributions, and the K-factor estimated from the measurements. Finally, Section 4.5 is devoted to the conclusions.

4.1 Introduction

With the continuous growth and expansion of cities, subways are gaining importance as they are considered the most efficient transportation system for commuter users [SR16; DEV89; AG84; PRO95; ROD16]. During transportation, people intensively employ mobile devices to work, to access social networks, or for entertainment purposes. Vehicles also produce mobile data, deserving special consideration safety-related applications since they impose stringent requirements on aspects such as reliability and low latency, although demanding relatively low throughputs [ROD16; EUR10]. Also, radio communications are required to provide subway users and staff with voice and data-based services.

Leaky feeders are one of the most popular technologies to provide wireless communications in tunnels. Although they do not require sophisticated channel models for system planning, they are unreliable in case of fire, breaking down the communications in the entire tunnel [HKJ14]. Moreover, leaky feeders become rather expensive for systems operating at high carrier frequencies, whereas maintenance becomes tedious once tunnels are under operation [GUA+12]. Using antennas instead of leaky feeders solves those problems. Antennas offer easier maintenance, a much higher upper frequency limit, a larger distance between repeaters, and they are ten times cheaper to deploy [GUA+12]. However, antennas require more sophisticated channel models for system design and planning to assure that quality of service (QoS) requirements are fulfilled.

Many channel models describing radio waves propagation inside tunnels were proposed in the literature (see [HKJ14; FOR+13] and the references therein). Most of them consider typical frequencies used for public wireless systems such as GSM, UMTS, Wi-Fi, or LTE. Basically, channel models for tunnels can be classified into two main groups: deterministic and empirical. Deterministic channel models use mathematical expressions to predict channel characteristics. Usually, three different deterministic approaches are distinguished in the literature: models based on solving Maxwell's equations [PZ00; KON+99; RM12; BER+09; MJ09], models based on modal analysis [ELS75; DUD+07; KB94; ZHA03; DER78; WAI80], and models based on geometric optics (GO) [CJ96; DID+00; KK00; MW74; MRJ04]. On the other hand, empirical models are based on measurements, like the widely used two-slope channel model [KB94; MAS+09; HKJ10; ZZS01].

Characterizing and modeling wireless channels for subway stations and their corresponding entrance tunnel is a topic greatly overlooked in the literature. In this regard, although not oriented to subway stations, the delay spread and path loss for $900\,\text{MHz}$ and $2.1\,\text{GHz}$ when entering tunnels were studied based on GO in [PJJ01]. Also, an analysis of different channel parameters such as power delay profile (PDP), root mean square (RMS) delay spread and path loss based on measurements and GO modeling for a receiver entering a tunnel was carried out in [MRJ04]. The path-loss characteristics in subway tunnels at $2.65\,\text{GHz}$ were also studied in [CHO+06]. More recently, a measurement campaign was carried out in underground subway

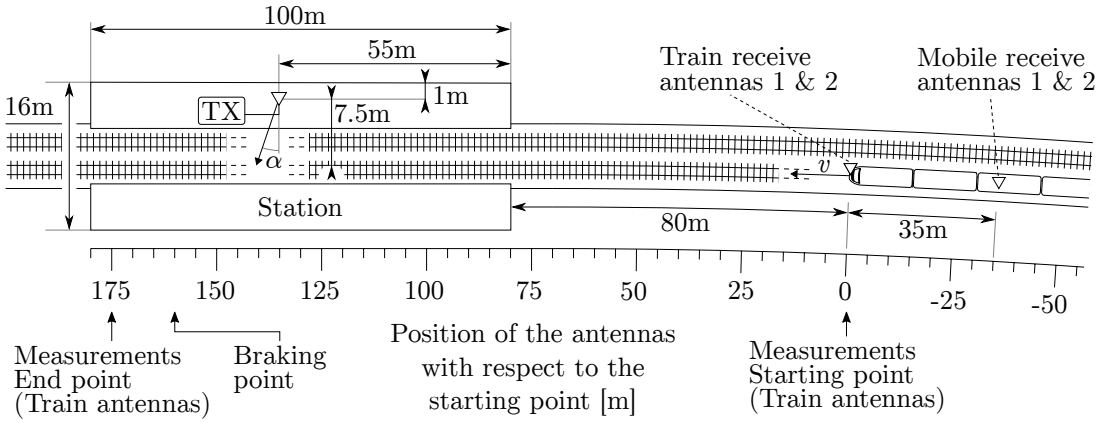

Figure 4.1: Schematic of the measurement scenario (not at scale) at "La Almudena" subway station, Madrid Metro, Spain. The scenario consists of a modern subway station and its corresponding entrance tunnel.

environments in Shanghai, China, and a channel model was developed for tunnel and station environments based on the clusters of the obtained channel impulse responses [CAI+16].

The Madrid Metro in Spain was the scenario of the channel measurements described in [ZHA+16a; ZHA+16b]. On the one hand, [ZHA+16a] details the wideband propagation modeling results (mainly mean power and delay spread) obtained from an extensive campaign of static wideband propagation measurements at 980 MHz and 2450 MHz carrier frequencies using a channel sounder. On the other hand, [ZHA+16b] describes the measurements carried out with two different testbeds. One of the testbeds was used to estimate both the signal-to-noise ratio (SNR) and the throughput of Mobile WiMAX transmissions, hence not focusing on channel characterization. The other testbed was used with a twofold objective. Firstly, the path loss was characterized based on narrowband measurements at 980 MHz, 2.4 GHz, and 5.7 GHz carrier frequencies for straight and curved tunnels and inside the station. Secondly, the PDP was estimated considering wideband signals at 1 GHz and 2.45 GHz carrier frequencies with the channel sounder transmitter and receiver installed on the station platform, not considering the tunnel nor its entrance. Notice that the channel responses in [ZHA+16a; ZHA+16b] were obtained using conventional techniques such as the narrow pulse technique, avoiding more powerful approaches such as the space-alternating generalized expectation-maximization (SAGE) technique proposed in this work and also in [CAI+16].

In this work we characterize the wireless channel at 2.6 GHz in "La Almudena" subway station[1] and its entrance tunnel (see Figs. 4.1 and 4.2). The main contributions and novelties of this paper are detailed below:

1. We consider a Long Term Evolution (LTE) Evolved Node B (eNodeB) transmit antenna located at the center of the platform and two receive antenna sets placed, inside and outside the subway train. We transmit standard-compliant frequency-division duplex

[1] Line 2 of "Metro de Madrid", Madrid Metro, Spain.

Figure 4.2: Picture taken from the train cabin while conducting measurements. The train is at the measurement starting point with the station visible at the end.

(FDD) LTE signals at 2.6 GHz with a 10 MHz bandwidth. During the measurements, the train moves from the entrance tunnel to the end of the station at a constant speed of 18 km/h, whereas the transmit signals are recorded continuously at the sampling frequency of $f_s = 15.36$ MHz. In contrast to the measurement-based channel characterizations provided in [DOM+17a; ZHA+16b], the delays, Doppler frequencies, and complex-valued amplitude coefficients of the multipath channel response components are estimated from the standard-compliant FDD LTE signals by means of the SAGE technique as described in [FLE+99].

2. The most important channel parameters —such as PDP, RMS delay spread, Doppler power spectral density (PSD), small-scale fading distribution, and K-factor— are estimated from the channel impulse response estimates obtained with the SAGE technique. We considered both outdoor and indoor receive antennas, which enables us to characterize two different links: the eNodeB-train and the eNodeB-mobile links. The eNodeB-train link (direct communication between an eNodeB and the outdoor receive antennas attached to the front window of the train cabin) would be the one used for the transmission of critical data and possibly to support passenger service provisioning based on a relay scheme (see [NET12]). On the other hand, the eNodeB-mobile link evaluation allows for characterizing the direct communication between a mobile user inside the train carriage and an eNodeB placed on the station platform.
3. We provide the mathematical description of all the procedures followed to obtain the results. In particular, mathematical descriptions are provided to obtain the estimated channel response parameters, such as PDP, RMS delay spread and Doppler PSD, from the delays, Doppler frequencies, and complex-valued amplitude coefficients of the multipath components estimated by the SAGE algorithm.

Although the measurement setup considered in this work is the same as that described in

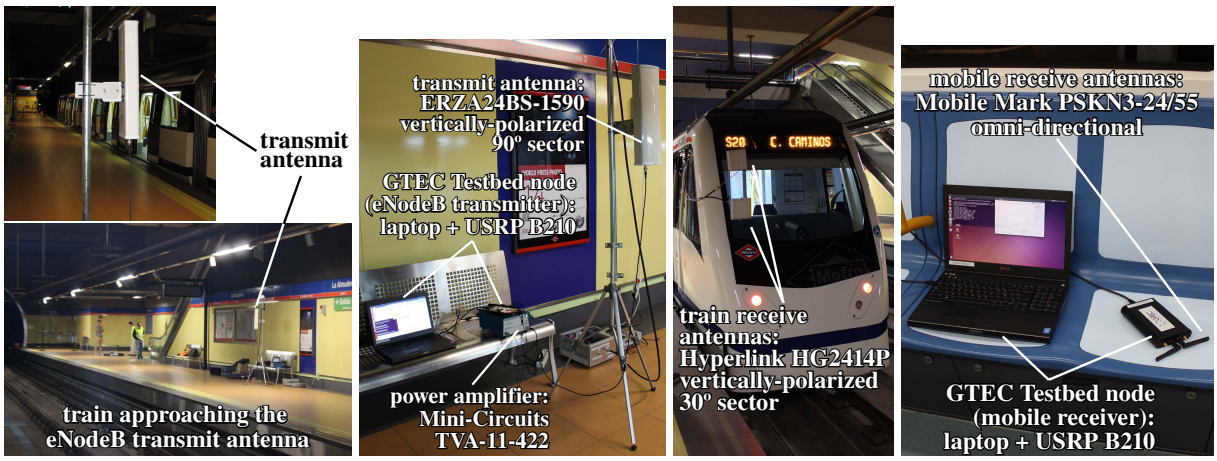

Figure 4.3: GTEC Testbed nodes and antennas used in the measurements: (a) eNodeB transmit antenna on the platform (top) and panoramic view of the platform (bottom). (b) GTEC Testbed node placed on a station bench and configured as an eNodeB transmitter with the corresponding antenna. (c) receive antennas of the eNodeB-train link placed on the train front window. (d) GTEC Testbed node placed on a train bench and configured as the receiver of the eNodeB-mobile link.

[ZHA+16b], both works are essentially different. Firstly, we consider in this work LTE instead of WiMAX transmissions. Secondly, the WiMAX transmissions in [ZHA+16b] were used to estimate SNR, error vector magnitude (EVM), and throughput, but not to characterize the wireless channel.

4.2 Experimental Setup

4.2.1 Measurement Environment

The measurement campaign took place in "La Almudena" subway station, which is a representative example of a modern subway station. A schematic and a picture of this measurement scenario are respectively shown in Figs. 4.1 and 4.2, whereas a 3D model of a typical modern subway station of the Madrid Metro can be found in [ZHA+16b, Fig. 2]. "La Almudena" station is 100 m long and the eNodeB transmit antenna (see Figs. 4.3a and 4.3b) is located approximately in its center, 55 m away from one of its edges. Although the entrance tunnel is slightly curved, we do not take it into account since such curvature is small (see Fig. 4.2).

For the eNodeB-train link, two antennas were placed outdoors on the train front window (see Figs. 4.1 and 4.3c). For the eNodeB-mobile link, two antennas were placed inside the train car, 35 m apart from the eNodeB-train receive antennas (see Figs. 4.1 and 4.3d). To reference the position of the antennas along the track we set the arbitrary point 0 to the location of the train antennas (eNodeB-train link) at the measurement starting point (see Fig. 4.1), where the

train was moving forward at a constant speed of $v = 18$ km/h, and it maintained the speed until it started to brake about 10 m before stopping, and thus ending the measurements. Signals for both the eNodeB-train and the eNodeB-mobile links where captured simultaneously. Therefore, for the train antennas, the measurement started at position 0, whereas for the mobile antennas the measurement started at position -35 m (see Fig. 4.1).

The measurement trajectory is further divided into several sections for both the eNodeB-train and the eNodeB-mobile links depending on the train position:

- **eNodeB-train link**: The position of the train outdoor antennas during the measurements ranges from 0 m to 175 m (see Fig. 4.1). Note that this position is also the distance traveled by the train during the measurements. We identify the following sections:
  - **Tunnel**: From 0 m to 80 m, the train antennas are inside the station entrance tunnel (see Fig. 4.2).
  - **Station (1)**: From 80 m to 135 m, the train antennas are inside the station before passing in front of the eNodeB transmit antenna (see Fig. 4.3a).
  - **Station (2)**: From 135 m to 160 m, the train antennas are inside the station after passing in front of the transmit antenna and before the train starts braking.
  - **Braking**: From 160 m to 175 m, the train brakes to finally stop.
- **eNodeB-mobile link**: The two antennas (see Fig. 4.3d) are located inside the train car and placed 35 m apart from the eNodeB-train receive antennas. Hence, the locations of these antennas during the measurements range from -35 m to 140 m (see Fig. 4.1). We identify the following sections:
  - **Tunnel:** From -35 m to 80 m, the mobile antennas are inside the entrance tunnel.
  - **Station:** From 80 m to 140 m, the mobile antennas are inside the station. In this case, the train starts braking a little before the mobile antennas reach the position of the transmit antenna. Once the train is stopped, the mobile antennas are located 5 m after passing in front of the transmit antenna.

Fig. 4.4 shows the SNR values along the train trajectory for the eNodeB-train and the eNodeB-mobile links. Such SNR curves were estimated in the time domain and smoothed by a moving average using a window length of $20\,\lambda$, where λ is the wavelength at the carrier frequency of 2.6 GHz. We can see that, for the mobile antennas, the highest SNR values are obtained when such antennas pass in front of the eNodeB transmit antenna. However, for the train antennas, due to their high directivity (see Section 4.2.2), the SNR does not vary significantly along the "Station (1)" section.

[2]For each LTE frame slot (a slot occupies half a subframe), the cyclic prefix length is 80 samples (5.2083 microseconds), whereas for the remaining six orthogonal frequency-division multiplexing (OFDM) symbols it is reduced to 72 samples (4.6875 microseconds

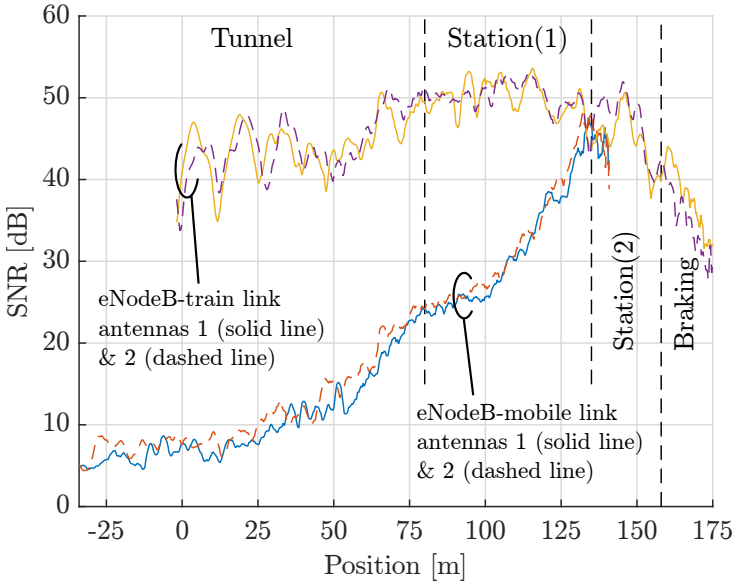

Figure 4.4: SNR for the eNodeB-train and eNodeB-mobile links. Note that the sections specified in the picture refer to the eNodeB-mobile link.

Table 4.1: FDD-LTE testbed configuration parameters.

Parameter	Value
Transmit power	18.5 dBm (at input antenna port)
Sampling frequency	15.36 MHz
Carrier frequency	2.6 GHz
Bandwidth	10 MHz (9 MHz occupied)
Number of subcarriers	1024 (600 used)
Cyclic prefix length	Normal [3GPb][2]

4.2.2 Measurement Equipment and Procedure

For the generation, transmission, acquisition and processing of LTE signals, the so-called GTEC Testbed was used. Notice that the GTEC Testbed has been extensively used in many vehicular measurement campaigns [SUÁ+14b; ZHA+16b; ZHA+17; DOM+17b; ROD+16a; FEI+16; ROD+16c; ROD+16b]. More specifically, one node was placed at the subway station to serve as an eNodeB (see Figs. 4.3a and 4.3b) which cyclically transmits the same LTE signal specified in Table 4.1, whereas two nodes were configured as receivers: one is attached to the train antennas placed on the train front window (see Fig. 4.3c) which corresponds to the eNodeB-train link, whereas the other is connected to the mobile antennas (see Fig. 4.3d) and corresponds to the eNodeB-mobile link. Although the GTEC Testbed supports time and frequency synchronization among nodes via GPS, this is not possible in underground scenarios, hence the two receivers

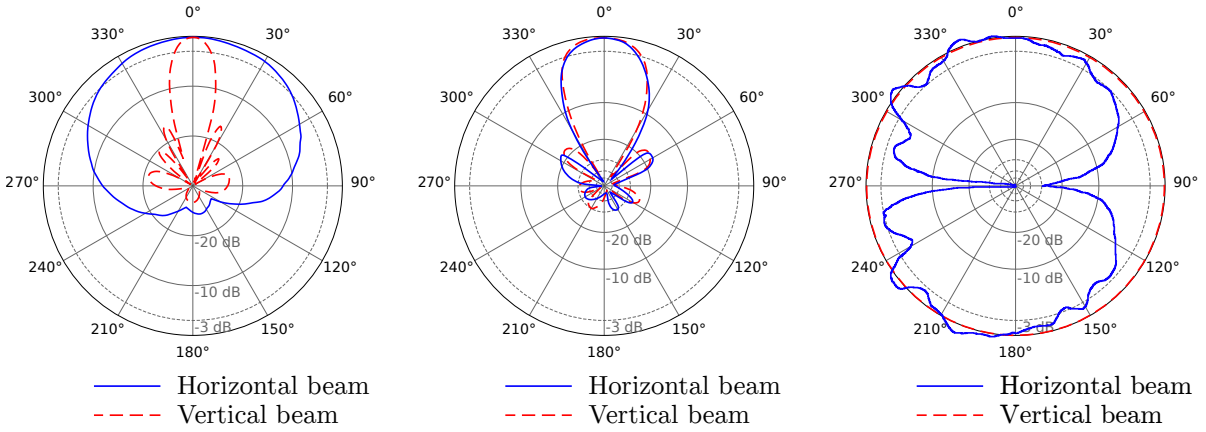

(a) eNodeB transmit antenna

(b) train antennas (eNodeB-train link).

(c) mobile antennas (eNodeB-mobile link).

Figure 4.5: Antenna radiation patterns.

and the transmitter were not synchronized.

4.2.2.1 eNodeB transmitter

The GTEC Testbed node serving as the eNodeB transmitter employs a Mini-Circuits TVA-11-422 power amplifier [MIN] and a vertically polarized $90°$ sector antenna "ERZA24BS-1590" (see Figs. 4.3a, 4.3b and 4.5a). Note that the eNodeB antenna was not completely perpendicular to the track, but a small angle of $\alpha \approx 10°$ was considered (see Fig. 4.3a). The transmit power at the input antenna port was set to 18.5 dBm.

4.2.2.2 eNodeB-train link equipment

Two vertically polarized $30°$ sector "Hyperlink Technologies HG2414P" antennas [TECb] (see Figs. 4.3c and 4.5b) were attached to the train front window. Note that the antenna placement is not optimal in the sense that a receive power deep loss is expected once the train passes in front of the transmit antenna due to the high directivity of the receive antennas as well as the blocking effect of the whole train that obstructs the direct line-of-sight (LoS). Unfortunately, for safety reasons and considering the dimensions of the tunnel, the antennas could not be placed on top of the train or attached to its lateral. Notice also that a similar setup employing the same antennas was considered in [ZHA+16a].

4.2.2.3 eNodeB-mobile link equipment

Two omni-directional and linearly-polarized "Mobile Mark PSKN3-24/55" antennas (see Figs. 4.3d and 4.5c) were located inside the train car, 35 m away from the train antennas (see Fig. 4.1).

4.3 Receiver Signal Processing

Many of the results presented in this chapter depend on the wireless channel response estimates obtained from the received LTE signals. The first step is to detect and synchronize the received LTE frames, which is performed by taking advantage of the Primary Synchronization Signal (P-SCH) and the Secondary Synchronization Signal (S-SCH) (see Section 3.3.1). LTE frames are detected and their time offsets are estimated by correlating the received signal with the P-SCH and the S-SCH associated to the configured eNodeB. The time offsets (or synchronization points) for each frame i, namely κ_i, are just the sample number over the discrete-time received signal where the frame was detected. However, in our case, the measurements obtained from the mobile antennas exhibit a very low SNR in the tunnel section, hence the time offsets estimated for those signals could be inaccurate or even totally wrong. Therefore, to obtain a more accurate estimation of the time offsets, and given that LTE signals are acquired continuously, we apply a robust fit linear regression method [HUB81] to the estimated time offsets from the LTE synchronization signals. Finally, the time offsets for each of the LTE frames are obtained from the robust fit regression line.

The channel response for each LTE frame is estimated by means of the SAGE algorithm, which allows for extracting the parameters of the multipath components of the channel impulse response (see [FLE+99] for details of the SAGE algorithm). The model of the channel impulse response for the ith LTE frame is formulated as

$$h_i(t,\tau) = \sum_{l=1}^{M} \alpha_{i,l} \exp\{j2\pi\nu_{i,l}t\}\delta(\tau - \tau_{i,l}), \tag{4.1}$$

where t is the time variable, τ is the delay variable, M is the number of waves or paths considered, and $\delta(\cdot)$ is the Dirac delta function. The parameters estimated by the SAGE algorithm are $\alpha_{i,l}$, $\nu_{i,l}$, and $\tau_{i,l}$, being $\alpha_{i,l} \in \mathbb{C}$ the lth-path amplitude, and $\nu_{i,l} \in \mathbb{R}$ and $\tau_{i,l} \in \mathbb{R}$ the respective Doppler frequency and delay for the lth path.

To estimate the channel with the SAGE algorithm, the time offsets are used to pick each of the individual frames and pass them to the algorithm. Therefore, the domain of t in Eq. (4.1) is $[0, T)$, being $T = 10\,\text{ms}$ the duration of an LTE frame, and the obtained delays $\tau_{i,l}$ are relative delays. To obtain the absolute delays we take into account the time offsets κ_i and the scenario geometry. However, as said before, note that the GTEC Testbed nodes were not synchronized in time nor in frequency due to the lack of GPS coverage inside the station. This introduces an additional error in the obtained time offsets with respect to the expected ones. Therefore, the absolute time delay for the lth tap of the ith frame, namely $\tilde{\tau}_{i,l}$, is obtained as

$$\tilde{\tau}_{i,l} = \tau_{i,l} + (\kappa_i - i \cdot N_s - \kappa_0)/f_s + i \cdot m + b, \tag{4.2}$$

where N_s is the number of samples of an LTE frame, b is the absolute delay of the first received LTE frame, and m is a factor (expressed in seconds per frame) to correct the error of the obtained

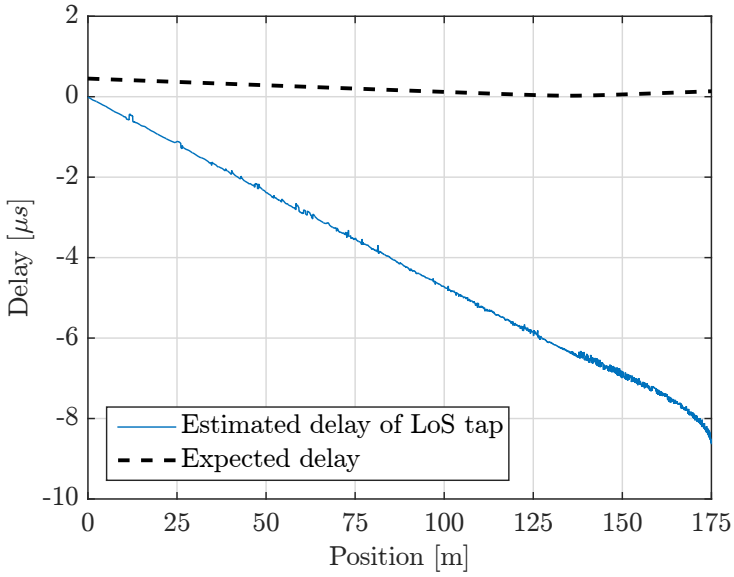

Figure 4.6: Estimated delay of the LoS path for the eNodeB-train link, antenna 1, before correction as indicated in Eq. (4.2).

delay. Based on the scenario geometry, considering that the path followed by the train is an straight line, the expected delay of the signals for a given time t is

$$\tau_{\text{exp}}(t) = \frac{\sqrt{(x_a - vt)^2 + x_p}}{c}, \tag{4.3}$$

where v is the speed of the train (given that in our measurements $v = 18$ km/h is constant, then vt is the distance traveled), $x_a = 135$ m is the position of the transmitter, $x_p = 7.5$ m is the perpendicular distance between the transmitter and the track (see Fig. 4.1), and c is the speed of light. In Fig. 4.6 we show the delay of the LoS tap for the antenna 1 of the eNodeB-train link before correction (hence, $m = 0$ and $b = 0$ in Eq. (4.2)), as well as the expected delay defined in Eq. (4.3). Based on the expected delay, we select the values of m and b in Eq. (4.2) to obtain the correct absolute delay values. Fig. 4.7 shows the delay of the LoS tap once the correction is applied together with the expected delay, revealing that now the estimated delay matches the expected one. Therefore, we define the corrected channel impulse response as

$$\tilde{h}_i(t,\tau) = \sum_{l=1}^{M} \tilde{\alpha}_{i,l} \exp\{j2\pi\tilde{\nu}_{i,l}t\}\delta(\tau - \tilde{\tau}_{i,l}), \tag{4.4}$$

where $\tilde{\tau}_{i,l}$ is the corrected delay defined in Eq. (4.2), $\tilde{\alpha}_{i,l} = \alpha_{i,l}$ and $\tilde{\nu}_{i,l} = \nu_{i,l}$.

Regarding the channel parameter estimation, as detailed in [FLE+99], we consider a sequence of N equally spaced OFDM symbols for each LTE frame. For the eNodeB-train link received signals we use $N = 5$ OFDM symbols, whereas for the eNodeB-mobile link signals we consider different values of N ranging from $N = 5$ for the frames with the highest SNR to $N = 140$ for the frames with lowest SNR (e.g, inside the tunnel). For both links, we estimated $M = 15$ paths using 10 iterations of the SAGE algorithm. Considering that an LTE frame lasts

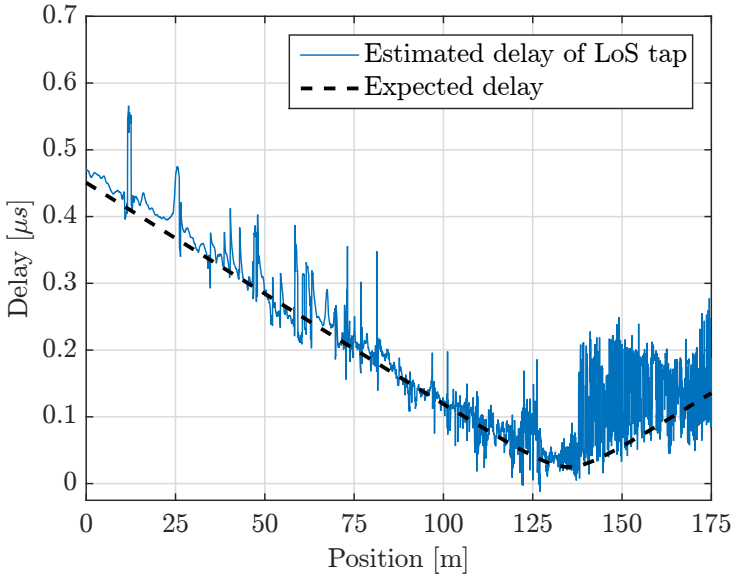

Figure 4.7: Estimated delay of the LoS path for the eNodeB-train link, antenna 1, after correction as indicated in Eq. (4.2).

for 10 ms, for the worst case considered with $N = 5$ the Doppler frequency estimation range is $[-200, 200]$ Hz. In our scenario, the train velocity is 18 km/h and hence the theoretically maximum absolute Doppler shift is 43.33 Hz at a carrier frequency of 2.6 GHz, which is within the estimation range. Also, during the 10 ms LTE frame duration, the train travels 0.05 m, which is much less than the distances between the transmitter antenna, the scatters, and the receive antenna. Therefore, we assume that the channel remains stationary during the duration of a single LTE frame, thus enabling the estimation of the dominant paths parameters using the SAGE algorithm [YIN+15].

Considering again that the LTE frame duration is 10 ms, we define the channel impulse response for the whole train trajectory, which is obtained by concatenating the different $\tilde{h}_i(t, \tau)$, as follows:

$$h(t, \tau) = \tilde{h}_{\lfloor t/(10\,\text{ms})\rfloor}(t - \lfloor t/(10\,\text{ms})\rfloor \cdot 10\,\text{ms}, \tau), \tag{4.5}$$

where $\lfloor \cdot \rfloor$ is the floor operator.

4.4 Measurement Results

In this section we show the results obtained from our measurements, both for the eNodeB-train and the eNodeB-mobile links. These results are the path loss, the power delay profile (PDP), the root mean square (RMS) delay spread, the Doppler power spectral density (PSD), the small-scale fading distribution, and the K-factor. Such results constitute an empirical characterization of the channel experienced by both links as the train approaches and enters the station. Note that for obtaining these results the impact of the antenna patterns has not been removed from the measurement data.

Table 4.2: Path loss estimated parameters for the double breakpoint model (estimating d_1). MSE stands for mean square error.

Antenna	γ_1	γ_2	b_1	b_2	d_1	σ_1^2	σ_2^2	MSE
mobile 1	2.590	3.694	38.819	20.337	47.181	2.800	1.184	2.412
mobile 2	2.614	3.702	37.564	18.930	51.531	3.011	0.595	2.370
train 1	-0.709	1.773	79.905	41.816	34.270	7.048	2.395	6.053
train 2	-0.329	2.037	74.801	36.433	41.865	6.632	2.334	5.462

4.4.1 Path Loss Estimation

Here we consider the path loss as defined in Section 3.4. The path loss is modeled by the following simple log-distance model (see Eq. (3.18), which is again reproduced here for the sake of clarity)

$$\mathrm{PL}(d) = \overline{\mathrm{PL}}(d_0) + 10\gamma \log_{10} \frac{d}{d_0} + X_\sigma = b + 10\gamma \log_{10} d + X_\sigma, \tag{4.6}$$

where d_0 is the so-called "break distance" (a reference distance relatively close to the transmitter [RAP+96]), $\overline{\mathrm{PL}}(d_0)$ is the mean path loss at the distance d_0, γ is the path loss exponent, and X_σ is a zero-mean Gaussian random variable. For simplicity, we factorize the d_0 terms into the intercept term $b = \overline{\mathrm{PL}}(d_0) - 10\gamma \log_{10}(d_0)$. Note that antenna gains are included in the path loss results.

Moreover, in our scenario, the transition from the tunnel to the station changes the signal propagation characteristics. Therefore, a two-breakpoint path loss model [RAP+96] is more suitable and is defined as

$$\mathrm{PL}(d) = \begin{cases} b_1 + 10\gamma_1 \log_{10}(d) + X_{\sigma,1}, & \text{if } d_0 \leq d \leq d_1 \\ b_2 + 10\gamma_2 \log_{10}(d) + X_{\sigma,2}, & \text{if } d_1 \leq d, \end{cases} \tag{4.7}$$

where we have two different regions with intercepts b_1 and b_2, path loss exponents γ_1 and γ_2, and zero-mean Gaussian random variables $X_{\sigma,1}$ and $X_{\sigma,2}$. Note that a consequence of this model is that the following equality holds

$$\overline{\mathrm{PL}}(d_1) = b_1 + 10\gamma_1 \log_{10}(d_1) = b_2 + 10\gamma_2 \log_{10}(d_1). \tag{4.8}$$

Therefore, we considered the following path loss models:

1. Single breakpoint model defined in Eq. (4.6). The intercept b and the path loss exponent γ are estimated by means of a least-squares fitting.
2. Double breakpoint model defined in Eq. (4.7). The intercept b_1, the path loss exponents γ_1 and γ_2, and the distance d_1 are estimated by a least-squares fitting. The intercept b_2 is obtained by means of Eq. (4.8).

The results obtained from the single and double breakpoint models are shown in Tables 4.2 and 4.3, respectively. According to the mean square error (MSE) (calculated considering the

Table 4.3: Path loss estimated parameters for the single breakpoint model.

Antenna	γ	b	σ^2	MSE
mobile 1	3.230	29.795	3.269	3.269
mobile 2	3.198	29.242	3.226	3.226
train 1	0.924	58.180	9.360	9.360
train 2	0.982	56.885	8.874	8.874

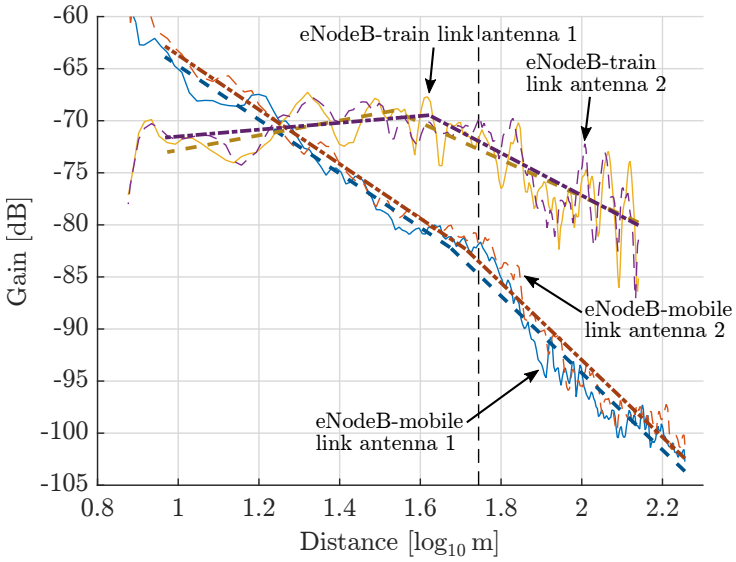

Figure 4.8: Gain ($-\mathrm{PL}(d)$) for the eNodeB-train and eNodeB-mobile links. Fittings obtained with the two breakpoint model are shown in black dashed lines.

path loss in logarithmic units), the double-breakpoint model provides a much better fit than the single-breakpoint one. For the eNodeB-mobile link, the results from the double-breakpoint model are very similar for both antennas (see Table 4.2), the MSE values are almost equal, and the estimated values for d_1 (47.181 m and 51.531 m) are relatively close to the actual distance to the tunnel (55.51 m). For the eNodeB-train link (outdoor receive antennas), the estimated d_1 values for antennas 1 and 2 are 34.270 m and 41.865 m, respectively. In this case, the estimated distances are not so close to the actual ones because of the high directivity of the receive antennas, which makes the receive power to depend not only on the distance but also on the respective angles between the receive and transmit antennas.

Fig. 4.8 shows the estimated gain (negative path loss) for all the four receive antennas considered. We plot superimposed the fittings of the double-breakpoint model (estimating also d_1). The curves shown in Fig. 4.8 were smoothed using a moving average with a window length of $20\,\lambda$ (at the carrier frequency of 2.6 GHz). A clear change in the propagation characteristics for tunnel and station scenarios can be appreciated for both the eNodeB-train and the eNodeB-mobile links. Tables 4.2 and 4.3 show that path loss exponents for the train antennas are slightly greater than 2 (free space). The results are coherent with those shown in [Cho+06], although

the path loss exponent in [CHO+06] is slightly lower than 2. Note that the estimated path loss exponents for the station section (γ_1) become negative due to the high directivity of the receive antennas, which causes the received power to become larger for longer distances if the beams of the transmit and receive antennas are better aligned than for shorter distances. Path loss exponents for the eNodeB-mobile link for the train station are lower than those measured in [ZHA+17], which found that $\gamma = 3.81$ at 2.4 GHz in a completely non-enclosed train station.

4.4.2 Power Delay Profile

The PDP contains information about how much power arrives at the receiver with a certain delay τ. The PDP for the case of a discrete time-delay channel impulse response function is defined in Eq. (3.19). In this chapter we considered a continuous time-delay channel impulse function as defined in Eq. (4.4). In this case, for $\hat{h}(t,\tau)$ being a continuous time-delay impulse response of a stationary channel, the PDP is defined as [MOL12]

$$P_{\hat{h}}(\tau) = R_{\hat{h}}(0,\tau,\tau) = \lim_{T\to\infty} \frac{1}{2T} \int_{-T}^{T} |\hat{h}(t,\tau)|^2 dt, \tag{4.9}$$

where

$$R_{\hat{h}}(\Delta t,\tau,\tau') = \lim_{T\to\infty} \frac{1}{2T} \int_{-T}^{T} \hat{h}(u+\Delta t,\tau)\hat{h}^*(u,\tau')du \tag{4.10}$$

is the autocorrelation function of $h(t,\tau)$. However, this definition for the PDP becomes problematic when the channel impulse response is defined as a sum of delta functions

$$\hat{h}(t,\tau) = \sum_{l=1}^{N} c_l(t)\delta(\tau-\tau_l), \tag{4.11}$$

where $c_l(t)$ is a stationary random process. In this case, using the definition in Eq. (4.9) to calculate the PDP would introduce a singularity problem. In fact, the resulting PDP would contain squared delta functions and it would not be possible to derive, e.g., the mean delay or the delay spread [MM14]. Following [MM14], this analytical problem can be avoided by using a different PDP definition. Assuming uncorrelated scatters, we can write the autocorrelation function as

$$R_{\hat{h}}(\Delta t,\tau,\tau') = \delta(\tau-\tau')P_{\hat{h}}(\Delta t,\tau), \tag{4.12}$$

where $P_{\hat{h}}(\Delta t,\tau)$ is the delay cross power spectral density, being the PDP $P_{\hat{h}}(\tau) = P_{\hat{h}}(0,\tau)$. Note that this PDP definition is not consistent with that in Eq. (4.9). Therefore, for the channel impulse response defined in Eq. (4.11), the PDP can be written as [MM14]

$$P_{\hat{h}}(\tau) = \sum_{l=1}^{N} \mathbb{E}\left[|c_l(t)|^2\right] \delta(\tau-\tau_l), \tag{4.13}$$

where $\mathbb{E}[\cdot]$ is the expectation operator. In practice, the PDP is obtained as the power for a certain timespan over which the channel is quasi-stationary [MOL12]. In our case, we calculate the

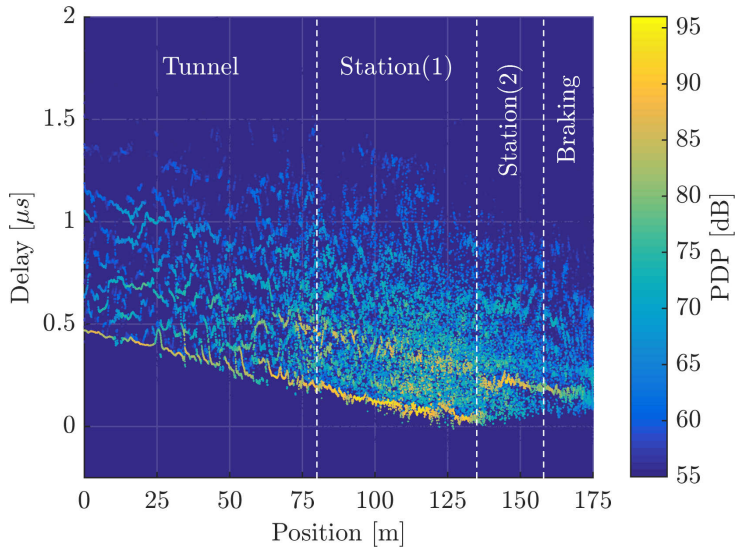

Figure 4.9: PDP scatter plot for the eNodeB-train link along the train trajectory (antenna 1).

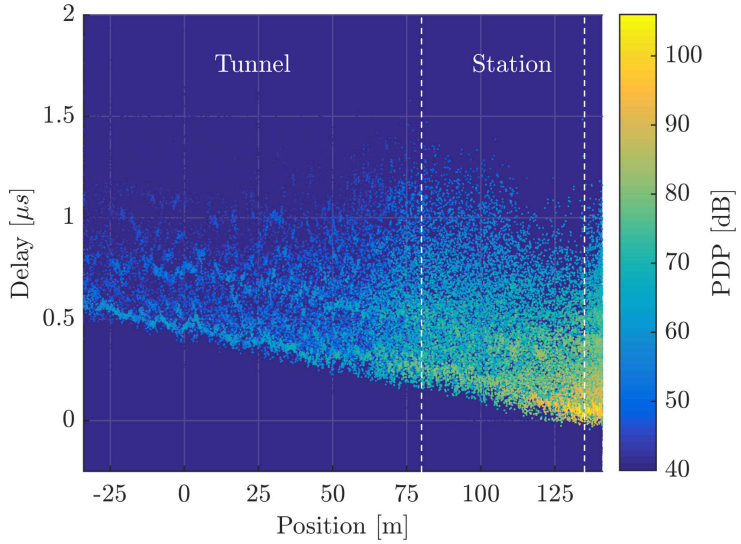

Figure 4.10: PDP scatter plot for the eNodeB-mobile link along the train trajectory (antenna 1).

PDP for each acquired LTE frame from the channel estimates produced by the SAGE algorithm (see Eq. (4.4)), thus obtaining the "instantaneous" PDP. Following [MM14], we define the "instantaneous" PDP for the ith LTE frame as

$$P_i(\tau) = \sum_{l=1}^{M} |\alpha_{i,l}|^2 \, \delta\left(\tau - \tau_{i,l}\right). \tag{4.14}$$

Figs. 4.9 and 4.10 show, respectively, the PDP for the eNodeB-train and the eNodeB-mobile links. The PDPs are drawn using an scatter plot where each point corresponds to the power of a single path, as shown in Eq. (4.14). The slope exhibited by the PDP curves accounts for the propagation delay.

We also calculate the so-called normalized mean PDP for the considered sections as the mean PDP after removing the propagation delay. The normalized mean PDP is useful in link-

level and system-level simulations where the path loss is modeled from the scenario geometry and the small-scale fading characteristics are extracted directly from the measurements.

The estimated propagation delay is computed by applying a robust fit algorithm with the delay of the most powerful taps of the LTE frames for each section, yielding the slope $\tilde{m}$ and intercept $\tilde{b}$. Next, in order to obtain the normalized mean PDP for each section, we sample the time-varying channel impulse response in the delay domain, hence obtaining the equivalent continuous-time versus discrete-delay channel impulse response. We just use a simple interpolation with a rectangular low-pass filter (convolution with a sinc pulse in the delay domain). Hence, the channel impulse response for the ith LTE frame is expressed as

$$\begin{aligned}\hat{h}_i(t, n_\tau) &= \frac{1}{\sqrt{f_\tau}} \left(\tilde{h}_i(t,\tau) * \mathrm{sinc}((\tau - \tilde{m}i - \tilde{b})f_\tau) \right)(n_\tau/f_\tau) \\ &= \frac{1}{\sqrt{f_\tau}} \int_{-\infty}^{\infty} \tilde{h}_i(t,u) \cdot \mathrm{sinc}((n_\tau/f_\tau - u - \tilde{m}i - \tilde{b})f_\tau) du \\ &= \frac{1}{\sqrt{f_\tau}} \sum_{l=1}^{M} \tilde{\alpha}_{i,l} \exp\{j2\pi\tilde{\nu}_{i,l}t\} \cdot \mathrm{sinc}(n_\tau - (\tilde{\tau}_{i,l} + \tilde{m}i + \tilde{b})f_\tau), \end{aligned} \tag{4.15}$$

where f_τ is the sampling frequency, $n_\tau = \tau/f_\tau$ such that $n_\tau \in \mathbb{Z}$ is the corresponding discrete-time index for the delay τ, $*$ is the convolution operator, and sinc is the normalized sinc function defined as $\mathrm{sinc}(t) = \sin(\pi t)/\pi t$. Note that, since the channel impulse response in Eq. (4.4) is expressed as a sum of delta functions, it is not band-limited. Since the impulse responses are estimated from the LTE received signal with a $10\,\mathrm{MHz}$ bandwidth, f_τ should be higher than $10\,\mathrm{MHz}$. However, considering values much higher than f_τ will not provide additional relevant information. For the results presented below we used $f_\tau = 10 f_S$, where $f_S = 15.36\,\mathrm{MHz}$ is the LTE signal sampling frequency. Then, the normalized mean sampled PDP for the ith LTE frame is

$$P_i[n_\tau] = \frac{1}{T} \int_0^T \left| \hat{h}_i(t, n_\tau) \right|^2 dt, \tag{4.16}$$

where $T = 10\,\mathrm{ms}$ is the duration of an LTE frame. Assuming that the channel is stationary, the formula is generalized to

$$\begin{aligned} P_i[n_\tau] &= \lim_{T\to\infty} \frac{1}{2T} \int_{-T}^{T} \left| \hat{h}_i(t, n_\tau) \right|^2 dt \\ &= \frac{1}{f_\tau} \sum_{l=1}^{M} \left| \tilde{\alpha}_{i,l} \cdot \mathrm{sinc}(n_\tau - (\tilde{\tau}_{i,l} + \tilde{m}i + \tilde{b})f_\tau) \right|^2. \end{aligned} \tag{4.17}$$

Finally, the normalized mean sampled PDP for each section $\mathcal{C}_j$ is obtained by dividing with respect to the total received power:

$$\begin{aligned} P_{\mathcal{C}_j}[n_\tau] &= \frac{1}{|\mathcal{C}_j|} \sum_{i\in\mathcal{C}_j} \frac{P_i[n_\tau]}{\sum_{n_\tau=-\infty}^{\infty} P_i[n_\tau]} \\ &= \frac{1}{|\mathcal{C}_j|} \sum_{i\in\mathcal{C}_j} \frac{P_i[n_\tau]}{\sum_{l=1}^{M} |\tilde{\alpha}_{i,l}|^2}, \end{aligned} \tag{4.18}$$

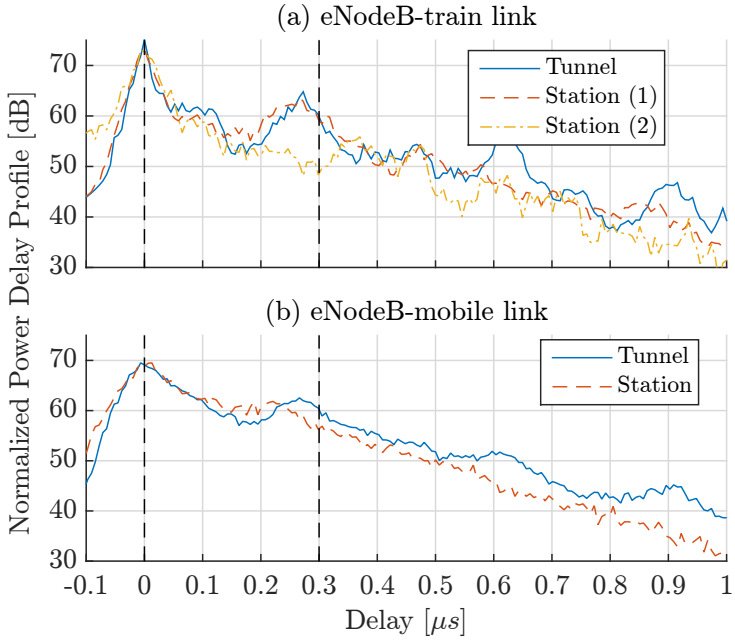

Figure 4.11: Normalized mean PDP (antenna 1).

where $\mathcal{C}_j$ is the set containing the indices i of the LTE frames received along the jth section. Note that parameters m and b in Eq. (4.15) are calculated for each section $\mathcal{C}_j$ considering the LTE frames with indices $i \in \mathcal{C}_j$.

Figs. 4.11a and 4.11b show the normalized mean PDP for the different sections considered for the eNodeB-train and eNodeB-mobile links, respectively. For the eNodeB-train link we see that the PDPs of the "tunnel" and "station (1)" sections are quite similar, and we observe delay clusters that are also coherent with the station geometry (see Fig. 4.1) and with the results reported in [CAI+16, Figs. 4 to 6]. A similar trend is also observed in [ZHA+16b; ZHA+17], although these results were obtained without using the SAGE algorithm. Notice that the most powerful paths correspond to delay $\tau = 0$, marked in Fig. 4.11a with the leftmost black dashed line. We can also see another peak for these two regions a bit earlier than $\tau = 0.3\,\mu s$. This delay corresponds to the signal bouncing on the other side of the station and coming back. Considering again the station geometry, the delay of this bounce is, as the best approximation, the time required by the signal to reach the back of the station and come back, which is $2 \cdot 45/c_0 = 0.3\,\mu s$, where c_0 is the speed of light in free space in m/s and $45\,m$ is the distance between the antenna and the back of the station (see Fig. 4.1). This delay is also marked in Fig. 4.11a with the rightmost black dashed line. The main and reflected paths appear clearly in Fig. 4.9. The "station (2)" section shown in Fig. 4.11a comes after the train passes in front of the transmit antenna. Fig. 4.9 shows that the main paths (the paths with lower delay) disappear when the train passes in front of the eNodeB transmit antenna and, after that point, the contribution to the received signal comes exclusively from the paths reflected on the back of the station. As commented above, this effect is due to the high directivity ($30°$) of the train antennas.

The normalized mean PDPs shown in Fig. 4.11b for the tunnel and station sections

correspond to the eNodeB-mobile link and they are coherent with the scenario geometry, given that the receive antennas are inside the train carriage and that its doors are closed all the time. Only when the mobile antennas are in front of the eNodeB transmit antenna the signal level is sufficiently high to observe significant peaks in the PDP. Again, as in Fig. 4.11a, the most powerful path is the one at delay $\tau = 0$ (marked in Fig. 4.11b with the leftmost black dashed line). As for the eNodeB-train link PDP shown in Fig. 4.11a, the rightmost black dashed curve in Fig. 4.11b, drawn a little bit before $\tau = 0.3\,\mu s$, corresponds to the delay needed by the signal bouncing on the other side of the station and coming back.

4.4.3 Root Mean Square Delay Spread

The RMS for a discrete time-delay channel impulse response is defined in Section 3.5.2. Considering the continuous time-delay channel impulse responses as defined in Eq. (4.4) and following [MM14], we define the RMS delay spread of the wireless channel as follows. Firstly, let us define the normalized PDP for the ith LTE frame as

$$\tilde{P}_i(\tau) = \frac{P_i(\tau)}{\int_{-\infty}^{\infty} P_i(\tau) d\tau} = \frac{\sum_{l=1}^{M} |\tilde{\alpha}_{i,l}|^2 \, \delta(\tau - \tilde{\tau}_{i,l})}{\sum_{l=1}^{M} |\tilde{\alpha}_{i,l}|^2}. \tag{4.19}$$

From the result in Eq. (4.19), the nth moment of the delay is

$$\mathbb{E}_i[\tau^n] = \int_{-\infty}^{\infty} \tilde{P}_i(\tau) \tau^n d\tau = \frac{\sum_{l=1}^{M} |\tilde{\alpha}_{i,l}|^2 \, \tilde{\tau}_{i,l}^n}{\sum_{l=1}^{M} |\tilde{\alpha}_{i,l}|^2}, \tag{4.20}$$

and the RMS delay spread is defined as

$$S_i = \sqrt{\mathbb{E}_i[\tau^2] - \mathbb{E}_i[\tau]^2}. \tag{4.21}$$

Figs. 4.12a and 4.12b show the RMS delay spread per frame for both the eNodeB-train and eNodeB-mobile links, respectively. Figs. 4.12a and 4.12b also show the smoothed results (dashed lines) using a moving average with a window length of $20\,\lambda$.

Figs. 4.13a and 4.13b show the RMS delay spread cumulative distribution functions (CDFs) for both the eNodeB-train and eNodeB-mobile links, respectively. Different CDFs were calculated for each section. In all cases, the data were fit to a distribution, which are also shown in Figs. 4.13a and 4.13b. For the case of the eNodeB-train link, we found that for the "tunnel", "station (1)", and "braking" sections, a normal distribution provides a good fit to the data. However, for the case of the "station (2)" section, a lognormal distribution offers a better fit. On the other hand, for the eNodeB-mobile link, the "tunnel" and the "station" sections are fitted with a normal distribution. Finally, Tables 4.4 and 4.5 summarize the fitting results for all antennas and sections of both links.

Some interesting points about the obtained delay spread results deserve to be emphasized. For the eNodeB-train link, the largest delay-spread variations occur inside the tunnel, where an oscillating pattern is observed. As shown in Fig. 4.12a, this is due to oscillations in the

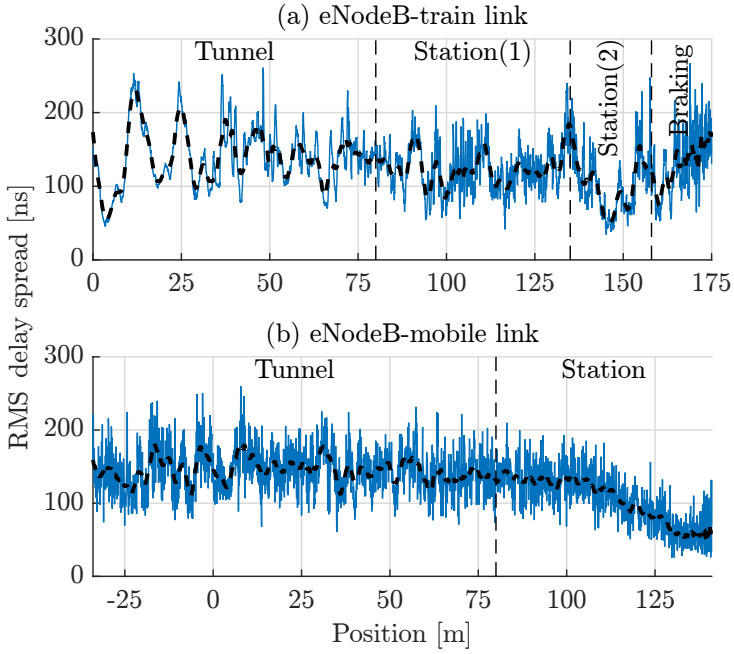

Figure 4.12: RMS delay spread (antenna 1).

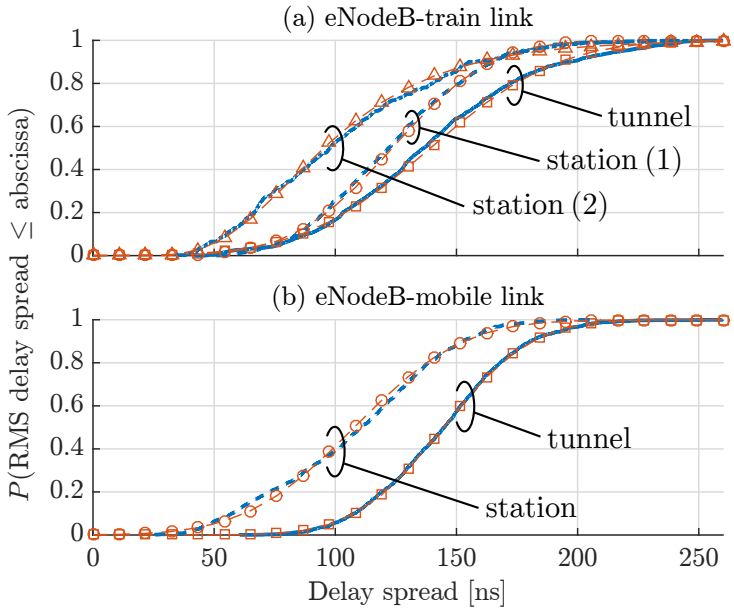

Figure 4.13: CDF of the delay spread (antenna 1) and fittings. Empirical CDFs are shown in thick blue lines, fittings of the CDFs are shown in thin red lines with markers. Results for the "braking" section are similar to those of the "tunnel" section and we omit them.

power of the dominant path, which can be explained by a 2-ray channel model. Exactly at the point where the transmit antenna is placed (marked with a dashed line between "station (1)" and "station (2)" in Fig. 4.12a), the delay spread exhibits a large peak because the LoS signal component is lost at that point (see the PDP around the position marked with the dashed line between the "station (1)" and the "station (2)" sections in Fig. 4.9). Notice that, analogously to

Table 4.4: RMS delay spread distribution fittings and 90 % value of CDF for the eNodeB-train link. Values are expressed in nanoseconds.

Section	Antenna	90 % value of CDF	Distribution fittings		
			Distribution	μ	σ
Tunnel	1	196.12	Normal	139.29	41.56
	2	195.86		145.74	37.13
Station (1)	1	165.40	Normal	123.53	31.91
	2	160.27		130.35	23.41
Station (2)	1	154.86	Lognormal	4.56	0.40
	2	120.08		4.26	0.41
Braking	1	186.54	Normal	138.97	39.25
	2	216.65		160.49	46.89

Table 4.5: RMS delay spread distribution fittings and 90 % value of CDF for the eNodeB-mobile link. Values are expressed in nanoseconds.

Section	Antenna	90 % value of CDF	Distribution fittings		
			Distribution	μ	σ
Tunnel	1	180.27	Normal	144.59	28.59
	2	183.85		144.78	31.02
Station	1	152.53	Normal	107.83	35.31
	2	150.79		106.94	36.30

the results reported in [ZHA+17], the average RMS delay spread does not change significantly from the tunnel to the station. For the case of the eNodeB-mobile link, we can see in Fig. 4.12b that the mean delay spread decreases noticeably when the mobile receive antennas are in the station.

4.4.4 Doppler Power Spectral Density

Analogously to the PDP case, the Doppler PSD function contains information about the power of the signals impinging the receiver with a given Doppler frequency. More specifically, the Doppler PSD is related to the angle of arrivals (AoAs) of the multipath components. Considering the stationary time-delay impulse response $\hat{h}(t, \tau)$, the Doppler PSD is defined as [MOL12]

$$D(\nu) = \int_{-\infty}^{\infty} |\hat{s}(\nu, \tau)|^2 d\tau, \tag{4.22}$$

where $\hat{s}(\nu, \tau)$ is the Doppler-variant impulse response

$$\hat{s}(\nu, \tau) = \mathcal{F}_t \left(\hat{h}(t, \tau) \right), \tag{4.23}$$

with $\mathcal{F}_t(\cdot)$ being the Fourier transform with respect to t. As for the PDP case, if we consider the channel impulse response in Eq. (4.11), which is defined as a sum of deltas, the resulting Doppler spread would contain square delta functions. If we now define the channel impulse response as

$$\hat{h}(t, \tau) = \sum_{l=1}^{N} \beta_l \exp(j2\pi\nu_l t)\delta(\tau - \tau_l), \tag{4.24}$$

where ν_l is the frequency of the lth tap and β_l is its random complex-valued amplitude, we can use an alternative definition for the Doppler PSD in the same fashion as we did in Section 4.4.2 for the PDP. Then, the Doppler PSD becomes

$$D(\nu) = \sum_{l=1}^{N} \mathbb{E}\left[|\beta_l|^2 \right] \delta(\nu - \nu_l). \tag{4.25}$$

As we did for the PDP, we calculate the Doppler PSD for each received LTE frame from the channel estimates defined in Eq. (4.4) and determined with the SAGE algorithm, thus obtaining the "instantaneous" Doppler PSD. Following an equivalent approach to the one shown in [MM14] for the PDP, we define the "instantaneous" Doppler PSD for the ith LTE frame as:

$$D_i(\nu) = \sum_{l=1}^{M} |\tilde{\alpha}_{i,l}|^2 \, \delta\left(\nu - \tilde{\nu}_{i,l}\right). \tag{4.26}$$

For each frame i, analogously to the mean delay obtained in Eq. (4.20) for $n = 2$, we can also obtain the mean Doppler PSD as:

$$\mathbb{E}_i[\nu] = \frac{\int_{-\infty}^{\infty} D_i(\nu)\nu d\nu}{\int_{-\infty}^{\infty} D_i(\nu) d\nu} = \frac{\sum_{l=1}^{M} |\tilde{\alpha}_{i,l}|^2 \tilde{\nu}_{i,l}}{\sum_{l=1}^{M} |\tilde{\alpha}_{i,l}|^2}. \tag{4.27}$$

Figs. 4.14 and 4.15 show the Doppler PSD for the eNodeB-train and eNodeB-mobile links, respectively. The Doppler PSDs are plotted using an scatter plot where each point corresponds to the power of a single path, as shown in Eq. (4.14). The smoothed mean of the Doppler PSD is also calculated for each frame as in Eq. (4.27) and plotted with a superimposed dashed line. As commented in Section 4.3, the theoretical maximum Doppler shift in our case, at a carrier frequency of 2.6 GHz and a train speed of 18 km/h, is $f_m = 43.33$ Hz.

Fig. 4.14 shows that the mean Doppler PSD for the "tunnel" section exhibits an oscillating pattern, reaching values close to the theoretical maximum Doppler shift f_m. At some points, we can see that the Doppler shift is larger than f_m, an effect explained by multiple bouncing of the incoming signal. In the "station (1)" section we observe how the mean Doppler shift decreases as the train passes in front of the transmitter, as expected. Finally, during the "braking" section,

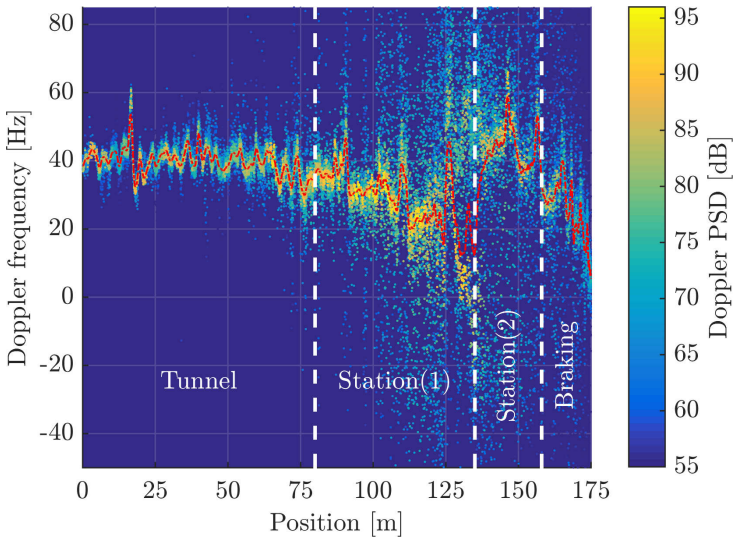

Figure 4.14: Doppler PSD for the eNodeB-train link (antenna 1).

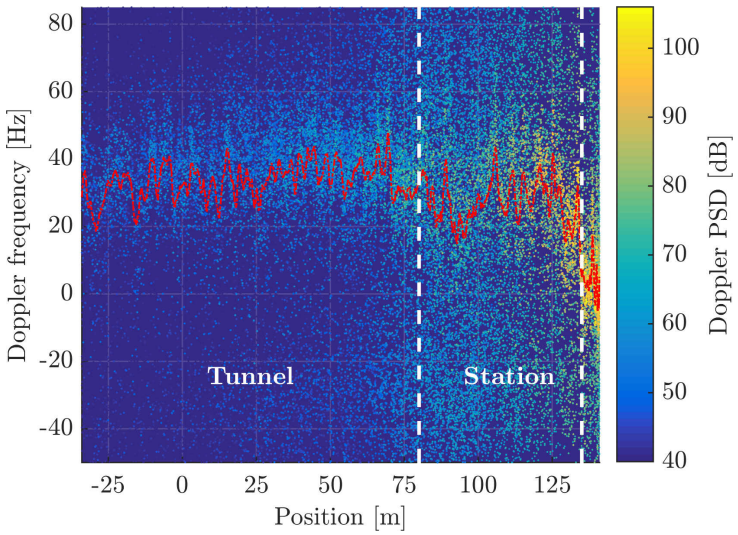

Figure 4.15: Doppler PSD for the eNodeB-mobile link (antenna 1).

the mean Doppler frequency diminishes due to the speed reduction of the train. For the eNodeB-train link, the Doppler components with a negative frequency are almost nonexistent, even when the train passes in front of the transmitter, due to the high directivity of the train receive antennas.

For the eNodeB-mobile link results shown in Fig. 4.15, we can see that the Doppler PSD has a much larger variance because the direct LoS component is not present. It is worth noting that, for both the eNodeB-train and the eNodeB-mobile links, the Doppler components are concentrated around the positive frequencies, whereas some components in the negative frequencies arise when the train is in the "station" section.

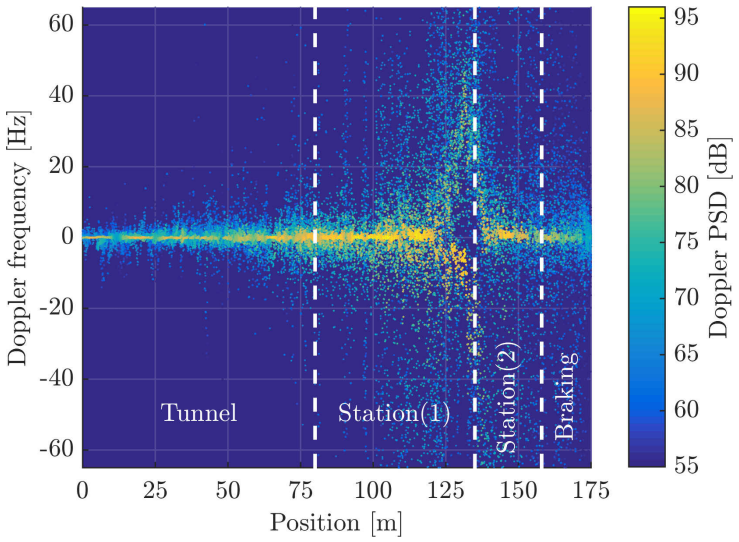

Figure 4.16: Mean-centered Doppler PSD for the eNodeB-train link (antenna 1).

4.4.5 Mean-Centered Doppler Power Spectral Density

One of the first steps in a digital receiver processing chain is to synchronize the received signals, hence estimating and correcting time and frequency offsets between the transmitter and the receiver. In the case of a frequency offset, a frequency shift is typically applied. The estimated frequency offset is the offset due to transmitter and receiver oscillators misalignments plus the mean Doppler frequency of the receive signal. Therefore, to characterize the Doppler PSD that actually impacts on the receiver after the (ideal) frequency offset correction, we subtract the mean Doppler frequency per frame from the calculated Doppler PSD, leading to the mean-centered Doppler PSD, defined as

$$D_i^{MC}(\nu) = D_i(\nu) - \mathbb{E}_i[\nu]. \tag{4.28}$$

Figs. 4.16 and 4.17 show the mean-centered Doppler PSD for both the eNodeB-train and the eNodeB-mobile links, respectively. Fig. 4.16 shows that the mean-centered Doppler PSD is close to zero almost all the time except for the "station (1)" section once the train passes the 120 m point. Again, this effect is due to the high directivity of the train receive antennas. The mean-centered Doppler PSD shown in Fig. 4.17 corresponds to the eNodeB-mobile link and is much wider than that observed for the eNodeB-train link (see Fig. 4.16) since the receive antennas are omni-directional in this case, resulting in a much higher number of acquired multipath components.

Analogously to the PDP case, we obtain the normalized mean-centered Doppler PSD for the different sections of both scenario links. Firstly, we consider the channel time-frequency

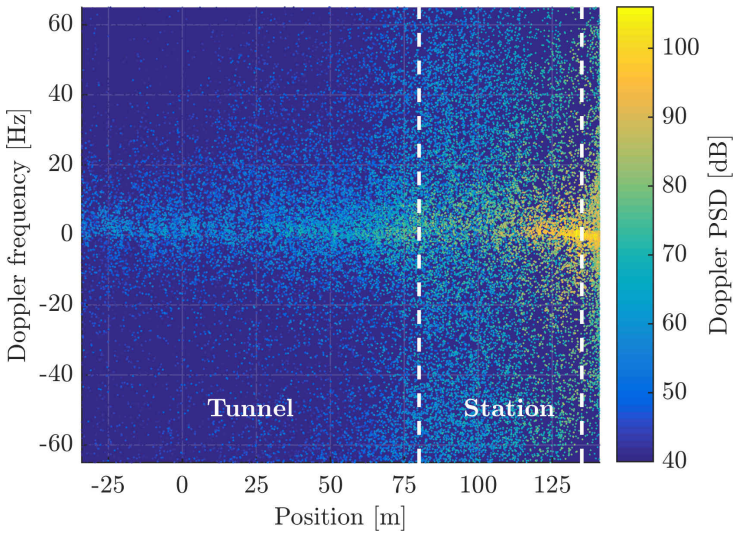

Figure 4.17: Mean-centered Doppler PSD for the eNodeB-mobile link (antenna 1).

response

$$\begin{aligned} H_i(t,f) &= \mathcal{F}_\tau\left(\tilde{h}_i(t,\tau)\right), \\ &= \sum_{l=1}^{M} \tilde{\alpha}_{i,l} \exp\{j2\pi(\tilde{\nu}_{i,l}t - f\tilde{\tau}_{i,l})\}, \end{aligned} \tag{4.29}$$

with $\mathcal{F}_\tau(\cdot)$ being the Fourier transform with respect to the delay τ. From the time-frequency response we obtain the Doppler-variant transfer function as

$$\begin{aligned} B_i(\nu,f) &= \mathcal{F}_t\left(H_i(t,f)\right) \\ &= \sum_{l=1}^{M} \tilde{\alpha}_{i,l}\delta(\nu - \tilde{\nu}_{i,l}) \exp\{-j2\pi f\tilde{\tau}_{i,l}\}. \end{aligned} \tag{4.30}$$

We next proceed as with the PDP to obtain a sampled version of this function by applying an interpolation filter, thus obtaining the sampled Doppler-variant transfer function

$$\begin{aligned} \hat{B}_i(n_\nu,f) &= \frac{1}{\sqrt{f_\nu}}\left(B_i(\nu,f) * \mathrm{sinc}((\nu f_\nu))\right)(n_\nu/f_\nu) \\ &= \frac{1}{\sqrt{f_\nu}}\int_{-\infty}^{\infty} B_i(\nu,f)\cdot \mathrm{sinc}(n_\nu)du \\ &= \frac{1}{\sqrt{f_\nu}}\sum_{l=1}^{M} \tilde{\alpha}_{i,l}\exp\{j2\pi\tilde{\tau}_{i,l}t\}\cdot \mathrm{sinc}(n_\nu - \tilde{\nu}_{i,l}f_\nu). \end{aligned} \tag{4.31}$$

Finally, the mean-centered Doppler PSD is obtained as

$$\begin{aligned} D_i[n_\nu] &= \lim_{F\to\infty}\frac{1}{2F}\int_{-F}^{F}|\hat{B}_i(n_\nu - \mathbb{E}_i[\nu],f)|^2 df \\ &= \sum_{l=1}^{M}|\tilde{\alpha}_{i,l}\cdot \mathrm{sinc}(n_\nu - \mathbb{E}_i[\nu] - \tilde{\nu}_{i,l}f_\nu)|^2, \end{aligned} \tag{4.32}$$

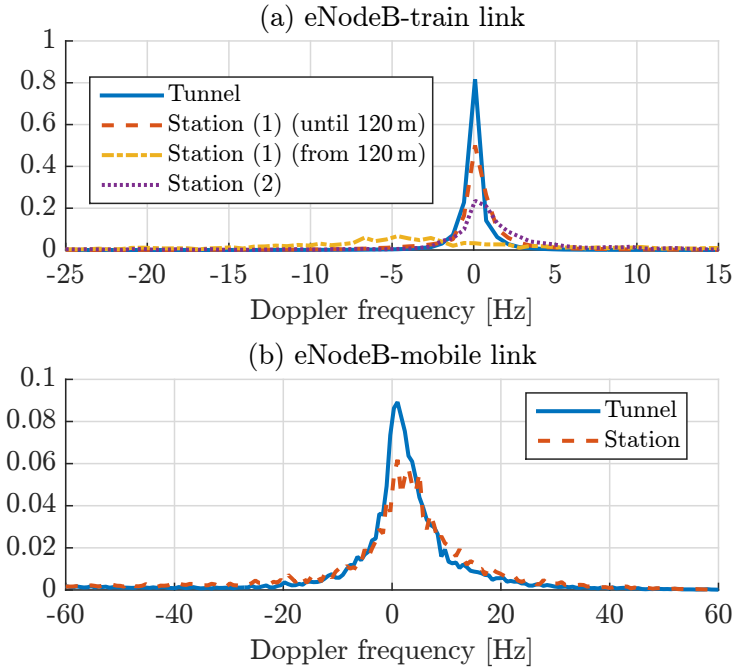

Figure 4.18: Normalized mean-centered Doppler PSD (antenna 1).

where f_ν is the sampling frequency and $n_\nu = \nu/f_\nu$ is the corresponding discrete-time index for the Doppler frequency ν. We finally obtain the normalized sampled Doppler PSD for each section $\mathcal{C}_j$ as

$$D_{\mathcal{C}_j}[n_\nu] = \frac{1}{|\mathcal{C}_j|}\sum_{i\in\mathcal{C}_j}\frac{D_i[n_\tau]}{\sum_{n_\tau=-\infty}^{n_\tau=\infty} D_i[n_\tau]} = \frac{1}{|\mathcal{C}_j|}\sum_{i\in\mathcal{C}_j}\frac{D_i[n_\tau]}{\sum_{l=1}^{M}|\tilde{\alpha}_{i,l}|^2}, \tag{4.33}$$

where $\mathcal{S}$ is the set containing the indices i of the LTE frames received in the corresponding section. We used $f_\nu = 2/3$ to calculate the results presented in this section.

Figs. 4.18a and 4.18b show the normalized mean-centered Doppler PSD for both the eNodeB-train and the eNodeB-mobile links, respectively. For the case of the eNodeB-train link (Fig. 4.18a) we divide the results for the "station (1)" in two parts: until 120 m and after 120 m (see Fig. 4.16). We observe that the Doppler PSD which effectively degrades the signal after the frequency offset correction (assuming a perfect frequency offset estimation and correction) is larger for the eNodeB-mobile link (see Fig. 4.18b) than for the eNodeB-train link (see Fig. 4.18a). In both cases, however, small Doppler shift values are observed, which is consistent with the low speed (18 km/h) of the train. The only exception is the "station (1)" section beyond 120 m (see Fig. 4.18a), which is due to the high directivity of the receive antennas, as explained above, and constitutes a good example of a receive signal degradation due to the significant spread of Doppler shift not caused by a high velocity of the train, but for a specific distribution of the AoA of the received multipath components.

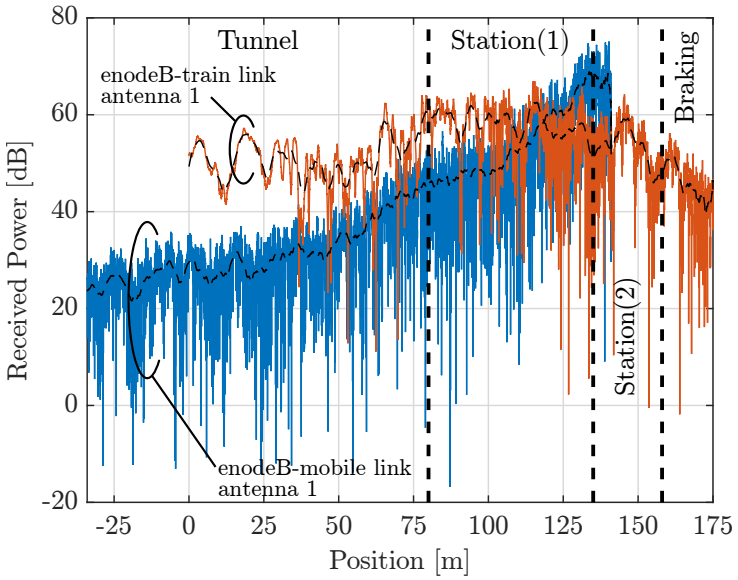

Figure 4.19: Received power for a single frequency $f_0 = 0$ both for eNodeB-train and eNodeB-mobile links. The large-scale fading corresponds to the black dashed curves.

4.4.6 Small-Scale Fading Analysis

Small-scale fading is the change in the received signal power due to the interference caused by the different multi path components [MOL12]. To characterize the small-scale fading we consider the wireless channel response amplitude for a single frequency f_0 (tone). We assume that the statistical distribution of the small-scale fading is the same for all the frequencies around 2.6 GHz within a 10 MHz of bandwidth. Firstly, we can express the time-frequency variant channel response for the ith LTE frame as

$$\begin{aligned} H_i(t,f) &= \mathcal{F}_\tau(\tilde{h}_i(t,\tau)) \\ &= \sum_{l=1}^{M} \tilde{\alpha}_{i,l} \exp\left(j2\pi(\tilde{\nu}_{i,l}t - f\tilde{\tau}_{i,l})\right), \end{aligned} \tag{4.34}$$

where $\mathcal{F}_\tau(\cdot)$ is the Fourier transform with respect to the delay τ. We define $H(t,f)$ as the channel time-frequency response for the whole subway trajectory, analogously to the the time-varying channel impulse response in Eq. (4.5). Then, the channel response amplitude for a given frequency f_0 is

$$E(t) = |H(t,f_0)|. \tag{4.35}$$

To analyze the small-scale fading we first remove the slow fading effects (large-scale fading). This is done by averaging over $E(t)$ using a sliding window. As discussed in [HE+13b], it is important to choose the correct window size to characterize the small-scale fading without the influence of the large-scale one. In accordance with the indications in [HE+13b; LEE85; AI+11; AI+09], we select a window length of $30\,\lambda$. Fig. 4.19 shows the received power for the eNodeB-train and the eNodeB-mobile links. Such received power is

calculated as $E^2(t)$. A superimposed black dashed curve shows the large-scale fading obtained by averaging the receive power with the above-mentioned sliding window.

In order to select the best-fitting model for the small-scale fading we use the Akaike's information criteria (AIC) method originally proposed in [AKA74]. Considering a set of models that may fit the data, the AIC method allows us to estimate the goodness of fit for each model. A good explanation on model selection and on the AIC method can be found in [BA03]. In particular, for selecting the best fitting model for the small-scale fading, the AIC method has been extensively used in the literature[SB07; WYN+09; MLN10; HE+15; ZHA+17]. In this work, we consider the AIC estimator as that derived in [SB07]. If we have a set of candidate probability distributions for our model, the AIC estimator value for the jth distribution is given by

$$\mathrm{AIC}_j = -2\sum_{n=1}^{N} \log g_{j,\hat{\theta}^j}(x_n) + 2U, \tag{4.36}$$

where g_j is the probability density function (pdf) of the jth candidate distribution; $x_1, x_2, ..., x_N$ are N fading samples; $\hat{\theta}^j$ is the distribution parameter set obtained from the data x_n by a maximum likelihood (ML) estimator; and U is the number of free parameters of the model (number of elements of $\hat{\theta}^j$).

To obtain meaningful AIC values, it is recommended that $N/U \gtrsim 40$ [SB07; BA03]. Also, to compare the relative fit of the different AIC_j values, the "Akaike weights" w_j are used. Firstly, the AIC differences are defined as

$$\Phi_j = \mathrm{AIC}_j - \min_i \mathrm{AIC}_i. \tag{4.37}$$

Next, the Akaike weights are computed as

$$w_j = \frac{\exp(-\Phi_j/2)}{\sum_i^J \exp(-\Phi_j/2)}, \tag{4.38}$$

where J denotes the number of models considered and $\sum_i^J w_j = 1$. These weights can be interpreted as the probability of the model to become the best fitting model for the data. Therefore, the best fitting model will be the one with the highest Akaike weights.

We applied the AIC method to the small-scale fading for both the eNodeB-train and the eNodeB-mobile links. More specifically, we considered 50 samples per meter. The results of the Akaike weights obtained for the different cases are summarized in Table 4.6.

Figs. 4.20 and 4.21 show the small-scale fading CDFs and the distribution fittings for both the eNodeB-train and the eNodeB-mobile links. In all cases, the Rician distribution is the most appropriate choice.

It is also interesting to consider the AIC weights for smaller signal sections, hence accounting for variations of the small-scale parameters for different regions along the train trajectory. Therefore, we also perform the AIC weights estimation considering a window of $15\,\mathrm{m}$ with a $5\,\mathrm{m}$ step between consecutive estimations. The results obtained are shown in

Table 4.6: AIC weights obtained for the small-scale fading.

Antenna	Section	Rician	Rayleigh	Nakagami	Lognormal
mobile 1	Tunnel	1	0	0	0
	Station	0.7709	0.1352	0.0939	0
mobile 2	Tunnel	1	0	0	0
	Station	0.8069	0.1365	0.0566	0
train 1	Tunnel	1	0	0	0
	Station (1)	1	0	0	0
	Station (2)	1	0	0	0
	Braking	0.9999	0	0.0001	0
train 2	Tunnel	1	0	0	0
	Station (1)	1	0	0	0
	Station (2)	0.9991	0	0.0009	0
	Braking	0.9524	0	0.0476	0

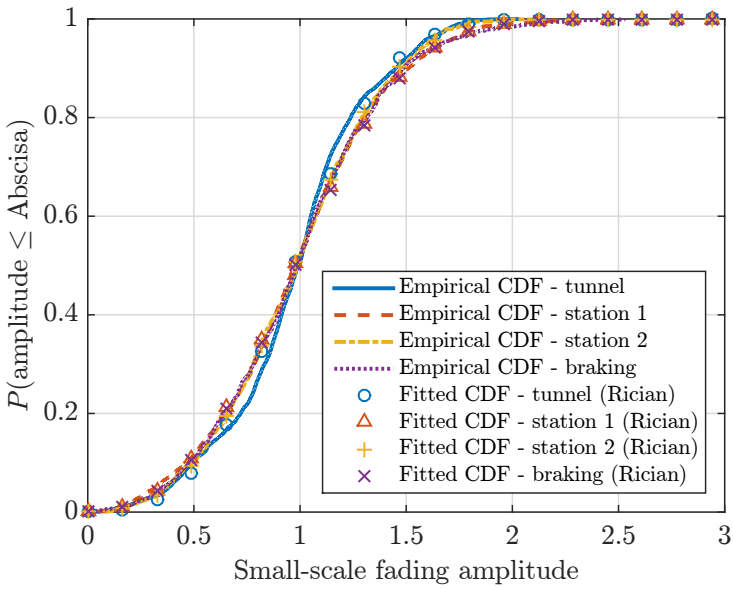

Figure 4.20: CDF and fittings of the small-scale fading for the eNodeB-train link (antenna 1).

Fig. 4.22 where, as indicated also in Table 4.6, the Rician distribution is the best fit. However, for some of the estimated windows, the Nakagami distribution is better. As shown in Fig. 4.22, this happens for the eNodeB-mobile link during some parts of the "tunnel" section and also at the start of the "station" section. In such cases, the parameter m of the Nakagami distribution is close to 1 (ranging from 0.96 to 1.15).

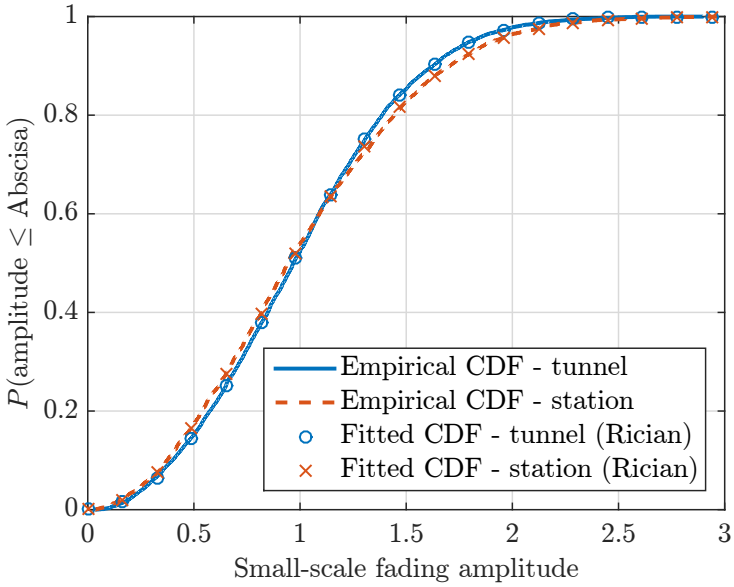

Figure 4.21: CDF and fittings of the small-scale fading for the eNodeB-mobile link (antenna 1).

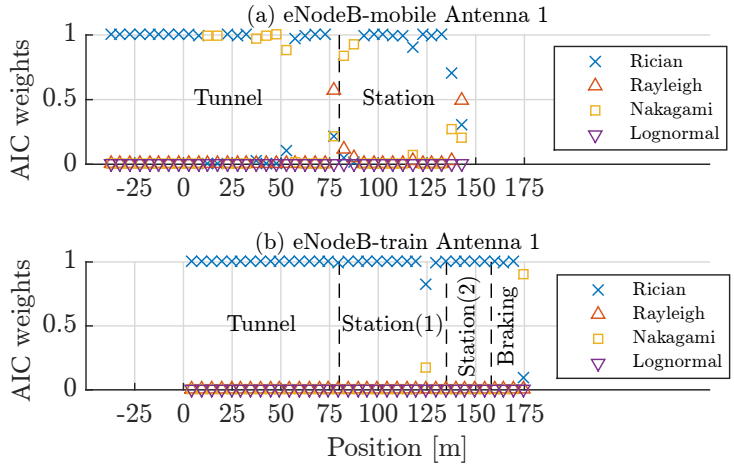

Figure 4.22: AIC weights considering small signal windows.

4.4.7 K-factor Analysis

Fig. 4.23 shows the K-factor, expressed in decibels, obtained for both the train antenna 1 and mobile antenna 1 along the whole train path. The K-factor values shown are computed from the parameters obtained for the Rice distribution fitting carried out to obtain the AIC weights and shown in Fig. 4.22.

In view of the results in Fig. 4.23, it is clear that the LoS component is almost never received by the mobile antennas since the K-factor is most of the time below 0 dB. The case of the eNodeB-train link is totally different because a strong LoS component is present during most of the train trajectory, except at those positions where strong reflections are observed, as shown in Fig. 4.9. Notice that the results in Fig. 4.23 for the eNodeB-train link are totally consistent with those shown in Fig. 4.12a for the delay spread, indicating that the dominant path, which is

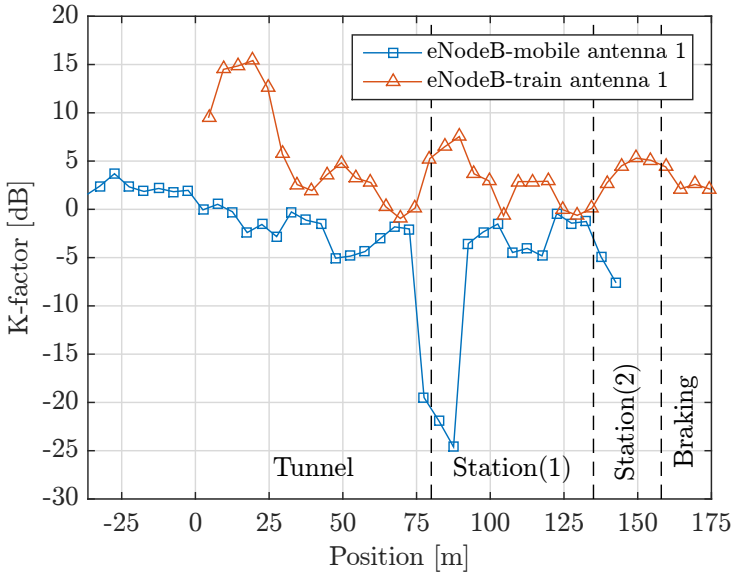

Figure 4.23: K-factor for both the eNodeB-train and the eNodeB-mobile links (antenna 1). Sections for the case of the eNodeB-mobile link are also shown.

the LoS path in our case, exhibits significantly larger power values than the other paths.

4.5 Conclusions

In this chapter, the wireless channel response of a modern subway station and its corresponding entrance tunnel in the Madrid Metro was characterized in detail. An LTE eNodeB transmitter was setup in the middle of the platform to cyclically transmit standard-compliant FDD LTE frames at a carrier frequency of 2.6 GHz with a bandwidth of 10 MHz. Two receivers were placed in the subway train to investigate both the eNodeB-train and the eNodeB-mobile links. The train was moving at a constant speed of 18 km/h from the entrance tunnel until it is completely stopped at the end of the station. We characterized the wireless channel response for both links based on the following parameters: PDP, RMS delay spread, Doppler PSD, small-scale fading distribution, and K-factor.

The GTEC Testbed in conjunction with the SAGE algorithm revealed themselves as excellent tools to characterize the response of doubly selective wireless channels like those in the considered subway scenario. The results show that the eNodeB-mobile link, in which the receive antennas are inside the train carriage, is the most challenging one, mainly due to the penetration losses. In addition, the geometry of the station and its entrance tunnel leads to scenarios with very specific propagation properties. More specifically, the RMS delay spread changes significantly from the tunnel to the station. Additionally, the estimated PDPs are consistent with those previously reported in the literature for similar scenarios. It is worth noting that the Doppler effect is actually an aggregation from different contributors, mainly carrier frequency and signal bandwidth, train speed, propagation environment, and the radiation

patterns of the transmit and receive antennas. In this case, highly directive receive antennas in the eNodeB-train link block the LoS component at the end of the train trajectory, which leads to a widely-spread Doppler PSD.

The actual Doppler effects present in the receive signal, after correcting the frequency offsets between the transmitter and the receiver, have been also characterized. Assuming an ideal frequency offset estimation and correction, and given the low measurement speed, it can be concluded that the observed Doppler effects are not very relevant to the receiver if a strong LoS component is present.

Finally, the small-scale fading was characterized. We used the AIC method to find the best fitting distribution for the small-scale fading. We considered four of the most common distributions used in the literature, namely Rayleigh, Rician, Nakagami, and Lognormal. The analysis revealed that the small-scale fading was best fitted by a Rician distribution for both links (eNodeB-mobile and eNodeB-train), and for the whole train trajectory. The calculated K-factor values for the eNodeB-mobile link were low (less than 0 dB most of the time). However, K-factor values for the eNodeB-train link exceeded 0 dB most of the time, indicating the presence of a dominant path in the signal.

Chapter V

Vehicle-to-Infrastructure Channel Characterization Based on LTE Measurements

Vehicle-to-infrastructure (V2I) is a fundamental technology for future transportation systems and will enable effective traffic management, as well as multimedia and data services provisioning to passengers. In this chapter we employ Long Term Evolution (LTE) signals (time-division duplex mode) to estimate and characterize the channel response in an urban scenario at the University of A Coruña, considering a V2I setup with a car equipped with four receive antennas. We study typical channel parameters such as signal-to-noise ratio (SNR), power delay profile (PDP), Doppler power spectral density (PSD), and root mean square (RMS) delay profile, together with a diversity gain assessment by means of typical antenna combining methods, namely selection combining (SC), equal gain combining (EGC), and maximum ratio combining (MRC). We show that, in this case, although EGC and MRC offer the best theoretical performance at the expense of a higher complexity, the presence of line-of-sight (LoS) conditions and a strong SNR difference between the receive antennas yield favorable conditions for simple schemes such as SC.

This chapter is mainly based on the following co-authored publication:

- Tomás Domínguez-Bolaño, José Rodríguez-Piñeiro, José Antonio García-Naya, Xuefeng Yin, and Luis Castedo. "**Vehicle-to-infrastructure channel characterization based on LTE measurements**". *Proc. of 19th IEEE International Workshop on Signal Processing Advances in Wireless Communications (SPAWC 2018).* Kalamata, Greece, 2018

5.1 Introduction

Vehicle-to-infrastructure (V2I) and vehicle-to-vehicle (V2V) communications aim, respectively, at exchanging information about infrastructure status or between vehicles. Both

V2I and V2V are fundamental technologies in the context of the so-called intelligent traffic control system (ITCS) [SHG15; MEN+16; BAC16; HR04]. More specifically, V2I will enable effective traffic management by transmitting information such as predicted vehicle queue length [MIL+12; BAC16]. Additionally, due to the non-stopping growth of multimedia and data-based services, passengers will use V2I to connect on the move for work-related purposes, entertainment or socialization [ROD16; SR16]. However, the noticeable performance reduction experienced by V2I links in the absence of direct line-of-sight (LoS) is still a challenge to be met [ABB+15; CHO+09; BAC16]. On the other hand, a mobile-relay technique was proposed in [NET12] as a way to provide coverage to passengers inside vehicles, hence demanding higher V2I data rates.

The performance of V2I communication systems has been assessed in previous works considering different transmit waveforms—such as Worldwide Interoperability for Microwave Access (WiMAX) or Long Term Evolution (LTE)—in railway [DOM+17a; ZHA+17; ROD+16c], subway [ZHA+16b], and road [SUÁ+14b; ROD+14; FEI+16; SUÁ+14a] transportation scenarios. Although most of the aforementioned works consider single-antenna links, vehicles such as cars allow for installing multiple antennas spaced enough to exploit spatial diversity. However, in practical V2I systems, LoS propagation conditions occur during most of the vehicle trajectory, hence limiting spatial diversity.

In this chapter, based on a previous time-division duplex (TDD) $2.6\,\text{GHz}$ LTE measurement campaign described in [FEI+16], we study the V2I communications channel between a single-antenna base station transmitter installed in the second floor of a building and a car equipped with four omni-directional receive antennas. We characterize the wireless channel based on different parameters, namely the signal-to-noise ratio (SNR) per antenna, the power delay profile (PDP), the Doppler power spectral density (PSD), the root mean square (RMS) delay spread, and the diversity gain for different antenna configurations considering selection combining (SC), equal gain combining (EGC), and maximum ratio combining (MRC) antenna combining methods.

5.2 Experimental Setup

5.2.1 Measurement Scenario

We employed the GTEC Testbed (see Chapter 2) to assess a V2I wireless link consisting of a single-antenna (vertically polarized element of X-pol Ubiquity AM-2G-15-120 [UBI]) base-station transmitter and a mobile unit receiver equipped with four (omni-directional) antennas (Taoglas GA110.101111 [TAO]) placed on a car roof (see Figs. 5.1 and 5.2). At the considered carrier frequency of $2.6\,\text{GHz}$, the receiver antennas feature a gain of $-4\,\text{dBi}$, whereas the transmitter antenna feature a gain of $18\,\text{dBi}$, and a half-power beam width of 70° (horizontal) and 9° (vertical), as imaged in the radiation pattern shown in Fig. 5.5. The measurements were

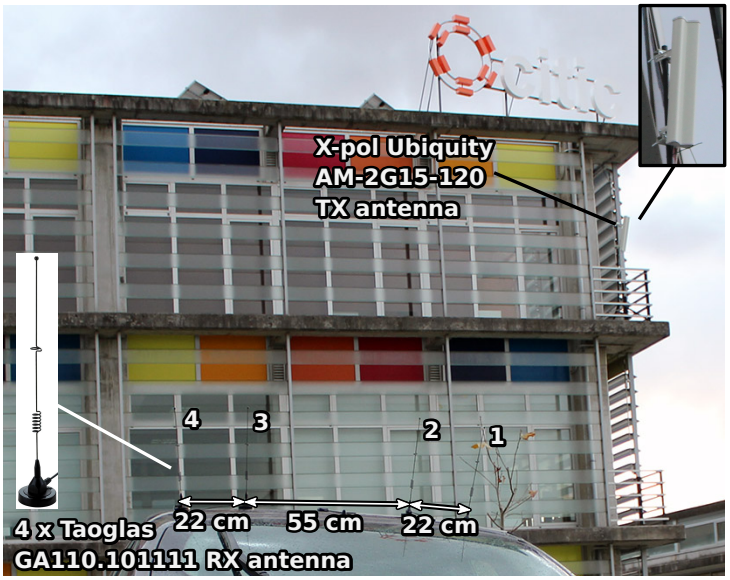

Figure 5.1: Mobile unit equipped with four omni-directional receive antennas mounted on a car and base-station with an X-pol transmit antenna panel. Only the vertically polarized transmit antenna element was used.

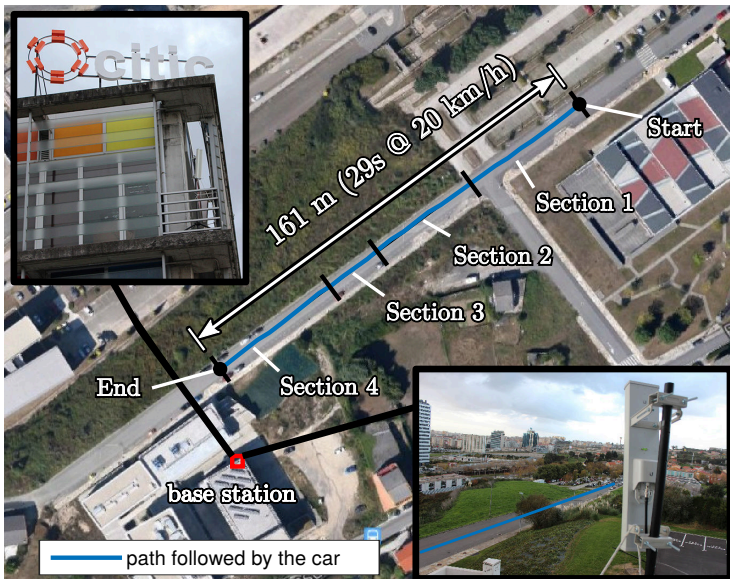

Figure 5.2: Measurement scenario: base-station transmitter and the path followed by the car based on the collected Global Positioning System (GPS) data.

carried out along a small road at the University of A Coruña (see Fig. 5.2). Three testbed nodes were used, one as the transmitter, and two as the receivers. Each of the receiver nodes was attached to two of the antennas placed on the top of the car. During the measurements, the car moved along the path (161 m long) trying to keep a constant speed of 20 km/h and completing the pass in 29 seconds. The actual speed of the car, as obtained from the GPS data, is shown in Fig. 5.3. As it can be seen in Fig. 5.3, the speed was between 20 and 23 km/h for the most part of the followed path. The base station downlink transmitter is placed on the corner of a building

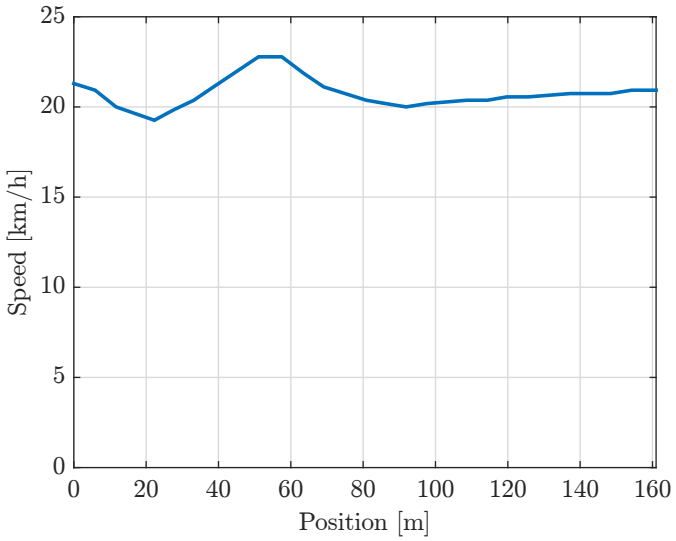

Figure 5.3: Speed of the car along the path according to the GPS data.

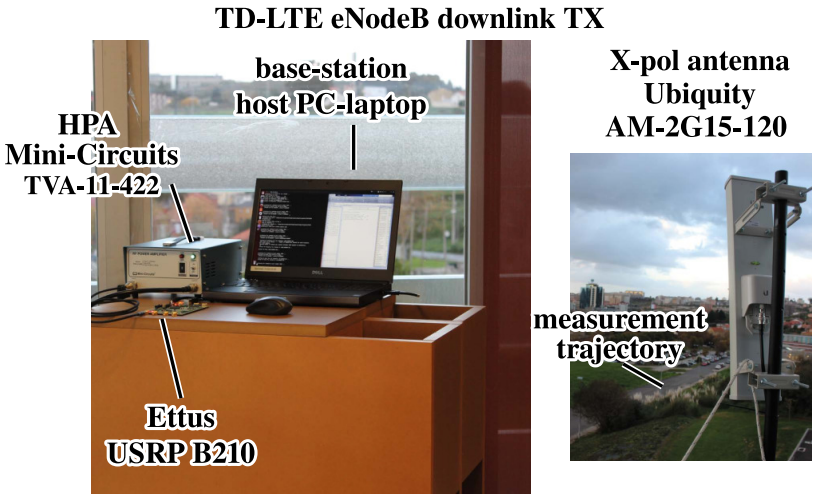

Figure 5.4: TD-LTE single-antenna downlink transmitter. We use the vertically polarized antenna element of the X-pol Ubiquity AM-2G-15-120.

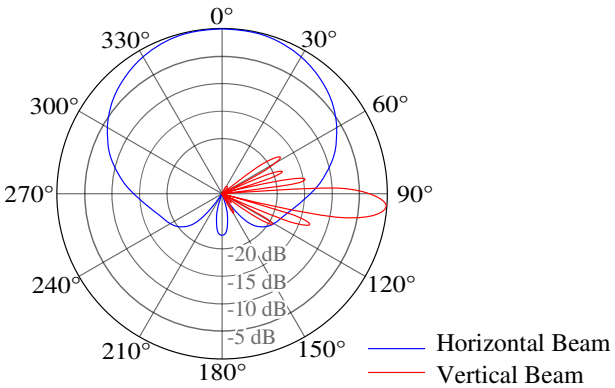

Figure 5.5: Radiation pattern for the horizontal element of the transmit antenna (X-pol Ubiquity AM-2G-15-120). Both the vertical and horizontal radiation patterns are shown.

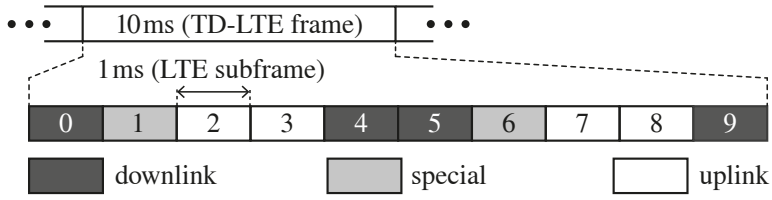

Figure 5.6: TD-LTE uplink-downlink configuration pattern considered in the measurements for the 10 LTE subframes composing a 10 ms LTE frame.

Table 5.1: LTE-TDD parameters used in the measurements.

Signal bandwidth	10 MHz (9 MHz occupied)
FFT size	1024
Number of used subcarriers	600 (excluding DC carrier)
RMC number	R.2 (4-QAM)
Carrier frequency	2.6 GHz
Transmit power	+18.5 dBm (at antenna port)
TDD configuration	mode #1

adjacent to the measurement path (see Fig. 5.4), with the starting point of the path being the farthest one from the base station. Some trees in the vicinity of the path produce shadowing effects about 100 m away from the starting point, while the building in front of the base station, although lower, partially blocks the signal for the last 20 m. One of the receiver nodes was equipped with a GPS antenna, allowing us to obtain the GPS data along the measurements.

Based on the estimated channel parameters described in Section 5.3, the measurement path is split into four sections (see Fig. 5.2) described below:

- **Section 1**: There are no obstacles blocking the LoS, but there is a rich multipath propagation.
- **Section 2**: Clear LoS.
- **Section 3**: LoS is blocked by trees and vegetation and there is also a rich multipath propagation.
- **Section 4**: Clear LoS, although the received power diminishes at the end due to the blocking effect caused by the building in front of the base-station antenna.

Note that sections 2, 3, and 4 correspond to a cutting (although not very deep).

5.2.2 Measurement Procedure

Note that, as said before, this work is based on a previous time-division duplex (TDD) LTE measurement campaign (described in [FEI+16]), where several measurements were performed by considering different parameters. For the work presented in this chapter, we considered the transmission of a standard-compliant TD-LTE frame [3GPa], generated following the uplink-

downlink configuration shown in Fig. 5.5. During the measurements, this frame is transmitted over the air by the base station in a cyclical fashion. The main parameters of the TD-LTE frame used in the measurements are summarized in Table 5.1.

5.3 Measurement Results

The estimation of channel parameters requires the availability of the channel responses, which are obtained from the collected TD-LTE signals. The first step is to synchronize the received LTE frames, which is performed by taking into account the Primary Synchronization Signal (P-SCH) and Secondary Synchronization Signal (S-SCH) signals of the frames (see Section 3.3.1). LTE frames are detected and their time offsets are estimated by correlating the received signal with the P-SCH and the S-SCH associated to the configured Evolved Node B (eNodeB). After obtaining the time offsets, we estimated the channel for each of the acquired LTE frames.

The space-alternating generalized expectation-maximization (SAGE) algorithm was used for the channel estimation, which allows us to estimate the different parameters of the impinging waves for the individual LTE frames. This is the same algorithm that was also used in Chapter 4 to estimate the channel (see Section 4.3). Here, as in Chapter 4, we consider the delay, the complex-valued amplitude, and the Doppler frequency for each path. The time offsets of the frames are taken into account to adjust accordingly both the estimated delays and complex-valued amplitudes of the paths. Therefore, the estimated time-varying channel impulse response for the ith LTE frame is expressed as:

$$h_i(t,\tau) = \sum_{l=1}^{M} \alpha_{i,l} \exp\{j2\pi\nu_{i,l}t\}\delta(\tau - \tau_{i,l}), \tag{5.1}$$

where M is the number of estimated paths, $\alpha_{i,l}$ is the complex-valued amplitude of the path, $\nu_{i,l}$ is its Doppler frequency, and $\tau_{i,l}$ is its delay, whereas $\delta(\cdot)$ is the Dirac delta function. For the results presented in this chapter we considered $M = 15$ paths. For the channel estimation, only the downlink orthogonal frequency-division multiplexing (OFDM) symbols, as shown in Fig. 5.6, are taken into account.

5.3.1 Signal-to-Noise Ratio

The SNR is calculated from the downlink subframes of the acquired LTE signal, yielding Fig. 5.7, which shows the obtained SNR along the whole path for each of the four receive antennas. Fig. 5.7 already reveals the convenience of splitting the path into four different sections. The SNR in section 1 exhibits some deep fading due to the scatters in the vicinity of the car. The fading becomes noticeably deeper in section 3 because trees and vegetation partially block the LoS. Finally, the strong SNR reduction in section 4 is caused by the blocking effect produced by the building in front of the base-station transmit antenna.

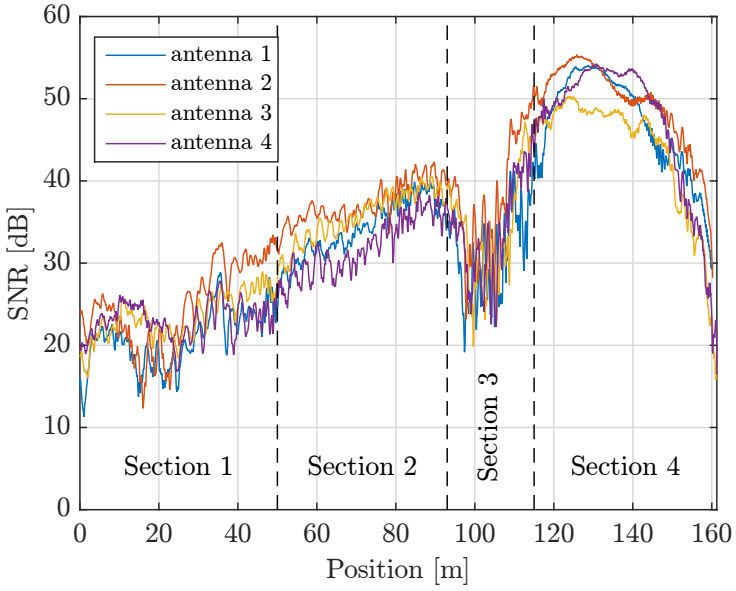

Figure 5.7: SNR versus the position of the car along the measurement path. Vertical dashed lines separate the four sections of the measurement path.

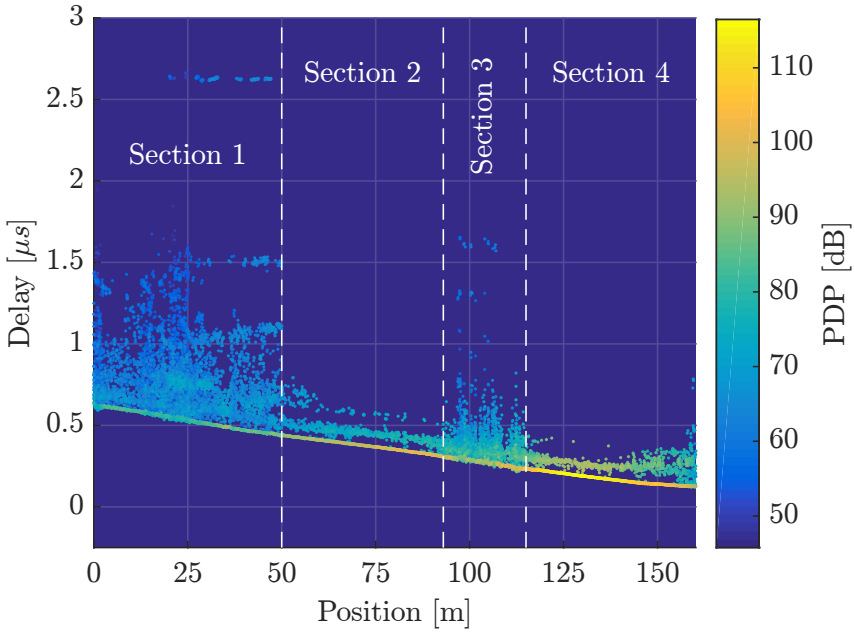

Figure 5.8: PDP for antenna 1 along the measurement path.

5.3.2 Power Delay Profile

The PDP is calculated for each acquired LTE frame from the channel responses produced by the SAGE algorithm (see Eq. (5.1)), thus obtaining the "instantaneous" PDP. Taking into account that the channel model in Eq. (5.1) is defined as a sum of Dirac deltas, we define the PDP for the ith frame as we did in Section 4.4.2:

$$P_i(\tau) = \sum_{l=1}^{M} |\alpha_{i,l}|^2 \, \delta\left(\tau - \tau_{i,l}\right). \tag{5.2}$$

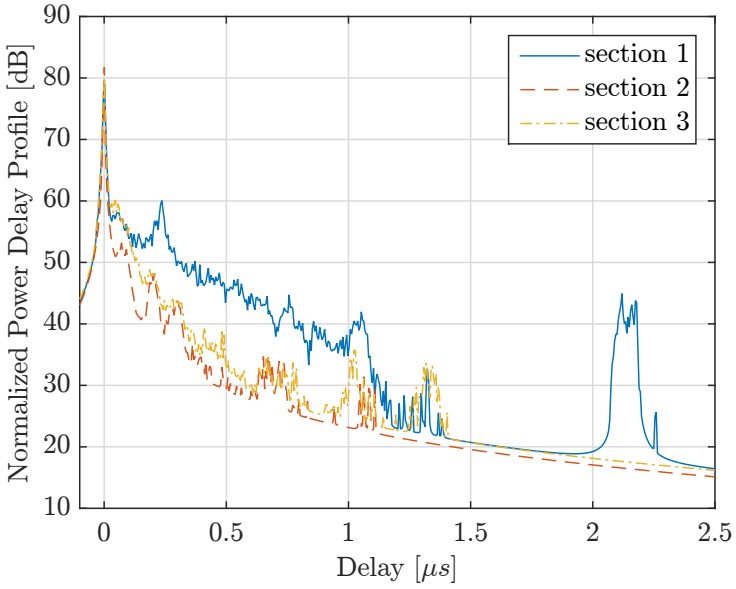

Figure 5.9: Normalized mean PDP for antenna 1. Results for section 4 are similar to the ones for section 2 and are omitted.

Fig. 5.8 shows the PDP using a scatter plot, where each dot represents the path gain for a given LTE frame. The PDP results are in agreement with those shown in Fig. 5.7 for the SNR: A rich multipath propagation is observed in section 1, whereas LoS predominates in sections 2 and 4, although the cutting in the scenario produces a reflected signal replica that originates a second delayed path. Finally, section 3 exhibits a rich multipath propagation due to the trees and vegetation blocking the LoS, thus significantly attenuating the signal.

We also calculate the so-called mean PDP for each of the considered sections, in the same way as we did in Section 4.4.2. Fig. 5.9 shows the normalized mean PDP for the antenna 1 for the different sections considered. Results for section 4 are similar to the ones for section 2 and are not shown in Fig. 5.9. As can be seen in Fig. 5.9, the spread of power in delay is considerably larger in section 1, but is similar in sections 2 and 3, being a little larger for section 2.

5.3.3 Doppler Power Spectral Density

Analogously as the PDP case, the Doppler PSD is calculated for each acquired LTE frame from the channel responses produced by the SAGE algorithm, thus obtaining the "instantaneous" Doppler PSD. We define the Doppler PSD for the ith LTE frame as we did in Section 4.4.4

$$D_i(\nu) = \sum_{l=1}^{M} |\alpha_{i,l}|^2 \, \delta\left(\nu - \nu_{i,l}\right). \tag{5.3}$$

Fig. 5.10 show the Doppler PSD along the path followed by the car. The Doppler PSD is plotted using an scatter plot where each point corresponds to the power of a single path, as shown in Eq. (5.3). The smoothed mean of the Doppler PSD is also calculated for each frame

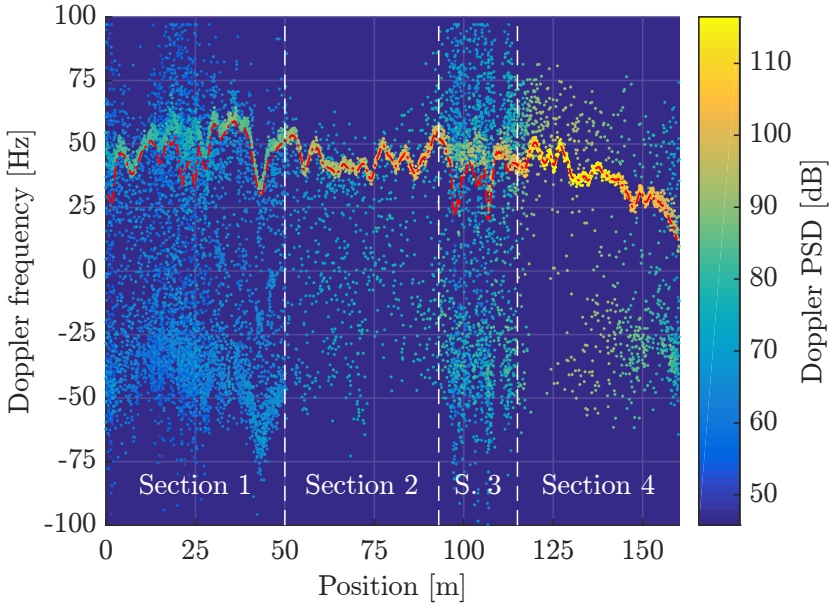

Figure 5.10: Doppler PSD for antenna 1.

Table 5.2: Delay spread lognormal fittings (μ, σ) for all the antennas and sections.

Section	Antenna 1	Antenna 2	Antenna 3	Antenna 4
1	$4.536, 0.526$	$4.127, 0.640$	$4.144, 0.533$	$4.377, 0.651$
2	$2.682, 0.418$	$2.545, 0.291$	$2.716, 0.376$	$3.262, 0.551$
3	$3.359, 0.711$	$2.802, 0.588$	$3.038, 0.681$	$3.235, 0.701$
4	$2.612, 0.428$	$2.528, 0.410$	$2.804, 0.683$	$2.811, 0.712$

as we did in Chapter 4 and plotted with a superimposed dashed line. For a car moving between 20 and 23 km/h, the theoretical maximum Doppler shifts at the carrier frequency of 2.6 GHz, would range from $|f_m| = 48.14$ Hz to $|f_m| = 55.37$ Hz. As can be seen in Eq. (5.3), the maximum estimated Doppler PSD values are close to the theoretical ones. At the end of the path, the Doppler frequency of the most powerful tap diminishes, due to the car approaching the transmitter. It can be seen from the results that section 1 is the most affected by multipath components, followed by section 3.

5.3.4 Root Mean Square Delay Spread

The RMS delay spread is calculated in the same way as in Section 4.4.3. Fig. 5.11 shows the RMS delay spread per frame along the path followed by the car. Fig. 5.11 also shows the smoothed RMS delay spread with a dashed line, obtained by averaging the results using a moving average with a window size of 30 λ. Fig. 5.12 shows the RMS delay spread cumulative distribution function (CDF) of the delay spread for antenna 1 in sections 1, 2, and 3. The CDF

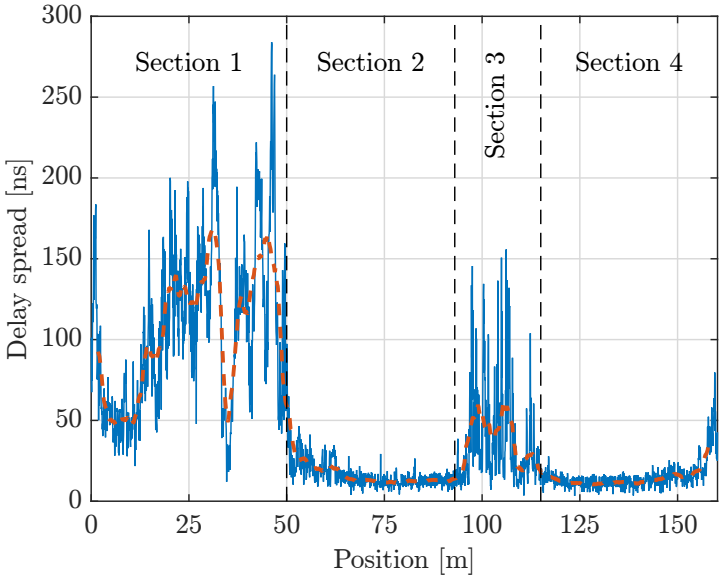

Figure 5.11: Delay Spread for antenna 1.

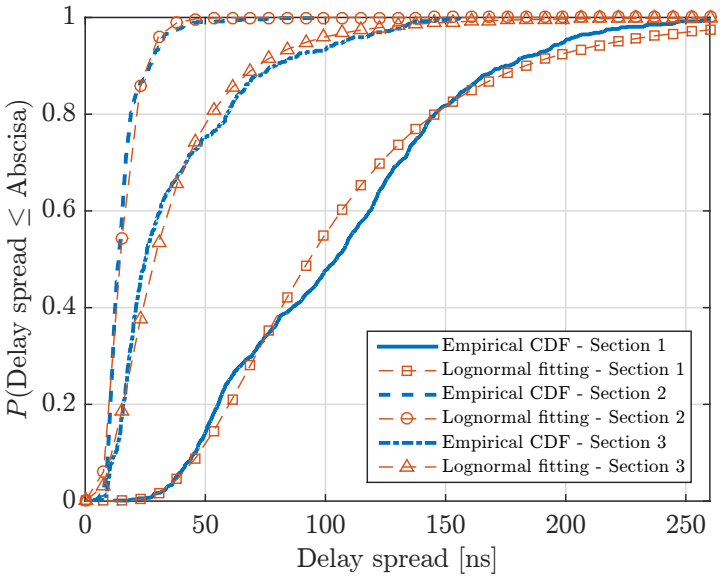

Figure 5.12: CDF of delay spread for antenna 1 and sections 1, 2, and 3. Curves of the lognormal fittings are also shown.

of the delay spread for section 4 is similar to that of section 2, so we omit it from the figure. In all cases, the data were fit to a distribution, which are also shown in Fig. 5.12. We found that, for all the case, a lognormal distribution provides a good fit to the data. The fitting results for all antennas and sections are summarized in Table 5.2. It can be seen from the results that section 1 is the most affected by multipath components, followed by section 3. On the other hand, sections 2 and 4 exhibit a clear LoS and no important scatters around, which makes the RMS delay spread to be very low.

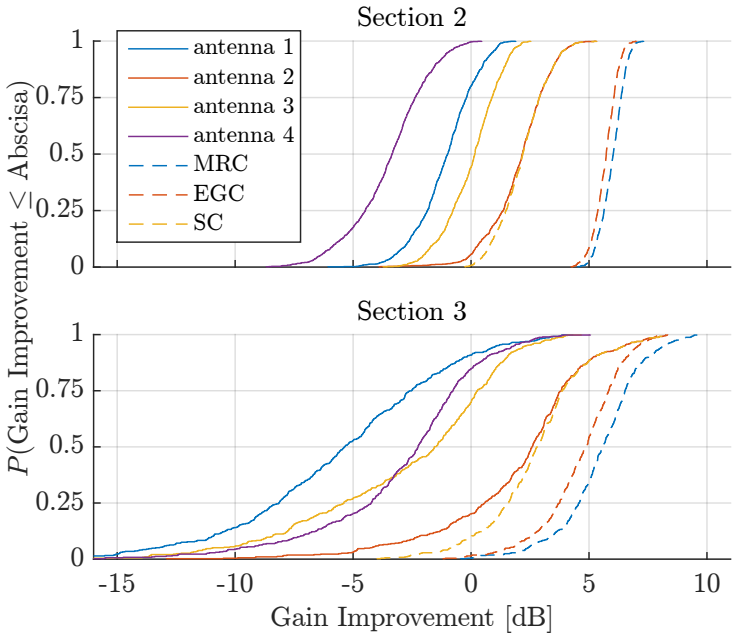

Figure 5.13: Gain improvements for sections 2 and 3. Solid lines show the excess path gain for the different antennas. Dashed lines show the diversity gain when using four antennas.

5.3.5 Diversity Gain

Table 5.3: Diversity gain mean and variance—expressed in natural units— for the different sections, combining methods, and antenna combinations. Footnote 1 explains how to read the values in the "Antennas" column.

Antennas	section 1			section 2			section 3			section 4		
	MRC	EGC	SC	MRC	EGC	SC	MRC	EGC	SC	MRC	EGC	SC
1100	2.07, 0.74	1.87, 0.58	1.57, 0.54	2.48, 0.23	2.38, 0.20	1.67, 0.19	2.39, 2.18	2.03, 1.83	1.97, 1.41	2.50, 0.40	2.41, 0.40	1.63, 0.24
1010	1.46, 0.18	1.39, 0.16	0.98, 0.11	1.86, 0.14	1.83, 0.14	1.09, 0.06	1.19, 0.34	1.03, 0.25	0.93, 0.27	1.36, 0.07	1.28, 0.06	0.97, 0.07
0110	2.43, 0.46	2.27, 0.40	1.75, 0.32	2.71, 0.20	2.64, 0.18	1.70, 0.17	2.71, 1.37	2.38, 0.91	2.07, 1.26	2.04, 0.33	1.83, 0.24	1.59, 0.29
1110	2.98, 0.58	2.69, 0.49	1.75, 0.32	3.52, 0.25	3.39, 0.24	1.71, 0.16	3.15, 1.97	2.58, 1.18	2.07, 1.25	2.95, 0.38	2.69, 0.26	1.63, 0.24
1001	1.52, 0.32	1.42, 0.26	1.06, 0.23	1.29, 0.07	1.25, 0.07	0.84, 0.04	1.09, 0.34	0.99, 0.29	0.81, 0.22	1.94, 0.29	1.88, 0.31	1.23, 0.11
0101	2.49, 0.28	2.27, 0.24	1.85, 0.27	2.15, 0.18	1.93, 0.12	1.67, 0.20	2.61, 1.49	2.31, 0.98	2.04, 1.30	2.62, 0.16	2.49, 0.17	1.76, 0.17
1101	3.04, 0.38	2.69, 0.36	1.86, 0.26	2.96, 0.20	2.72, 0.14	1.67, 0.19	3.05, 2.20	2.53, 1.46	2.04, 1.29	3.53, 0.24	3.34, 0.24	1.76, 0.16
0011	1.89, 0.62	1.84, 0.61	1.18, 0.22	1.52, 0.09	1.45, 0.08	1.05, 0.07	1.41, 0.53	1.32, 0.51	0.97, 0.25	1.48, 0.28	1.39, 0.23	1.05, 0.21
1011	2.44, 0.66	2.29, 0.55	1.21, 0.20	2.34, 0.16	2.24, 0.14	1.09, 0.06	1.84, 0.55	1.61, 0.44	1.08, 0.25	2.39, 0.28	2.24, 0.25	1.24, 0.10
0111	3.41, 0.33	3.12, 0.29	1.89, 0.24	3.19, 0.16	2.95, 0.12	1.70, 0.17	3.37, 1.48	2.89, 0.98	2.11, 1.19	3.07, 0.24	2.79, 0.27	1.76, 0.17
1111	3.95, 0.43	3.55, 0.41	1.90, 0.23	4.00, 0.21	3.74, 0.17	1.71, 0.16	3.80, 2.05	3.13, 1.18	2.12, 1.18	3.98, 0.24	3.65, 0.23	1.76, 0.16

Due to the availability of 4 receive antennas, we also consider the diversity gain in our analysis. The diversity gain is assessed considering three well-known methods for antenna combining, namely SC, EGC, and MRC [PAR00]. Note that we consider the received signal power over the full LTE bandwidth (10 MHz), hence taking into account both the spatial and the frequency diversity. A fair comparison —in terms of gain versus the measurement path— requires the large-scale fading effects to be removed from the channel responses.

Table 5.4: Excess path gain mean and variance—expressed in natural units—when a single antennas is selected. Footnote 1 explains how to read the values in the "Antennas" column.

Antennas	section 1	section 2	section 3	section 4
1000	$0.55, 0.05$	$0.81, 0.05$	$0.44, 0.19$	$0.91, 0.11$
0100	$1.52, 0.62$	$1.67, 0.20$	$1.96, 1.44$	$1.59, 0.29$
0010	$0.91, 0.13$	$1.04, 0.07$	$0.75, 0.29$	$0.45, 0.03$
0001	$0.97, 0.28$	$0.48, 0.03$	$0.66, 0.19$	$1.03, 0.22$

Firstly, the mean path gain is calculated by averaging out the individual path gains of the four receive antennas. Next, the large-scale fading is calculated by computing a moving average of the mean path gain using a window length of $30\,\lambda$. The large-scale fading is then subtracted from the path gain of each antenna, hence obtaining the so-called excess (path) gain [SPF13] for each of the four receive antennas. Finally, diversity gain is obtained for the three considered methods as in [PAR00]. Table 5.3 includes the mean and variance of the obtained diversity gains for all the combinations of antennas and sections, whereas Table 5.4 contains the mean and variance of the excess path gains for all the antennas and sections.

In the following, for the sake clarity, we will only show graphic results for sections 2 (clear LoS) and 3 (rich multipath). Fig. 5.13 shows the CDF of the excess path gain per antenna as well as the diversity gain for SC, EGC, and MRC when up to four antennas are considered. The excess path gain varies noticeably between different antennas, being always worse for section 3 than for section 2, which is consistent with the SNR results shown in Fig. 5.7. In particular, antenna 2 is the best performing one.

We can also see in Fig. 5.13 that the mean gain improvement obtained with SC is very low compared to that of the best antenna, but there is a substantial gain with respect to the other three antennas. Moreover, we can see that SC effectively reduces the fading, specially in section 3, where the fading affecting the different antennas is larger. The other two antenna combining methods (EGC and MRC) exhibit a much higher diversity gain than SC, although the performance of EGC is very close to that of MRC.

However, the results shown so far correspond to the case when all the antennas are considered. One might wonder if the increase in complexity of using four antennas with respect to using two or three pays off. Hence, we show in Fig. 5.14 the CDF of the diversity gain for the best antenna combining scheme (MRC) when two, three, or four antennas are considered. We analyzed two cases when two or three antennas are selected: including the best performing antenna (antenna 2) and excluding it[1]. It can be seen that, in the case of combinations with

[1]Legends in Figs. 5.14 and 5.15, and also in the "Antennas" column in Tables 5.3 and 5.4, represent the antenna combinations from antenna 1 to antenna 4. 0 means that the antenna is excluded and 1 means that the antenna is included. For example, "0101" means that antennas 2 and 4 are the only ones considered.

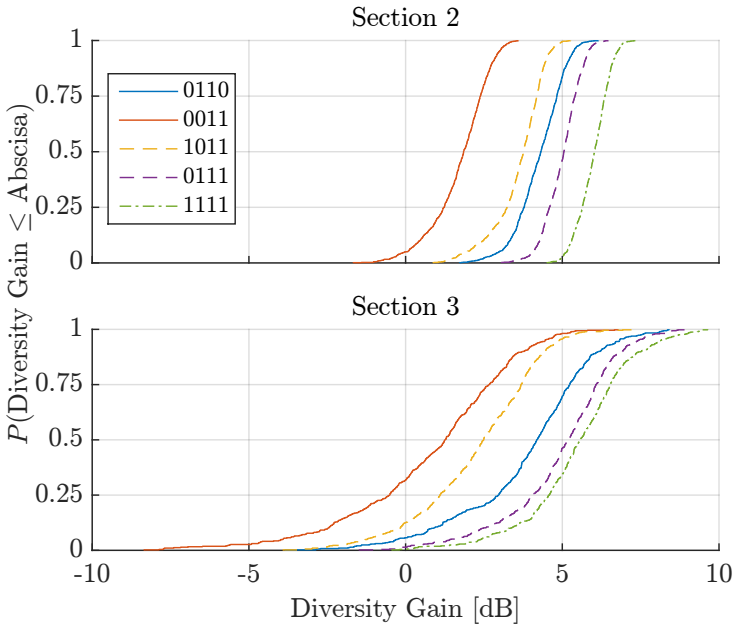

Figure 5.14: Diversity gain for sections 2 and 3 and MRC considering different antenna combinations. Footnote 1 explains how to read the legends.

three antennas not including the best performing antenna, the performance is worse than that of the case with two antennas including the best performing antenna. If we include the best performing antenna, the mean gain from two to three antennas is about 1 dB. If we use all the antennas, the extra gain is approximately 1 dB in section 2, whereas the gain in section 3 reduces significantly.

Analyzing all the antenna combinations in more detail (see Tables 5.3 and 5.4), we conclude that in those sections with a strong LoS (2 and 4), the mean gain when using two antennas ranges from about 0 dB (if we do not include the best performing antenna in the combination) to about 3 dB (when the best performing antenna is included). However, for sections 1 and 3, the single-antenna receiver greatly outperforms the two-antenna receivers when not including the best performing antenna.

The results shown in Fig. 5.14 only consider MRC. However, this is by far the most complex antenna combining method among the three considered. Hence, it is interesting to compare its performance with respect to that of EGC and SC. Fig. 5.15 shows the diversity gain CDF when up to three antennas are selected and for all the antenna combining methods. Again, we consider combinations including and excluding the best performing antenna. For section 2, Fig. 5.14 shows that MRC and EGC perform similarly regardless of the best performing antenna being included or not. For the case of SC, the mean gain loss is about 4 dB. Similar results are obtained for section 3, although the variance increases and the difference in excess path gain between including and excluding the best performing antenna decreases slightly. Indeed, the performance of SC when considering the best performing antenna is similar to that of MRC without the best performing antenna. More detailed results are shown in Tables 5.3 and 5.4,

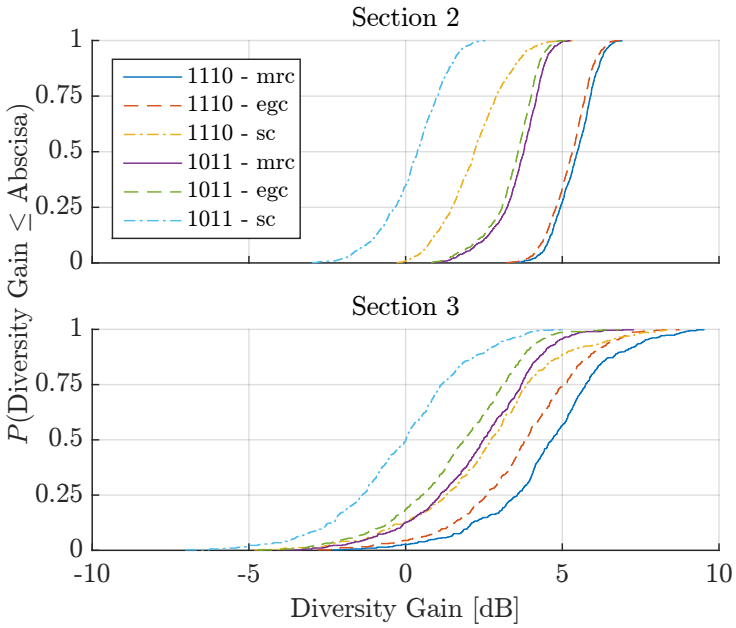

Figure 5.15: Diversity gain for sections 2 and 3 for different combinations of three antennas and the three antenna combining methods: SC, EGC, and MRC.

where all the antenna combinations are considered.

5.4 Conclusions

V2I communications are called to play an important role in traffic congestion management and provision of broadband connections to vehicle passengers. In this chapter we studied, by means of LTE measurements at 2.6 GHz, the V2I wireless link between a single-antenna base station transmitter installed in the second floor of a building and a car equipped with four omni-directional receive antennas. The measurements were carried out on a road at the campus of the University of A Coruña. During the measurements the car moved along the road at 20 km/h along 161 m. We characterized the wireless channel based on the following parameters: the SNR per antenna, the PDP, the Doppler PSD, the RMS delay spread, and the diversity gain for different antenna configurations considering SC, EGC, and MRC antenna combining methods.

The results showed different propagation characteristics along the measurement path. The results of PDP, Doppler PSD and RMS delay spread showed that there are two sections in the path where the signal is affected by significant multipath components, whereas the rest of the path presents clear LoS propagation conditions. Regarding the diversity results, for all the considered configurations, EGC and MRC exhibited a better performance than SC. However, MRC just slightly outperforms EGC. In general, the performance of SC gets closer to that of EGC and MRC when the number of multipath components increases (weak LoS). On average, we could observe an excess path gain of about 1 dB when increasing from two to three antennas. For regions with strong LoS, similar gains are observed when increasing from three to four

antennas. However, in our case, when the number of multipath components increases, the diversity gain is reduced. In cases in which the receive antennas experience a noticeable SNR difference between them, and under strong LoS conditions, simple antenna combining methods such as SC provide a significant gain, while requiring much less signal processing compared to more complex schemes such as EGC or MRC.

Chapter VI

Experimental Evaluation of FBMC

Orthogonal frequency-division multiplexing (OFDM) is a widely used modulation scheme in wireless communications due to its robustness against channel multi-path. Unfortunately, the time-domain rectangular-shape of the OFDM-modulated symbols leads to a frequency response with high side lobes, thus producing adjacent-channel interference. More recently, filter bank multicarrier (FBMC) modulation schemes have been proposed as an alternative to OFDM due to their better spectral efficiency and more degrees of freedom to define well localized prototype filters.

In this chapter, the performance of two common prototype filters for FBMC is studied twofold: analytically, by means of computer simulations considering standardized channel models for static scenarios, and experimentally through over-the-air transmissions in different environments using the GTEC Testbed. The results are also compared to OFDM in terms of the bit error rate (BER) with respect to the average E_b/N_0, leading to similar values in all the cases. This is mainly because the considered channel models and measurement scenarios are quasi-static and we have considered an isolated point-to-point link, thus not including other advantages of FBMC schemes, which can be exploited without additional performance losses with respect to OFDM.

Next, we analyze experimentally the performance of FBMC in high-speed scenarios. We also include the results obtained for OFDM signals for comparison purposes. For performing this analysis, we considered a technique to induce effects caused by highly time-varying channels on multicarrier signals while conducting measurements at low speeds. This technique has been proved to be accurate for the cases of WiMAX and Long Term Evolution (LTE) signals, as well as the waveforms proposed for fifth generation (5G) systems, such as FBMC.

This chapter is mainly based on the following co-authored publications:

- Tomás Domínguez-Bolaño, José Rodríguez-Piñeiro, José A. García-Naya, and Luis Castedo. "**Experimental evaluation of 5G modulation schemes in quasi-static scenarios**". *Proc. of 20th International ITG Workshop on Smart Antennas (WSA 2016)*. Munich, Germany, 2016
- José Rodríguez-Piñeiro, Tomás Domínguez-Bolaño, José Antonio García-Naya, and Luis

Castedo Ribas. "**Performance assessment of 5G-candidate waveforms in high speed scenarios**". *Proc. of 27th IEEE International Symposium on Personal, Indoor and Mobile Radio Communications (PIMRC'16).* Valencia, Spain, 2016

- Tomás Domínguez-Bolaño, José Rodríguez-Piñeiro, José Antonio García-Naya, and Luis Castedo. "**Throughput-based performance evaluation of 5G-candidate waveforms in high speed scenarios**". *Proc. of 25th European Signal Processing Conference (EUSIPCO 2017).* Kos, Greece, 2017

This chapter is structured as follows. Section 6.1 introduces the chapter. Section 6.2 provides a concise introduction to the FBMC modulation scheme. In Section 6.3 the performance of FBMC is assessed in static environments, through both simulations and over-the-air transmissions. In Section 6.4 the performance of FBMC is evaluated in high-speed environments by over-the-air transmissions. Finally, Section 6.5 is devoted to the conclusions.

6.1 Introduction

Orthogonal frequency-division multiplexing (OFDM) is currently one of the most used multi carrier modulation (MCM) schemes for wireless communications. OFDM is currently used, among others, in Wi-Fi, Long Term Evolution (LTE), and Digital Video Broadcasting - Terrestrial (DVB-T). More recently, the 3rd Generation Partnership Project (3GPP) decided that OFDM will also be used for the 5G physical layer [TECa]. Some of the most remarkable advantages of OFDM are its robustness against multi-path propagation (frequency-selective channels), and that it can be implemented very efficiently using an inverse fast Fourier transform (IFFT) block at the transmitter, a fast Fourier transform (FFT) block at the receiver, and a single tap per subcarrier zero-forcing (ZF) equalizer. However, the robustness against multi-path channels is achieved by inserting a cyclic prefix (CP) to each OFDM symbol, which reduces the spectral efficiency, and the time-domain rectangular-shape of the symbols leads to a large out-of-band power radiation.

Over the last few years, schemes based on filter bank multicarrier (FBMC) using offset quadrature amplitude modulation (OQAM) have received some attention as a promising alternative to OFDM [FAR11]. In OQAM a time-offset of half the quadrature amplitude modulation (QAM) symbol duration is introduced between the real and the imaginary parts. These systems are known in the literature as FBMC/OQAM, OFDM/OQAM [FAB95], staggered multitone (SMT) [FAR11], or just FBMC.

FBMC systems offer several advantages over OFDM. FBMC uses non-orthogonal pulses (prototype filters) with very low out-of-band power emission. This has several advantages. First, FBMC systems do not use a CP, so they provide a higher bandwidth efficiency. The usage of pulses with low out-of-band power emission means that FBMC can be used for uplink without the need of synchronization between all the users in an easier way. Moreover, the considered prototype filter can be adapted to the time and frequency dispersion characteristics of

the given channel. Hence, FBMC offers a more localized frequency response, leading to a better performance in some situations (e.g., reducing the inter-carrier interference (ICI) due to Doppler spread in doubly dispersive channels). Finally, FBMC systems can be also implemented efficiently using an IFFT block at the transmitter and an FFT block at the receiver by using a so-called polyphase filter [SGA12]. However, FBMC also presents some disadvantages due to the use of non-orthogonal pulses. Symbols orthogonality in FBMC only holds for the real-valued part, whereas interference is present in the imaginary part. This causes simple procedures in OFDM, such as pilot-based channel estimation or the usage of space-time block codes (STBCs), to require specific techniques to cancel the interference.

In this chapter we analyze the performance of FBMC in static situations. OFDM waveforms are also evaluated for comparison purposes. We show results based on simulations considering different standardized channel models, and also from over-the-air transmissions in indoor office scenarios. Two of the proposed prototype filters for FBMC systems are evaluated, namely the one defined by the PHYDYAS project [BEL+10] and the so-called Hermite pulse [HB97]. The bit error rate (BER) versus the E_b/N_0 at the receiver is the selected figure of merit.

We next focus our attention on high-speed scenarios. In theory, FBMC can offer a better optimization for channels exhibiting both time and frequency selectivity [FAR11; HB97]. Therefore, although it is expected that FBMC outperforms OFDM in doubly selective scenarios [FAB95; ALA01; HB97; SB03; AMI+10], measurement-based analyses are required to validate the theoretical predictions, which is one of the main objectives of this chapter. Unfortunately, performing measurements at high speeds (i.e., in a high-speed train) is extremely expensive and takes too much time in advance for their preparation. To mitigate this problem, we have previously proposed and validated a technique to emulate high speeds by means of inducing their effects in multicarrier signals (OFDM and FBMC) whereas the measurements are performed at much more affordable velocities [ROD+15a; ROD+15b; ROD+16b; ROD+16d]. Based on the scenario described in Chapter 5, we performed over-the-air measurements to assess the performance of FBMC and OFDM based on the BER (coded and uncoded), the error vector magnitude (EVM), and the throughput. Results are presented considering speeds up to 500 km/h.

6.2 Introduction to FBMC

FBMC is a type of multicarrier modulation technique that has currently gained attention as an alternative to OFDM for new generation wireless systems. Multicarrier modulation systems have become widespread (mainly using the OFDM technique), because they allow to consider a frequency-selective channel as a group of narrowband subchannels with flat gains, thus simplifying transmitter and receiver designs. In general, the transmit signal for an FBMC

modulation can be expressed as

$$x(t) = \sum_{n=-\infty}^{\infty} \sum_{k \in \mathcal{K}} s_k[n] p_{T,k,n}(t), \tag{6.1}$$

where $s_k[n]$ are the transmitted constellation symbols, n is the time index, k is the subcarrier index, $p_{T,k,n}(t)$ is the transmit pulse for time n and subcarrier k, $\mathcal{K}$ is the set of subcarrier indices used. The transmit pulse $p_{T,k,n}(t)$ can be written as

$$p_{T,k,n}(t) = p_T(t - nT) \exp(j2pif_k t) \exp(j\phi_{k,n}), \tag{6.2}$$

where f_k is the carrier frequency for the subcarrier k, T is the symbol period, $\phi_{k,n}$ is a phase term dependent on the time and subcarrier index, and $p_T(t)$ is the transmit prototype filter. Assuming an ideal channel, the following orthogonality condition should be fulfilled in order to recover the transmitted symbols $s_k[n]$

$$\langle p_{T,k,n}(t), p_{R,l,n}(t) \rangle = \int_{-\infty}^{\infty} p_{T,k,n}(t) p^*_{R,l,n}(t) dt = \delta_{kl}\delta_{mn}, \tag{6.3}$$

where $p_{R,l,n}(t)$ is the receive pulse, and δ_{kl} is the Kronecker delta function defined as

$$\delta_{kl} = \begin{cases} 1 & \text{if } k = l \\ 0 & \text{if } k \neq l. \end{cases} \tag{6.4}$$

When designing multicarrier systems, following the Balian-Low theorem, it is impossible to fulfill simultaneously the following properties [NSR17]:

1. Maximum symbol density: $1/(TF) = 1$, being F the frequency spacing of the symbols.
2. Time dispersion of $p(t)$: $\sigma_t = \sqrt{\int_{\infty}^{\infty} t^2 |p(t)|^2 dt} < \infty$.
3. Frequency dispersion of $P(f)$: $\sigma_f = \sqrt{\int_{\infty}^{\infty} f^2 |P(f)|^2 df} < \infty$.
4. Orthogonality condition: $\langle p_{T,k,n}(t), p_{R,l,n}(t) \rangle = \delta_{kl}\delta_{mn}$.

For example, in the case of OFDM (considering the addition of a CP), only properties 2 and 4 are fulfilled. More specifically, if T_{cp} is the duration of the CP and T_s the duration of the OFDM symbol (not considering the CP), the symbol density is just $T_s/(T_{cp} + T_s)$. However, for the general case of a FBMC systems, pulses can be designed so that the maximum symbol density of 1 can be reached. For this, we set the transmission symbols on Eq. (6.1) to be real-valued (i.e., PAM constellation symbols), the symbol period is set to half of the original period, and $\phi_{n,k} = (n + k)\pi/2$ in Eq. (6.2). Note that the real-valued symbol density for this system setup is $1/((T/2) \times (1/T)) = 2$, hence the equivalent complex-valued symbol density is 1. However, for such a system setup, the orthogonality condition no longer holds in the general case, but only for the real-valued part. Hence, only the following can be asserted

$$\Re \{ \langle p_{T,k,n}(t), p_{R,l,n}(t) \rangle \} = \delta_{kl}\delta_{mn}. \tag{6.5}$$

Eq. (6.5) means that when demodulating FBMC symbols, interference from the surrounding symbols will be present in the imaginary part. Therefore, procedures like channel estimation or the usage of STBCs, which rely on the orthogonality condition, cannot be implemented directly, and special techniques must be used instead. More specifically, for the case of the channel estimation, several methods have been proposed in the literature. In [JLR03], one symbol adjacent to each pilot is employed to cancel the interference of the imaginary part. This adjacent symbol was named later in [STI+10] as auxiliary pilot (AP). More recently, in [CUI+15], a more sophisticated channel estimation method named coded auxiliary pilot (CAP) was proposed. This method is based on the same idea of canceling the interference but applying linear coding to the data symbols surrounding the pilot. As shown in [CUI+15], the AP takes up a significant amount of power overhead to cancel the interference, which can be reduced significantly by applying the proposed CAP method.

One of the key parameters to choose in FBMC is the prototype filter to be used. In this chapter we consider two different prototype filters, the one defined by the PHYDYAS project [BEL+10] and the so-called Hermite pulse [HB97]. The PHYDYAS pulse (considering $K = 4$ coefficients), is expressed as [BEL+10]

$$p(t) = \begin{cases} 1 + \sum_{k=1}^{4} H_k \cos(2\pi kt/(KT)), & -KT/2 \leq t \leq KT/2 \\ 0, \qquad \text{otherwise}, \end{cases} \tag{6.6}$$

where the coefficients H_k are

$$H_1 = 1,\ H_2 = 0.971960,\ H_3 = \sqrt{(2)}/2,\ H_4 = 0.235147. \tag{6.7}$$

On the other hand, the Hermite pulse is defined based on Hermite polynomials as [HB97]

$$p(t) = \sum_{k=0}^{4} H_{4k} h_{4k}(2\sqrt{\pi}t/T) \exp(-2\pi(t/T)^2), \tag{6.8}$$

where h_n is the nth-degree Hermite polynomial, and the coefficients H_n are

$$\begin{aligned} H_0 &= 1.1850899 & H_4 &= -1.9324881 \cdot 10^{-3} \cdot H_0 \\ H_8 &= -7.3110588 \cdot 10^{-6} \cdot H_0 & H_{12} &= -3.1542096 \cdot 10^{-9} \cdot H_0 \\ H_{16} &= 9.6634138 \cdot 10^{-13} \cdot H_0 \end{aligned} \tag{6.9}$$

In Fig. 6.1 we show the considered FBMC pulses both in the time and frequency domains. We also show the OFDM (rectangular) pulse (without considering the CP) for comparison purposes. It is worth noting that the Hermite pulse is specially suited for multicarrier transmissions over doubly dispersive channels since it minimizes both ICI and inter-symbol interference (ISI) by means of a good localization in time and frequency [HB97].

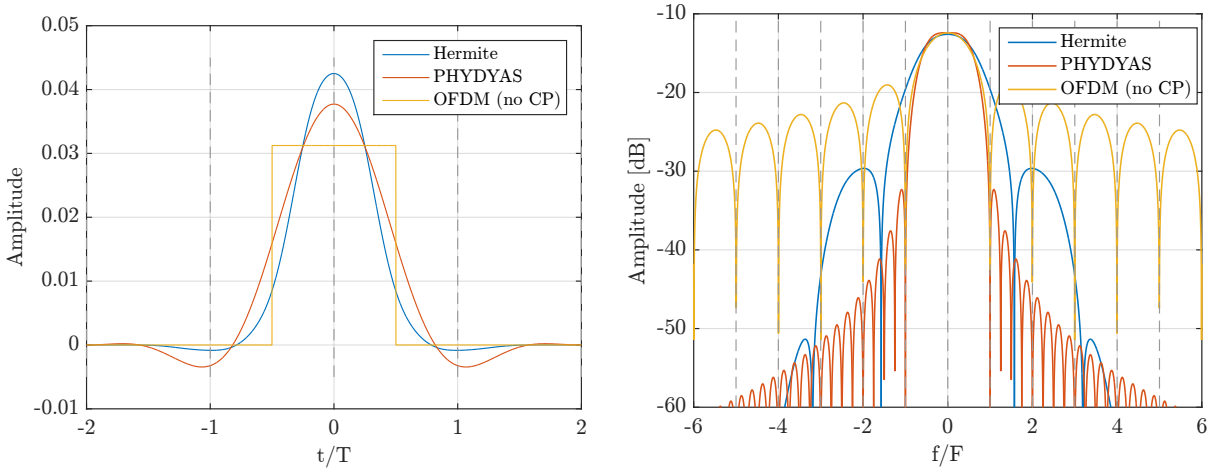

(a) Pulses in time domain.

(b) Pulses in frequency domain.

Figure 6.1: FBMC pulses considered. The OFDM pulse is also shown (without the CP) for comparison purposes. Note that the period T of OFDM is twice the period for the FBMC waveforms for a given frequency spacing.

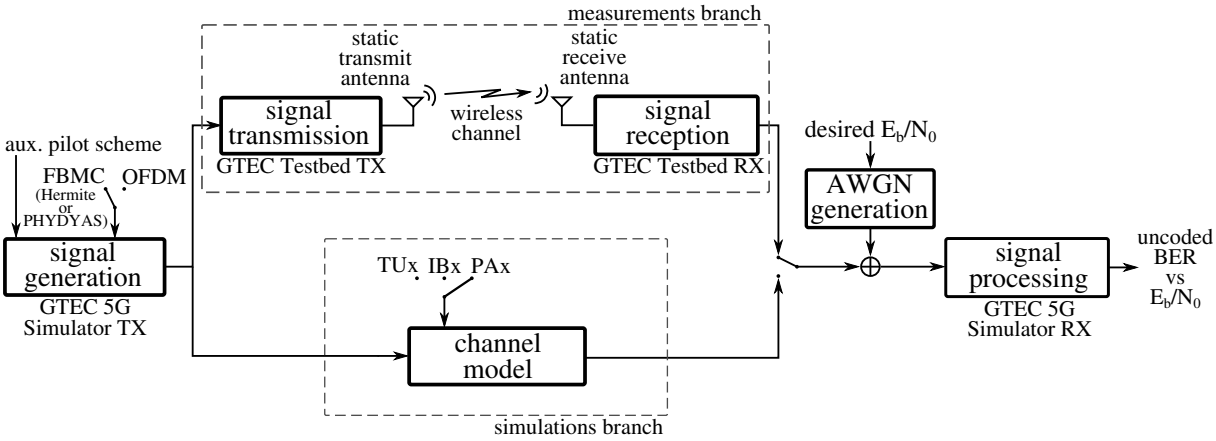

Figure 6.2: Block diagram of the performance evaluation setup.

6.3 FBMC Evaluation in Quasi-static Environments

This section details the performance evaluation of FBMC and its comparison with respect to OFDM in quasi-static environments. Analytic results —both for additive white gaussian noise (AWGN) and Rayleigh channel models— are also included as a reference. The strategy followed for the evaluation is shown in Fig. 6.2, where the first block (labeled as "signal generation") is in charge of generating the transmit signals, which move forward through one of the two possible branches:

1. The "measurements branch" involves the GTEC Testbed to perform over-the-air FBMC and OFDM transmissions with near-perfect frequency synchronization. We consider three measurement scenarios detailed in Section 6.3.2: a medium-sized office with and without direct line-of-sight (LoS) conditions, a small office with LoS, and an indoor

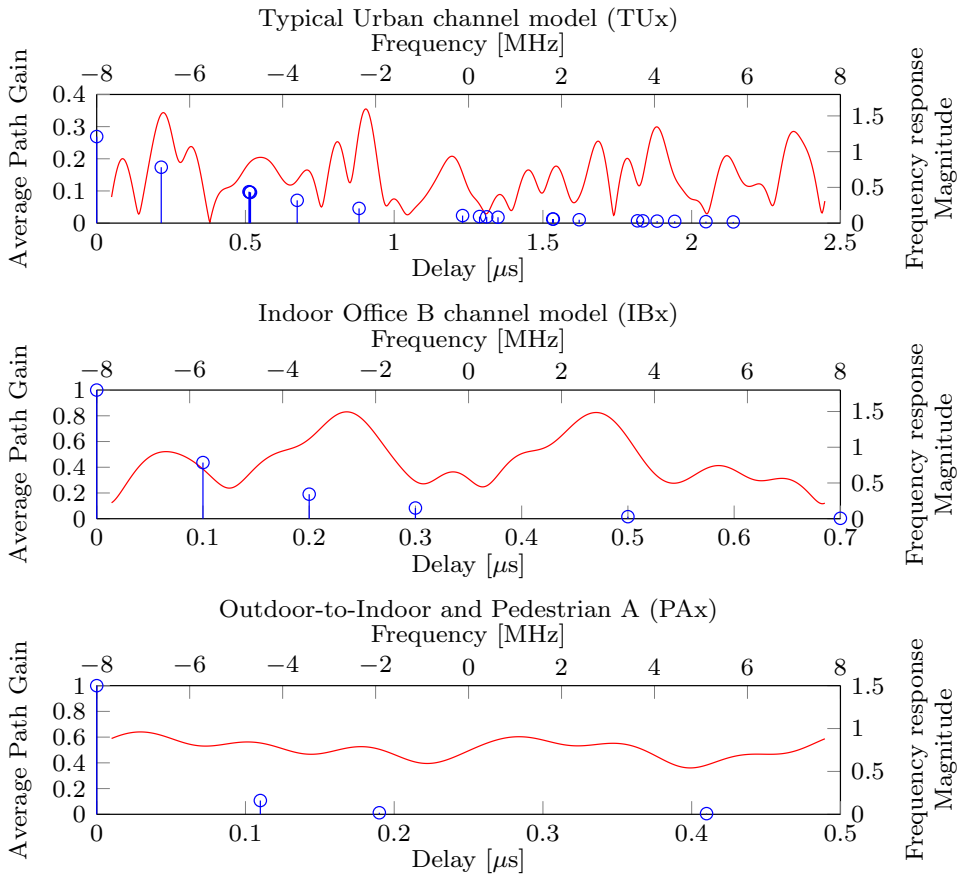

Figure 6.3: PDP and frequency response (of a realization) of the considered channel models (typical urban channel model, indoor office b and outdoor-to-indoor and pedestrian A).

corridor.

2. The "simulations branch" considers three different channel models (their power delay profile (PDP) is shown in Fig. 6.3) to evaluate typical scenarios for a pedestrian user:
   - TUx for urban areas, specified by the 3GPP [NET04].
   - IBx for indoor environments, from the ITU Radiocommunication Sector (ITU-R) third generation (3G) channel models [ITU97].
   - PAx for an outdoor-to-indoor link, also from the ITU-R 3G channel models [ITU97].

   In all models, the Doppler spread is configured according to the carrier frequency and the target receiver speed: 0 km/h for static and 3 km/h for pedestrian mobility.

6.3.1 Testbed Setup

The experimental evaluations are carried out with the GTEC Testbed (described in Chapter 2) using two nodes: a transmit-only node and a receive-only node. For each node, its corresponding USRP board is connected to a laptop equipped with two solid-state drives: one containing a GNU/Linux operating system and the custom-developed measurement software,

whereas the other is dedicated to storing the transmit/acquired signals.

The transmitter is equipped with two Mini-Circuits TVA-11-422 high-power amplifiers [MIN], one per antenna. The antennas employed at the transmitter and receiver nodes, namely Mobile Mark PSKN3-24/55 [MAR], are omnidirectional.

At the transmitter side, the samples are first pre-processed and saved into a dedicated solid-state drive. Next, such samples are transmitted over the air in a cyclic fashion using a single antenna at a time from the set of two available. Switching the transmit antenna allows for obtaining different channel realizations from distinct spatial positions and polarizations. At the receiver, the samples coming out of the two antennas (out of the four receive antennas available) of the USRP are read through the USB and stored first in the computer memory, and eventually recorded in a solid-state drive together with logging information useful for documenting the measurements. Notice that the receiver node acquires signals simultaneously from two different antennas although a single-input-single-output (SISO) system is being assessed. Switching between the two sets, each with two antennas, allows for obtaining different channel realizations, leading to eight different channel realizations without moving the transmit nor the receive node. More channel realizations are obtained by moving the transmitter and the receiver in a small area (typically of $3\,\lambda \times 3\,\lambda$ [CGR11], where λ is the carrier wavelength). In order to ensure a fair comparison, all waveforms under test are transmitted sequentially under the same conditions (recall that we are assuming quasi-static wireless channels).

6.3.2 Measurement Scenarios

We considered the following scenarios:

1. A medium-sized office represented by the laboratory of our research group at the University of A Coruña. The laboratory is located in the second floor of a building with coordinates $43°19'59.3''$ N, $8°24'33.2''$ W and it occupies an area of $82\,\mathrm{m}^2$. This setup is shown in Fig. 6.4 and Fig. 6.6 with transmitter TX1 and receiver RX1 for the case with direct LoS.
2. Transmitter and receiver in static condition with non-line-of-sight (NLoS) in a medium-sized office. This setup is shown in Fig. 6.4 with transmitter TX2 and receiver RX2. The receiver in this evaluation was in the same location as in 1).
3. A small office with approximately $19\,\mathrm{m}^2$, represented by a room in the third floor of the aforementioned building, located above the laboratory. This setup is shown in Fig. 6.5 with transmitter TX3 and receiver RX3.
4. Corridors. Large buildings usually have corridors, which exhibit specific propagation conditions for wireless signals. Therefore, we also consider corridors as typical indoor scenarios. This setup is shown in Fig. 6.4 and Fig. 6.7 with transmitter TX4 and receiver RX4 moving at approximately $3\,\mathrm{km/h}$.

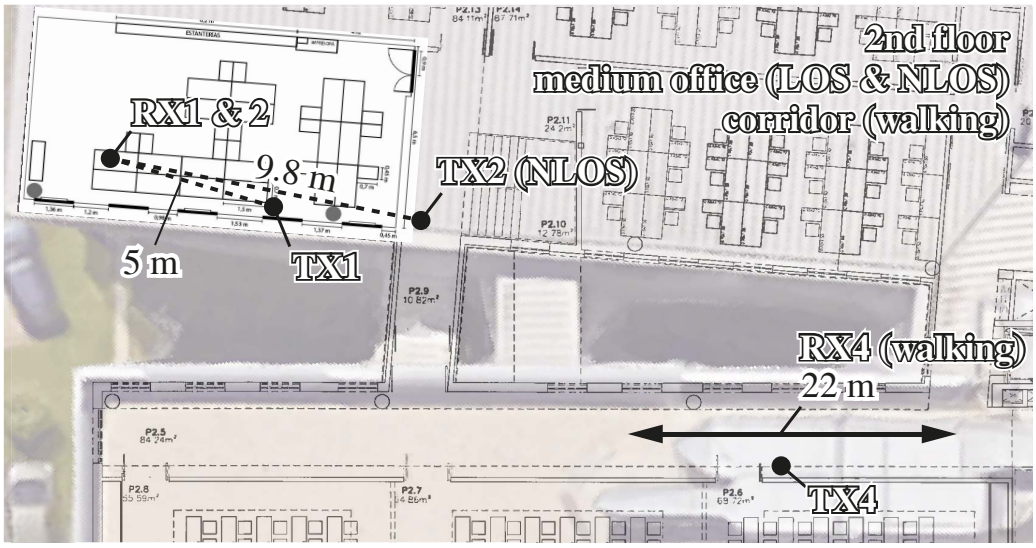

Figure 6.4: Map of the medium-sized office and corridor scenarios.

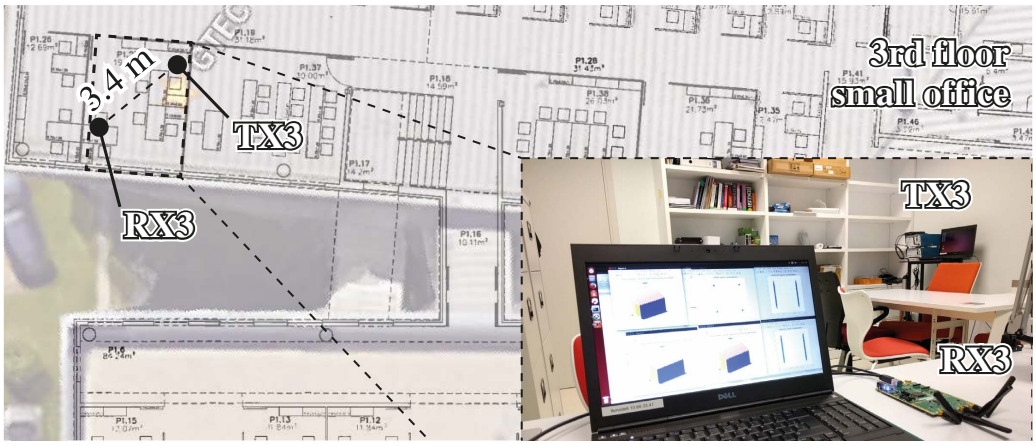

Figure 6.5: Map and picture of the small office scenario.

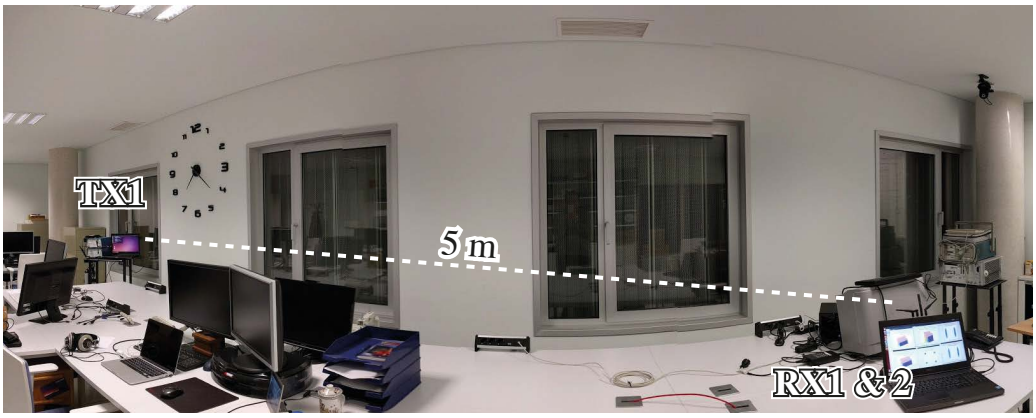

Figure 6.6: Picture of the medium-sized office scenario with LoS.

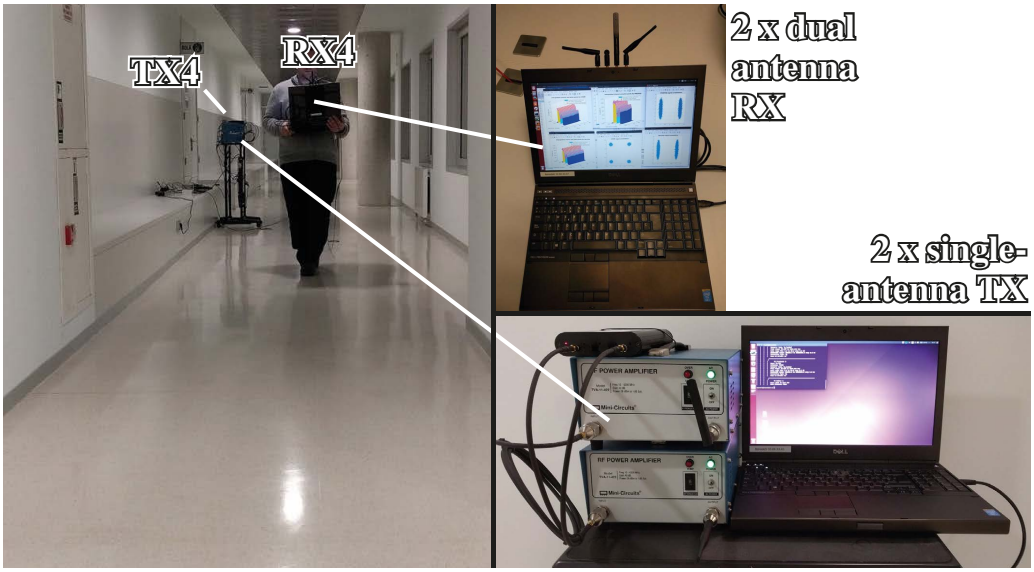

Figure 6.7: Picture of the corridor scenario with the receiver moving at 3 km/h.

6.3.3 Evaluation Procedure

In order to compare the results for the different considered modulations (OFDM and FBMC with Hermite and PHYDYAS pulses), the following aspects were considered:

- The number of data subcarriers, as well as the subcarrier spacing, are the same in all cases. More specifically, 600 subcarriers are used, while the subcarrier spacing was set to 15 kHz. These parameters correspond to the typical configuration for the 10 MHz downlink LTE profile.
- The pilot density considered for channel estimation is equivalent in all cases. Note that in the case of FBMC some additional symbols, namely the APs, are required to minimize the interference caused by the lack of orthogonality of the received pilots [FAR11]. More specifically, a rectangular grid of pilots was used. Such pilot spacing in the time-frequency grid is of 8 subcarriers in the frequency dimension and of 10 symbols in the time dimension for FBMC signals (5 symbols in the case of OFDM given that consecutive symbols do not overlap).
- The same algorithms for channel estimation, interpolation and equalization are considered for each of the modulations.
- A 2-PAM constellation is used for the FBMC transmissions, while 4-QAM is considered for OFDM, since the symbols are complex-valued in the latter case.
- The same number of user data bits is considered per transmission. Taking into account that real-valued symbols are used in FBMC, whereas complex-valued ones are used for OFDM, more time-positions in the time-frequency grid are required for FBMC signals with respect to OFDM for the same number of transmitted bits. However, provided that consecutive FBMC symbols partially overlap in the time domain, this does not mean that in order to transmit the same amount of data bits we need twice the time for FBMC with

Table 6.1: Main parameters used in the experiments.

parameter	value
Sampling frequency, F_s	15.36 MHz
FFT size	1024
Number of used subcarriers	600 (excluding DC)
CP length (OFDM)	72 samples
Constellations	2-PAM (FBMC), 4-QAM (OFDM)
Pilot spacing	8 subcarriers (frequency dimension)
	10 symbols (time dimension, FBMC)
	5 symbols (time dimension, OFDM)
auxiliary pilot (AP) scheme	CAP (8 surrounding symbols) [CUI+15]
Carrier frequency, f_c	2.6 GHz
E_b/N_0	from 0 to 40 dB (simulations)

respect to OFDM. With the considered model, the user bit rate is approximately the same for both OFDM and FBMC, with slight differences caused by the length of the OFDM cyclic prefix and the time dispersion of the prototype filters in FBMC.

- The signals are scaled to ensure that the transmitted energy per bit for the data symbols is the same for both OFDM and FBMC.

We consider the uncoded BER (i.e., the BER after the symbol hard-decision) as the figure of merit for the results evaluation, since it is one of the most used performance metrics in wireless communications. Table 6.1 details the most relevant parameters.

6.3.4 Simulation Results

Fig. 6.8a shows the BER versus E_b/N_0 for the TUx channel model when a static scenario is considered ($v \approx 0$ km/h). Additionally, the analytic curves for the AWGN and Rayleigh channel models are included. It can be seen that the BER for the OFDM curve fits well to the analytical BER for a Rayleigh channel. For the case of FBMC, the BER is almost the same as OFDM for E_b/N_0 values smaller than 25 dB. However, for larger E_b/N_0 values ($E_b/N_0 > 25$ dB), the FBMC BER starts to diverge from the OFDM one, saturating around 40 dB of E_b/N_0. The performance of both the FBMC pulses considered (Hermite and PHYDYAS) is almost identical, being the PHYDYAS pulse a little better for high values of E_b/N_0. The worse performance of FBMC is explained because the FBMC pulses are affected by the high frequency selectivity of the TUx channel, and therefore the channel distorting each subcarrier is not completely flat. The performance of FBMC in channels with high frequency selectivity such as this one improves when using the better minimum mean square error (MMSE) channel equalizer [IL09; NRM17].

Fig. 6.8b shows the same results as Fig. 6.8a but when the IBx channel model is considered.

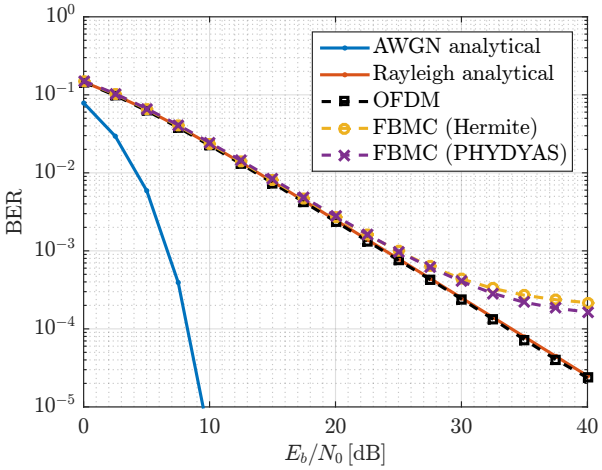

(a) Results for the TUx channel model

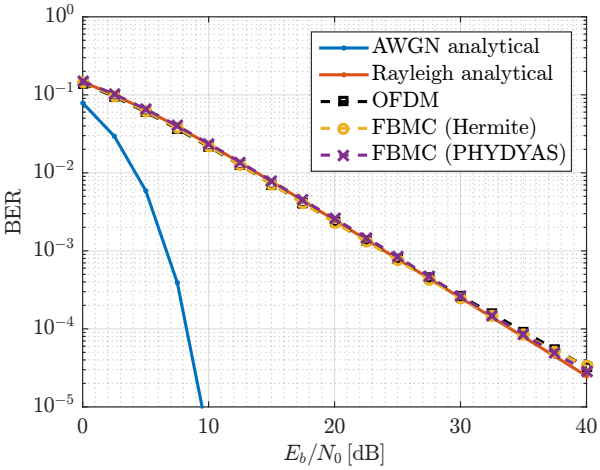

(b) Results for the IBx channel model.

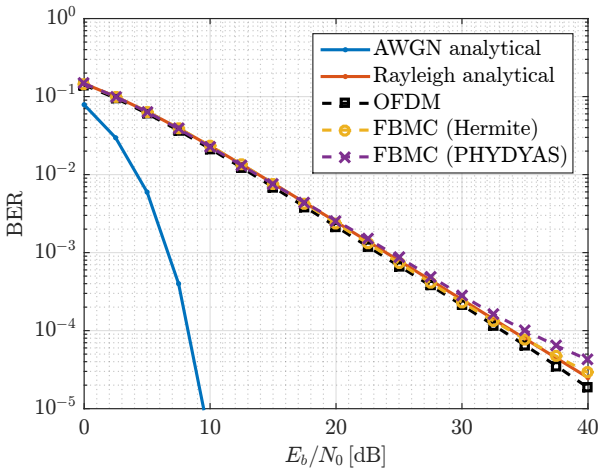

(c) Results for the PAx channel model.

Figure 6.8: BER versus E_b/N_0 for the different considered channel models. A 4-QAM constellation is considered for OFDM, and a 2-PAM one is considered for FBMC.

Notice that all the schemes perform similarly and fit well to the Rayleigh BER curve because the frequency selectivity of this channel is much lower than that of the TUx channel model (see Fig. 6.3). This explains why the FBMC schemes do not reach a saturation point as in the TUx case.

Finally, Fig. 6.8c shows the same results as Figs. 6.8a and 6.8b but when the PAx channel model is considered. As shown in Fig. 6.3, this channel has a low frequency selectivity, and the results are similar to those of the IBx channel model.

6.3.5 Measurement Results

Figures 6.9a to 6.9d show the results obtained from the measurements. With the objective of estimating the accuracy of the results, 95 % confidence intervals are also included. Figures 6.9a and 6.9c shows the results when measuring inside medium and small-sized offices, respectively,

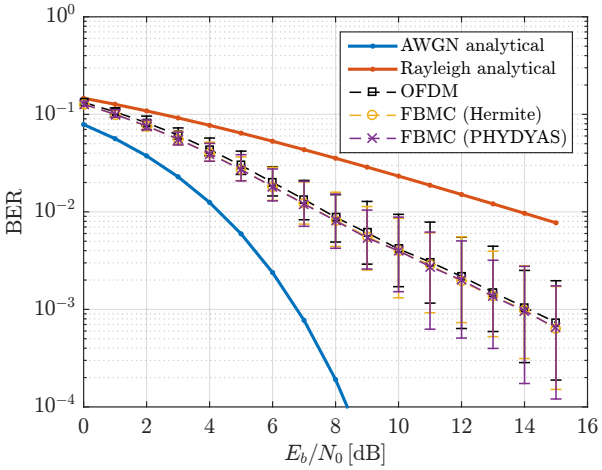

(a) Transmitter and receiver in static condition and LoS in a medium-sized office.

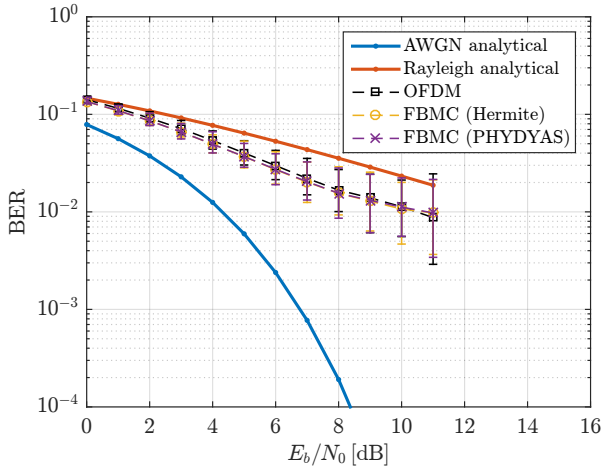

(b) Transmitter and receiver in static condition and NLoS in a medium-sized office.

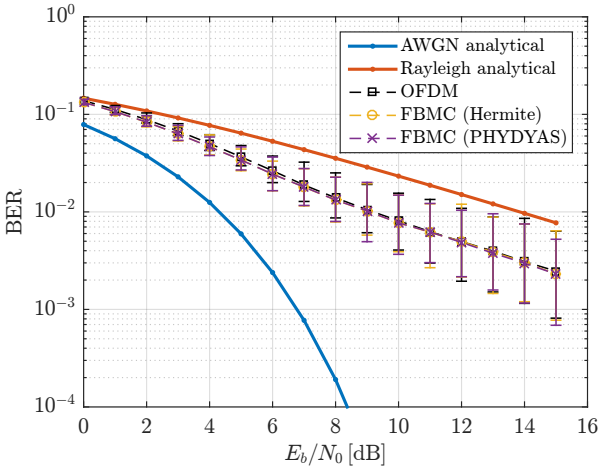

(c) Transmitter and receiver in static condition and LoS in a small office.

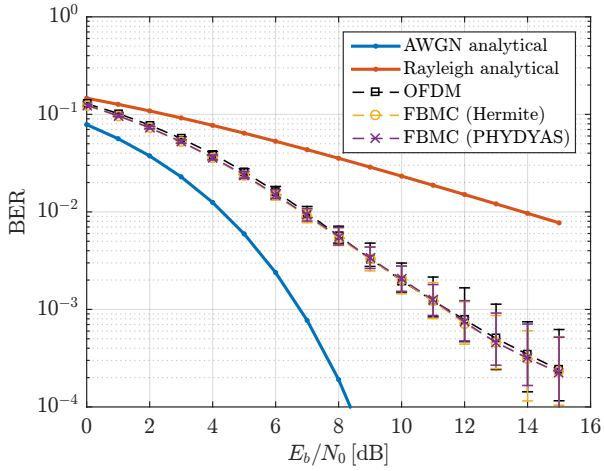

(d) Transmitter in static condition and receiver moving at approximately 3 km/h in a corridor.

Figure 6.9: BER versus E_b/N_0 for the measurements in four different scenarios.

under LoS conditions (see Figs. 6.5 and 6.6). Figure 6.9b show the results when placing the receiver inside the medium-sized office and the transmitter in the corridor, hence under NLoS conditions (see Fig. 6.4). Finally, Fig. 6.9d shows the results obtained when the transmitter is located in a corridor and the receiver is moving along the same corridor at a speed of approximately 3 km/h, passing in front of the transmitter (see Fig. 6.7).

For all the scenarios, the results for the different modulation schemes (OFDM and FBMC) are very similar. There is little difference between the results for the considered scenarios for low E_b/N_0 values since, in these cases, the noise is the main contributor to the signal distortion. For higher E_b/N_0 values, the performance obtained for the medium-sized office is slightly better than that for the small-sized office (see Figs. 6.9a and 6.9c). In fact, the results for small-sized office are closer to the analytical results obtained for the Rayleigh channel, which is consistent with the fact that the multipath components are received with more power with respect to the

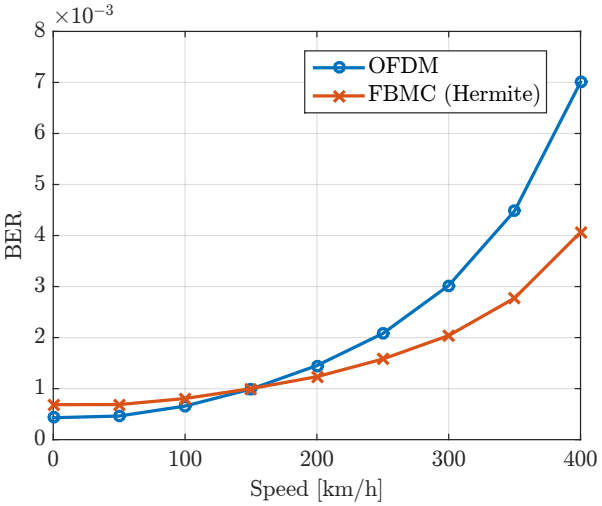

(a) TUx channel model.

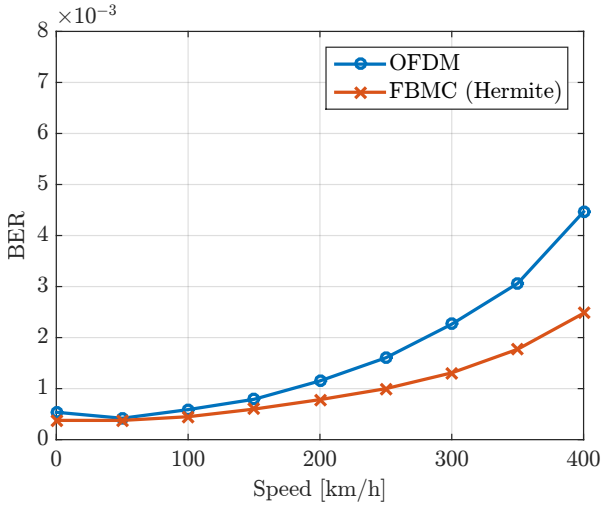

(b) IBx channel model.

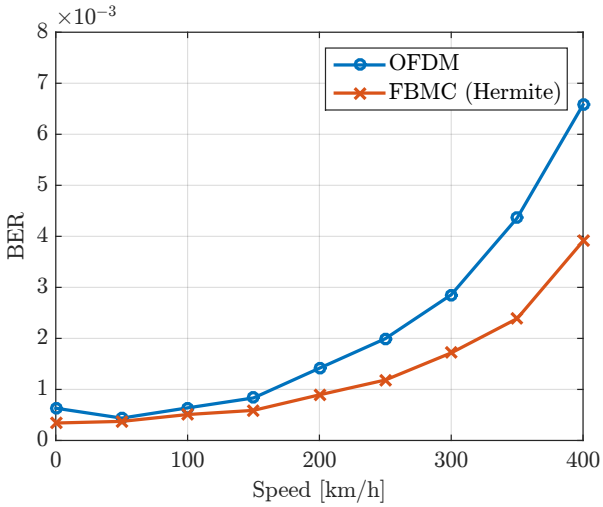

(c) PAx channel model.

Figure 6.10: BER versus speed for $E_b/N_0 = 30\,\text{dB}$ for the different considered channel models.

case of the medium-sized office. The results for NLoS conditions are even closer to the Rayleigh analytical ones (see Fig. 6.9b), as expected. However, there is a lower bound for the BER which is achieved at $E_b/N_0 \approx 12\,\text{dB}$. According to Fig. 6.9d, the scenario providing the best average performance results is the one in which the receiver is moving. This is because the speed is too low to cause a strong signal distortion whereas, on the other hand, when it passes in front of the transmitter the distance between them is very small.

6.4 FBMC Evaluation in High-Speed Environments

In this section the performance of FBMC and OFDM in high speed environments is evaluated both by means of simulations and over-the-air transmissions.

6.4.1 Simulation Results

All the results included in this subsection are expressed in terms of BER with respect to the receiver speed and considering $E_b/N_0 = 30\,\text{dB}$. A 4-QAM constellation is used for the case of OFDM and a 2-PAM one for the case of FBMC.

Fig. 6.10a shows the BER versus the receiver speed for the TUx channel model considering $E_b/N_0 = 30\,\text{dB}$. For low speed values, OFDM performs a little better than FBMC, which is in accordance with the results presented in Fig. 6.8a. As expected, the BER for both modulation schemes increases with the speed due to the ICI, although the higher the speed the better the performance of FBMC with respect to OFDM.

Fig. 6.10b shows the same results as in Fig. 6.10a but when the IBx channel model is considered. In this case, even for lower speeds, FBMC performs a little better than OFDM. Finally, Fig. 6.10c shows the same results as Figs. 6.10a and 6.10b but when the PAx channel model is considered. The obtained results are similar to those of the IBx channel model.

6.4.2 Emulating High Speeds by Time Interpolation

When multicarrier systems are used in time-selective channels, ICI arises in the received signal. The amount of ICI relates to the normalized Doppler spread of the channel, which is given by $D_n = f_d T$, being f_d the maximum Doppler frequency and T the FBMC symbol period.

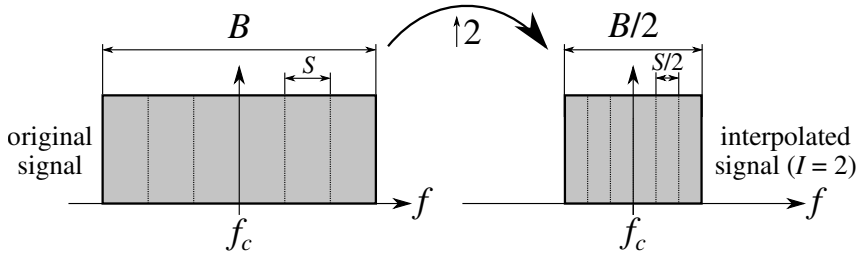

Figure 6.11: Example of spectrum compression due to a time interpolation factor $I = 2$. It is straightforward to see that the subcarrier spacing S is also reduced by a factor of $I = 2$ since the total bandwidth B is also reduced by the same factor.

As proposed in our previous work [ROD+14], the parameter T can be adjusted by time interpolation by a factor I, yielding an FBMC symbol period $T^{(I)} = IT$, and consequently an I times narrower signal bandwidth (see Fig. 6.11), which leads to a reduced subcarrier spacing (also by a factor of I). Therefore, given the actual velocity v of the mobile receiver, the normalized Doppler spread impacting the time-interpolated FBMC signal can be written as

$$D_n^{(I)} = f_d T^{(I)} = f_d IT = \frac{IT f_c v}{c} = \frac{T f_c}{c} v^{(I)}, \tag{6.10}$$

with f_c the carrier frequency, c the speed of light, and $v^{(I)} = Iv$ the emulated speed as a result of an actual measurement speed v and an interpolation factor I. Consequently, enlarging the

symbol period $T^{(I)}$ by adjusting I allows for the emulation of a velocity $v^{(I)}$ while conducting measurements at a (presumably much lower) speed v. Note that the statistical properties of the noise are not changed by the decimation process regardless of the interpolation factor.

The technique involves three major steps: 1) interpolate the original signal, 2) transmit over the air the interpolated signal, and 3) decimate the signal at the receiver. To show the effects caused by this process on the signal, let us consider a transmit signal $s(t)$, which leads to a received signal $r(t)$ expressed as

$$\begin{aligned} r(t) &= h(t,\tau) * s(t) + w(t) \\ &= \int_{-\infty}^{\infty} h(t,\tau) s(t-\tau) d\tau + w(t), \end{aligned} \tag{6.11}$$

where $*$ is the convolution operator (in this case a time varying convolution), $h(t,\tau)$ is the time-varying channel impulse response, and $w(t)$ corresponds to uncorrelated complex-valued white Gaussian noise with variance σ_w^2.

Next, consider the following time-varying channel model

$$h(t,\tau) = \sum_i \alpha_i(t) \exp\big(j2\pi\nu_i(t)t\big)\delta\big(\tau - \tau_i(t)\big), \tag{6.12}$$

where $\delta(\cdot)$ is the Dirac delta, and for each path i, $\alpha_i(t)$ is the complex amplitude, $\nu_i(t)$ is the Doppler frequency, and $\tau_i(t)$ is the path delay. Note, that we consider a general channel model where the α_i, ν_i, and τ_i are actually time dependent.

The first step in our technique is the interpolation of the transmit signal. Consider the signal $s(t)$ interpolated by a factor I, $s_I(t) = s(t/I)$. This signal is transmitted over the air leading to the following received signal

$$\begin{aligned} r(t) &= h(t,\tau) * s_I(t) + w(t) \\ &= \sum_i \alpha_i(t) \exp\big(j2\pi\nu_i(t)t\big) s_I\big(t - \tau_i(t)\big) \\ &= \sum_i \alpha_i(t) \exp\big(j2\pi\nu_i(t)t\big) s\big(t/I - \tau_i(t)/I\big). \end{aligned} \tag{6.13}$$

At the receiver, $r(t)$ is decimated by the same factor I, obtaining

$$r_{1/I}(t) = r(tI) = \sum_i \alpha_i(tI) \exp\big(j2\pi[\nu_i(tI)I]t\big) s\big(t - \tau_i(tI)/I\big), \tag{6.14}$$

which is equivalent to transmitting the signal $s(t)$ through the time varying channel

$$\hat{h}(t,\tau) = h(tI,\tau I) = \sum_i \alpha_i(tI) \exp\big(j2\pi[\nu_i(tI)I]t\big)\delta\big(\tau I - \tau_i(tI)\big)/I. \tag{6.15}$$

Therefore, it can be seen that the delays $\tau_i(t)$ are transformed into $\tau_i(tI)/I$ (i.e., frequency selectivity is reduced by a factor I), and, on the other hand, the Doppler frequency values $\nu_i(t)$ are transformed into $\nu_i(tI)I$ (i.e., time selectivity is increased by a factor I). Note that the I term dividing the expression in Eq. (6.15) is just a normalization term because $\delta(\alpha x) = (1/|\alpha|)\delta(x)$.

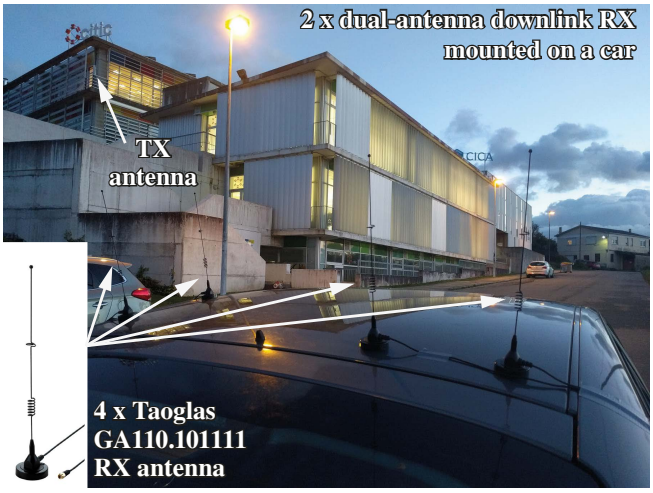

Figure 6.12: FBMC/OFDM dual-antenna receiver nodes mounted on a car.

6.4.3 Measurement Setup and Procedure

Considering the measurement scenario described in Chapter 5 (also shown here in Fig. 6.13 for clarity) and the GTEC Testbed detailed in Chapter 2, we now evaluate the performance of FBMC in high-speed environments by means of over-the-air transmissions and employing the technique explained in Section 6.4.2 to emulate high speeds. We also evaluate the performance of OFDM for comparison purposes.

More specifically, in the measurement scenario, a car equipped with two mobile downlink receiver units (see Fig. 6.12) moves along the path (161 m long) at a constant (and convenient) speed of 20 km/h, completing each pass in 29 seconds. The base station downlink transmitter is placed on the corner of a building adjacent to the measurement path (see Fig. 6.14), with the starting point of the path being the farthest one from the base station. Some trees in the vicinity of the path produce shadowing effects about 100 m away from the starting point (see Chapter 5).

The whole evaluation setup shown in Fig. 6.15. Recall that with the aim of extending the range of signal-to-noise ratio (SNR) values under evaluation, we simply add the required AWGN to the received signals before processing them.

Two measurement campaigns were carried out. For the first one a frame consisting of nine subframes is generated as shown in Fig. 6.16. We consider three modulation schemes (OFDM and two FBMC signals, each one considering a different prototype filter: the one defined by the PHYDYAS project [BEL+10] and the so-called Hermite pulse [HB97]) and three constellation sizes per each modulation scheme (2-PAM, 4-PAM and 8-PAM for the FBMC case and 4-QAM, 16-QAM and 64-QAM for the OFDM case). This allows us to obtain the results of BER and EVM for the different modulation schemes. A second measurement campaign was carried out considering the same modulation schemes as the first one, but incorporating channel coding to the signals, hence allowing for a measurement-based throughput analysis considering different modulations and coding schemes. The frame used for these measurements is shown in Fig. 6.17.

Figure 6.13: Measurement scenario with the car trajectory and the location of the base station.

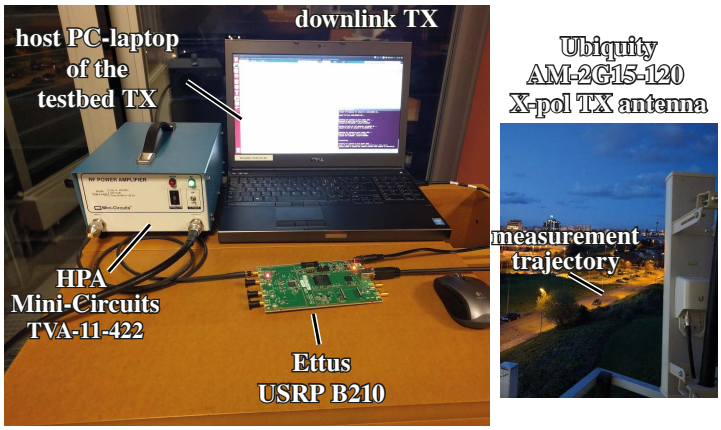

Figure 6.14: Single-antenna base station. We use the vertically polarized antenna element of the X-pol Ubiquity AM-2G-15-120.

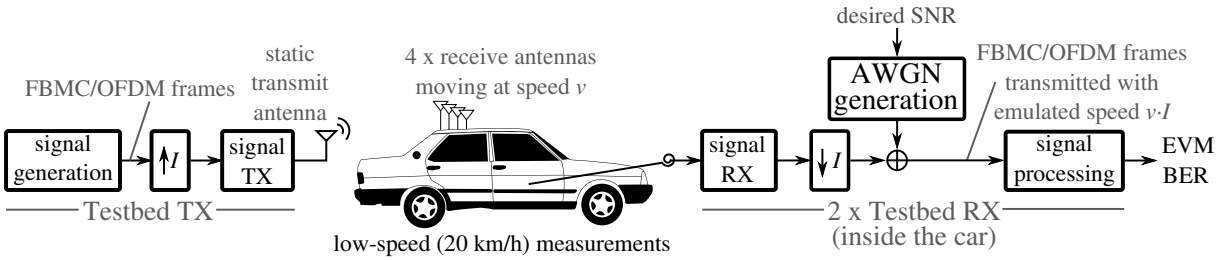

Figure 6.15: Measurement setup. FBMC and OFDM frames are evaluated for the emulated speed values: 200, 300, 420, and 500 km/h.

The sole configuration parameter changed during the experimental evaluation is the time interpolation factor $I \in \{10, 15, 21, 25\}$. This way, we emulate a Doppler spread similar to that obtained with a speed increase by a factor of I. In order to preserve the average energy per FBMC/OFDM symbol —and keeping a constant transmit power value regardless of the interpolation factor— the interpolated signals are scaled in amplitude by a factor of $\sqrt{I}$ before being transmitted. Given that the actual speed of the car is fixed at 20 km/h, the four

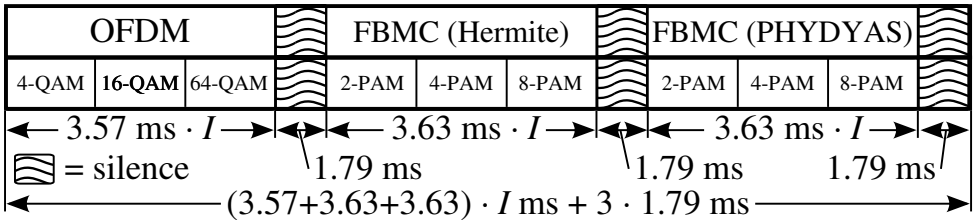

Figure 6.16: Transmitted frame structure in function of the interpolation factor I.

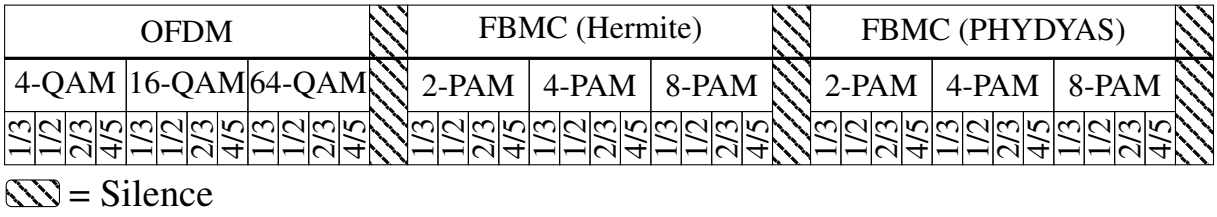

Figure 6.17: Frame structure considered for the measurements. The different blocks with the constellations and coding rates considered are shown.

interpolation factors considered yield the emulated speed values of 200, 300, 420, and 500 km/h, correspondingly. We chose such high-speed values because, on the one hand, they are practical for high-speed train scenarios and, on the other hand, for speed values below 200 km/h the differences in terms of performance are not significant, as shown in Section 6.4.1.

During the measurements, a frame corresponding to a single interpolation factor is transmitted over the air by the base station in a cyclical fashion. At the same time, the two receiver nodes mounted on the car acquire from the four available antennas, while the car completes the trajectory shown in Fig. 6.13 at the constant speed of 20 km/h. The measurement is repeated twice without modifying any parameter, therefore obtaining three measurements (each one consisting of four acquired records, one per each of the four available receive antennas) for each time-interpolation factor.

To calculate a certain performance metric for a given interpolation factor, and SNR value, we first add the necessary AWGN to obtain the target SNR (if possible, i.e., the SNR of the received signal should be higher than the desired SNR, otherwise the frame is discarded). Next, we demodulate each frame and calculate the performance metric for the frames accordingly. Then, the results are averaged out for all the frames. For the case of the throughput metric, we first find out the block with the highest number of bits among those received without errors and then divide the total number of bits in that block by the block duration (calculated as the number of multicarrier symbols times the symbol period).

The different aspects discussed in Section 6.3.3 were also considered for these measurements. Table 6.2 details the most relevant parameters of the measurements.

Table 6.2: Main parameters used in the experiments.

parameter	value
signal bandwidth, F_s	10 MHz (9 MHz used)
FFT size	1024 points
number of used subcarriers	600 (excluding DC)
CP length (OFDM)	72 samples
constellations	2-PAM, 4-PAM and 8-PAM (FBMC)
	4-QAM, 16-QAM and 64-QAM (OFDM)
pilot spacing	8 subcarriers (frequency dimension)
	8 symbols (time dimension, FBMC)
	4 symbols (time dimension, OFDM)
auxiliary pilot scheme	CAP (8 surrounding symbols)
actual velocity, v	20 km/h
carrier frequency, f_c	2.6 GHz
transmit power	$+18.5$ dBm (at antenna port)
interpolation factors, I	10 (200 km/h), 15 (300 km/h),
	21 (420 km/h), and 25 (500 km/h)
SNR	from 0 to 25 dB
coding rates	$1/3$, $1/2$, $2/3$, and $4/5$

6.4.4 Different Channel Realizations

As it was commented above, three car passes are carried out for each interpolation-factor. In other words, for each interpolation factor (emulated speed), the car moves three times along the measurement path. Actually, two identical dual-antenna receivers are mounted on the car, thus four antennas acquire simultaneously, leading to twelve measurement records for each interpolation-factor.

On the other hand, given that each frame is $T_F + T_0 = 10.83 + 5.37 = 16.2$ ms long, the total duration of each time-interpolated frame is $T_F \cdot I + T_0$ (see Fig. 6.16). Considering $I = 25$, the duration of the time-interpolated frame is 276.12 ms, thus 105 complete frames can be acquired by each of the four antennas during the 29 s of a single measurement pass, leading to 1260 acquired frames in total (4 antennas times 3 passes) for $I = 25$. For lower values of I, more frames are acquired since the duration of each time-interpolated frame is shorter, but the actual speed of the car is the same.

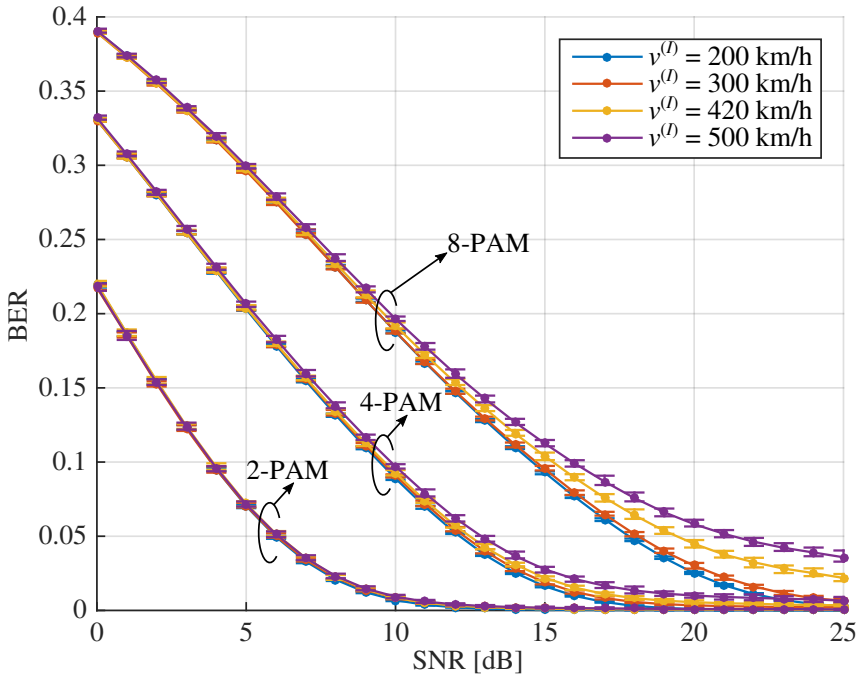

Figure 6.18: BER vs SNR for FBMC using the Hermite prototype filter for all the considered emulated speed values and constellation sizes.

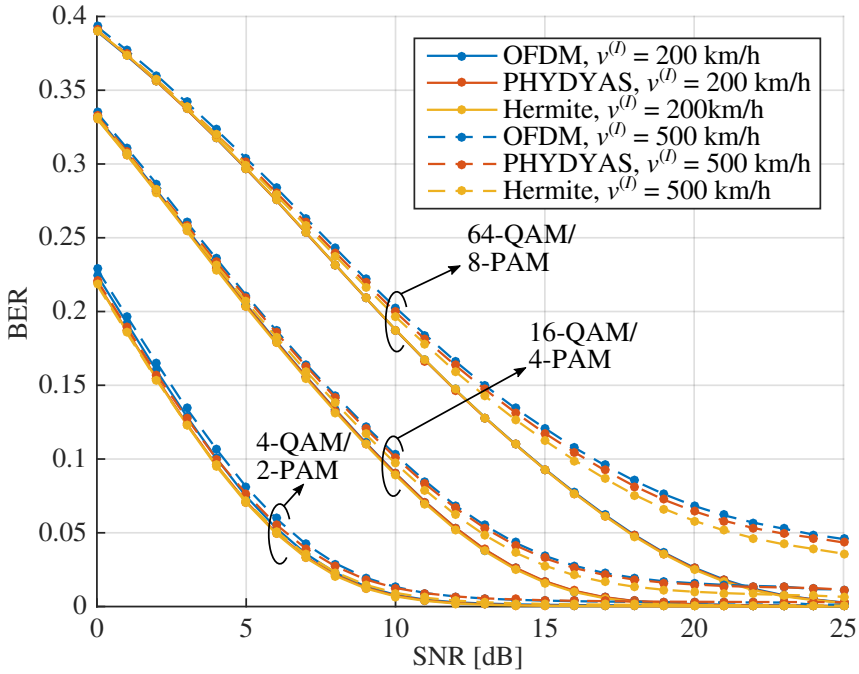

Figure 6.19: BER vs SNR for the minimum and the maximum emulated speeds considered. All the modulation schemes and the constellation sizes are shown.

6.4.5 Measurement Results

Uncoded BER and EVM

Fig. 6.18 shows the uncoded BER vs SNR for FBMC using a Hermite prototype filter for all the considered emulated speed values and constellation sizes. We estimate the precision of the results by means of $95\,\%$ confidence intervals for the mean obtained applying bootstrapping. The rest of the result figures do not include confidence intervals for the sake of readability, and because their lengths do not change significantly. For 2-PAM the BER does not change regardless of the emulated speed, whereas the higher the constellation size, the larger the impact of the speed on the BER. However, for speeds below $300\,$km/h, such a difference is not significant. This effect is also found in the other considered modulation schemes. On the other hand, for a threshold BER of $10\,\%$, an SNR of at least $15\,$dB is required for 8-PAM, $10\,$dB for 4-PAM, and only $4\,$dB for 2-PAM.

Fig. 6.19 shows the same results as Fig. 6.18 for the three modulation schemes, but only for the maximum and the minimum emulated speed values. Again, the higher the constellation size, the larger the impact of the speed on the BER. Whereas for 200 km/h the performance is basically the same for all the schemes, FBMC with the Hermite prototype filter performs better than the other alternatives at 500 km/h. This shows the superior performance of the Hermite prototype filter with respect to the PHYDYAS one for doubly dispersive channels. In any case, the performance differences are not very significant and therefore the theoretical advantages of FBMC waveforms (such as their better bandwidth efficiency and the minimization of multiple-access interference in the uplink) can be exploited without additional performance losses. Finally, for low SNR values, the noise becomes the dominant interference factor, hence all curves overlap.

Fig. 6.20 shows the same results as Fig. 6.19 in terms of EVM vs SNR, but excluding the modulation scheme corresponding to the PHYDYAS prototype filter. Noticeable performance differences are only found for high SNR values and high emulated speeds, i.e., when the ICI becomes the dominant interference factor. These results agree with those shown in Fig. 6.19.

Finally, Fig. 6.21 shows the BER vs emulated speed for an SNR value of 23 dB when 16-QAM is employed in OFDM and 4-PAM is used for FBMC. The shaded areas around the curves correspond to the 95 % confidence intervals for the mean. The performance is almost the same for speed values lower than 300 km/h regardless of the modulation scheme considered. As the speed increases, however, the BER difference between the schemes becomes larger. In other words, using the Hermite prototype filter becomes advantageous only for very high-speed values ($> 300\,$km/h).

For the three constellation mappings employed, it is worth noting that the performance differences in terms of BER between the three modulation schemes considered is not very significant. What we can safely conclude from the results is that FBMC schemes do not exhibit any a priori performance degradation in terms of uncoded BER with respect to OFDM.

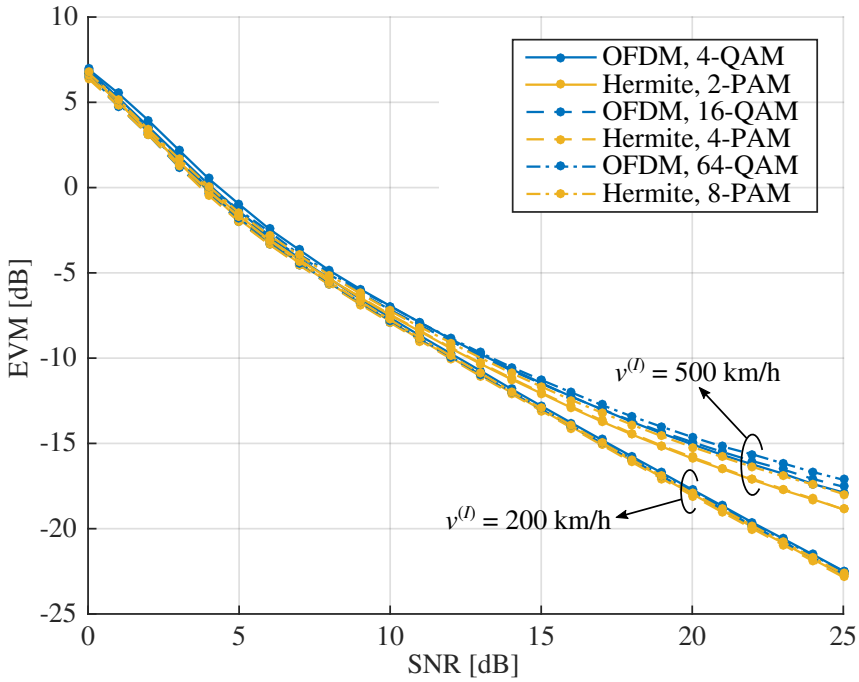

Figure 6.20: EVM vs SNR for the minimum and the maximum emulated speeds considered. All the constellation sizes are shown for Hermite and OFDM.

Coded BER and Throughput

Depending on the considered communication system, it could be desirable to minimize the latency (e.g., critical communications related with vehicle control and safety) or to maximize the throughput (e.g., provisioning of non-critical services to vehicle passengers). In the first case, the goal is to reduce the BER to the minimum achievable level, hence minimizing the number of retransmissions. For the second case, by considering a less conservative coding rate, we can transmit more data bits per frame, possibly increasing the latency since more retransmissions will be required. In this section we evaluate the performance of the system both in terms of coded BER as well as throughput.

Fig. 6.22 shows the coded BER versus SNR for the case of an FBMC modulation (Hermite pulse) when considering a 2-PAM constellation. The uncoded BER results are also shown for comparison purposes. We plot the coded BER for the highest and the lowest coding rates as well as the maximum and minimum emulated speeds (see Table 6.2). It can be seen that, for very low SNR values, the channel coding is not able to outperform the case in which the coding is not considered. Hence, when the coding rate is not robust enough to correct the errors introduced by the channel, the effective energy devoted to transmitting the data bits decreases with respect to the uncoded case since the transmit power is constant and part of the energy is lost by the redundancy bits. Consequently, coding increases the BER for low SNR values. For SNR values higher than a certain level, the coded BER values are lower than their corresponding uncoded counterparts. This effect can be also appreciated by means of the coding gain shown at the

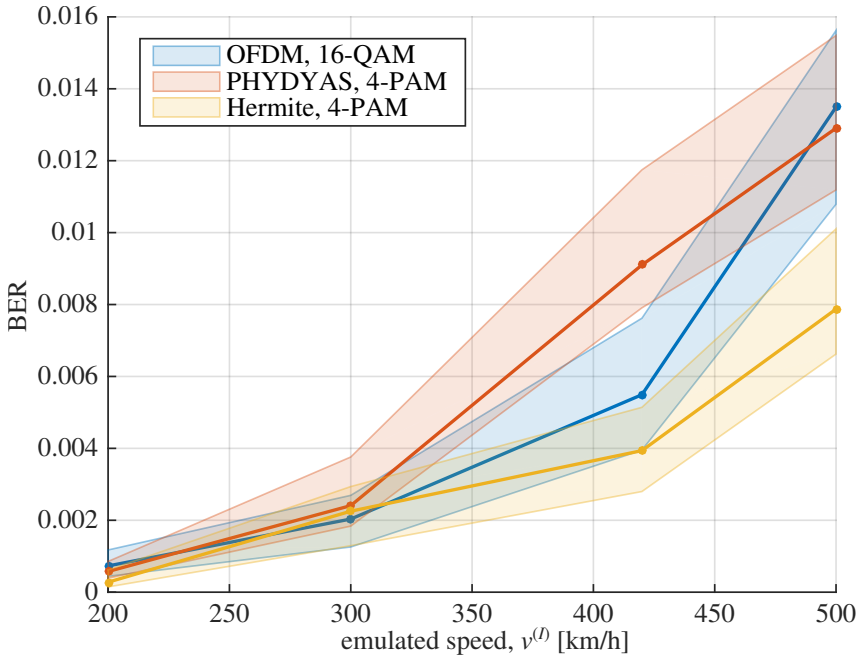

Figure 6.21: BER vs emulated speed for an SNR value of 23 dB.

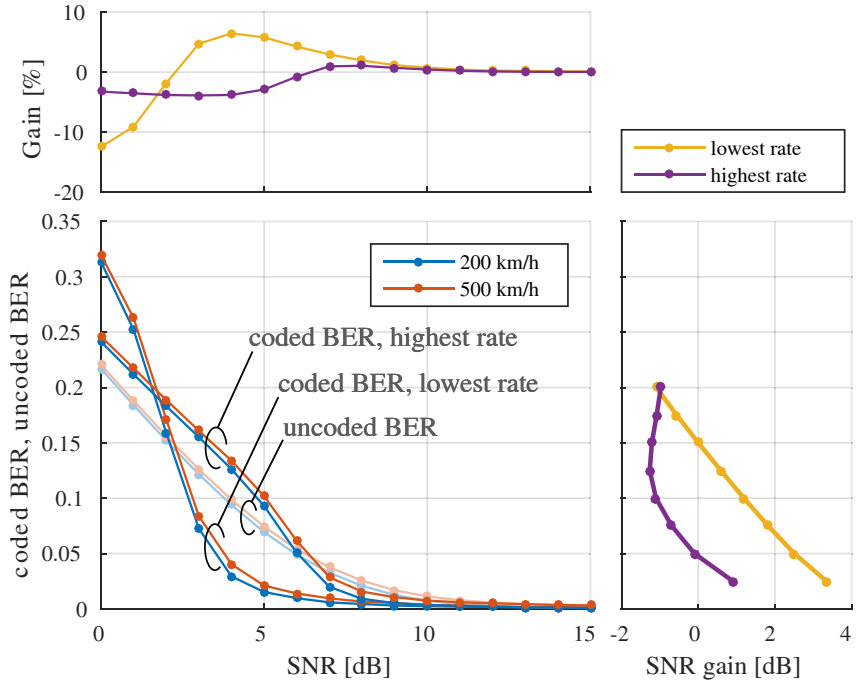

Figure 6.22: Coded and uncoded BER versus SNR for the minimum and maximum emulated speeds for FBMC (Hermite case) and 2-PAM constellation. The coding gain for the case of the maximum speed is also provided, both in terms of BER and effective SNR.

top of Fig. 6.23, calculated as the difference between the ratio of correctly received bits for the coded and uncoded cases. If we consider the coding rate $r \in \mathcal{R} = \{1/3, 1/2, 2/3, 4/5\}$ and the constellation $c \in \mathcal{C} = \{\text{2-PAM}, \text{4-PAM}, \text{8-PAM}, \text{4-QAM}, \text{16-QAM}, \text{64-QAM}\}$ (where PAM constellations correspond to the FBMC case and QAM constellations to OFDM), the coding

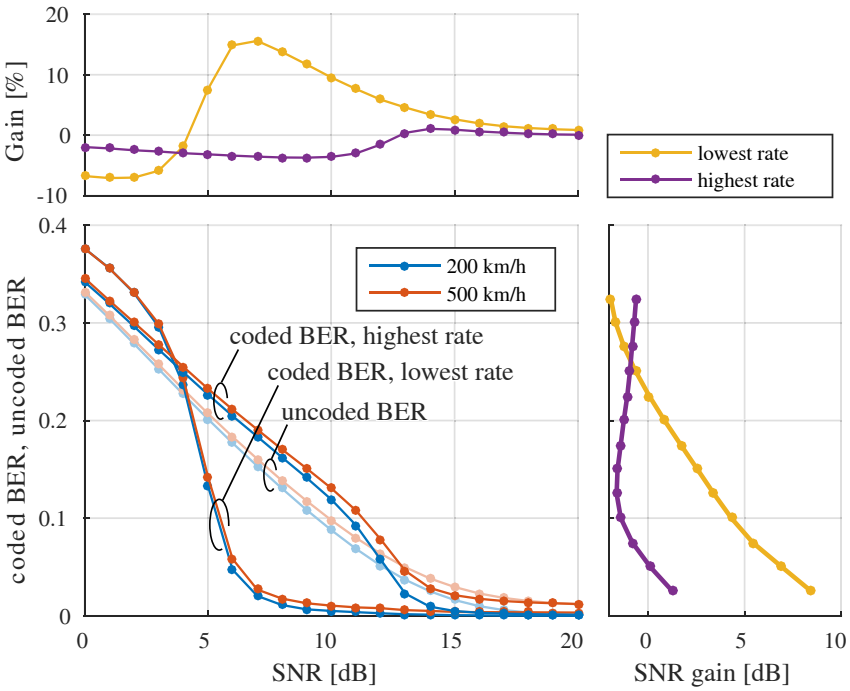

Figure 6.23: Coded and uncoded BER versus SNR for the minimum and maximum emulated speeds for FBMC (Hermite case) and 4-PAM constellation. The coding gain for the case of the maximum speed is also provided, both in terms of BER and effective SNR.

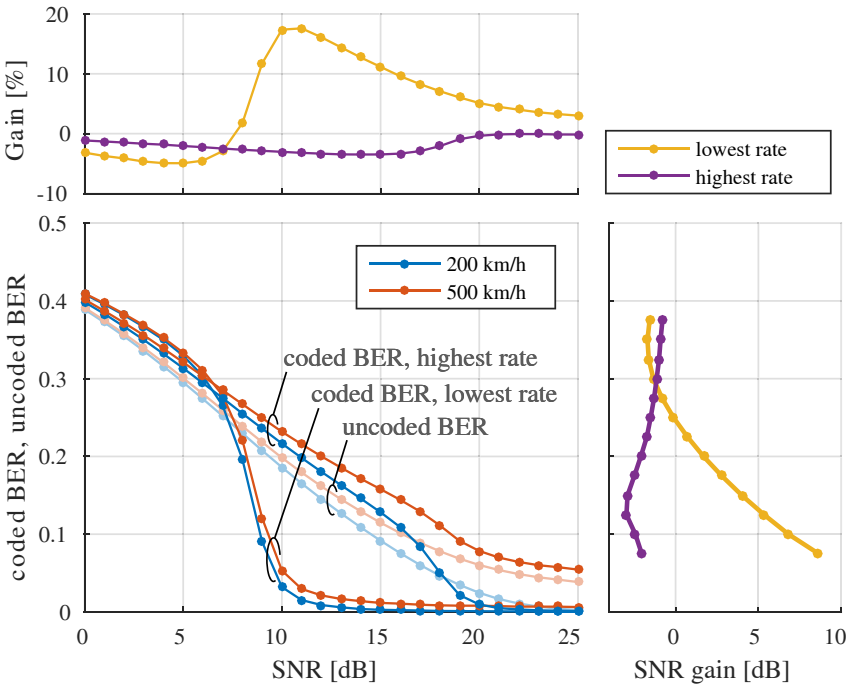

Figure 6.24: Coded and uncoded BER versus SNR for the minimum and maximum emulated speeds for FBMC (Hermite case) and 8-PAM constellation. The coding gain for the case of the maximum speed is also provided, both in terms of BER and effective SNR.

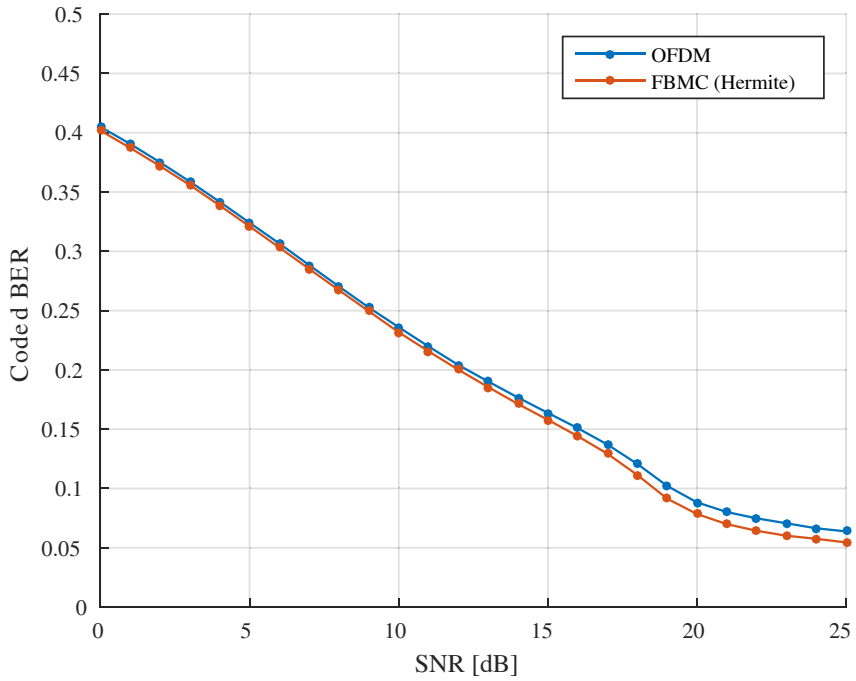

Figure 6.25: Coded BER versus SNR for FBMC (8-PAM) and OFDM (64-QAM), the maximum emlated speed, and the highest coding rate.

gain for the l-th frame is calculated as:

$$G_{\text{cod}}^{(r,c,l)} = 100 \times \left(\frac{C_{\text{cod}}^{(r,c,l)}}{D_{\text{cod}}^{(r,c)}} - \frac{C_{\text{uncod}}^{(r,c,l)}}{D_{\text{uncod}}^{(r,c)}} \right), \tag{6.16}$$

where $C_{\text{cod}}^{(r,c,l)}$ and $C_{\text{uncod}}^{(r,c,l)}$ are the number of correctly received bits for the coded and the uncoded case, respectively, and $D_{\text{cod}}^{(r,c)}$ and $D_{\text{uncod}}^{(r,c)}$ the number of data bits transmitted for each case. Note that, for the sake of brevity, only the emulated velocity of 500 km/h was considered for the gain curves.

An alternative way to evaluate the coding gain is to check the difference in terms of SNR for each BER value when coding is considered with respect to the uncoded case. The results for the highest and the lowest considered coding rates are shown at the rightmost part of Fig. 6.22. Coherently with the previous results, it can be seen that the gain is negative for higher BER values, which corresponds to the cases with lower SNR values.

Figs. 6.23 and 6.24 show the same results as Fig. 6.22 when 4-PAM and 8-PAM constellations are considered respectively instead of 2-PAM. It can be seen that the larger the constellation size, the higher the SNR value required to ensure a specific BER value. Furthermore, the achieved coding gains are slightly increased with the constellation order when the lowest coding rate is used. It is worth noting that when the constellation order is increased, a larger SNR is required to achieve positive coding gain values. In fact, for extreme cases (e.g., 8-PAM and the highest coding rate) the obtained gain was negative for the whole SNR range considered.

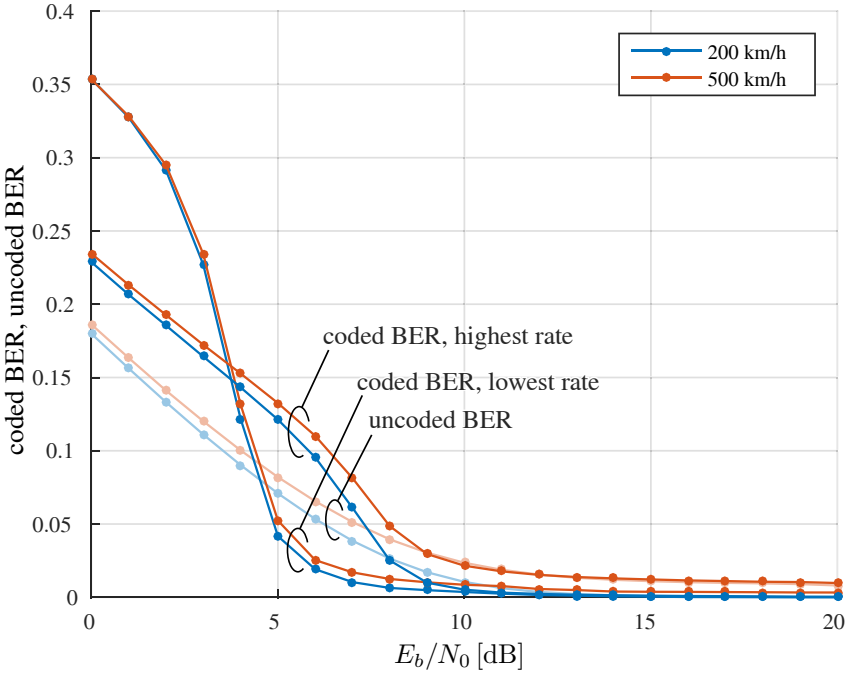

Figure 6.26: Coded and uncoded BER versus E_b/N_0 for the minimum and maximum emulated speeds for FBMC (Hermite case) and 4-PAM constellation.

Note that only the results for FBMC (Hermite case) were shown. This is because the results for other modulation schemes are very similar. In fact, the results for FBMC with the Hermite and the PHYDYAS prototype filters show no significant difference. The largest difference occurs when comparing the coded BER for OFDM and FBMC (e.g., with Hermite pulse) for a receiver moving at 500 km/h and using the largest constellation order and the highest coding rate. Fig. 6.25 shows the BER curves corresponding to the aforementioned case, showing that the differences are almost negligible except for high SNR values.

Another way of analyzing the BER results is to represent them with respect to the transmitted energy per data bit, namely E_b, instead of the SNR. Fig. 6.26 shows the coded BER versus E_b/N_0 for an FBMC modulation (Hermite pulse) and when considering a 4-PAM constellation, whereas also the uncoded BER results previously obtained in [ROD+16a] are included. We show the coded BER for the highest and the lowest coding rates, as well as the maximum and minimum emulated speeds (see Table 6.2). In other words, the same results shown in Fig. 6.23 are plotted with respect to E_b/N_0. While the SNR accounts for the transmit energy both for the data and the redundancy, the E_b/N_0 considers exclusively the energy used to transmit the data bits. Hence, if we compare Figs. 6.23 and 6.26 we can see that coded BER curves are shifted horizontally to the left in the second case when the coding rate is increased.

Fig. 6.27 shows the throughput versus SNR for the minimum and the maximum emulated speeds and all the modulation schemes. We can see that the performance for the two FBMC prototype filters considered is very similar, exhibiting a significant improvement in terms of throughput with respect to OFDM, which is because of the better spectral efficiency of FBMC

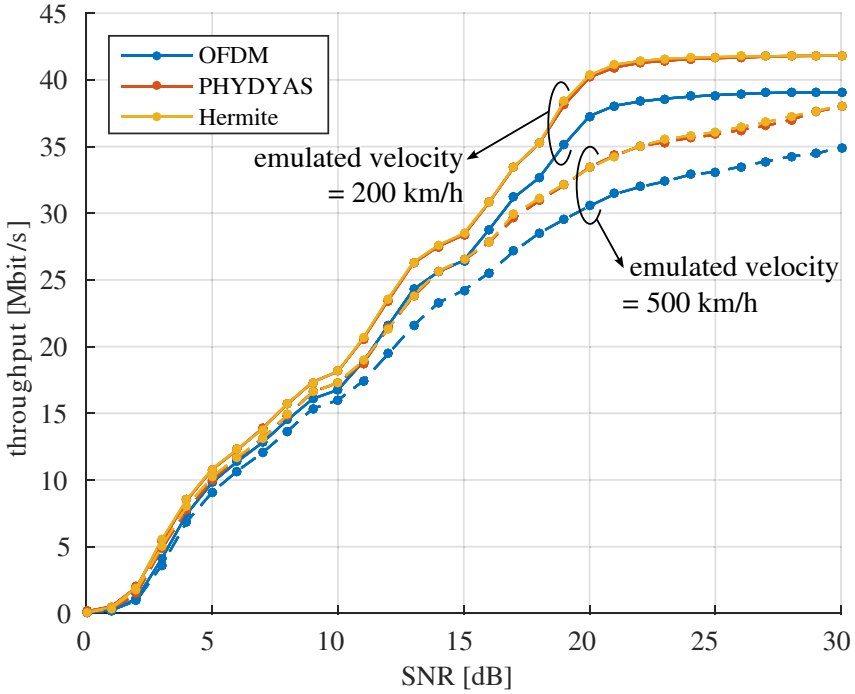

Figure 6.27: Throughput versus SNR for the minimum and maximum emulated speeds. All the modulation schemes are shown.

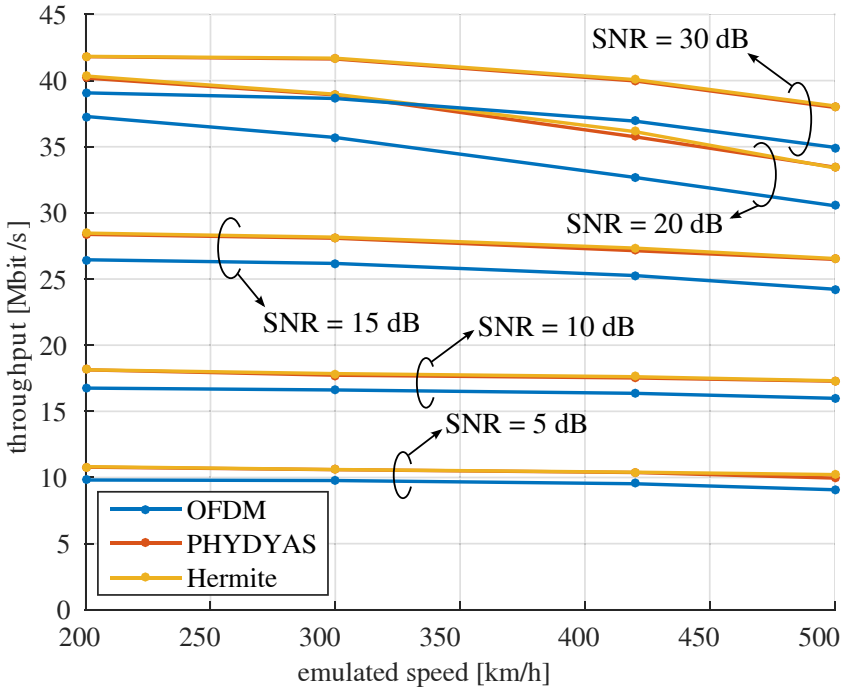

Figure 6.28: Throughput versus emulated speed for different SNR values.

due to the absence of a cyclic prefix[1] and the better performance of FBMC for doubly dispersive

[1]Considering a bit rate b in FBMC, the corresponding bit rate of OFDM would be $bT_s/(T_s + T_{cp})$, being T_s the OFDM symbol period and T_{cp} the cyclic prefix duration.

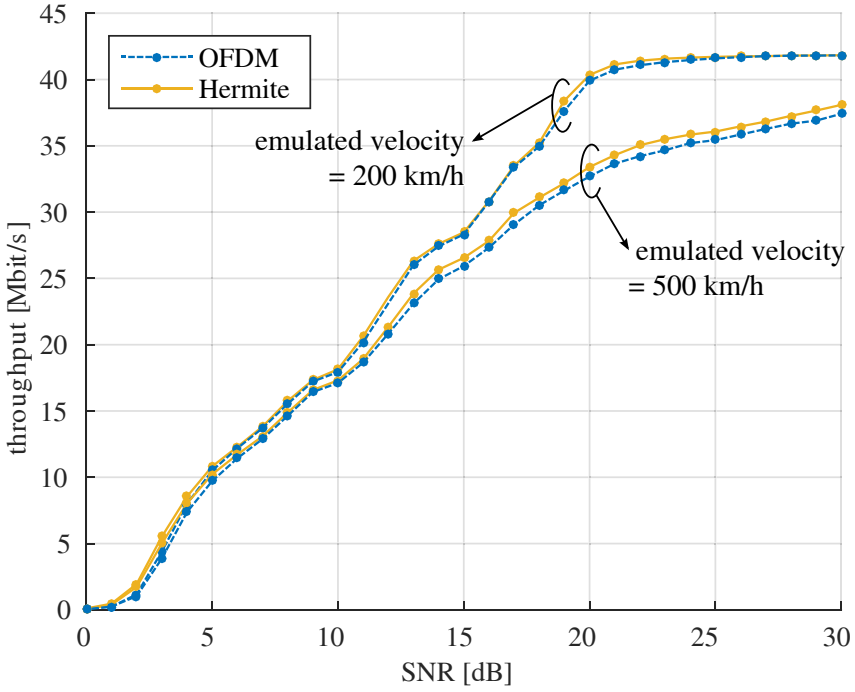

Figure 6.29: Throughput versus SNR for the minimum and maximum emulated speeds. The OFDM results are scaled to compensate for the spectral efficiency loss due to the CP.

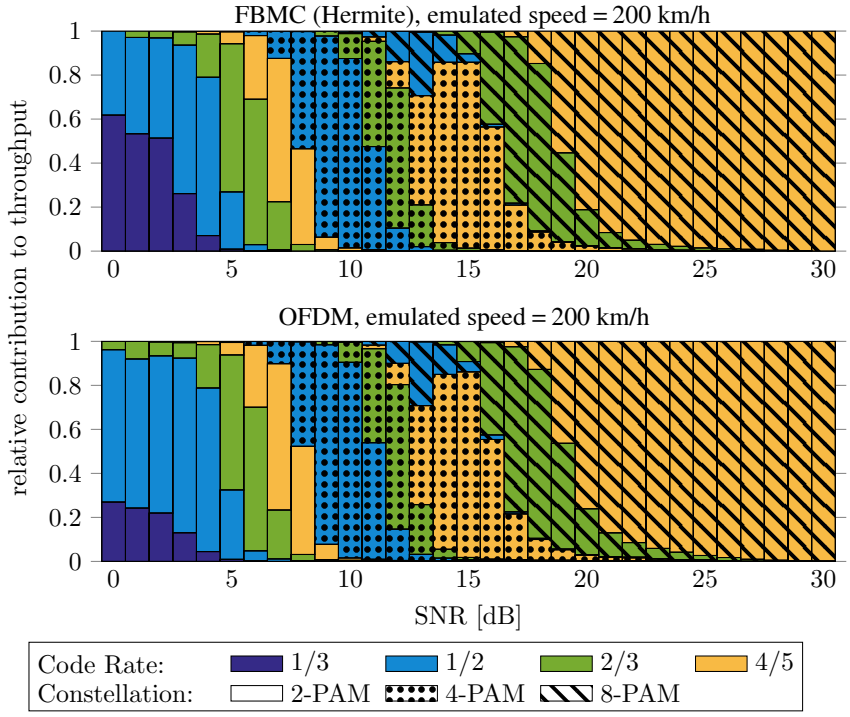

Figure 6.30: Relative contribution per constellation and code rate to the total throughput for all the considered SNR values for OFDM and FBMC (Hermite case) and the minimum speed considered.

channels. As stated before, BER results for OFDM and FBMC are very similar, hence we can expect that the main factor for the difference in terms of throughput is the absence of a cyclic

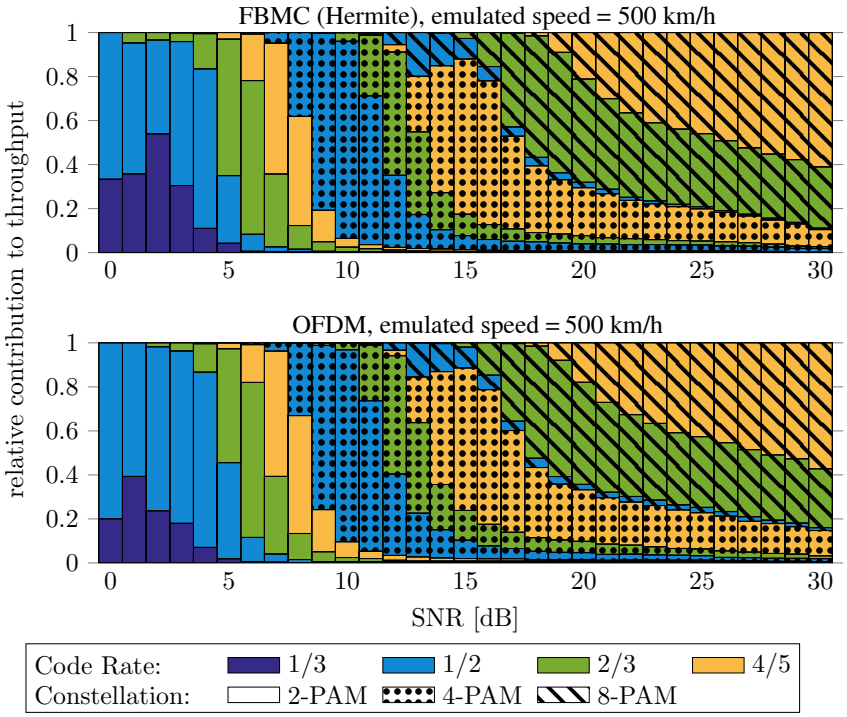

Figure 6.31: Relative contribution per constellation and code rate to the total throughput for all the considered SNR values for OFDM and FBMC (Hermite case) and the maximum speed considered.

prefix in FBMC. The performance for all the speed values is shown in Fig. 6.28.

Fig. 6.29 compares the throughput for the Hermite and the OFDM cases, but compensating the latter for the spectral efficiency loss due to the cyclic prefix (multiplying by $(T_s+T_{cp})/T_s$, as shown in Footnote 1). We can see that the FBMC and OFDM curves overlap for the minimum speed. For the maximum speed, when the SNR value is high and thus the ICI is the dominant effect, FBMC slightly outperforms OFDM. In view of Fig. 6.29, although FBMC with the Hermite pulse is spectrally more efficient than OFDM, once the loss due to the cyclic prefix is removed, their throughput performance is very similar in a scenario with a high time selectivity (200 and 500 km/h for a carrier frequency of 2.6 GHz).

Finally, Figs. 6.30 and 6.31 show the relative contribution per constellation size and code rate to the total throughput for the OFDM and FBMC (Hermite pulse) cases, when the receiver speed is 200 km/h and 500 km/h, respectively. The results for FBMC with the PHYDYAS pulse are similar to those with the Hermite pulse. It can be seen that the 4-QAM (OFDM case) and the 2-PAM (FBMC case) constellations contribute the most to the total throughput for SNR values lower than 8 dB, regardless of the receiver speed. For the minimum speed, the 16-QAM (OFDM case) and the 4-PAM (FBMC case) constellations contribute the most to the total throughput for SNR values between 9 and 16 dB, whereas for higher SNR values the 64-QAM (OFDM case) and the 8-PAM (FBMC case) constellations are the best choice. For the maximum speed, higher SNR values are required for the 64-QAM (OFDM case) and the 8-PAM (FBMC case) constellations to be the main contributors to the throughput. However,

unlike in the minimum speed case, the 16-QAM (OFDM case) and the 4-PAM (FBMC case) constellations significantly contribute to the throughput regardless of the SNR. According to the results shown, the differences between the OFDM and the FBMC cases are negligible.

6.5 Conclusions

This chapter presented an exhaustive study on the performance of FBMC (considering Hermite and PHYDYAS prototype pulses) with respect to OFDM in quasi-static scenarios as well as in high-speed environments. All the analyses are based both on computer simulations considering a plethora of channel models and on over-the-air transmissions using the GTEC Testbed at the University of A Coruña.

With respect to the quasi-static scenarios, a similar performance was obtained for the three modulation schemes considered: OFDM, FBMC with the PHYDYAS prototype filter, and FBMC with the Hermite prototype filter. This result was confirmed both by simulations and over-the-air transmissions. Summarizing, FBMC did not exhibit any performance loss with respect to OFDM in the considered measurements and simulation scenarios.

Making use of a previously developed methodology for evaluating the performance of multicarrier transmissions in real-world scenarios affected by large Doppler spreads while conducting measurements at low speeds, we assessed the vehicle-to-infrastructure (V2I) downlink performance for FBMC (with Hermite and PHYDYAS prototype pulses) and OFDM by means of car measurements. More specifically, we evaluated the BER (coded and uncoded) and the throughput obtained by using the aforementioned modulation techniques. The emulated speeds range from 200 to 500 km/h being typical in high-speed train scenarios.

The obtained results show, on the one hand, that the main performance degradation sources are the link SNR and the speed of the mobile receiver. In terms of BER, it was shown that for high speeds (exceeding 300 km/h), FBMC is a better choice than OFDM when well localized prototype filters, both in time and in frequency, are employed, e.g. the Hermite pulse. However, for velocities smaller than 300 km/h the performance difference is not significant.

It was shown that the throughput of FBMC is higher due to the improved spectral efficiency, although its theoretically better suitability than OFDM for doubly dispersive channels was not appreciated, neither in terms of BER nor throughput. While for low speeds ($\lesssim 200$ km/h) and high SNR values ($\gtrsim 20$ dB) it is possible to achieve the maximum throughput by using 8-PAM (FBMC case) or 64-QAM (OFDM case), low-order constellations are required to decrease the coded BER, hence reducing the number of retransmissions, which results in lower delays, as required by critical services such as train control systems.

On the other hand, a reliable and low-latency link at very high speeds demands for small-size constellations such as 4-QAM. Adaptive modulation and coding schemes in these scenarios are hence less attractive since a potential throughput increment when increasing the constellation size leads to a high BER with a very high probability, therefore requiring more retransmissions

and impacting on both the delay and the jitter of the link.

Finally, recall that along this chapter we limited to the consideration of an isolated point-to-point link which does not exploit all the potential advantages of FBMC, mainly their better bandwidth efficiency which is very important, for example, for the co-existence between current communication systems (such as Global System for Mobile Communications (GSM) or GSM for Railways (GSM-R)) and the new broadband wireless systems, as well as to avoid multiple-access interference in the uplink. The obtained results confirm that FBMC advantages can be exploited in high-speed environments without *a priori* performance losses.

Chapter VII

Air-to-Ground Communications with Lightweight Remotely Piloted Aircrafts

The so-called remotely piloted aircrafts (RPAs) are becoming very popular for general-purpose civil and commercial applications such as transportation, video surveillance, search, and rescue operations among others. In this chapter we assess the performance of orthogonal frequency-division multiplexing (OFDM) and filter bank multicarrier (FBMC) signals —in terms of coded and uncoded bit error rate (BER) and throughput— in the downlink of two air-to-ground (A2G) suburban scenarios at the carrier frequency of 2.5 GHz, and considering quasi-omnidirectional as well as sector transmit antennas at the ground station. The resulting wireless links are characterized in terms of the signal-to-noise ratio (SNR) observed at the receiver (RPA). The influence of the RPA flight height and the transmit antenna type employed at the base station on the system performance is also studied.

This chapter is structured as follows. Section 7.1 introduces the chapter. Section 7.2 describes the measurement environment, the equipment used for the measurements and the OFDM/FBMC transmit signals. Section 7.3 describes in detail the results obtained when analyzing the acquired OFDM/FBMC frames. Finally, Section 7.4 summarizes the main findings of this chapter.

7.1 Introduction

Historically, remotely piloted aircrafts (RPAs) were devoted to military operations in harsh environments [VV14] mainly due to their size, weight, cost, and the skills required to fly them. However, in the last few years, most of the aforementioned inconveniences were overcome, making RPAs a very attractive solution for general-purpose applications such as search and rescue operations, transportation, weather monitoring or surveillance [TRA13b]. Within the field of wireless communications, RPAs have been proposed as base station relays in crowded environments and also to rapidly deploy networks in case of a disaster, which is one of the key

scenarios considered for fifth generation (5G) systems [ZZL16].

RPAs are limited by law in many countries to visual line-of-sight (LoS) flights and with a maximum fly height between 100 m and 150 m [GRO+13]. Under these conditions, standard cellular networks can be used to provide RPA communications, and the feasibility of serving RPAs with general-purpose Long Term Evolution (LTE) network deployments has been recognized as a priority by the 3rd Generation Partnership Project (3GPP) [IE17b; IE17a].

The link between an RPA and a ground base station can be used for general-purpose data traffic applications (e.g., real-time video transmission) and to support control and non-payload communications (CNPC) [GRO+13; MU17; LN17; TRA13a]. Different from classical air-to-ground (A2G) links, no dedicated highly-elevated antennas with high transmit power are considered, whereas the requirements in terms of throughput can be much more stringent. In order to study this link, we carried out a measurement campaign transmitting orthogonal frequency-division multiplexing (OFDM) and filter bank multicarrier (FBMC) signals. High-level figures of merit such as the coded and uncoded bit error rate (BER) were evaluated as well as the throughput and the signal-to-noise ratio (SNR).

During the measurement campaign we performed several flights with an RPA varying different parameters. On the one hand, horizontal flights at 8 different height values, ranging from 15 m to 105 m, were performed for two different suburban scenarios with different obstacle density. On the other hand, vertical flights, from 20 m to 100 m, were also considered for different horizontal distances to the transmitter. In order to study the effect of the radiation pattern of the transmit antenna, two antennas were considered: omnidirectional and a typical sector base station one, both at the carrier frequency of 2.5 GHz.

7.2 Measurement Environment and Procedure

This section describes a measurement campaign to evaluate A2G communications for lightweight RPAs at low fly heights, funded by ZTE Corporation[1] (Shenzhen, China). The measurement campaign was performed at the Jiading Campus of the Tongji University (Shanghai, China).

Section 7.2.1 introduces the employed measurement equipment, including the air part (loaded in an RPA) as well as the ground one (see Fig. 7.1). The measurement scenarios as well as the flight routes are detailed in Section 7.2.2. Finally, Section 7.2.3 provides the details of the transmit signals used for the evaluations.

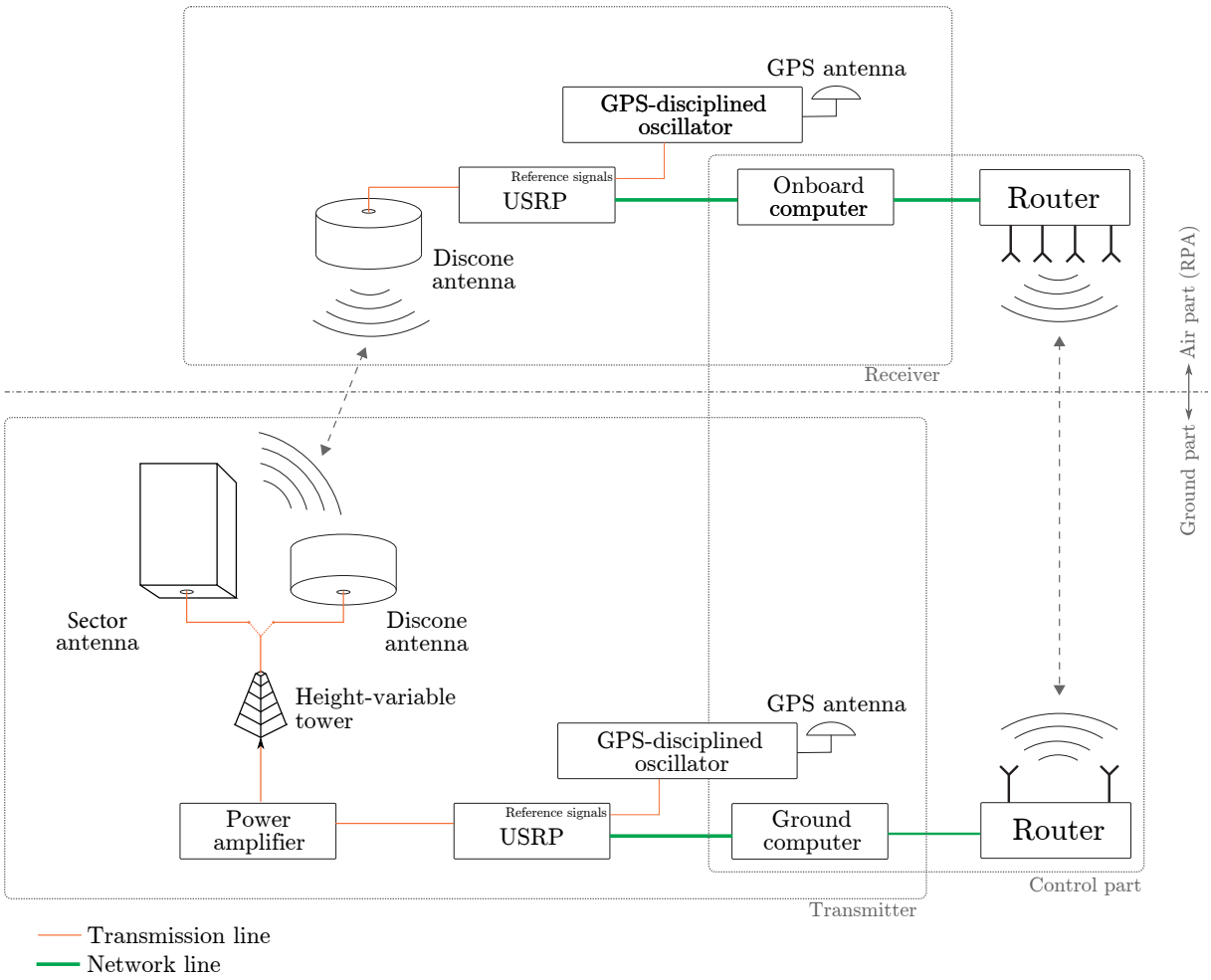

Figure 7.1: Block diagram of the measurement setup.

7.2.1 Measurement Equipment

Fig. 7.1 illustrates the measurement equipment used for recording the downlink signals and consists of two parts, i.e., the air part and the ground part. The air part was loaded on the RPA, as shown in Fig. 7.2, and contains the following components: a quasi-omnidirectional packaged discone antenna that works in the 1-8 GHz frequency band, a Universal Software Radio Peripheral (USRP™) N-210 device, a Global Positioning System (GPS)-disciplined oscillator that generates accurate 10 MHz as well as 1 pulse per second (PPS) references to be provided to the USRP™, a small computer base unit that controls the USRP™ and stores the received data, and a commercial Wi-Fi router. The ground part contains another USRP™ and a GPS-disciplined oscillator, a power amplifier and two antennas (see Fig. 7.3a), being one of them the same model mounted at the receiver and the other a typical sector antenna (see Fig. 7.3b). Both antennas are mounted at a height-variable tower, as shown in Fig. 7.3c, being only one used at a time. Finally, another laptop is connected to the ground USRP™ to act as

[1]We explicitly thank Dr. Li Tian, Dr. Jianwu Do and Nan Zhang for their advises and comments on the results, as well as for allowing us to include them in this thesis.

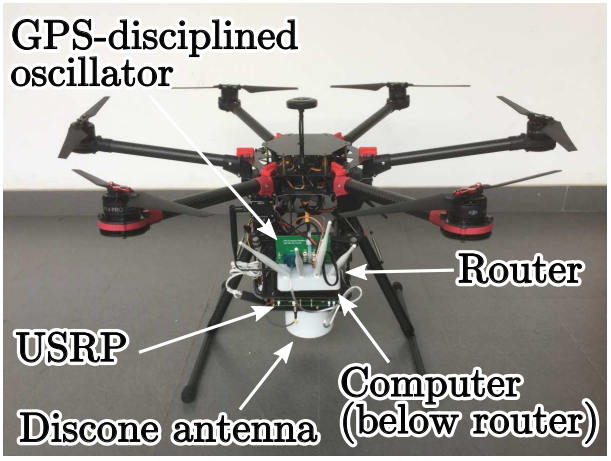

Figure 7.2: Picture of the air part of the measurement equipment (receiver).

(a) **(b)** **(c)**

Figure 7.3: Ground part of the measurement devices (transmitter). (a) Equipments mounted on top of the variable-height tower; (b) transmit antennas; and (c) picture of the variable-height tower.

a transmitter. Furthermore, by using another commercial Wi-Fi router, a local area network is established with the computer on the RPA allowing for controlling the onboard equipment remotely. It is worth noting that the routers worked in the 2.4 GHz frequency band, hence avoiding interferences to the measurements. Finally, another computer is dedicated to control the RPA.

7.2.2 Measurement Scenarios and Flight Routes

This section details the considered measurement scenarios and flying routes. Two different kinds of flights were considered, namely the horizontal ones and the vertical ones. While Section 7.2.2 describes the horizontal case into detail, Section 7.2.2 considers the vertical

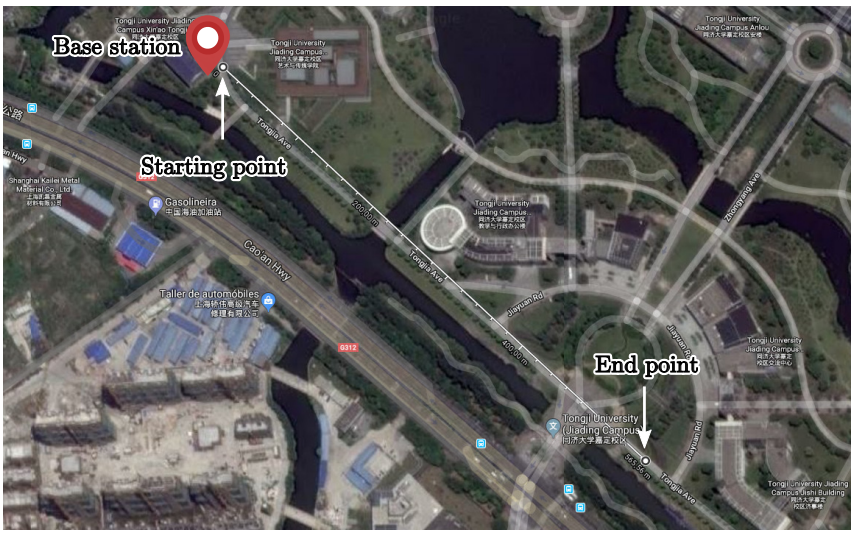

Figure 7.4: Measurement Scenario I. The transmitter location is marked with a red dot. The trajectory of the UAV is also indicated.

flights.

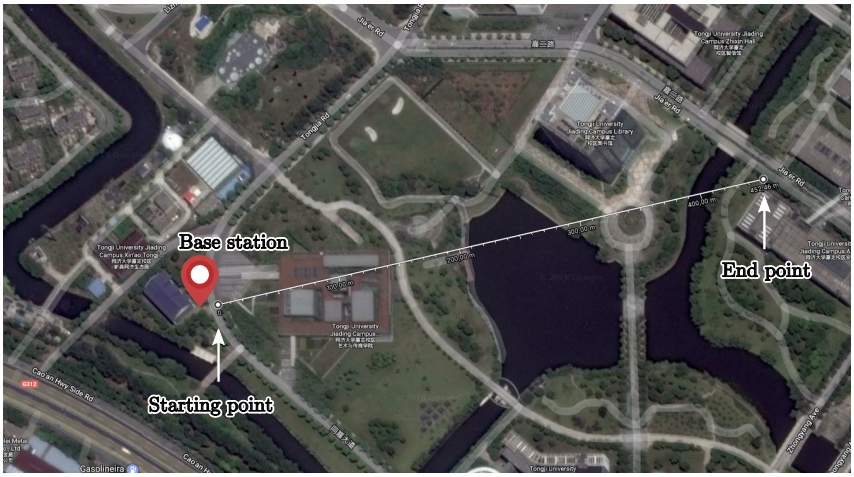

Figure 7.5: Measurement Scenario II. The transmitter location is marked with a red dot. The trajectory of the UAV is also indicated.

Horizontal flights

The measurement campaign was conducted in a suburban environment in Jiading Campus, Tongji University, Shanghai. Two scenarios were considered, referred to as Scenario I and Scenario II, imaged in Figs. 7.4 and 7.5, respectively. The figures show the position of the

Figure 7.6: Picture of the UAV close to the landing point.

Flight number	Height flight for outward trip [m]	Height flight for return trip [m]
1	15	25
2	35	45
3	60	75
4	90	105

Table 7.1: Height flight values for the different horizontal flights considered.

transmitter[2], as well as the starting and end points of each route[3]. The Scenario I consists of a straight flight along a road without obstacles, being the total length about $560\,\text{m}$. For the Scenario II, a straight flight in which the RPA flies between several buildings is considered, being its length about $450\,\text{m}$. Fig. 7.6 shows a picture of the RPA close to the starting point of the flight trajectories.

For each flight scenario, several horizontal flights are considered (see Table 7.1) and, for each flight, two different height values were considered, one for the outward trip and another one for the return trip. Given that we employ two transmit antenna types (one at a time), each flight is repeated twice, once per antenna. The obtained results are used to decide about the feasibility of serving aerial vehicles using LTE network deployments with base station antennas targeting terrestrial coverage.

[2]Coordinates of the transmitter in (lat, long) format are: $(31.2873872°, 121.2040907°)$.

[3]Coordinates of the starting point and end point in (lat, long) format are: $(31.287433°, 121.204179°)$ and $(31.284102°, 121.208412°)$ for the Scenario I; and $(31.287433°, 121.204179°)$ and $(31.288310°, 121.208793°)$ for the Scenario II.

Flight number	Distance to transmitter [m]
1	25
2	50
3	100

Table 7.2: Distance values to the transmitter for the different vertical flights considered.

Vertical Flights

Vertical flights were also considered. In this case, the flights take place at three different distances from the transmitter over the route for the so-called Scenario I. Table 7.2 shows such distance values for the three considered flights. Similarly to the case of the horizontal flights, two transmit antennas are employed, one at a time.

parameter	**value**
sampling frequency	15.36 MSamples/s (upsampled to 25 MSamples/s before being transmitted)
FFT size	1024 points
used subcarriers	600 (excluding DC)
subcarrier spacing	15 kHz
effective used bandwidth	9 MHz
CP length (OFDM)	72 samples
pilot spacing	frequency: 6 subcarriers time: 8 symbols (FBMC), 4 (OFDM)
symbols per block	8 (FBMC), 4 (OFDM)

Table 7.3: Parameters of the OFDM/FBMC transmit frames.

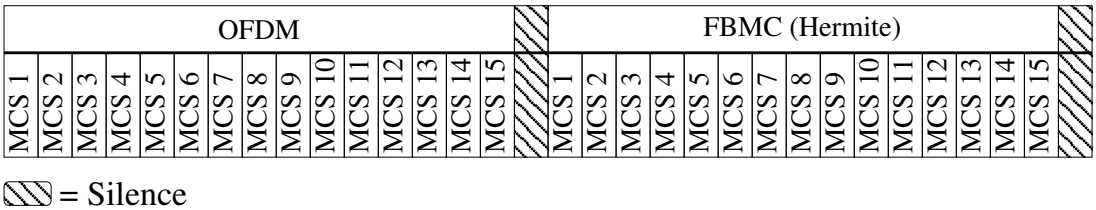

Figure 7.7: Frame structure considered for the measurements. The different blocks with the different modulation and coding schemes (MCSs) are shown (see Table 7.4).

7.2.3 Transmit Signals

The transmit power and the gain values at the transmitter and receiver sites are calibrated to prevent saturation effects and to avoid using automatic gain control (AGC) at the receiver while,

MCS index	constellation (OFDM)	constellation (FBMC)	code rate $\times 1024$	efficiency
1	4-QAM	2-PAM	78	0.1523
2	4-QAM	2-PAM	120	0.2344
3	4-QAM	2-PAM	193	0.3770
4	4-QAM	2-PAM	308	0.6016
5	4-QAM	2-PAM	449	0.8770
6	4-QAM	2-PAM	602	1.1758
7	16-QAM	4-PAM	378	1.4766
8	16-QAM	4-PAM	490	1.9141
9	16-QAM	4-PAM	616	2.4063
10	64-QAM	8-PAM	466	2.7305
11	64-QAM	8-PAM	567	3.3223
12	64-QAM	8-PAM	666	3.9023
13	64-QAM	8-PAM	772	4.5234
14	64-QAM	8-PAM	873	5.1152
15	64-QAM	8-PAM	948	5.5547

Table 7.4: Details of the MCSs used for the OFDM/FBMC signals.

at the same time, maximizing its dynamic range.

Both OFDM and FBMC (with the Hermite prototype filter [HB97]) signals are generated according to the parameters specified in Table 7.3 and employing the LTE channel coding scheme, which corresponds to the configuration of the 10 MHz downlink LTE profile. Next, they are cyclically transmitted in a frame (see Fig. 7.7) divided into blocks, each one with a different MCS value according to Table 7.4, which correspond to those from the LTE standard and specified in [3GPc, Table 7.2.3-1]. Note also that the frame includes some silence periods which allows us to accurately estimate the mean SNR per data subcarrier following the approach detailed in Section 3.3.3 (see [ROD16, Section 4.5.2] and [ROD+15a]).

The GTEC 5G Simulator is used for generating and processing all the signals and to estimate the considered figures of merit: SNR, coded and uncoded BER and throughput (following the approach described in Section 6.4.3).

7.3 OFDM/FBMC Measurements Results

In this section, the results obtained when analyzing the acquired OFDM/FBMC frames are described in detail and some representative figures are provided. Section 7.3.1 shows a summary of the results when OFDM frames are considered and Section 7.3.2 compares them with those obtained with FBMC. Section 7.3.3 analyzes the effect of the flight height for the horizontal flights, whereas Section 7.3.4 focuses on the vertical flights.

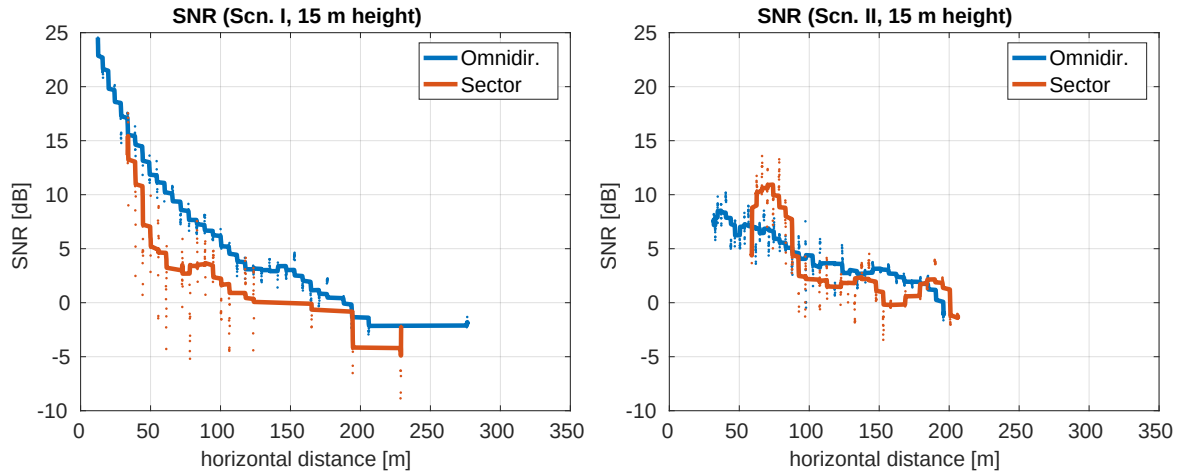

(a) Scenario I, 15 m height

(b) Scenario II, 15 m height

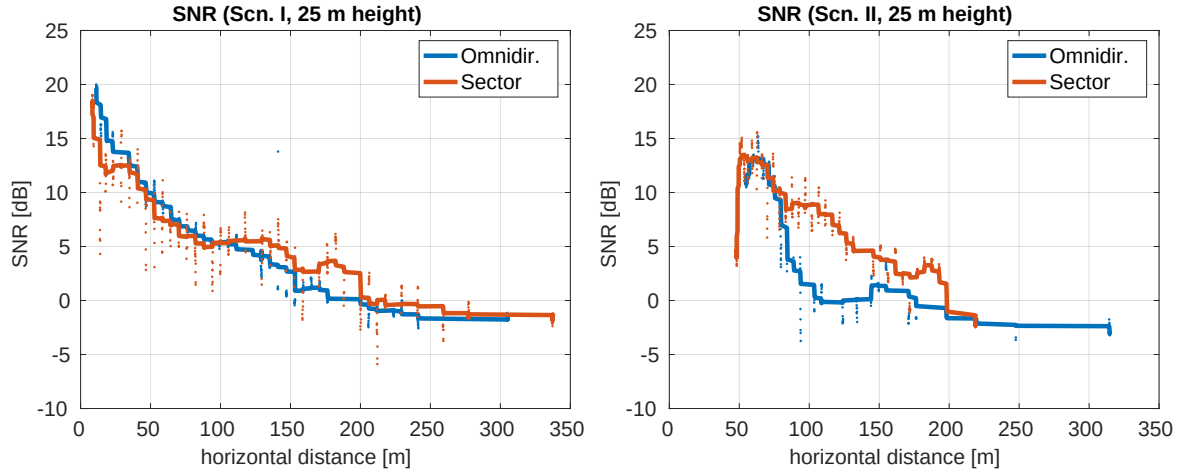

(c) Scenario I, 25 m height

(d) Scenario II, 25 m height

Figure 7.8: SNR results for horizontal flights at the heights of 15 m and 25 m for both scenarios.

7.3.1 Results for OFDM Signals

Fig. 7.8 shows the SNR results for scenarios I and II (see Section 7.2.2) when transmitting an OFDM signal for the first horizontal flight (which corresponds to a height of 15 m for the outward trip and 25 m for the return trip). The blue dots correspond to the case in which the discone antenna is used, whereas red ones correspond to the usage of the sector antenna. In all cases, each dot represents the individual mean SNR value for a single OFDM frame. For readability purposes, a curve is fitted by applying a moving average.

The X-axes in Fig. 7.8 represent the horizontal distance to the transmit antenna (i.e., the flight height is not taken into account for the distance calculation). It is worth noting that not all the curves have the same range with respect to the X-axis since we only analyze those frames that could be detected at the receiver. Different antenna configurations, measurement scenarios and flying heights result in different SNR values with respect to the distance, preventing some frames to be synchronized.

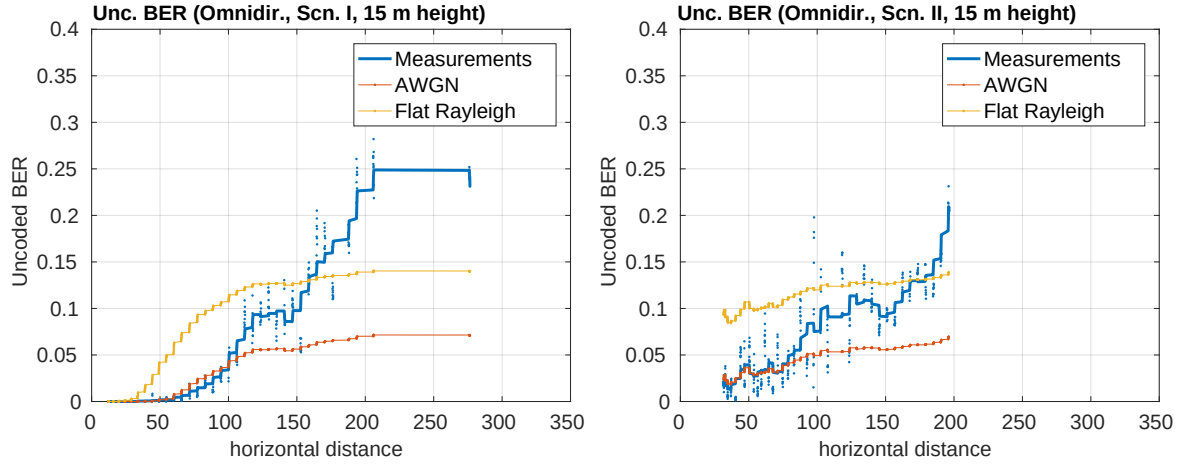

(a) Scenario I, 15 m height.

(b) Scenario II, 15 m height.

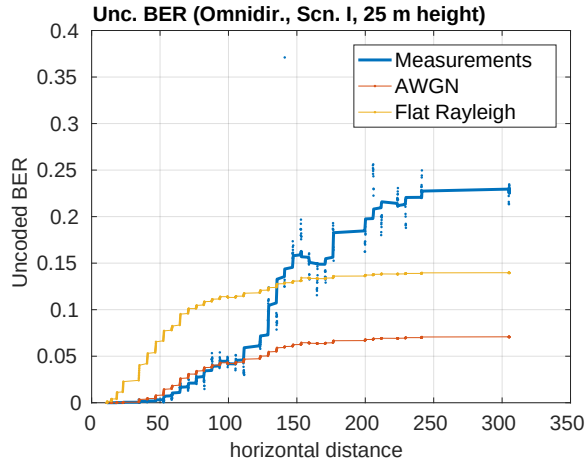

(c) Scenario I, 25 m height.

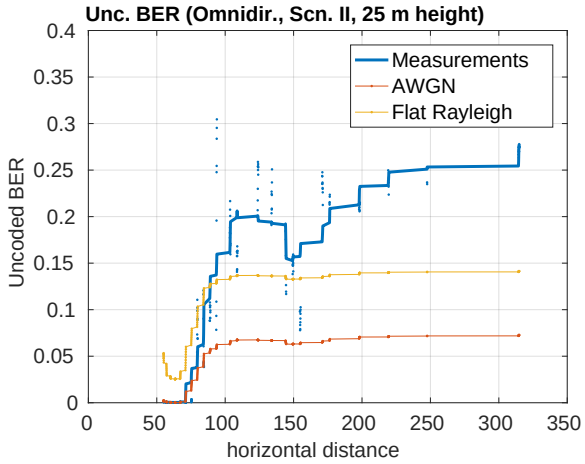

(d) Scenario II, 25 m height.

Figure 7.9: Uncoded BER results (4-QAM constellation) for horizontal flights at the heights of 15 m and 25 m for both scenarios. The omnidirectional antenna is considered at the transmitter.

By comparing Figs. 7.8a and 7.8b with Figs. 7.8c and 7.8d, respectively, we conclude that, for the 15 m height case, the omnidirectional antenna outperforms the sector antenna. However, when the height is increased, the opposite situation occurs. This is mainly because of the radiation pattern of the receive (onboard) antenna. When the RPA flies at a height of 15 m and the sector (directive) antenna is used at the transmitter, both transmit and receive antennas are at about the same height but, while the transmit antenna is vertically oriented, the receive one faces down and hence the radiation pattern of the receive antenna affects negatively. When the RPA flies at a height of 25 m, the receive antenna is 10 m above the transmit one and in this case the SNR is larger than for the case of a height of 15 m. Finally, it can be seen that for the points close to the transmitter, no frames can be synchronized and therefore no SNR values can be estimated.

Fig. 7.9 shows the uncoded BER results when transmitting OFDM for the first horizontal flight considered and employing the omnidirectional transmit antenna. Along with the uncoded

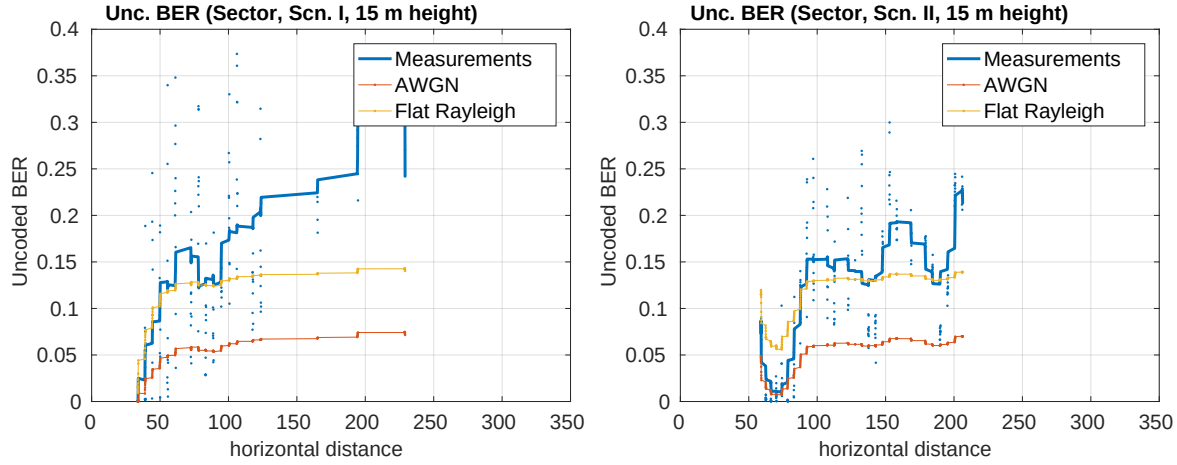

(a) Scenario I, 15 m height.

(b) Scenario II, 15 m height.

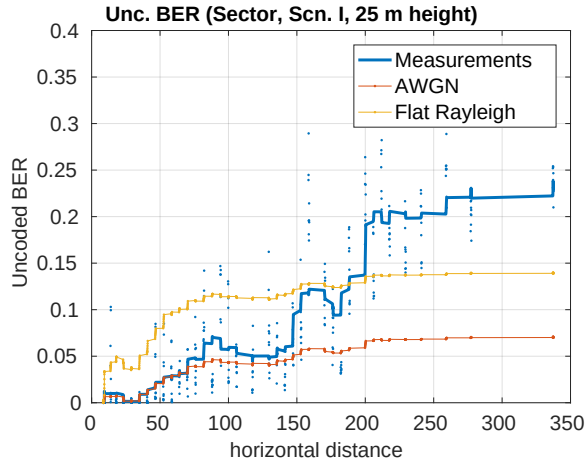

(c) Scenario I, 25 m height.

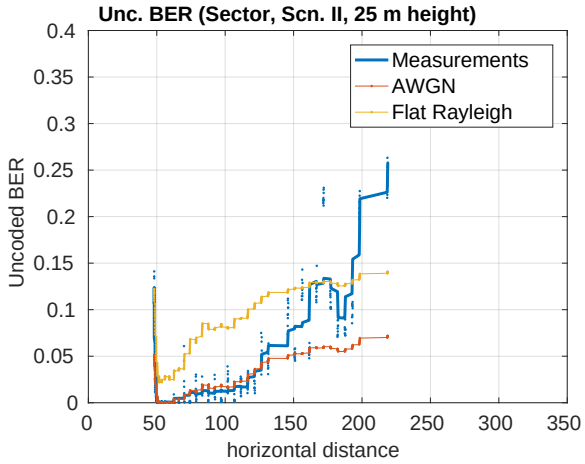

(d) Scenario II, 25 m height.

Figure 7.10: Uncoded BER results (4-QAM constellation) for horizontal flights at the heights of 15 m and 25 m for both scenarios. The sector (directive) antenna is considered at the transmitter.

BER results, two analytical curves are provided: the red one corresponds to the analytical BER for the additive white gaussian noise (AWGN) channel, whereas the yellow one corresponds to a flat Rayleigh fading channel [MOL12]. Notice that the resolution in terms of BER evaluations is limited by the number of frames being processed, since a single flight per configuration (antenna, route, and height value) could be performed. For the points close to the base station (up to 75 m or 100 m), the AWGN case represents a very good approximation to the measured results. When the distance becomes larger, the BER results are much higher than the ones for the analytical Rayleigh fading case. It can be seen that the BER increase can be quite abrupt in some cases (between about 75 m and 125 m away from the transmit antenna) and that the trend of the curves is quite dependent on the measurement scenario.

Fig. 7.10 shows the same results when the sector antenna is employed. No significant differences can be appreciated for the considered height values. The analytical AWGN curve still represents a good approximation for distances close to the transmitter. For any of the

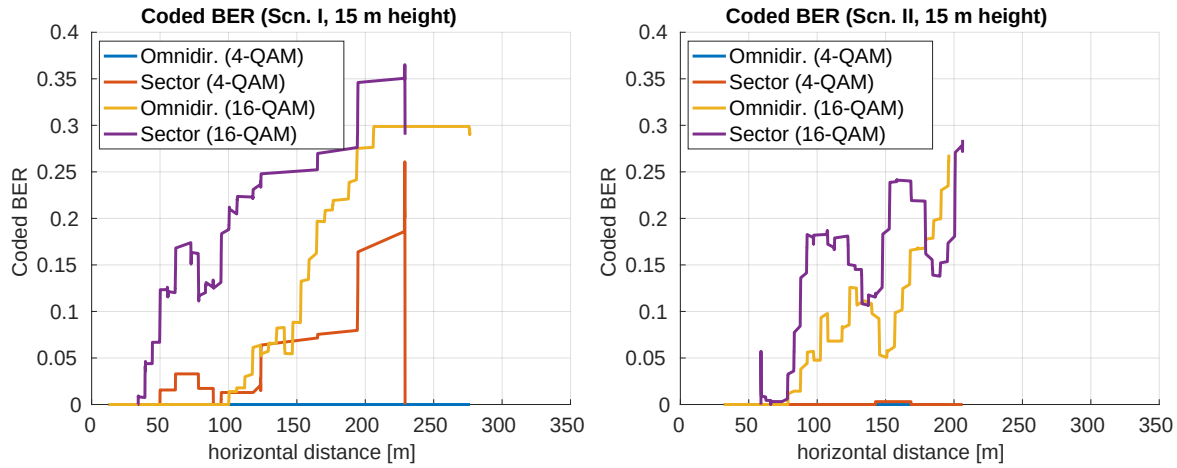

(a) Scenario I, 15 m height.

(b) Scenario II, 15 m height.

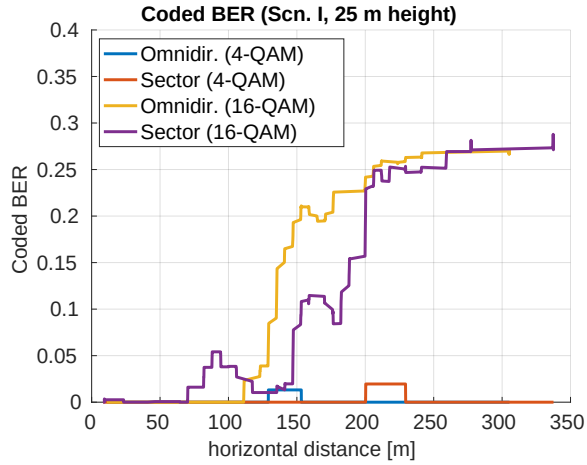

(c) Scenario I, 25 m height.

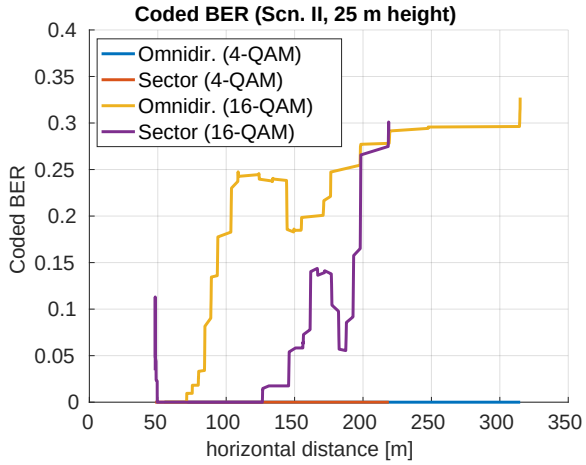

(d) Scenario II, 25 m height.

Figure 7.11: Coded BER results (4-QAM and 16-QAM constellations) for horizontal flights at the heights of 15 m and 25 m for both scenarios. The sector (directive) antenna is employed at the transmitter.

considered antenna configurations, the results show that the BER dramatically increases when the distance to the base station exceeds 200 m.

Fig. 7.11 shows the coded BER results for both scenarios and both transmit antenna types when transmitting an OFDM signal for the first horizontal flight considered. Two MCS values are considered: 4-QAM with a coding rate equal to 0.0762 and 16-QAM with coding rate 0.3691. Interestingly, the coded BER for the 4-QAM constellation in the Scenario II (see Figs. 7.11b and 7.11d) is almost zero all the time, whereas this is not true for the Scenario I and the sector antenna (see Figs. 7.11a and 7.11c). This is due to the low SNR values of the frames, as shown in Figs. 7.8a and 7.8c. For the case of the 16-QAM constellation, the BER increases, as expected. These results show that, even for not so long distances from the receiver, very low MCS values should be selected in order to have a highly-reliable communication with a low latency (e.g., for control purposes).

Fig. 7.12 shows the throughput results for both scenarios and both transmit antenna types

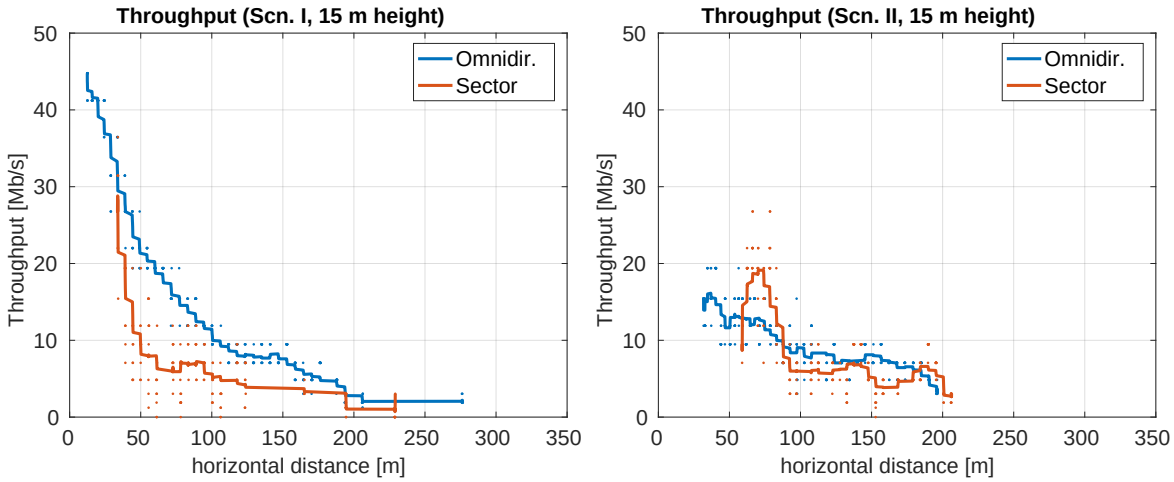

(a) Scenario I, 15 m height.

(b) Scenario II, 15 m height.

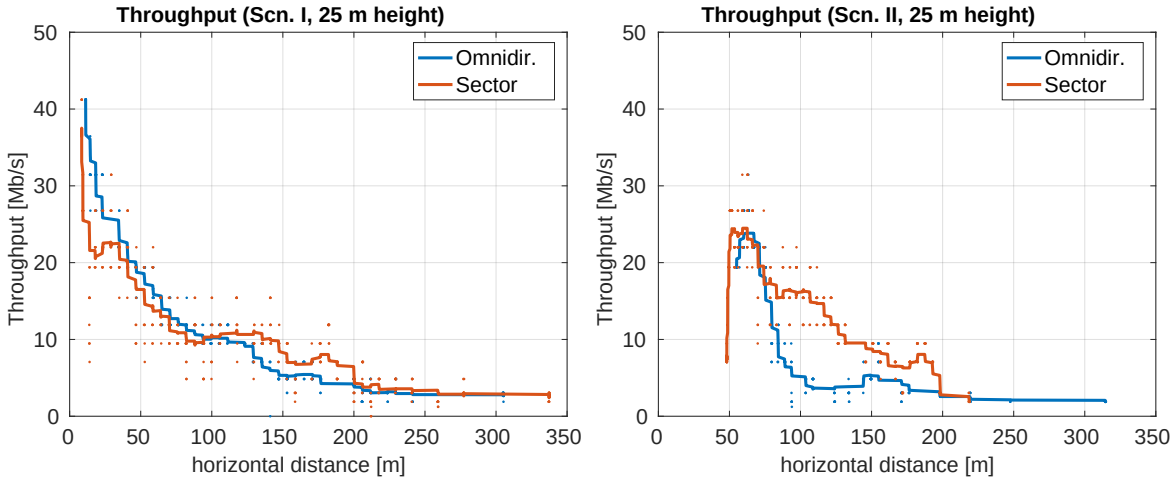

(c) Scenario I, 25 m height.

(d) Scenario II, 25 m height.

Figure 7.12: Throughput results for horizontal flights at the heights of 15 m and 25 m for both scenarios and antenna types.

when transmitting OFDM for the first horizontal flight considered. By comparing Fig. 7.12 and Fig. 7.8, it can be noticed that the trends of the throughput curves follow the ones corresponding to the SNR. This way we can assume that an almost direct relationship between the throughput and the SNR can be established. In order words, we could accurately estimate the throughput by evaluating the SNR at the receiver. It can be seen that, according to the SNR results, the throughput for the Scenario II greatly reduces with respect to that of the Scenario I.

7.3.2 Results for FBMC Signals

Fig. 7.13 shows the uncoded BER results for scenarios I and II and the omnidirectional transmit antenna when transmitting an OFDM signal as well as an FBMC one for the first horizontal flight. It can be seen that the BER curves for OFDM and FBMC almost overlap, showing that FBMC could be used with no performance loss regardless of the scenario considered as well as

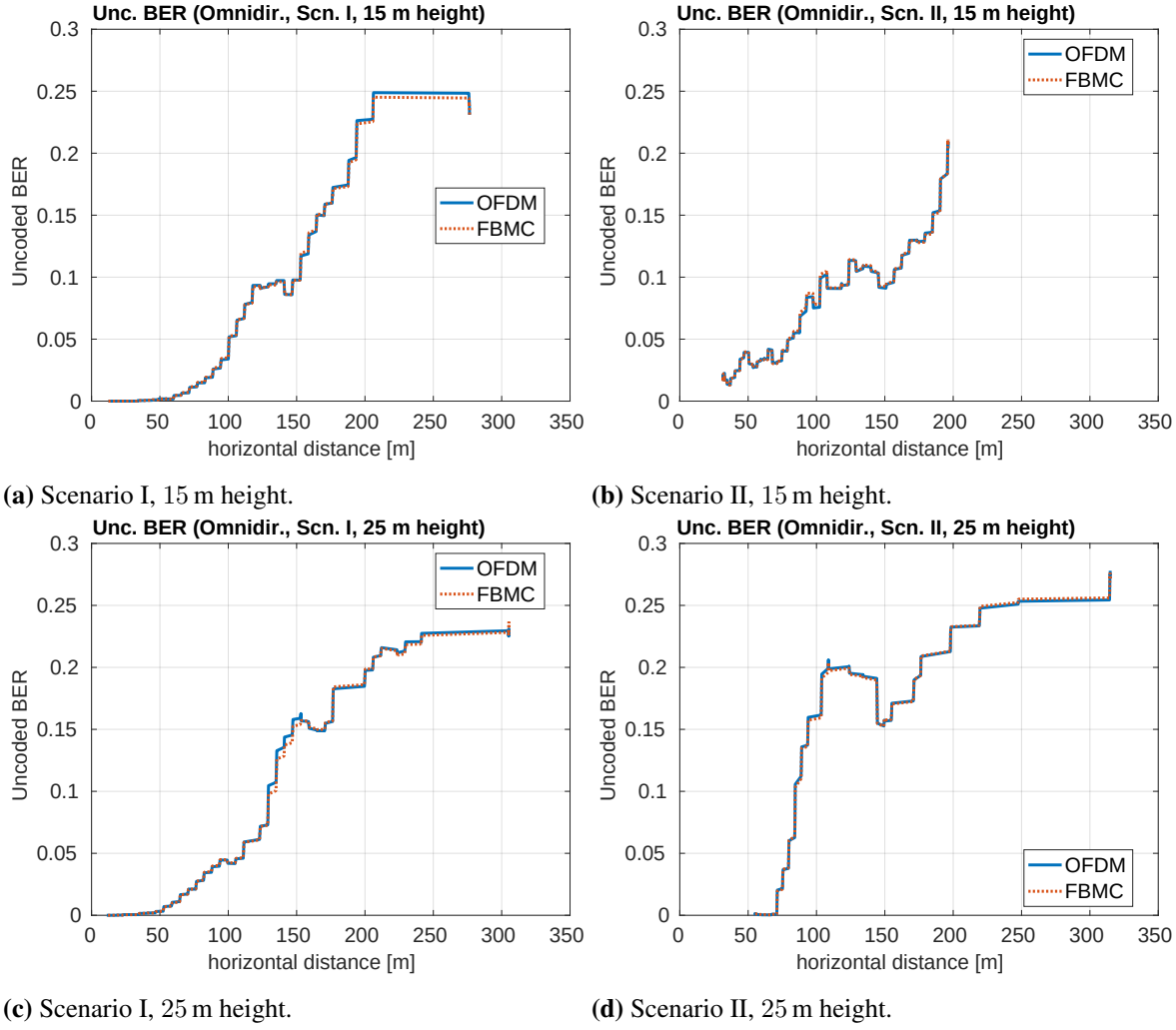

(a) Scenario I, 15 m height.

(b) Scenario II, 15 m height.

(c) Scenario I, 25 m height.

(d) Scenario II, 25 m height.

Figure 7.13: Uncoded BER results for OFDM and FBMC signals (4-QAM and 2-PAM constellations, respectively) for horizontal flights at the heights of 15 m and 25 m for both scenarios. The omnidirectional antenna is employed at the transmitter.

the height value.

Fig. 7.14 shows the same results as Fig. 7.13 but in terms of throughput. Again, it can be seen that the throughput difference between FBMC andOFDM is almost negligible. The slight gain in throughput is due to the fact that FBMC is spectrally more efficient since it does not need the use of a cyclic prefix. However, this could lead to the wrong conclusion that there is almost no gain by using FBMC with respect to OFDM. It has to be also considered that the same number of subcarriers is used in both cases. However, if we take a look at the frequency spectrum of both signals (see Fig. 7.15), it can be seen that OFDM has much larger side lobes. Hence, for a common spectral mask at the transmitter, we can increase the number of subcarriers used in FBMC with respect to OFDM.

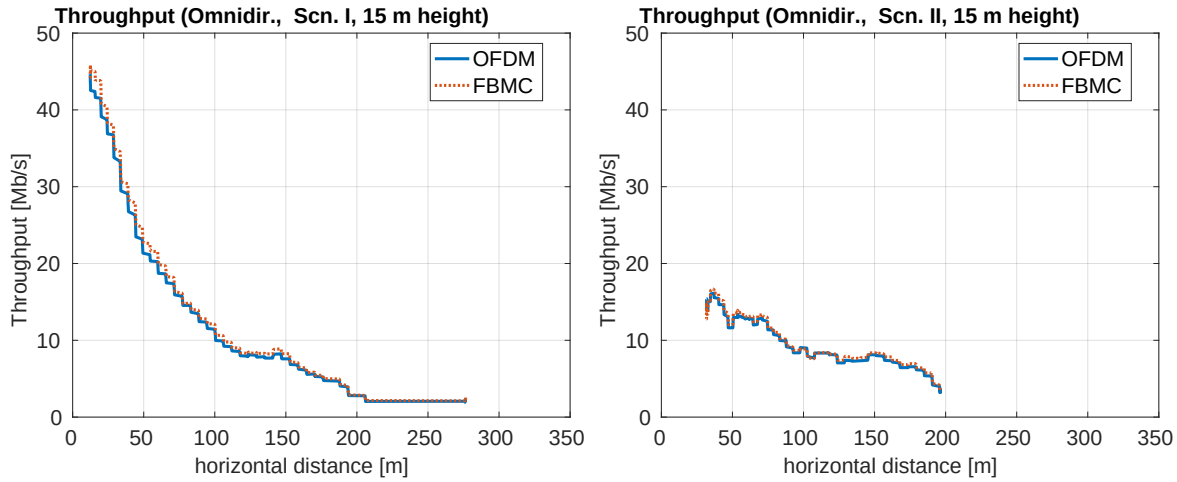

(a) Scenario I, LoS, 15 m height.

(b) Scenario II, NLoS, 15 m height.

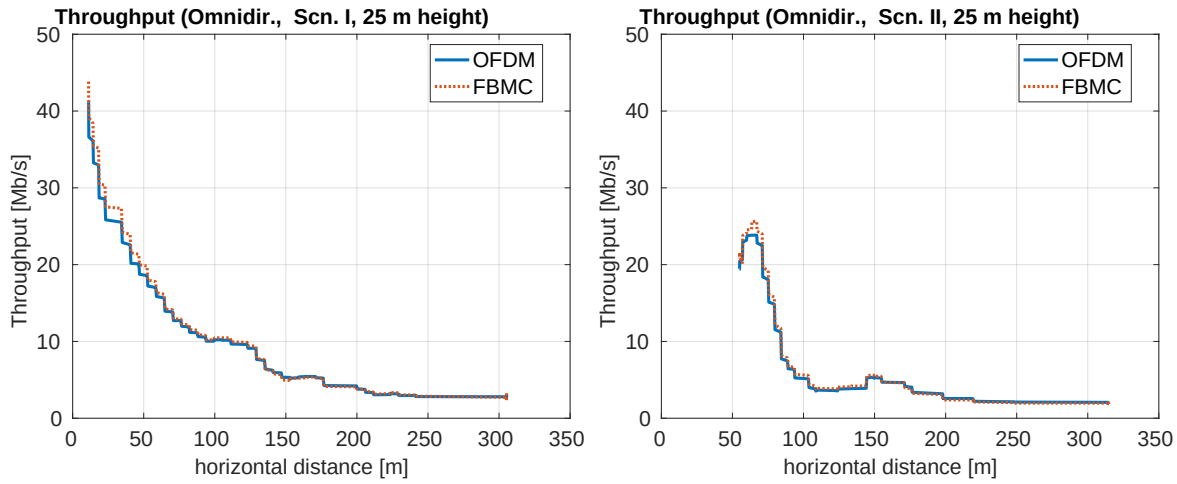

(c) Scenario I, LoS, 25 m height.

(d) Scenario II, NLoS, 25 m height.

Figure 7.14: Throughput results for OFDM and FBMC signals for horizontal flights at the heights of 15 m and 25 m for both scenarios. The omnidirectional antenna is employed at the transmitter.

7.3.3 Effects of the Flight Height

Fig. 7.16 shows the SNR results for all the considered height values in horizontal flights when both scenarios as well as transmit antenna types are considered. The results in Fig. 7.16a corresponding to the Scenario I when the omnidirectional antenna is used show that the SNR is low when the RPA is close to the transmit antenna, then the SNR increases sharply till its maximum and, finally, decreases when the distance between the RPA and the transmit antenna increases. There are cases in which the SNR increases for the points close to the transmit antenna (e.g., flight heights of 15 m or 35 m) because the first transmitted frames could not be detected, thus the SNR estimation is not available. The trend of the SNR curves is similar in most of the cases, although for large height flight values (e.g., 75 m or 105 m) the SNR at the points close to the transmit antenna is noticeably lower (although the effect is not so apparent for longer distances). Finally, the cases with a height flight equal to 60 m and 90 m perform

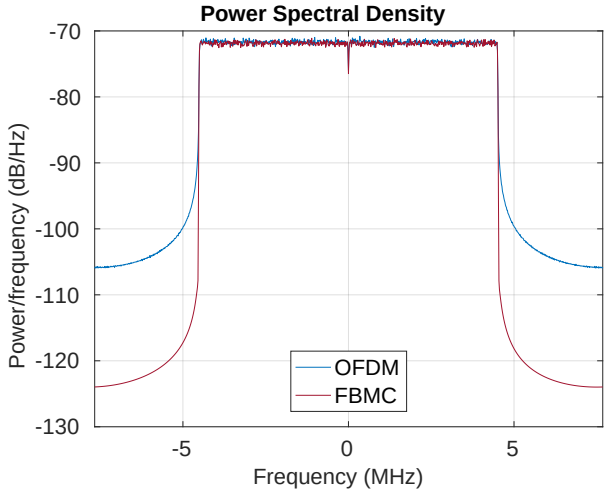

Figure 7.15: Power Spectral Density for OFDM and FBMC transmit signals.

clearly different than the others. In both cases, for distances close to the transmit antenna, the performance is very poor (the received frames could not be detected), whereas for larger distances the performance is significantly better than for the other height values.

Fig. 7.16b shows the results for the omnidirectional antenna in the Scenario II. The observed effects are similar to those in Fig. 7.16, although in accordance with the results shown in Fig. 7.8, leading to peak SNR values reduced about 5 dB regardless of the considered height. Again, the maximum SNR values are not measured at the points closer to the transmit antenna. Moreover, such maximum SNR values are noticeably far away from the transmitter with respect to the results in Scenario I (see Fig. 7.16). Similarly to the Scenario I, the cases with a flight height equal to 60 m and 90 m perform differently.

Figs. 7.16c and 7.16d are similar but for the cases in which the sector antenna is employed. Many of the comments mentioned regarding the Scenario I (Fig. 7.16a) are still valid. However, it can be seen that for the extreme height values (15 m and 105 m) the performance is now much worse, especially for the latter one, whereas the best performance (at least for the points not very far away from the transmitter) occurs at 25 m and 35 m flight heights. The cases corresponding to the heights of 60 m and 90 m present a similar behavior to the one described for the omnidirectional antenna (see Figs. 7.16 and 7.16b), although for 90 m height is even more extreme now. Note that, for most of the height values, the sector (directive) antenna provides no SNR gain. The Scenario II for the sector transmit antenna is considered in Fig. 7.16d. In this case, performance for the heights equal to 105 m and 75 m is not low as in other cases and the peak SNR values are comparable to those obtained with the omnidirectional transmit antenna (see Fig. 7.16b). However, the presence of a local maximum in the SNR for distances not so close to the transmit antenna can be appreciated (as before) for the height values equal to 60 m and 90 m, and also for 35 m and 45 m. Actually, even for other height values, some not so obvious local maximums can be distinguished.

Fig. 7.17 shows the performance results in terms of throughput for different heights, both

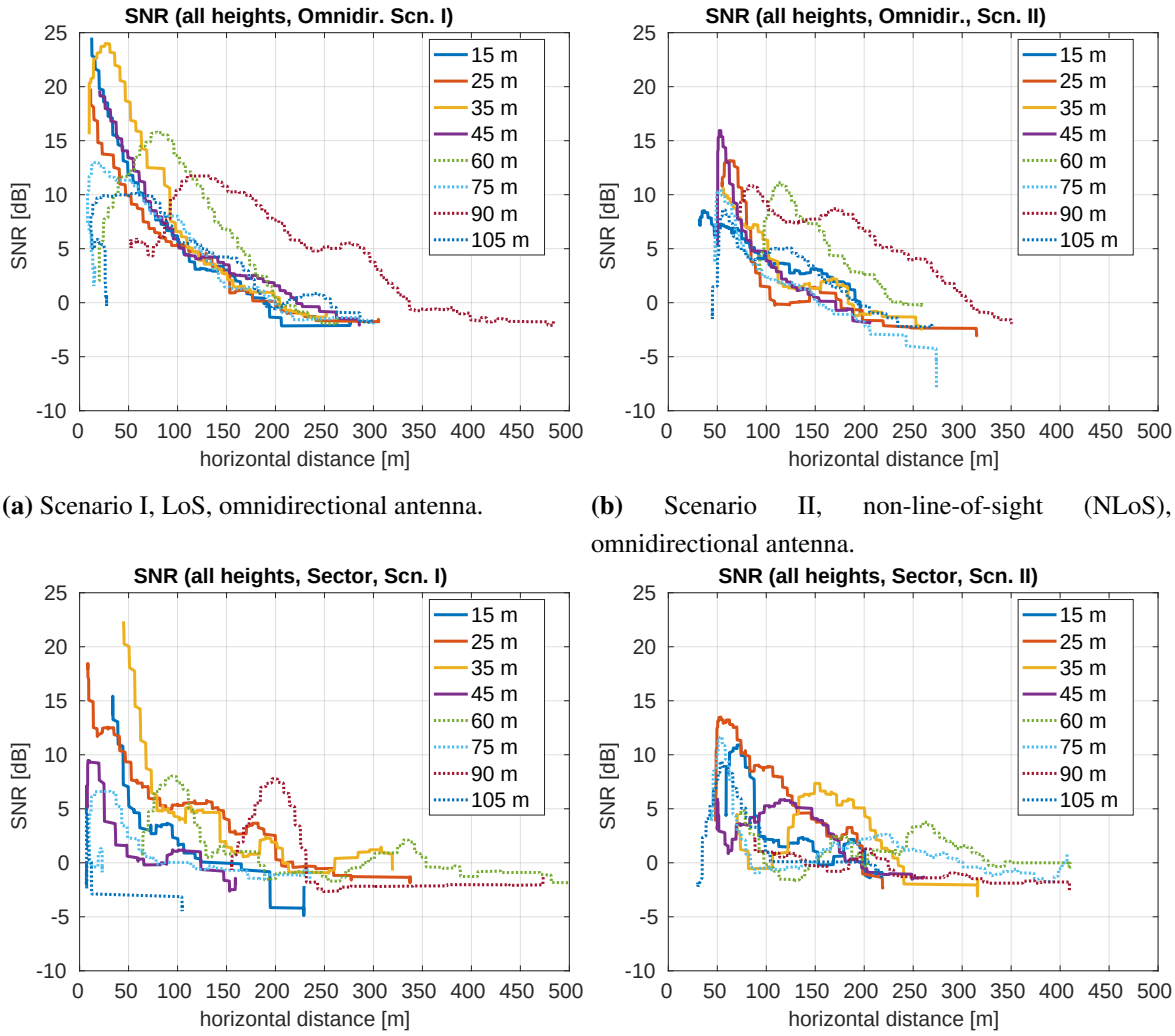

(a) Scenario I, LoS, omnidirectional antenna.

(b) Scenario II, non-line-of-sight (NLoS), omnidirectional antenna.

(c) Scenario I, LoS, sector antenna.

(d) Scenario II, NLoS, sector antenna.

Figure 7.16: SNR results for horizontal flights at different height values between 15 m and 105 m for both scenarios and antenna types.

transmit antenna types, and both measured scenarios. Not surprisingly, the trends of the throughput curves are similar to those of the SNR shown in Fig. 7.16. Hence, the behaviors described there are valid for the throughput evaluations.

7.3.4 Results for Vertical Flights

Fig. 7.18 shows the SNR results for all the vertical flights in the down direction for both transmit antenna types when transmitting an OFDM signal (the results for the up flight direction are similar). Notice that the vertical flight at a horizontal distance of 100 m was not measured for the sector transmit antenna due to technical problems with the RPA. The X-axes of the plots represent the instantaneous flight height value.

The results in Fig. 7.18 exhibit a strong dependency with the height and the antenna type

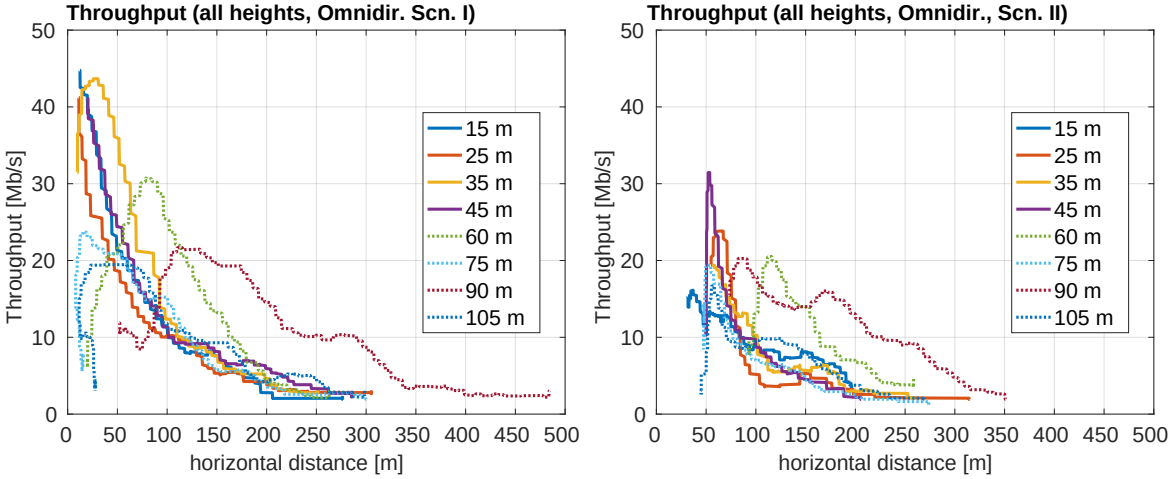

(a) Scenario I, omnidirectional antenna.

(b) Scenario II, omnidirectional antenna.

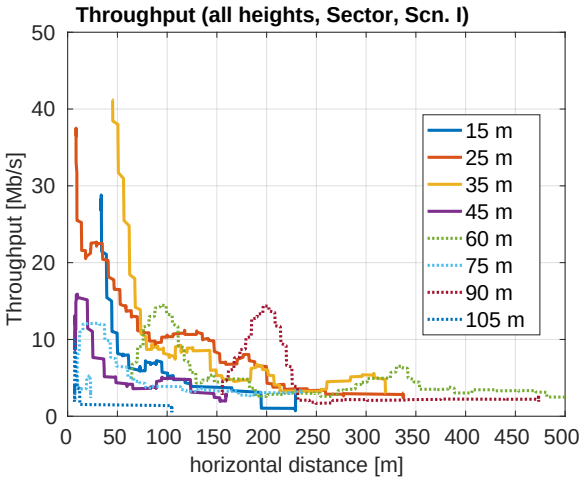

(c) Scenario I, directional antenna.

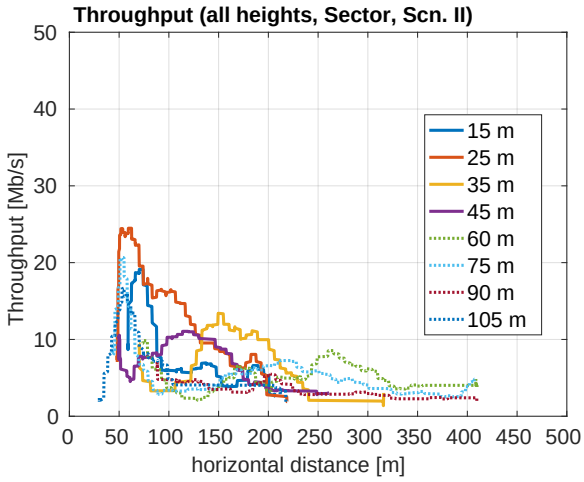

(d) Scenario II, directional antenna.

Figure 7.17: Throughput results for horizontal flights in both scenarios at different flight height values between 15 m and 105 m.

employed. A very noticeable SNR drop can be appreciated for the maximum horizontal distance to the transmitter (100 m) with respect to the other two cases (25 m and 50 m). For both transmit antenna types, the performance is better when the height values are moderate at the horizontal distance of 25 m, while the optimum height values increase for the horizontal distance of 50 m. However, in the case of the omnidirectional antenna, the changes in performance with height are much less abrupt. The best performing height range for a horizontal distance of 25 m is about $[40, 60]$ m in this case, whereas for the directional antenna the range reduces to the $[30, 40]$ m range. This is consistent with the narrower expected beamwidth of the sector transmit antenna with respect to the omnidirectional one. For the case of the flight at a horizontal distance of 50 m, the best performing height range for the omnidirectional antenna is about $[60, 100]$ m, whereas for the sector antenna the range becomes $[40, 60]$ m. As mentioned before, the reduction of the performance with height is much more obvious for the case of the sector antenna, which is coherent with its radiation pattern. Once more, throughput results shown in

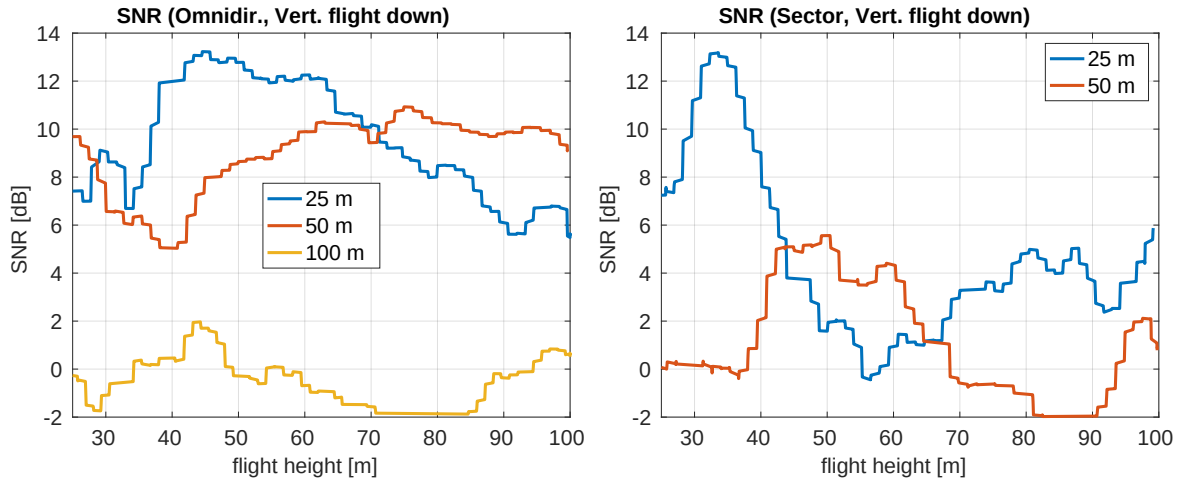

(a) SNR for the omnidirectional antenna

(b) SNR for the directional antenna

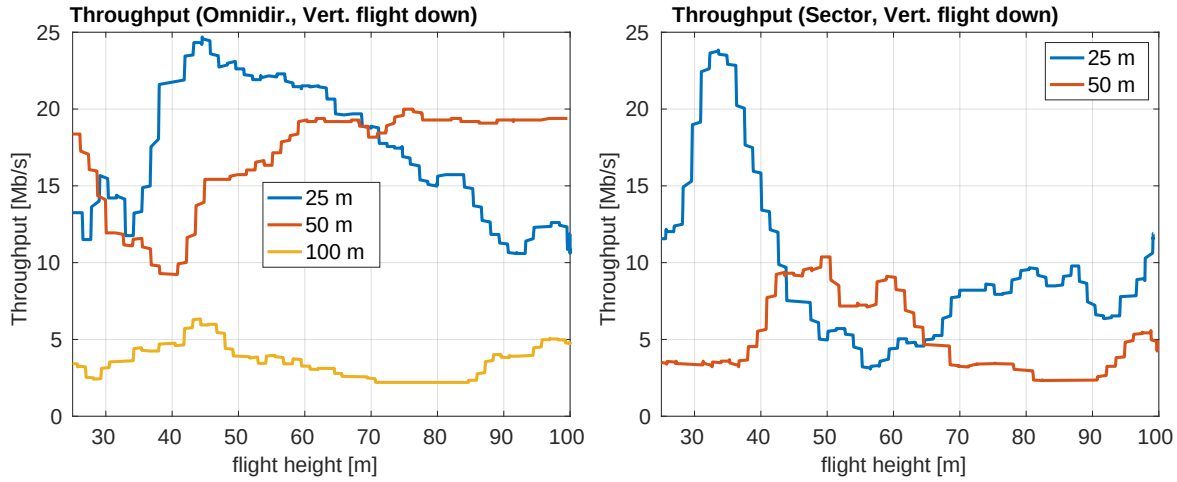

(c) Throughput for the omnidirectional antenna

(d) Throughput for the directional antenna

Figure 7.18: SNR and throughput results in the Scenario I for vertical flights at the horizontal distances of 25 m, 50 m and 100 m. Both the omnidirectional and the sector transmit antennas are employed.

Figs. 7.18c and 7.18d are in accordance with those of SNR.

Based on the presented results, one may think that there is no advantage when using a sector (directive) transmit antenna with respect to the omnidirectional one. However, note that the gain values both at the transmitter and receiver sites were calibrated to maximize the dynamic range without saturating the receiver nor the transmit power amplifier and such gain values were kept fixed during the whole measurement campaign. Consequently, if an AGC would have been employed at the receiver, the received power could be increased for high height values. However, it is clear that a single fixed sector antenna is not the optimum choice to serve an RPA. Moreover, in our experiment the antenna was not down-tilted. In the case of antennas devoted to terrestrial users, they are usually down-tilted to maximize the coverage for ground users and limit the interference to neighboring cells. In this sense, it is expected that the results shown in Figs. 7.18b and 7.18d become even less favorable for high heights, especially when the RPA is close to the base station antenna.

7.4 Conclusions

The main conclusions of this chapter are summarized below:

- A complex A2G measurement campaign was performed in a systematic way and including the evaluation of different parameters, such as the horizontal distance to the transmitter, the flight height, the radiation pattern of the transmit antenna, the MCS, and the density of obstructions in the scenario. The influence of such parameters on different performance metrics such as the SNR, coded and uncoded BER, and throughput has been analyzed. With the aim of drastically increasing the value of this study we also considered waveforms proposed for 5G systems. More specifically, both OFDM and FBMC with the Hermite pulse were employed.
- The obtained results are significantly affected by the radiation pattern of the transmit antennas employed and, in several situations, the omnidirectional antenna outperforms the sector one.
- The considered scenario also impacts on the results. Even when the obstructions (e.g., buildings) are noticeably lower than the flight height, they can cause a non-negligible SNR loss with respect to when there are no obstacles.
- For low distance values to the transmitter, the uncoded BER can be well approximated by an analytical curve corresponding to the AWGN case with identical receive SNR. For larger distances, an abrupt increase of the uncoded BER can be appreciated, being the results much higher than the ones corresponding to a flat Rayleigh channel case.
- When the channel coding is considered, the lowest MCS values enable the correction of almost all the errors when the frames are detected. Coded BER results also show that, even for not so large distances between the transmitter and the RPA, only low MCSs values ensure a highly reliable communications link with a low latency.
- Throughput results are almost perfectly correlated with the receive SNR.
- Results for FBMC exhibit almost the same performance in terms of coded BER as the OFDM ones. A slight gain in terms of throughput is appreciated due to the absence of cyclic prefix. From a different perspective, no performance loss is appreciated when using FBMC with respect to the OFDM case. However, due to the much better spectral efficiency of FBMC with respect to OFDM, the number of occupied subcarriers can be increased satisfying the same spectral mask as OFDM.
- For almost all the flight height values, a common trend exhibited by the SNR with respect to the horizontal distance to the transmitter are appreciated. For the closest points to the transmitter, the SNR is usually low and increases sharply with the distance up to its maximum. Next, it progressively reduces its value with the distance. There are two height values that perform clearly different than the others, which are $60\,\mathrm{m}$ and $90\,\mathrm{m}$. In those cases, the peaks in the SNR curves are reached for longer distances to the transmitter. This way, the performance is definitely superior for longer horizontal distances with respect to

the other cases.

- When a sector antenna is used, the performance is worse for the extreme height values due to the radiation pattern of the antenna, obtaining the best results for moderate heights such as 25 m or 35 m. The same effects described previously for heights equal to 60 m and 90 m can be appreciated and, under some circumstances (e.g., measurements at the Scenario II), similar effects also occur for flight heights between 35 m and 45 m.
- The results for the vertical flights show a strong dependency with the height as well as the transmit antenna radiation pattern. A large performance difference is observed between the cases at horizontal distances to the transmitter equal to 25 m and 50 m and the one at 100 m. For both transmit antenna types, the range of heights maximizing the performance becomes higher when the horizontal distance to the transmitter is increased. However, the performance change with respect to the height is more abrupt when the sector antenna is used.
- It is clear that a single fixed sector antenna can be a bad choice to serve an RPA if a wide range of flight heights is expected. Moreover, in our experiment the antenna was not down-tilted. In the case of antennas devoted to terrestrial users, they are usually down-tilted to maximize the coverage for ground users and to limit the interference to neighboring cells. In this sense, it is expected that the results be even less favorable for RPAs served by commercial LTE deployments for ground users, especially when RPAs are close to the base station.

Chapter VIII

Conclusions and Future Work

In this work, a complete characterization of wireless channels was first presented for the cases of a high-speed train, a subway in a station of the Madrid Metro, and a vehicle-to-infrastructure scenario. The channel response was characterized assessing different parameters such as the signal-to-noise ratio (SNR), the K-factor, the power delay profile (PDP), etc. Then, filter bank multicarrier (FBMC) was evaluated experimentally. We initially considered the evaluation of FBMC in high-speed environments, and compared it with the performance of orthogonal frequency-division multiplexing (OFDM). Then, we analyzed the performance of FBMC and OFDM in the practical use case of a remotely piloted aircraft (RPA). In this final chapter, Section 8.1 presents the main conclusions, whereas Section 8.2 proposes some future study lines.

8.1 Conclusions

Channel characterization is essential when planning wireless communication deployments. In this thesis we devoted three entire chapters to the characterization of channels in three different scenarios: high-speed trains, subways, and vehicle-to-infrastructure (V2I) in roads. In this regard, the rapid evolution of nowadays wireless communication systems constitutes a challenge for their versatile and flexible evaluation by means of over-the-air transmissions under different scenarios. In order to perform many different kinds of measurement campaigns and evaluate wireless communication systems, a testbed and a modular link-level simulator, named GTEC Testbed and GTEC 5G Simulator, respectively, were developed at the GTEC group of the University of A Coruña. The GTEC Testbed and the GTEC 5G Simulator were presented in Chapter 2. The testbed and the simulator were used to obtain many of the results presented along the thesis. We showed the overall structure of the link-level simulator as well as the details of its main blocks, and how the simulator is fully integrated with the GTEC Testbed, enabling us to perform evaluations both by means of simulations and by over-the-air measurements. Finally, we described how to use the simulator, including the typical workflow followed during

a measurement campaign.

Once the GTEC Testbed and the GTEC 5G simulator were presented, we characterized the channel responses for the three aforementioned scenarios. First of all, we provided in Chapter 3 the complete and detailed channel characterization of the downlink (frequency-division duplex (FDD) Long Term Evolution (LTE) for the 10 MHz profile) between a commercial LTE Evolved Node B (eNodeB) and a train moving at high velocities along a track in commercial operation in a rural area of Spain, considering a carrier frequency of 2.6 GHz. The downlink channel characterization consisted in assessing the path loss, the SNR, the K-factor, the PDP, the delay spread, and the Doppler power spectral density (PSD) for different train speeds. In this scenario, a large penetration loss was observed for the case of an indoor receiver. This would justify the utilization of a relay scheme for provisioning services to the users in a practical deployment. For a receiver placed on the top of the train, results showed that there was a strong line-of-sight (LoS), but we observed periodic abrupt transitions in the Doppler PSD along the whole measured path. Such transitions —similar to the ones occurring when the train passes by in front of the eNodeB antennas— were mainly caused by the masts supporting the overhead line. This showed that, although there was a strong LoS for the considered environment, reflections caused by the railway infrastructure elements may lead to noticeable Doppler components in other frequencies.

We provided in Chapter 4 the channel characterization of the wireless channel response of a modern subway station and its corresponding entrance tunnel in the Madrid Metro. An LTE eNodeB transmitter was setup in the middle of the platform to cyclically transmit standard-compliant FDD LTE signals at a carrier frequency of 2.6 GHz with a bandwidth of 10 MHz. The train moved at a constant speed of 18 km/h from the entrance tunnel to the end of the station where it completely stopped. We investigated two different links, an eNodeB-train link and an eNodeB-mobile one. As in the case of Chapter 3, we also characterized the channel in terms of the the path loss, the SNR, the K-factor, the PDP, the delay spread, and the Doppler PSD, and additionally we also assessed the small-scale fading distribution. The results showed that the eNodeB-mobile link, in which the receive antennas are inside the train carriage, has a large penetration loss. We observed a significant change in the propagation channel characteristics when the train enters the station, i.e., the root mean square (RMS) delay spread changes significantly from the tunnel to the station. Finally, The calculated K-factor values for the eNodeB-mobile link were low (less than 0 dB most of the time). However, K-factor values for the eNodeB-train link exceeded 0 dB most of the time, indicating the presence of a dominant path in the signal.

The remainder scenario in which we characterized the channel is a V2I one, which was presented in Chapter 5. In this case we studied, by means of 2.6 GHz LTE measurements, the V2I communications channel between a single-antenna base station transmitter installed in the second floor of a building and a car equipped with four omni-directional receive antennas. The measurements were carried out on a road at the University of A Coruña. During the

measurements, the car moved along the road at 20 km/h during 161 m. The wireless channel was characterized based on the SNR per antenna, the PDP, the Doppler PSD, the RMS delay spread, and the diversity gain for different antenna configurations considering selection combining (SC), equal gain combining (EGC), and maximum ratio combining (MRC) antenna combining methods. The results showed distinct propagation characteristics along the path where the measurements were carried on. In our case, the receive antennas experienced a noticeable SNR difference between them and, together with strong LoS conditions, simple antenna combining methods like SC provided a significant gain, while requiring much less signal processing compared to more complex schemes such as EGC or MRC.

After presenting the work on channel characterization, we devoted the remaining chapters to assess the performance of FBMC waveforms. In Chapter 6 we assessed the downlink performance of FBMC (considering Hermite and PHYDYAS prototype pulses), as well as OFDM. We performed over-the-air measurements at low speeds and used a previously proposed technique to emulate the results for the high-speed case. This way, we evaluated the bit error rate (BER) (coded and uncoded) and the throughput by using the aforementioned modulation techniques. The emulated speeds range from 200 to 500 km/h being typical in high-speed train scenarios. The obtained results showed, on the one hand, that the main performance degradation sources were the SNR of the link and the speed of the mobile receiver. In terms of BER, it was shown that for high speeds (exceeding 300 km/h), FBMC can be a better choice than OFDM when well localized prototype filters, both in time and in frequency, are employed, e.g., the Hermite pulse. However, for practical high-speed train velocities (around 300 km/h) the performance difference was not significant. Moreover, the throughput of FBMC was higher due to the improved spectral efficiency.

Finally, we assessed in Chapter 7 the downlink performance for FBMC, as well as for OFDM, considering the practical use case of an RPA. Several parameters were taken into account for the measurement campaign such as the horizontal distance to the transmitter, the flight height, the radiation pattern of the transmit antenna (we considered a sector and an omnidirectional antenna), the modulation and coding scheme (MCS) or the density of obstructions in the scenario (we considered two scenarios). The influence of such parameters on different performance metrics, such as the SNR, coded/uncoded BER or throughput, was analyzed. With respect to FBMC, the BER results showed an almost identical performance to OFDM, although the throughput of FBMC was higher because of the improved spectral efficiency. In general, the results showed that the system performance is greatly affected by the radiation pattern of the antennas employed. When the transmit sector antenna is used, the performance degrades for the extreme height values due to the small vertical beamwidth of the antenna. However, in several of the other situations, the omnidirectional antenna outperformed the sector one. The considered scenario also affected the results. In this regard, when obstructions (e.g., buildings) are noticeably lower than the flight height, they can cause a non-negligible SNR loss with respect to the case of not being present. We could see how

the channel coding was able to correct almost all the errors when the lowest MCS values were considered. Therefore, we concluded that a single fixed sector antenna is a bad choice to serve RPAs if a wide range of flight heights is expected. Moreover, in our experiment the antenna was not down-tilted. In the case of antennas devoted to terrestrial users, they are usually down-tilted to maximize the gain for ground users and limit the interference to neighboring cells. In this sense, it is expected that the results would be even less favorable for RPAs served by a commercial LTE deployment for ground users, especially when the RPA is close to the base station.

8.2 Future Work

A large number of ideas presented in this thesis can be further investigated. In the ensuing subsections we present some possible future study lines.

8.2.1 High-Speed Train Channel Modeling

In Chapter 3 we characterized the downlink between an LTE eNodeB and a high-speed train based on measurements carried out in a commercial high-speed train line. The channel was characterized by assessing the path loss, the SNR, the K-factor, the PDP, the delay spread, and the Doppler PSD for different train speeds. This characterization was done by means of the estimated channels from the LTE downlink frames. More advanced high resolution parameter estimation (HRPE) algorithms, such as the space-alternating generalized expectation-maximization (SAGE) one [FLE+99], could be used to estimate the parameters of the channel. The proposed SAGE algorithm in [FLE+99] requires knowing the transmitted signals, and in our case we did not know them. However, it should be possible to derive a SAGE algorithm to estimate the channel from the pilot symbols of the LTE signals. This would allow us to analyze better the characteristics of the channel and build better channel models of the scenario.

8.2.2 High-Speed Emulation

In Chapter 6 the performance of OFDM and FBMC was experimentally assessed in high-speed scenarios. For performing this analysis, we used a technique to induce the effects caused by highly time-varying channels on multicarrier signals while conducting measurements at low speeds. However, the technique currently used has the disadvantage of modifying the transmitted signal (the signal is interpolated) and thus the observed communication channel is not the same (a much narrower bandwidth is observed). In order to avoid this problem, a different approach can be applied. Instead of using a measurement-only approach, we could use a hybrid approach. First, estimate the channel along a given path at low speeds by means of over-the-air measurements. Next, the estimated channels are modified to obtain equivalent

high-speed channels. Finally, these new equivalent high-speed channels are used to perform simulations. Theoretically, by using this approach we could assess accurately the performance of communication systems for a given scenario and any desired speed.

8.2.3 Air-to-Ground Communications with Lightweight Remotely Piloted Aircrafts

In Chapter 7 we assessed the performance of OFDM and FBMC signals —in terms of coded and uncoded BER and throughput— in the downlink of two air-to-ground suburban scenarios at the carrier frequency of 2.5 GHz and considering quasi-omnidirectional as well as sector transmit antennas at the ground station. However, only a small percentage of the acquired signals was analyzed. For instance, in Chapter 7 we only have shown the data corresponding to the 2.5 GHz carrier frequency, although we have recorded data for five different carrier frequencies ranging from 800 MHz to 3500 MHz. Moreover, in the same measurement campaign, pseudo-noise (PN) signals were also transmitted to characterize the channel. Using these data, we could obtain channel models and correlate the effects seen in the performance of the system with the effects observed in the communication channel.

8.2.4 5G Communication Systems

The new standards for fifth generation (5G) communications are already being released. Among others, 5G will introduce significant new features, such as the usage of new millimeter wave frequency bands (24-86 GHz) or the usage of massive multiple-input-multiple-output (MIMO). In addition to this, 5G will introduce new use cases for communications. Hence, experimental evaluations will be required to assess the performance of these new systems. In this thesis, we have only considered experimental evaluations at a carrier frequency of 2.6 GHz (2.5 GHz for the case of the results shown in Chapter 7). Therefore, some of these new features can be considered as future research lines from an experimental evaluation perspective.

Appendix I

Resumen de la Tesis

Los servicios multimedia y basados en datos experimentaron un crecimiento ininterrumpido en los últimos años, y se espera que crezcan aún más en los próximos años. Las personas utilizan cada vez más sus dispositivos móviles para acceder a servicios de datos con fines relacionados con el trabajo, el entretenimiento o la socialización en línea. Además, las comunicaciones masivas de tipo máquina también están en aumento (por ejemplo, comunicaciones de transporte y logística, sensores, servicios de Internet de las cosas, etc.) y serán muy importantes para la nueva generación de sistemas de comunicaciones sin hilos. Para hacer frente al aumento esperado en el uso de servicios multimedia y basados en datos, así como para soportar nuevos casos de uso que no son posibles hoy en día, se requiere una nueva generación de sistemas de comunicaciones sin hilos. Para esto, se espera que el estándar 5G aporte las mejoras necesarias: mayores tasas de datos, menores latencias, mejor eficiencia energética, alta fiabilidad, etc.

El conocimiento de las características del canal sin hilos es una base fundamental para la planificación de redes de comunicaciones sin hilos y el diseño de transceptores. Como primer paso, centramos este trabajo en la caracterización completa del canal para diferentes escenarios, tales como trenes de alta velocidad, metro, y comunicaciones vehículo a infraestructura (V2I) en carreteras. El canal se caracterizó por medio de la relación señal a ruido (SNR), la pérdida de trayecto (path loss) y los llamados parámetros condensados de canal (por ejemplo, el factor K, el perfil potencia-retardo (power delay profile) y la densidad espectral de potencia Doppler).

Además, para la nueva interfaz aérea de las redes 5G, una de las preguntas principales ha sido la forma de onda a usar. Finalmente, el 3rd Generation Partnership Project (3GPP) decidió usar la tecnología de multiplexación por división de frecuencias ortogonales (OFDM por sus siglas en inglés). Esto es una elección lógica, debido a las muchas ventajas exhibidas por OFDM y dado que también es la técnica de modulación empleada en las redes 4G. Sin embargo, en los últimos años, los esquemas de multiportadoras basados en bancos de filtros (FBMC por sus siglas en inglés) han recibido una gran atención como una alternativa a OFDM debido a sus ventajas: no usan un prefijo cíclico (lo que proporciona una mayor eficiencia espectral), los usuarios no necesitan sincronizarse en el enlace ascendente, y presentan un mejor rendimiento teórico en escenarios de alta velocidad debido a una menor interferencia entre subportadoras.

En este trabajo hemos comparado experimentalmente el rendimiento de FBMC y OFDM en entornos de alta velocidad. También hemos analizado el rendimiento de FBMC y OFDM en el caso de uso práctico de un vehículo aéreo tripulado remotamente (RPA). La mayor parte del trabajo llevado a cabo en esta tesis ha requerido el diseño y desarrollo del denominado GTEC 5G Simulator, que se ha utilizado junto con el GTEC Testbed para realizar la mayoría de las campañas de medidas y evaluaciones de rendimiento por medio de transmisiones por aire.

A.1 Caracterización Experimental de Canales de Comunicaciones sin Hilos

El primer resultado de este trabajo ha sido la caracterización de canales de comunicaciones para tres escenarios distintos: un tren de alta velocidad, un metro, y un escenario vehículo a infraestructura (V2I) en carretera. A continuación se resume cada una de ellas.

A.1.1 Trenes de Alta Velocidad

Las comunicaciones ferroviarias se pueden dividir en dos grupos: (a) señalización de control del tren y comunicaciones relacionadas con la seguridad; y (b) comunicaciones no críticas, tanto para el personal del tren como para los pasajeros. Si bien el primer tipo de comunicaciones generalmente no requiere altas tasas de datos, a su vez impone restricciones estrictas sobre la calidad del servicio (QoS). Los requisitos operativos y funcionales para el entorno ferroviario requieren, de hecho, latencias o tiempos de establecimiento de llamada reducidos, así como interrupciones de servicio muy reducidas. El segundo tipo de comunicaciones ferroviarias exige un mayor rendimiento (por ejemplo, acceso a servicios multimedia), pero no impone requisitos tan estrictos en términos de fiabilidad.

Hoy en día, la tecnología más utilizada para la señalización de control y comunicaciones de seguridad entre trenes se basa en GSM para Ferrocarriles (GSM-R) y requiere un despliegue de red específico con estaciones base ubicadas a lo largo de la vía. GSM-R, que se basa en la vetusta tecnología del Sistema Global de Comunicaciones Móviles (GSM), proporciona un canal de comunicación continuo entre el controlador del tren y los controladores de tierra, y es ideal para realizar llamadas de emergencia, llamadas telefónicas selectivas o transmisión de datos pequeños. Sin embargo, GSM-R tiene capacidades reducidas para soportar servicios más avanzados, como el piloto automático o la provisión de comunicaciones de banda ancha al personal del tren.

Teniendo en cuenta el gran éxito del estándar Long Term Evolution (LTE) en la evolución de las redes móviles, parece razonable considerar a LTE como el mejor candidato para sustituir a GSM-R como la tecnología fundamental para las comunicaciones ferroviarias, así como para proporcionar servicios a los pasajeros. El primer paso para migrar GSM-R a LTE es evaluar el rendimiento de dicho sistema de comunicaciones para el entorno ferroviario.

En esta tesis presentamos una caracterización completa y detallada del canal del enlace descendente entre un eNodeB[1] comercial y un tren que se mueve a altas velocidades a lo largo de una vía en funcionamiento en un área rural en España, considerando una frecuencia de portadora de 2.6 GHz.

El eNodeB se instaló en la misma ubicación donde estaba desplegada una estación base GSM-R. Consideramos dos enlaces: uno entre el eNodeB y antenas ubicadas en el techo del tren, y el enlace directo entre el eNodeB y un receptor dentro del tren. Con respecto a nuestro hardware, se utilizaron dos nodos del GTEC Testbed como receptores para adquirir los datos de transmisión y se equiparon con módulos GPS. La caracterización del canal del enlace descendente consistió en evaluar la pérdida de trayecto (path loss), la SNR, el factor K, el perfil potencia-retardo (PDP), y la densidad de potencia espectral Doppler para diferentes velocidades de tren. Suponiendo un modelo simplificado de distancia logarítmica, estimamos el exponente de la pérdida de trayecto y la varianza del desvanecimiento de media y pequeña escala. Aunque el exponente de pérdida de trayecto resultó ser muy similar en todos los casos (antenas receptoras interiores y exteriores), se observó una gran pérdida de penetración para el receptor interior. Esto justificaría la utilización de un esquema de retransmisión para el suministro de servicios a los usuarios en una implementación práctica. Para el caso del enlace externo (entre el eNodeB y las antenas exteriores), el factor K mostró la presencia de un componente de línea de visión directa dominante a lo largo de la vía. Las mismas conclusiones se obtuvieron a partir de los resultados del PDP. Uno de los efectos más importantes observados en el escenario fueron las transiciones abruptas y periódicas en la densidad espectral de potencia Doppler a lo largo de toda la trayectoria medida. Dichas transiciones, similares a las que ocurren cuando el tren pasa frente a las antenas del eNodeB, son causadas principalmente por los mástiles que soportan la catenaria. Esto muestra que, aunque hay una línea de visión directa fuerte para el entorno considerado, las reflexiones causadas por los elementos de la infraestructura ferroviaria pueden dar lugar a componentes Doppler notables en otras frecuencias.

A.1.2 Estación Moderna de Metro

Con el continuo crecimiento y expansión de las ciudades, los metros están ganando importancia, ya que se considera que es el sistema de transporte más eficiente para los desplazamientos de personas. Durante el transporte, las personas emplean de forma intensiva dispositivos móviles para trabajar, acceder a redes sociales o para fines de entretenimiento. Los vehículos también producen datos móviles, que merecen especial consideración por las aplicaciones relacionadas con la seguridad, ya que imponen requisitos estrictos en aspectos como la fiabilidad y baja latencia, aunque exigen rendimientos relativamente bajos. Además, se requieren comunicaciones radio para proporcionar servicios de voz y basados en datos tanto a los usuarios

[1]El eNodeB es el componente de LTE encargado de proveer la interfaz de capa física con los dispositivos móviles.

del metro como al personal.

Los cables radiantes son una de las tecnologías más populares para proporcionar comunicaciones sin hilos en túneles. Aunque no requieren sofisticados modelos de canal para la planificación del sistema, no son fiables en caso de incendio, ya que romperían las comunicaciones en todo el túnel. Además, los cables radiantes son bastante caros para los sistemas que operan a altas frecuencias de portadora, a la vez que el mantenimiento se vuelve tedioso una vez que los túneles están en funcionamiento. Usar antenas en lugar de cables radiantes resuelve esos problemas. Las antenas ofrecen un mantenimiento más fácil, un límite de frecuencia superior mucho más alto, una distancia mayor entre los repetidores y son diez veces más baratas de desplegar. Sin embargo, las antenas requieren modelos de canal más sofisticados para el diseño y la planificación del sistema para garantizar que se cumplan los requisitos de QoS.

Hemos realizado una caracterización del canal inalámbrico a $2.6\,\text{GHz}$ en la estación "La Almudena" del metro de Madrid y su túnel de entrada. Consideramos una antena de transmisión ubicada en el centro del andén y dos conjuntos de antena receptoras ubicados, respectivamente, dentro y fuera del metro. Nombramos a estos enlaces como eNodeB-móvil y eNodeB-tren, respectivamente. Transmitimos señales estándar LTE con una frecuencia de portadora de $2.6\,\text{GHz}$ y un ancho de banda de $10\,\text{MHz}$. Durante las mediciones, el tren se desplazaba a una velocidad constante de $18\,\text{km/h}$ desde el túnel de entrada hasta detenerse por completo al final de la estación.

La caracterización del canal se llevó a cabo en función del PDP, la dispersión de retardo, la densidad espectral de potencia Doppler, la distribución del desvanecimiento a pequeña escala y el factor K. Los resultados mostraron que el enlace eNodeB-móvil, en el que las antenas de recepción se encuentran dentro del vagón del tren, es el más desafiante, principalmente debido a las pérdidas por penetración. Los resultados también mostraron cómo las propiedades de propagación cambian significativamente cuando el tren entra en la estación. Por ejemplo, la dispersión del retardo cambia significativamente del túnel a la estación. Respecto a la densidad espectral de potencia Doppler, debe tenerse en cuenta que en realidad se trata de una agregación de diferentes contribuciones, principalmente la frecuencia de portadora y el ancho de banda de señal, la velocidad del tren, el entorno de propagación y los patrones de radiación de las antenas de transmisión y recepción. En este caso, las antenas receptoras altamente directivas en el enlace eNodeB-tren bloquean la componente de línea de visión directa al final de la trayectoria del tren, lo que conduce a una densidad de potencia espectral Doppler ampliamente dispersa. Finalmente, para caracterizar el desvanecimiento a pequeña escala, se utilizó el método del criterio de información de Akaike (AIC) para encontrar la distribución con el mejor ajuste. El análisis reveló que el desvanecimiento a pequeña escala se ajusta mejor mediante una distribución de tipo Rice para ambos enlaces (eNodeB-móvil y eNodeB-tren) y para toda la trayectoria del tren. Los valores del factor K calculados para el enlace eNodeB-móvil fueron bajos (menos de $0\,\text{dB}$ la mayor parte del tiempo). Sin embargo, los valores de factor K para el

enlace eNodeB-tren excedieron los 0 dB la mayor parte del tiempo, lo que indica la presencia de un trayecto de propagación dominante en la señal.

A.1.3 Escenario Vehículo a Infraestructura

Las comunicaciones V2I y de vehículo a vehículo (V2V) se orientan, respectivamente, al intercambio de información sobre el estado de la infraestructura o entre vehículos. Tanto V2I como V2V son tecnologías fundamentales en el contexto del llamado sistema inteligente de control de tráfico (ITCS). Más específicamente, V2I permitirá la gestión efectiva del tráfico mediante la transmisión de información tal como la longitud pronosticada de la cola del vehículo. Además, debido al crecimiento ininterrumpido de los servicios multimedia y basados en datos, los pasajeros utilizarán V2I para conectarse mientras se desplazan con fines relacionados con el trabajo, el entretenimiento o la socialización. Sin embargo, la notable reducción del rendimiento experimentada por los enlaces V2I en ausencia de línea de visión directa sigue siendo un desafío por resolver. Por otro lado, existen propuestas para usar relés móviles como una manera de proporcionar cobertura a los pasajeros dentro de los vehículos y, por lo tanto, exigir mayores velocidades de datos V2I.

Hemos estudiado, mediante medidas a 2.6 GHz con señales LTE, el canal de comunicaciones V2I entre una estación base transmisora de una sola antena instalada en el segundo piso de un edificio y un automóvil equipado con cuatro antenas receptoras omnidireccionales. Las mediciones se llevaron a cabo en una carretera del campus de la Universidad de A Coruña. Durante las mediciones, el automóvil se movió a lo largo de la carretera a 20 km/h durante 161 m. El canal inalámbrico se caracterizó en función de los siguientes parámetros: la SNR, el PDP, la densidad espectral de potencia Doppler, la dispersión de retardo y la ganancia de diversidad para diferentes configuraciones de antena considerando los métodos de combinación de antena “selection combining” (SC), “equal gain combining” (EGC) y “maximum ratio combining” (MRC). Los resultados mostraron que se podían observar diferentes características de propagación a lo largo del camino donde se realizaban las mediciones. Los resultados de PDP, Doppler PSD y la dispersión de retardo mostraron que había dos secciones en la ruta donde la señal se veía afectada por componentes multitrayecto significativos mientras que el resto de la ruta presentaba condiciones de propagación con clara línea de visión directa. En cuanto a los resultados de diversidad, de entre todas las configuraciones consideradas, EGC y MRC exhibieron un rendimiento mejor que SC. Sin embargo, MRC solo superó ligeramente a EGC. En general, el rendimiento de SC se acercó más al de EGC y MRC cuando aumentó el número de componentes multitrayecto (línea de visión directa débil). En promedio, podríamos observar una ganancia de aproximadamente 1 dB al aumentar de dos a tres antenas. Para regiones con una línea de visión directa fuerte, se observaron ganancias similares al aumentar de tres a cuatro antenas. Sin embargo, en nuestro caso, cuando aumenta el número de componentes multitrayecto, la ganancia de diversidad

se reduce. En casos como el presentado en este capítulo, en el que las antenas receptoras experimentan una notable diferencia de SNR entre ellas, y en condiciones de fuerte línea de visión directa, los esquemas de combinación simples como SC proporcionan una ganancia significativa, mientras que requieren de mucho menos procesamiento de señal en comparación con esquemas como EGC o MRC.

A.2 Evaluación Experimental del Rendimiento de FBMC

Otro de los trabajos llevados a cabo en esta tesis es el análisis experimental del rendimiento de sistemas FBMC. En primer lugar se ha realizado un análisis del rendimiento de FBMC en entornos estáticos y de alta velocidad. Finalmente, se ha analizado también el rendimiento de FBMC para el caso práctico de un vehículo aéreo no tripulado. En todos los análisis se ha considerado también el esquema de modulación OFDM con fines comparativos.

A.2.1 Entornos de Alta Velocidad

OFDM es un esquema de modulación ampliamente utilizado en las comunicaciones sin hilos debido a su robustez frente al multitrayecto del canal. Desafortunadamente, la forma rectangular en el dominio del tiempo de los símbolos OFDM produce una respuesta en frecuencia con importantes lóbulos laterales, causando así interferencia entre portadoras. Más recientemente, los esquemas FBMC se han propuesto como una alternativa a OFDM debido a su mejor eficiencia espectral y mayor número de grados de libertad para definir filtros prototipo bien localizados en frecuencia.

En esta tesis analizamos primero el rendimiento de FBMC en entornos estáticos. Las formas de onda OFDM también se han evaluado con fines comparativos. Mostramos resultados basados en simulación considerando diferentes modelos de canal estandarizados, y también de evaluaciones experimentales (por medio de transmisiones por aire) en escenarios de oficinas. Se evaluaron dos de los filtros prototipo propuestos para FBMC, el definido por el proyecto PHYDYAS y el llamado pulso de Hermite.

A continuación centramos nuestra atención en entornos de alta velocidad. En teoría, FBMC ofrece una mejor optimización para canales que exhiben simultáneamente selectividad en tiempo y frecuencia. Por lo tanto, aunque se espera que FBMC supere a OFDM en escenarios doblemente selectivos, se requieren análisis basados en mediciones para validar las predicciones teóricas. Desafortunadamente, realizar mediciones a altas velocidades (por ejemplo en un tren de alta velocidad) es extremadamente costoso y requiere de mucha antelación para su preparación. Para mitigar este problema propusimos y validamos previamente una técnica para emular altas velocidades mediante la inducción de sus efectos en señales multiportadoras (como OFDM y FBMC), mientras que las mediciones se realizarían a velocidades mucho más asequibles.

Se realizaron mediciones por el aire para evaluar el rendimiento de FBMC y OFDM en función de la tasa de errores de bit (BER), la magnitud del vector de error (EVM) y throughput. Las velocidades emuladas oscilan entre 200 y 500 km/h, siendo típicas en los escenarios de trenes de alta velocidad. Los resultados obtenidos muestran, por un lado, que las principales fuentes de degradación del rendimiento son la SNR del enlace y la velocidad del receptor móvil. En términos de BER, se demostró que para velocidades altas (superiores a 300 km/h), FBMC puede ser una mejor opción que OFDM cuando se emplean filtros prototipo bien localizados, tanto en tiempo como en frecuencia, como por ejemplo el pulso de Hermite. Sin embargo, para velocidades prácticas (de hasta 300 km/h) la diferencia de rendimiento no es significativa. Además, la eficiencia espectral de FBMC es mayor que la de OFDM debido a la ausencia del prefijo cíclico.

A.2.2 Comunicaciones Aire-Tierra con un Vehículo Aéreo no Tripulado

Históricamente, los RPAs se usaban principalmente para operaciones militares en entornos hostiles. En los últimos años, el costo y el tamaño de los RPAs han disminuido significativamente, lo que los ha hecho más accesibles para aplicaciones de propósito general, como operaciones de búsqueda y rescate, transporte, monitorización y vigilancia del clima, etc. Otro caso importante de uso para vehículos aéreos no tripulados es actuar como relés para estaciones base (BS) en entornos congestionados o como respaldo temporal después de daños en la infraestructura de red, que es uno de los escenarios clave considerados para los sistemas de quinta generación (5G).

Los RPA están limitados por la ley en muchos países a vuelos con línea de visón directa y con una altura máxima entre 100 y 150 m. Por lo tanto, bajo estas condiciones, las redes celulares estándar podrían usarse para soportar comunicaciones de RPA. La viabilidad de servir RPAs con implementaciones de redes LTE de uso general ha sido reconocida como una prioridad por el 3rd Generation Partnership Project (3GPP).

Hemos llevado a cabo una campaña de medición transmitiendo señales OFDM y FBMC y hemos realizado una evaluación mediante figuras de mérito de alto nivel como la BER, la SNR, o el throughput. Durante la campaña de medidas, realizamos varios vuelos con un RPA variando diferentes parámetros. Por un lado, se realizaron vuelos horizontales considerando 8 valores de altura diferentes, que van desde 15 m hasta 105 m, para dos escenarios suburbanos diferentes con diferente densidad de obstáculos. Por otro lado, también se consideraron vuelos verticales, con distancias horizontales al transmisor desde 20 m hasta 100 m. Para estudiar el efecto del patrón de radiación de la antena de transmisión, se consideraron dos antenas, una antena omnidireccional y una estación base típica (direccional).

Los resultados mostraron que el rendimiento del sistema se ve muy afectado por el patrón de radiación de las antenas utilizadas. Cuando se utiliza una antena direccional, el rendimiento es peor para los valores de alturas extremos debido a la pequeña anchura del haz vertical de la

antena. Sin embargo, en muchas de las otras situaciones, la antena omnidireccional superó a la direccional. El escenario considerado también afectó los resultados. A este respecto, cuando las obstrucciones (por ejemplo, edificios) son notablemente más bajas que la altura del vuelo, pueden causar una pérdida de SNR no despreciable con respecto al caso de no estar presente. Pudimos ver cómo la codificación del canal pudo corregir casi todos los errores cuando se consideraron los valores más bajos del esquema de modulación y codificación (MCS). Los resultados de rendimiento obtenidos se correlacionaron casi perfectamente con los de SNR para cualquiera de las mediciones realizadas; de esta manera, el rendimiento se podía estimar fácilmente midiendo la SNR en el receptor. En cuanto a FBMC, el rendimiento en términos de BER fue casi idéntico al de OFDM. Se aprecia una ligera ganancia en términos de tasa de bit debido a la ausencia de prefijo cíclico. Desde otra perspectiva, no se aprecia pérdida de rendimiento cuando se utiliza FBMC con respecto a OFDM. Teniendo en cuenta estos resultados, está claro que una sola antena direccional fija podría ser una mala elección para dar servicio a RPA si se espera que se considere una amplia gama de alturas de vuelo. Además, uno puede considerar que en nuestro experimento la antena no estaba inclinada. En el caso de las antenas dedicadas a usuarios terrestres, generalmente están inclinadas hacia abajo para maximizar la ganancia hacia los usuarios de tierra y limitar la interferencia a las células vecinas. En este sentido, se espera que los resultados sean aún menos favorables para los RPAs servidos por un despliegue comercial terrestre de LTE, especialmente cuando los RPAs estén cerca de la estación base.

Appendix II

List of Acronyms

3G third generation
4G fourth generation
5G fifth generation
3GPP 3rd Generation Partnership Project
A2G air-to-ground
ADC analog to digital converter
ADIF Spanish Railway Infrastructure Administrator
AGC automatic gain control
AIC Akaike's information criteria
AoA angle of arrival
AP auxiliary pilot
AP access point
AWGN additive white gaussian noise
BER bit error rate
BS base station
CAP coded auxiliary pilot
CDF cumulative distribution function
CNPC control and non-payload communications
CP cyclic prefix
DAC digital to analog converter
DC direct current
DVB-T Digital Video Broadcasting - Terrestrial
eMBB enhanced mobile broadband
EGC equal gain combining
eNodeB Evolved Node B
ERTMS/ETCS European rail traffic management system/European train control system
ETCS European Train Control System
EVM error vector magnitude

FBMC filter bank multicarrier
FDD frequency-division duplex
FEC forward error correction
FFT fast Fourier transform
GO geometric optics
GPS Global Positioning System
GSM Global System for Mobile Communications
GSM-R GSM for Railways
GTIS GTEC Testbed interface software
HRPE high resolution parameter estimation
HST high-speed train
IBx indoor office b
ICI inter-carrier interference
IFFT inverse fast Fourier transform
IoT Internet of things
IMT-Advanced international mobile telecommunications advanced
ISI inter-symbol interference
ITCS intelligent traffic control system
ITU-R ITU Radiocommunication Sector
KP kilometric point
LoS line-of-sight
LTE Long Term Evolution
MCM multi carrier modulation
MCS modulation and coding scheme
MIMO multiple-input-multiple-output
ML maximum likelihood
MMSE minimum mean square error
mMTC massive machine-type communications
MRC maximum ratio combining
MSE mean square error
NLoS non-line-of-sight
NMEA National Marine Electronics Association
NR new radio
OFDM orthogonal frequency-division multiplexing
OQAM offset quadrature amplitude modulation
PAx outdoor-to-indoor and pedestrian A
pdf probability density function
PDP power delay profile
PN pseudo-noise

PPS pulse per second
PSD power spectral density
P-SCH Primary Synchronization Signal
QAM quadrature amplitude modulation
QoS quality of service
RMS root mean square
RF radio frequency
SAGE space-alternating generalized expectation-maximization
SC selection combining
SISO single-input-single-output
SMT staggered multitone
S-SCH Secondary Synchronization Signal
SNR signal-to-noise ratio
STBC space-time block code
TDD time-division duplex
TUx typical urban channel model
RPA remotely piloted aircraft
UHD USRP™ hardware driver
URLLC ultra-reliable and low-latency communications
USRP™ Universal Software Radio Peripheral
V2I vehicle-to-infrastructure
V2V vehicle-to-vehicle
VoIP voice over Internet Protocol
VSWR voltage standing wave ratio
WiMAX Worldwide Interoperability for Microwave Access
ZF zero-forcing

References

[3GPa] 3GPP. *TS 36.101: E-UTRA; User Equipment (UE) radio transmission and reception*. Tech. rep.

[3GPb] 3GPP. *TS 36.211 V14.2.0: E-UTRA; Physical channel and modulation*. Tech. rep.

[3GPc] 3GPP. *TS 36.213 V14.2.0: E-UTRA; Physical layer procedures*. Tech. rep.

[ABB+15] Taimoor Abbas, Jörg Nuckelt, Thomas Kürner, Thomas Zemen, Christoph F Mecklenbräuker, and Fredrik Tufvesson. "**Simulation and measurement-based vehicle-to-vehicle channel characterization: accuracy and constraint analysis**". *IEEE Transactions on Antennas and Propagation*, vol. 63, no. 7, 2015, pp. 3208–3218.

[AG84] Jean Alias and P Gentil. ***La voie ferrée: techniques de construction et d'entretien***. Eyrolles, 1984.

[AI+09] B. Ai, Z. D. Zhong, G. Zhu, and J. P. Liu. "**Novel statistical processing methods for wireless field strength prediction**". *Proc. of Proc. of IET International Communication Conference on Wireless Mobile and Computing (CCWMC 2009)*. 2009, pp. 129–132.

[AI+11] B. Ai, Z. D. Zhong, G. Zhu, and M. Zhao. "**Novel statistical criteria for local mean power estimation in wireless coverage prediction**". *Antennas Propagation IET Microwaves*, vol. 5, no. 5, 2011, pp. 596–604. ISSN: 1751-8725.

[AI+14] Bo Ai, Xiang Cheng, Thomas Kürner, Zhang-Dui Zhong, Ke Guan, Rui-Si He, Lei Xiong, David W Matolak, David G Michelson, and Cesar Briso-Rodriguez. "**Challenges toward wireless communications for high-speed railway**". *IEEE transactions on intelligent transportation systems*, vol. 15, no. 5, 2014, pp. 2143–2158.

[AKA74] Hirotugu Akaike. "**A new look at the statistical model identification**". *IEEE Transactions on Automatic Control*, vol. 19, no. 6, 1974, pp. 716–723.

[ALA01] Michel Alard. **Construction of a multicarrier signal**. US Patent 6,278,686. 2001.

[AMI+10]
Pooyan Amini, Chung Him Yuen, Rong-Rong Chen, and Behrouz Farhang-Boroujeny. "**Isotropic filter design for MIMO filter bank multicarrier communications**". *Proc. of Sensor Array and Multichannel Signal Processing Workshop (SAM), 2010 IEEE*. IEEE. 2010, pp. 89–92.

[ANA] Analog Devices, Inc. **Analog devices AD9361 RFIC**. Online access: http://www.analog.com/en/rfif-components/rfif-transceivers/ad9361/products/product.html.

[BA03] Kenneth P Burnham and David R Anderson. ***Model selection and multimodel inference: a practical information-theoretic approach***. Springer Science & Business Media, 2003.

[BAC16] Ben Benzaman, Abdulla Al-Dhaheri, and David Claudio. "**Discrete event simulation of green supply chain with traffic congestion factor**". *Proc. of Proc. of Winter Simulation Conference (WSC), 2016*. IEEE. 2016, pp. 1654–1665.

[BEL+10] M Bellanger, D Le Ruyet, D Roviras, M Terré, J Nossek, L Baltar, Q Bai, D Waldhauser, M Renfors, T Ihalainen, et al. *FBMC physical layer: a primer*. Tech. rep. PHYDYAS FP7 Project Document, 2010.

[BER+09] Paolo Bernardi, Diego Caratelli, Renato Cicchetti, Vincenzo Schena, and Orlandino Testa. "**A numerical scheme for the solution of the vector parabolic equation governing the radio wave propagation in straight and curved rectangular tunnels**". *IEEE Transactions on Antennas and Propagation*, vol. 57, no. 10, 2009, pp. 3249–3257.

[CAI+16] Xuesong Cai, Xuefeng Yin, Xiang Cheng, and Antonio Pérez Yuste. "**An empirical random-cluster model for subway channels based on passive measurements in umts**". *IEEE Transactions on Communications*, vol. 64, no. 8, 2016, pp. 3563–3575.

[CGR11] Sebastian Caban, Jose A. Garcia-Naya, and Markus Rupp. "**Measuring the physical layer performance of wireless communication systems: Part 33 in a series of tutorials on instrumentation and measurement**". *IEEE Instrumentation and Measurement Magazine*, vol. 14, no. 5, 2011, pp. 8–17. ISSN: 1094-6969. DOI: 10.1109/MIM.2011.6041377.

[CHO+06] Myung-Sun Choi, Do-Youn Kim, Han-Shin Jo, Jong-Gwan Yook, and Han-Kyu Park. "**Path-loss characteristics in subway tunnels at 2.65 GHz**". en. *Microwave and optical technology letters*, vol. 48, no. 2, 2006, pp. 383–386. ISSN: 0895-2477, 1098-2760. Online access: http://doi.wiley.com/10.1002/mop.21357 (visited on 10/31/2017).

[CHO+09] Chien-Ming Chou, Chen-Yuan Li, Wei-Min Chien, and Kun-chan Lan. "**A feasibility study on vehicle-to-infrastructure communication: WiFi vs. WiMAX**". *Proc. of Proc. of 10th International Conference on Mobile Data Management: Systems Services and Middleware 2009 (MDM'09)*. IEEE. 2009, pp. 397–398.

[CJ96] Shin-Hon Chen and Shyh-Kang Jeng. "**SBR image approach for radio wave propagation in tunnels with and without traffic**". *IEEE Transactions on Vehicular Technology*, vol. 45, no. 3, 1996, pp. 570–578.

[CUI+15] W. Cui, D. Qu, T. Jiang, and B. Farhang-Boroujeny. "**Coded auxiliary pilots for channel estimation in FBMC-OQAM systems**". *IEEE Transactions on Vehicular Technology*, vol. PP, no. 99, 2015, pp. 1–1. ISSN: 0018-9545.
DOI: 10.1109/TVT.2015.2448659.

[DA+] Beman Dawes, David Abrahams, et al. **Boost C++ libraries**. Online access: http://www.boost.org/.

[DER78] Louis Deryck. "**Natural propagation of electromagnetic waves in tunnels**". *IEEE Transactions on Vehicular Technology*, vol. 27, no. 3, 1978, pp. 145–150.

[DEV89] Pierre Devaux. ***Les chemins de fer***. Presses universitaires de France, 1989.

[DID+00] D. Didascalou, T. M. Schafer, F. Weinmann, and W. Wiesbeck. "**Ray-density normalization for ray-optical wave propagation modeling in arbitrarily shaped tunnels**". *IEEE Transactions on Antennas and Propagation*, vol. 48, no. 9, 2000, pp. 1316–1325. ISSN: 0018-926X.

[DOM+16a] Tomás Domínguez-Bolaño, José Rodríguez-Piñeiro, José A. García-Naya, and Luis Castedo. "**Experimental evaluation of 5G modulation schemes in quasi-static scenarios**". *Proc. of 20th International ITG Workshop on Smart Antennas (WSA 2016)*. Munich, Germany, 2016.

[DOM+16b] Tomás Domínguez-Bolaño, José Rodríguez-Piñeiro, José A. García-Naya, and Luis Castedo. "**The GTEC 5G link-level simulator**". *Proc. of International Workshop on Link- and System-Level Simulations (IWSLS2 2016)*. Vienna, Austria, 2016, pp. 64–69.

[DOM+17a] Tomás Domínguez-Bolaño, José Rodríguez-Piñeiro, José Antonio García-Naya, and Luis Castedo. "**Experimental characterization and modeling of LTE wireless links in high-speed trains**". *Wireless Communications and Mobile Computing*, vol. 2017, no. 5079130, 2017, pp. 1–20.
DOI: 10.1155/2017/5079130.

[DOM+17b] Tomás Domínguez-Bolaño, José Rodríguez-Piñeiro, José Antonio García-Naya, and Luis Castedo. "**Throughput-based performance evaluation of 5G-candidate waveforms in high speed scenarios**". *Proc. of 25th European Signal Processing Conference (EUSIPCO 2017)*. Kos, Greece, 2017.

[DOM+18a] Tomás Domínguez-Bolaño, José Rodríguez-Piñeiro, José Antonio García-Naya, Xuefeng Yin, and Luis Castedo. "**Measurement-based characterization of train-to-infrastructure 2.6 GHz propagation channel in a modern subway station**". Accepted in *IEEE Access*, 2018.

[DOM+18b] Tomás Domínguez-Bolaño, José Rodríguez-Piñeiro, José Antonio García-Naya, Xuefeng Yin, and Luis Castedo. "**Vehicle-to-infrastructure channel characterization based on LTE measurements**". *Proc. of 19th IEEE International Workshop on Signal Processing Advances in Wireless Communications (SPAWC 2018)*. Kalamata, Greece, 2018.

[DUD+07] Donald G Dudley, Samir F Mahmoud, Martine Lienard, and Pierre Degauque. "**On wireless communication in tunnels**". *Proc. of Antennas and Propagation Society International Symposium, 2007 IEEE*. IEEE. 2007, pp. 3305–3308.

[ELS75] ALFRED Emslie, ROBERT Lagace, and PETER Strong. "**Theory of the propagation of UHF radio waves in coal mine tunnels**". *IEEE Transactions on Antennas and Propagation*, vol. 23, no. 2, 1975, pp. 192–205.

[EUR10] European Economic Interest Group European Rail Traffic Management System. **ETCS/GSM-R Quality of Service – operational analysis**. ERTMS Std. 04E117. 2010.

[FAB95] Bernard Le Floch, Michel Alard, and Claude Berrou. "**Coded orthogonal frequency division multiplex [tv broadcasting]**". *Proceedings of the IEEE*, vol. 83, no. 6, 1995, pp. 982–996.

[FAR11] Behrouz Farhang-Boroujeny. "**OFDM versus filter bank multicarrier**". *Signal Processing Magazine, IEEE*, vol. 28, no. 3, 2011, pp. 92–112.

[FEI+16] Dan Fei, José Rodríguez-Piñeiro, José Antonio García-Naya, Luis Castedo, and Lei Xiong. "**TD-LTE downlink performance assessment in high speed scenarios**". *Proc. of 2016 IEEE 83rd Vehicular Technology Conference (VTC2016-Spring)*. Accepted at the track named "2nd International Workshop on Wireless Communications for High Speed Railways (HSRCom2016)". Nanjing, China, 2016.

[FLE+99] Bernard H Fleury, Martin Tschudin, Ralf Heddergott, Dirk Dahlhaus, and K Ingeman Pedersen. "**Channel parameter estimation in mobile radio environments using the SAGE algorithm**". *IEEE Journal on Selected Areas in Communications*, vol. 17, no. 3, 1999, pp. 434–450.

[FOR+13] Arghavan Emami Forooshani, Shahzad Bashir, David G Michelson, and Sima Noghanian. "**A survey of wireless communications and propagation modeling in underground mines**". *IEEE Communications Surveys and Tutorials*, vol. 15, no. 4, 2013, pp. 1524–1545.

[FRA+15] Paula Fraga-Lamas, José Rodríguez-Piñeiro, José A. García-Naya, and Luis Castedo. "**Unleashing the potential of LTE for next generation railway communications**". *Proc. of 8th International Workshop on Communication Technologies for Vehicles (Nets4Cars / Nets4Trains / Nets4Aircraft 2015)*. Sousse, Tunisia, 2015, pp. 153–164.
DOI: 10.1007/978-3-319-17765-6_14.

[FRE] Free Software Foundation, Inc. **GNU general public license (version 3)**. Online access: https://www.gnu.org/licenses/gpl-3.0.html.

[GME99] Larry J Greenstein, David G Michelson, and Vinko Erceg. "**Moment-method estimation of the Ricean K-factor**". *IEEE Communications Letters*, vol. 3, no. 6, 1999, pp. 175–176.
DOI: 10.1109/4234.769521.

[GRO+13] European RPAS Steering Group et al. "**Roadmap for the integration of civil remotely-piloted aircraft systems into the European aviation system**". *European RPAS Steering Group, Tech. Rep*, 2013.

[GUA+12] Ke Guan, Zhangdui Zhong, José I Alonso, and Cesar Briso-Rodríguez. "**Measurement of distributed antenna systems at 2.4 GHz in a realistic subway tunnel environment**". *IEEE Transactions on Vehicular Technology*, vol. 61, no. 2, 2012, pp. 834–837. ISSN: 0018-9545.

[HB97] Ralf Haas and Jean-Claude Belfiore. "**A time-frequency well-localized pulse for multiple carrier transmission**". *Wireless Personal Communications*, vol. 5, no. 1, 1997, pp. 1–18.

[HE+11a] Ruisi He, Zhangdui Zhong, Bo Ai, and Jianwen Ding. "**An empirical path loss model and fading analysis for high-speed railway viaduct scenarios**". *IEEE antennas and wireless propagation letters*, vol. 10, 2011, pp. 808–812.

[HE+11b] Ruisi He, Zhangdui Zhong, Bo Ai, Lei Xiong, and Hong Wei. "**A novel path loss model for high-speed railway viaduct scenarios**". *Proc. of Wireless Communications, Networking and Mobile Computing (WiCOM), 2011 7th International Conference on*. IEEE. 2011, pp. 1–4.

[HE+13a] R. He, Z. Zhong, B. Ai, J. Ding, Y. Yang, and A. F. Molisch. "**Short-term fading behavior in high-speed railway cutting scenario: measurements, analysis, and statistical models**". *IEEE Transactions on Antennas and Propagation*, vol. 61, no. 4, 2013, pp. 2209–2222. ISSN: 0018-926X.

[HE+13b] R. He, Z. Zhong, B. Ai, G. Wang, J. Ding, and A. F. Molisch. "**Measurements and analysis of propagation channels in high-speed railway viaducts**". *IEEE Transactions on Wireless Communications*, vol. 12, no. 2, 2013, pp. 794–805. ISSN: 1536-1276.

[HE+13c] Ruisi He, Andreas F Molisch, Zhangdui Zhong, Bo Ai, Jianwen Ding, Ruifeng Chen, and Zheda Li. "**Measurement based channel modeling with directional antennas for high-speed railways**". *Proc. of Wireless Communications and Networking Conference (WCNC), 2013 IEEE*. IEEE. 2013, pp. 2932–2936.

[HE+13d] Ruisi He, Zhangdui Zhong, Bo Ai, Gongpu Wang, Jianwen Ding, and Andreas F Molisch. "**Measurements and analysis of propagation channels in high-speed railway viaducts**". *IEEE Transactions on Wireless Communications*, vol. 12, no. 2, 2013, pp. 794–805.

[HE+15] Ruisi He, Bo Ai, Zhangdui Zhong, Andreas F Molisch, Ruifeng Chen, and Yaoqing Yang. "**A measurement-based stochastic model for high-speed railway channels**". *IEEE Transactions on Intelligent Transportation Systems*, vol. 16, no. 3, 2015, pp. 1120–1135.

[HKJ10] A Hrovat, G Kandus, and T Javornik. "**Four-slope channel model for path loss prediction in tunnels at 400 MHz**". *IET microwaves, antennas & propagation*, vol. 4, no. 5, 2010, pp. 571–582.

[HKJ14] A. Hrovat, G. Kandus, and T. Javornik. "**A Survey of Radio Propagation Modeling for Tunnels**". *IEEE Communications Surveys and Tutorials*, vol. 16, no. 2, 2014, pp. 658–669. ISSN: 1553-877X.

[HR04] Kasun N Hewage and Janaka Y Ruwanpura. "**Optimization of traffic signal light timing using simulation**". *Proc. of 36th conference on Winter simulation*. Winter Simulation Conference. 2004, pp. 1428–1436.

[HUB81] Peter J Huber. ***Robust Statistics***. Wiley-Interscience, 1981.

[IE17a] NTT DOCOMO INC and Ericsson. *New SID on Enhanced Support for Aerial Vehicles*. Tech. rep. 3GPP RP-170779. 2017.

[IE17b] NTT DOCOMO INC and Ericsson. *New WID on Enhanced LTE Support for Aerial Vehicles*. Tech. rep. 3GPP, RP-172669. 2017.

[IL09] Aissa Ikhlef and Jérôme Louveaux. "**An enhanced MMSE per subchannel equalizer for highly frequency selective channels for FBMC/OQAM systems**". *Proc. of Signal Processing Advances in Wireless Communications, 2009. SPAWC'09. IEEE 10th Workshop on*. IEEE. 2009, pp. 186–190.

[ITU17] ITU-R. *ITU-R M.[IMT-2020.TECH PERF REQ] - Minimum Requirements Related to Technical Performance for IMT-2020 Radio Interface(s)*. Tech. rep. ITU-R M.2410-0. 2017.

[ITU97] ITU-R. **Guidelines for evaluation of radio transmission technologies for IMT-2000. ITU-R Recommendation M.1225**. 1997.

[JLR03] Jean-Philippe Javaudin, Dominique Lacroix, and Alexandre Rouxel. "**Pilot-aided channel estimation for OFDM/OQAM**". *Proc. of Vehicular Technology Conference, 2003. VTC 2003-Spring. The 57th IEEE Semiannual*. Vol. 3. IEEE. 2003, pp. 1581–1585.

[KB94] Thomas Klemenschits and Ernst Bonek. "**Radio coverage of road tunnels at 900 and 1800 MHz by discrete antennas**". *Proc. of Personal, Indoor and Mobile Radio Communications, 1994. Wireless Networks-Catching the Mobile Future., 5th IEEE International Symposium on*. Vol. 2. IEEE. 1994, pp. 411–415.

[KK00] Mohammad Haeri Kermani and Mahmuoud Kamarei. "**A ray-tracing method for predicting delay spread in tunnel environments**". *Proc. of Personal Wireless Communications, 2000 IEEE International Conference on*. IEEE. 2000, pp. 538–542.

[KON+99] George D Kondylis, Franco De Flaviis, Gregory J Pottie, and Yahya Rahmat-Samii. "**Indoor channel characterization for wireless communications using reduced finite difference time domain (R-FDTD)**". *Proc. of IEEE VTS 50th Vehicular Technology Conference (VTC 1999-Fall)*. Vol. 3. IEEE. 1999, pp. 1402–1406.

[LAM+12] Paula Fraga Lamas, José Rodríguez-Piñeiro, José A. García-Naya, and Luis Castedo. "**A survey on LTE networks for railway services**". *Proc. of IEEE Congreso de Ingeniería en Electro-Electrónica, Comunicaciones y Computación ARANDUCON 2012*. 2012.

[LEE85] W. C. Y. Lee. "**Estimate of local average power of a mobile radio signal**". *IEEE Transactions on Vehicular Technology*, vol. 34, no. 1, 1985, pp. 22–27. ISSN: 0018-9545.

[LIU+12] Liu Liu, Cheng Tao, Jiahui Qiu, Houjin Chen, Li Yu, Weihui Dong, and Yao Yuan. "**Position-based modeling for wireless channel on high-speed railway under a viaduct at 2.35 GHz**". *IEEE Journal on Selected Areas in Communications*, vol. 30, no. 4, 2012, pp. 834–845.

[LN17] Alcatel-Lucent Shanghai Bell Labs and Nokia. *Evaluation scenarios and channel models for drones*. Tech. rep. R1-1704430. 2017.

[MAR] Mobile Mark. **PSKN3-24/55 omnidirectional antenna**. Online access: http://www.mobilemark.com/download/specification-sheets/gps-multi-band/PSKN3-24-55%20%285-6%20GHz%29-pat.pdf.pdf.

[MAS+09] Emilie Masson, Pierre Combeau, Marion Berbineau, Rodolphe Vauzelle, and Yannis Pousset. "**Radio wave propagation in arched cross section tunnels-simulations and measurements**". *Journal of Communication*, vol. 4, no. 4, 2009, pp. 276–283.

[MEN+16] Rodolfo I Meneguette, PR Geraldo Filho, Daniel L Guidoni, Gustavo Pessin, Leandro A Villas, and Jó Ueyama. "**Increasing intelligence in inter-vehicle communications to reduce traffic congestions: experiments in urban and highway environments**". *PLoS one*, vol. 11, no. 8, 2016, e0159110.

[MIL+12] Vicente Milanes, Jorge Villagra, Jorge Godoy, Javier Simo, Joshué Pérez, and Enrique Onieva. "**An intelligent V2I-based traffic management system**". *IEEE Transactions on Intelligent Transportation Systems*, vol. 13, no. 1, 2012, pp. 49–58.

[MIN] Mini-Circuits. **TVA-11-422 amplifier**. Online access: http://www.minicircuits.com/pdfs/TVA-11-422.pdf.

[MJ09] Richard Martelly and Ramakrishna Janaswamy. "**An ADI-PE approach for modeling radio transmission loss in tunnels**". *IEEE Transactions on Antennas and Propagation*, vol. 57, no. 6, 2009, pp. 1759–1770.

[MLN10] Xiao Hong Mao, Yee Hui Lee, and Boon Chong Ng. "**Statistical modeling of signal variation for propagation along a lift shaft**". *IEEE Antennas and Wireless Propagation Letters*, vol. 9, 2010, pp. 752–755.

[MM14] Arjan Meijerink and Andreas F Molisch. "**On the physical interpretation of the Saleh–Valenzuela model and the definition of its power delay profiles**". *IEEE Transactions on Antennas and Propagation*, vol. 62, no. 9, 2014, pp. 4780–4793.

[MOL12] Andreas F Molisch. ***Wireless communications***. Vol. 34. John Wiley & Sons, 2012.

[MRJ04] J-M Molina-Garcia-Pardo, J-V Rodriguez, and Leandro Juan-Llácer. "**Wide-band measurements and characterization at 2.1 GHz while entering in a small tunnel**". *IEEE Transactions on Vehicular Technology*, vol. 53, no. 6, 2004, pp. 1794–1799.

[MU17] ZTE Microelectronics and Tongji University. *Consideration on the channel model for LTE-based aerial vehicles*. Tech. rep. R1-1705163. 2017.

[MW74] Samir F Mahmoud and James R Wait. "**Geometrical optical approach for electromagnetic wave propagation in rectangular mine tunnels**". *Radio Science*, vol. 9, no. 12, 1974, pp. 1147–1158.

[NET04] Technical Specification Group Radio Access Network. *Univerlsal Mobile Telecommunications System (UMTS); Deployment aspects*. Tech. rep. 3GPP 25.943. ETSI, 2004.

[NET12] Technical Specification Group Radio Access Network. *Mobile Relay for E-UTRA*. Tech. rep. 3GPP TR 36.836. 3GPP, 2012.

[NRM17] Ronald Nissel, Markus Rupp, and Roman Marsalek. "**FBMC-OQAM in doubly-selective channels: a new perspective on MMSE equalization**". *Proc. of IEEE International Workshop on Signal Processing Advances in Wireless Communications (SPAWC), Sapporo, Japan*. 2017.

[NSR17] Ronald Nissel, Stefan Schwarz, and Markus Rupp. "**Filter bank multicarrier modulation schemes for future mobile communications**". *IEEE Journal on Selected Areas in Communications*, vol. 35, no. 8, 2017, pp. 1768–1782.

[PAR00] John David Parsons. ***The Mobile Radio Propagation Channel***. Wiley, 2000.

[PJJ01] F. M. Pallares, F. J. P. Juan, and L. Juan-Llacer. "**Analysis of path loss and delay spread at 900 MHz and 2.1 GHz while entering tunnels**". *IEEE Transactions on Vehicular Technology*, vol. 50, no. 3, 2001, pp. 767–776. ISSN: 0018-9545.

[POP+18] Petar Popovski, Kasper F Trillingsgaard, Osvaldo Simeone, and Giuseppe Durisi. "**5G wireless network slicing for eMBB, URLLC, and mMTC: a communication-theoretic view**". *arXiv preprint arXiv:1804.05057*, 2018.

[PRO95] Vassilios Profillidis. ***Railway Engineering***. ISBN: 0 291 39828 6. Cambridge University Press, 1995.

[PZ00] A. V. Popov and Ning Yan Zhu. "**Modeling radio wave propagation in tunnels with a vectorial parabolic equation**". *IEEE Transactions on Antennas and Propagation*, vol. 48, no. 9, 2000, pp. 1403–1412. ISSN: 0018-926X.

[RAP+96] Theodore S Rappaport et al. ***Wireless communications: principles and practice***. Vol. 2. Prentice Hall PTR New Jersey, 1996.

[RESa] Ettus Research. **Ettus USRP B210**. Online access: https://www.ettus.com/product/details/UB210-KIT.

[RESb] Ettus Research. **Ettus USRP hardware driver (UHD)**. Online access: http://files.ettus.com/manual/page_uhd.html.

[RM12] Md Masud Rana and Ananda Sanagavarapu Mohan. "**Segmented-locally-one-dimensional-FDTD method for EM propagation inside large complex tunnel environments**". *IEEE Transactions on Magnetics*, vol. 48, no. 2, 2012, pp. 223–226.

[ROD+12] José Rodríguez-Piñeiro, Paula Fraga Lamas, José A. García-Naya, and Luis Castedo. "**LTE security analysis for railway communications**". *Proc. of IEEE Congreso de Ingeniería en Electro-Electrónica, Comunicaciones y Computación ARANDUCON 2012*. 2012.

[ROD+13] José Rodríguez-Piñeiro, José A. García-Naya, Ángel Carro-Lagoa, and Luis Castedo. "**A testbed for evaluating LTE in high-speed trains**". *Proc. of Proc. of 16th Euromicro Conference on Digital System Design (DSD 2013)*. Online access: http://dx.doi.org/10.1109/DSD.2013.27. 2013, pp. 175–182.

[ROD+14] José Rodríguez-Piñeiro, Pedro Suárez-Casal, José A. García-Naya, Luis Castedo, César Briso-Rodríguez, and J. Ignacio Alonso-Montes. "**Experimental validation of ICI-aware OFDM receivers under time-varying conditions**". *Proc. of IEEE 8th Sensor Array and Multichannel Signal Processing Workshop (SAM 2014)*. A Coruña, Spain, 2014.

[ROD+15a] José Rodríguez-Piñeiro, Martin Lerch, José A. García-Naya, Sebastian Caban, Markus Rupp, and Luis Castedo. "**Emulating extreme velocities of mobile LTE receivers in the downlink**". *"EURASIP Journal on Wireless Communications and Networking"*, vol. 2015, no. 106, 2015.

[ROD+15b] José Rodríguez-Piñeiro, Pedro Suárez-Casal, Martin Lerch, Sebastian Caban, Jose A. Garcia-Naya, Luis Castedo, and Markus Rupp. "**LTE downlink performance in high speed trains**". *Proc. of Proc. of 2015 IEEE 81st Vehicular Technology Conference (VTC2015-Spring)*. Glasgow, United Kingdom, 2015, pp. 1–5. ISBN: 9781479980895.

[ROD+16a] José Rodríguez-Piñeiro, Tomás Domínguez-Bolaño, José Antonio García-Naya, and Luis Castedo Ribas. "**Performance assessment of 5G-candidate waveforms in high speed scenarios**". *Proc. of 27th IEEE International Symposium on Personal, Indoor and Mobile Radio Communications (PIMRC'16)*. Valencia, Spain, 2016.

[ROD+16b] José Rodríguez-Piñeiro, Tomás Domínguez-Bolaño, Pedro Suárez-Casal, José Antonio García-Naya, and Luis Castedo Ribas. "**Affordable evaluation of 5G modulation schemes in high speed train scenarios**". *Proc. of ITG Workshop on Smart Antennas (WSA 2016)*. Online access: https://www.vde-verlag.de/proceedings-en/454177072.html. Munich, Germany, 2016.

[ROD+16c] José Rodríguez-Piñeiro, José A. García-Naya, Pedro Suárez-Casal, César Briso-Rodríguez, J. I. Alonso-Montes, and Luis Castedo. "**Assessment of channel propagation conditions for FDD LTE transmissions in the Spanish high-speed railways**". *Proc. of Proc. of 10th European Conference on Antennas and Propagation (EuCAP 2016)*. Davos, Switzerland, 2016.

[ROD+16d] José Rodríguez-Piñeiro, Martin Lerch, Tomás Domínguez-Bolaño, José Antonio García-Naya, Sebastian Caban, and Luis Castedo. "**Experimental assessment of 5G-candidate modulation schemes at extreme speeds**". *Proc. of Ninth IEEE Sensor Array and Multichannel Signal Processing Workshop (SAM 2016)*. Río de Janeiro, Brazil, 2016.

[ROD16] José Rodríguez-Piñeiro. "Broadband wireless communication systems for high mobility scenarios". PhD thesis. Universidade da Coruña, 2016.

[RST16] Markus Rupp, Stefan Schwarz, and Martin Taranetz. ***The Vienna LTE-Advanced Simulators: Up and Downlink, Link and System Level Simulation***. 1st ed. Signals and Communication Technology. Springer Singapore, 2016. ISBN: 978-981-10-0616-6. DOI: 10.1007/978-981-10-0617-3.

[SB03] Thomas Strohmer and Scott Beaver. "**Optimal OFDM design for time-frequency dispersive channels**". *Communications, IEEE Transactions on*, vol. 51, no. 7, 2003, pp. 1111–1122.

[SB07] U. G. Schuster and H. Bolcskei. "**Ultrawideband channel modeling on the basis of information-theoretic criteria**". *IEEE Transactions on Wireless Communications*, vol. 6, no. 7, 2007, pp. 2464–2475. ISSN: 1536-1276.

[SC97] Timothy M Schmidl and Donald C Cox. "**Robust frequency and timing synchronization for OFDM**". *IEEE Transactions on Communications*, vol. 45, no. 12, 1997, pp. 1613–1621.

[SGA12] Alphan Sahin, Ismail Guvenc, and Huseyin Arslan. "**A survey on multicarrier communications: prototype filters, lattice structures, and implementation aspects**". *Communications Surveys & Tutorials, IEEE*, vol. 16, no. 3, 2012, pp. 1312–1338.

[SHG15] Rajeshwari Sundar, Santhoshs Hebbar, and Varaprasad Golla. "**Implementing intelligent traffic control system for congestion control, ambulance clearance, and stolen vehicle detection**". *IEEE Sensors Journal*, vol. 15, no. 2, 2015, pp. 1109–1113.

[SPF13] Michal Simunek, Pavel Pechac, and Fernando P Fontan. "**Feasibility of UAV link space diversity in wooded areas**". *International Journal of Antennas and Propagation*, vol. 2013, 2013.

[SR16] Stefan Schwarz and Markus Rupp. "**Society in motion: challenges for LTE and beyond mobile communications**". *IEEE Communications Magazine*, vol. 54, no. 5, 2016, pp. 76–83.

[STB11] Stefania Sesia, Issam Toufik, and Matthew Baker, eds. ***LTE The UMTS Long Term Evolution from theory to practice***. 2nd. John Wiley & Sons, 2011.

[STI+10] Tobias Hidalgo Stitz, Tero Ihalainen, Ari Viholainen, and Markku Renfors. "**Pilot-based synchronization and equalization in filter bank multicarrier communications**". *EURASIP Journal on Advances in Signal Processing*, vol. 2010, 2010, p. 9.

[SUÁ+14a] P. Suárez-Casal, José Rodríguez-Piñeiro, José A. García-Naya, and Luis Castedo. "**Experimental assessment of WiMAX transmissions under highly time-varying channels**". *Proc. of Eleventh International Symposium on Wireless Communication Systems (ISWCS)*. Barcelona, Spain, 2014, pp. 717–721.
DOI: 10.1109/ISWCS.2014.6933447.

[SUÁ+14b] Pedro Suárez-Casal, José Rodríguez-Piñeiro, José A. García-Naya, and Luis Castedo. "**Experimental evaluation of the WiMAX downlink physical layer in high-mobility scenarios**". *"EURASIP Journal on Wireless Communications and Networking"*, vol. 2015, no. 109, 2014.

[TAO] Taoglas. **M-2G15-120 GA.110.101111 omnidirectional antenna**. Online access: http://taoglas.com/images/product_images/original_images/GA.110.101111.pdf.

[TEA] The GTEC Testbed Project Development Team. **GTEC Testbed Project**. Online access: https://bitbucket.org/tomas_bolano/gtec_testbed_public.git.

[TECa] Technical Specification Group Radio Access Network. *NR; Physical channels and modulation*. Tech. rep. 3GPP TR 38.211. 3GPP.

[TECb] Hyperlink Technologies. **2.4 GHz 14 dBi mast mount flat patch wireless LAN antenna (HG2414P)**. Online access: http://www.l-com.com/multimedia/datasheets/DS_HG2414P.pdf.

[TRA13a] US Department of Transportation. *Integration of civil unmanned aircraft systems (UAS) in the national airspace system (NAS) roadmap*. Tech. rep. 2012-AJG-502. 2013.

[TRA13b] US Department of Transportation. *Unmanned aircraft system (UAS) Service Demand 2015-2035: Literature Review & Projections of Future Usage*. Tech. rep. v.0.1 DOT-VNTSC-DoD-13-01. 2013.

[UBI] Ubiquity. **AM-2G15-120 cross polarized antenna**. Online access: http://dl.ubnt.com/datasheets/airmaxsector/airMAX_Sector_Antennas_DS.pdf.

[VV14] Kimon P Valavanis and George J Vachtsevanos. ***Handbook of unmanned aerial vehicles***. Springer Publishing Company, Incorporated, 2014.

[WAI80] JR Wait. "**Propagation in rectangular tunnel with imperfectly conducting walls**". *Electronics Letters*, vol. 16, no. 13, 1980, pp. 521–522.

[WC 74] Jakes WC Jr. **Microwave mobile communications**. 1974.

[WEI+11] Hong Wei, Zhangdui Zhong, Lei Xiong, Bo Ai, and Ruisi He. "**Study on the shadow fading characteristic in viaduct scenario of the high-speed railway**". *Proc. of Communications and Networking in China (CHINACOM), 2011 6th International ICST Conference on*. IEEE. 2011, pp. 1216–1220.

[WIK] Wikipedia. **Kilometric point**. Online access: https://en.wikipedia.org/wiki/Kilometric_point.

[WYN+09] Shurjeel Wyne, Amit P Singh, Fredrik Tufvesson, and Andreas F Molisch. "**A statistical model for indoor office wireless sensor channels**". *IEEE Transactions on Wireless Communications*, vol. 8, no. 8, 2009.

[YIN+15] Xuefeng Yin, Xuesong Cai, Xiang Cheng, Jiajing Chen, and Meng Tian. "**Empirical geometry-based random-cluster model for high-speed-train channels in UMTS networks**". *IEEE Transactions on Intelligent Transportation Systems*, vol. 16, no. 5, 2015, pp. 2850–2861.

[ZC14] Yonghong Zeng and Meng Wan Chia. "**Joint time-frequency synchronization and channel estimation for FBMC**". *Proc. of IEEE 25th Annual International Symposium on Personal, Indoor, and Mobile Radio Communication (PIMRC 2014)*. IEEE. 2014, pp. 438–442.
DOI: 10.1109/PIMRC.2014.7136205.

[ZHA+14] Yan Zhang, Zunwen He, Wancheng Zhang, Limin Xiao, and Shidong Zhou. "**Measurement-based delay and doppler characterizations for high-speed railway hilly scenario**". *International Journal of Antennas and Propagation*, vol. 2014, 2014.

[ZHA+16a] Lei Zhang, Cesar Briso, Jean Raphaël Olivier Fernandez, José I Alonso, Carlos Rodríguez, Juan Moreno García-Loygorri, and Ke Guan. "**Delay spread and electromagnetic reverberation in subway tunnels and stations**". *IEEE Antennas and Wireless Propagation Letters*, vol. 15, 2016, pp. 585–588.

[ZHA+16b] Lei Zhang, P. Suárez-Casal, Jean Fernandez, José Rodríguez-Piñeiro, J. Calle-Sánchez, Jose A. Garcia-Naya, Luis Castedo, C. Rodríguez-Sánchez, J. Moreno, C. Briso-Rodríguez, and J.I. Alonso-Montes. "**Experimental evaluation of 4G technologies in metro tunnel scenarios**". *Proc. of 10th European Conference on Antennas and Propagation (EuCAP 2016)*. Davos, Switzerland, 2016, pp. 1–5.

[ZHA+17] Lei Zhang, J. Rodríguez-Piñeiro, Jean R.O. Fernández, José A. García-Naya, David W. Matolak, Cesar Briso, and Luis Castedo. "**Propagation modeling for outdoor-to-indoor and indoor-to-outdoor wireless links in high-speed train**". *Measurement*, vol. 110, 2017, pp. 43–52. ISSN: 0263-2241.
DOI: 10.1016/j.measurement.2017.06.014.

[ZHA03] Y. P. Zhang. "**Novel model for propagation loss prediction in tunnels**". *IEEE Transactions on Vehicular Technology*, vol. 52, no. 5, 2003, pp. 1308–1314. ISSN: 0018-9545.

[ZHO+14] Tao Zhou, Cheng Tao, Liu Liu, and Zhenhui Tan. "**A semi-empirical MIMO channel model for high-speed railway viaduct scenarios**". *Proc. of Communications (ICC), 2014 IEEE International Conference on*. IEEE. 2014, pp. 5854–5858.

[ZZL16] Yong Zeng, Rui Zhang, and Teng Joon Lim. "**Wireless communications with unmanned aerial vehicles: opportunities and challenges**". *IEEE Communications Magazine*, vol. 54, no. 5, 2016, pp. 36–42.

[ZZS01] Yue Ping Zhang, Guo Xin Zheng, and JH Sheng. "**Radio propagation at 900 MHz in underground coal mines**". *IEEE Transactions on Antennas and Propagation*, vol. 49, no. 5, 2001, pp. 757–762.